Star Formation and Structure Formation at Redshifts $1 < z < 4$

Thesis by

Kurt L. Adelberger

In partial fulfillment of the requirements

for the degree of

Doctor of Philosophy

California Institute of Technology

Pasadena, California

2002

(Submitted February 22, 2001)

Acknowledgements

At my age Alexander had reached India, Marco Polo had met Kublai Khan, Nietzsche had written the Birth of Tragedy, Charlie Parker had recorded his Mood, Nero had burned Rome, Eisenstein had filmed the Battleship Potemkin, Mozart was completing the Marriage of Figaro, Blake was writing the Songs of Innocence, and Elvis was the undisputed king. My sole accomplishment is this interminable screed. I can't imagine that anyone will feel flattered to be associated with my feat, but humor me. There's a lot that I feel thankful for.

Caltech was a wonderful place to be a grad student. The administration let us lead lives occupied with nothing but thoughts. The department educated and fed us, allowed us to use some of the best telescopes on earth, and supported us with an excellent army of engineers and night assistants. Though Caltech paid my bills, the free and heedless life I enjoyed was founded on the sacrifices, achievements, insights, virtues, and crimes of a thousand generations, was preserved by millions of people I do not know, some of whom were killed, and was financed by contributions from the wealthy, the curious, and the taxed. This small section cannot possibly express how much I owe these strangers.

Most of us are shoddy creations, failed experiments, indifferent drafts; but every now and then god tosses one of his masterpieces down to earth, and I am deeply grateful that several have fallen in my path. MPC, who always had the energy to grab more from life, who recognized early what matters in life, who never let me rest until I was exhausted, who always had a plan, who tolerated my blasphemy, who smuggled

the Nebuchadnezzar to Rialto, who taught me by example whatever I might know about finding happiness—MPC is surely one. His exploits will go down in famy. I am amazed at my good fortune in meeting him when I was only five. Stephen Belton materialized unexpectedly in my 10th grade history class. His excellence became clear five years later when he joined our reindeer games. He never tried but was always better than the rest of us; he suffered fools gladly; he accompanied us on our adventures and remained cheerful and bemused even as they came to the grief he'd foreseen. Daron Standley must have been sent to Claremont to rescue our hapless play. It quickly became obvious that this magnificent Caliban had been raised without parental supervision. He stunned me with unorthodox perceptions, astonished me with bizarre, tenacious, stupid, backward, and unaccountably successful assaults on every obstacle, and influenced my life in ways that I am still struggling to comprehend. Ben Oppenheimer landed in Caltech shortly before my arrival. His exuberance and profane eloquence are a lasting source of inspiration. Natasja Ahlers fell to earth one summer in Missoula. She shone more brightly for a few short moments than the rest of the universe in its life. The days we spent together were a dream that I was afraid would end if I slept. I stumbled across Tom Abel several times before I appreciated his extraordinary qualities. I'm glad I was given the chance. He possesses an immane and relentless appetite for life that makes the rest of us look frail. He introduced me to the pleasures of talking about science. He educated me more in a few evenings at Bukowski's than many professors could in a semester. His spectacularly ebrious existence was a source of amusement and near fatal distraction while this thesis was being completed.

Thanks are also due to Konrad and Derrick. They helped make Mudd tolerable and (with Prof. John Townsend) forcefully persuaded me to do more with life than play piano and hike and ride. Nina, MaryBeth, and Yuka taught me things that I will appreciate until I die. So did Charles despite himself. David Rees introduced

me to the splendors of Journey. David Grosskopf made a mean humus. John, Peter, Froney, and Mike were good friends at MIT and beyond. Life in the Super-D would not have been the same without my officemates Erik, Rob, and especially Josh, whose wit, intelligence, and muscle all helped to control the outbursts of our Tourettic friend from Fundunst. I am sure that Alice's enthusiasm and warm personality have more than compensated Super-D for whatever minuscule loss it suffered when I left. Rosalba made me feel welcome at Harvard and cunningly secured a private office for me. Skating with her provided some of the better moments in these dismal last days of writers' block and doubt. Rupert and Gaitee educated me while we worked and amused me after hours. Sarah showed me a different and strangely beautiful approach to life. Life: everything reminds me that it will end too soon. Our skulls laugh for only a flicker of time in the darkness. But I could not ask for better solace than I have received from these friends.

I hope I will not be abusing this soapbox too badly if I take a minute to express my appreciation of the inhuman. e.g., food, the smell of autumn, the way the city looks at sunrise. Also: The silence of a snowboard flying through powder. Crawdads in Mobile. Wolves on the Noatak. Coffee. Et al. The first hint of hunger on Sunday. Afternoon sunlight through the bedroom blinds. The sound of a canoe on Holland Lake. Tuscany. Wyoming. Music. Pianos. The way love is before it becomes bitter. Turtles at Kee Beach. The picayune scritchyscratch they store in museums. The empty roads of the west. Aja Sofia. Manhattan. Mountain goats at Logan Pass, fog descending on Stony Indian. Aching from the cold Pacific in winter. The Virgin Narrows in thunderstorm and flood. Language. Chevrotains. Jumbo Rocks at midnight. 50 cent beers in Prague. Ella. The Sunday paper. Dissonance. Driftwood fires on Rialto Beach. Skates. The four last songs. I couldn't live without these. Thanks!

Now is the time to thank my family. I can see that I take them for granted.

Sometimes I dwell too much on our shortcomings. But when I think about Sunday afternoons tossing the football with dad, or about answering his math questions from the backseat, or about rafting through Alaska with him, or about any of our dozens of trips together; or when I remember mom teaching me to swim and handle a canoe, or racing the car downhill to make me laugh, weightless on the bumps, or when I remember the way she'd take me to Herfy's, and tell me stories and sing before I slept—all this fills me with a feeling of love and gratitude that my lame writing cannot express. I know that I have been lucky. And not only in my parents. My sister Karen protected me when I was little, taught me to untuck my Izod, and remains a wonderful co-conspirator. My admiration for her is so strong that it occasionally expresses itself as immature jealousy. Public apology extended.

Special thanks go to Chuck Steidel. He was always interested and always encouraging. He knew when to let me think in peace and when to offer criticism. He admitted his rare ignorance as freely as he shared his wide knowledge and that made him the perfect teacher for me. I will never understand why he took a chance on this music school dropout, but it has changed my life forever. My debt to him is difficult to acknowledge and impossible to repay.

Neither this thesis nor anything else would have been possible without Bobbie, the goddess of my idolatry. She loved me at my most abject, gripped me with a passion I could not deserve or understand, taught me everything I know about joy and misery and loss, and convinced me, too late, that nothing matters more than trust and love. She always swore I'd never finish this thesis, but she was wrong. I can smell the last period. It is inevitable. A few more words and it will be done. But I would have happily traded it all to make things different between us.

Abstract

The universe of galaxies beyond redshift one has finally become relatively easy to observe. While only a handful of galaxies with redshifts $z > 1$ were known 10 years ago, more than 2000 have spectroscopic redshifts today. These surveys are beginning to provide us with a detailed view of the first half of cosmic history. Their creation and interpretation is the subject of this thesis. Chapter 1 describes efficient techniques that can be used to locate galaxies at $1 \lesssim z \lesssim 5$ among the numerous foreground and background objects in deep optical images. Chapter 2 characterizes the effects of dust obscuration on the resulting large high-redshift samples. The remainder of the thesis attemps to place star-forming high-redshift galaxies into a larger cosmological context. Chapter 3 investigates the spatial clustering of galaxies at $z \sim 3$, finds it to be strong, and shows that this suggests a close link between rapidly star-forming galaxies and massive virialized objects in the underlying distribution of dark matter. Chapter 4 analyses the curious spatial association of high-redshift galaxies with intergalactic hydrogen and metals, and finds some evidence that the numerous supernova explosions in young galaxies may profoundly affect the evolution of the universe's baryons.

Introduction

An ambitious goal in cosmology is to understand how the universe evolved from its presumed beginning in the Big Bang to the familiar collection of stars and galaxies that we observe around us today. The last decade has seen tremendous progress in understanding the large role that gravitational instability almost certainly played. Although we still do not have complete analytic understanding, reasonable analytic approximations for the growth of gravitationally driven perturbations are now known, and sophisticated N-body simulators and simulations are freely available for obtaining more precise or detailed information. Remarkable progress has also been made in observationally constraining the initial conditions that are required as input to the simulations or approximations. The available data appear largely consistent with the idea that primordial fluctuations were Gaussian (e.g., Bromley & Tegmark 1999) with a power-spectrum similar to that of an adiabatic ΛCDM model over $\gtrsim 5$ orders of magnitude in spatial scale (e.g., de Bernardis *et al.* 2001; White, Efstathiou, & Frenk 1993; Croft et al. 1999).

But gravitational instability is only half—the easy half!—of the story. It alone cannot tell us how or when the stars that populate the universe today were formed. Presumably stars began to form within overdensities in the matter distribution as these overdensities slowly evolved from small ripples in the initial conditions into the large collapsed objects of today, but modeling this has proved tremendously difficult. We cannot easily model the formation of a single star, let alone the ten billion stars in a typical galaxy. Even the most sophisticated theoretical treatments of galaxy

formation rely on simplified "recipes" for associating the formation of stars with the gravitationally driven growth of perturbations in the underlying matter distribution. The adopted recipes for star formation, although physically plausible, are by far the most uncertain component in theoretical treatments of galaxy formation. We will need to check them through observations of star-forming galaxies at high-redshift before we can be confident that our understanding of galaxy formation is reasonably correct. These observations, and their implications, are the subject of my thesis.

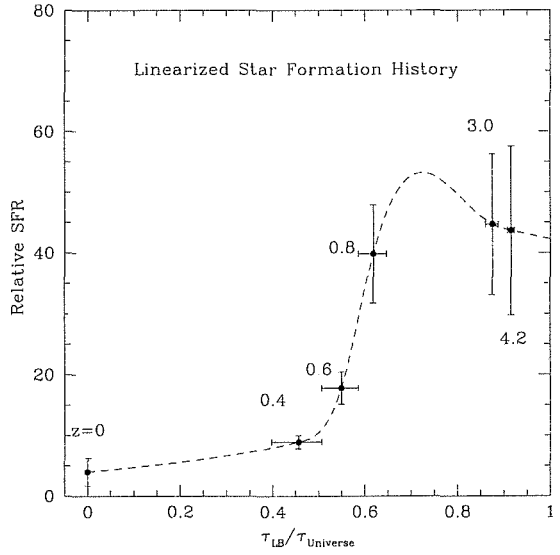

Figure 1 The relative comoving star-formation density in the universe as a function of lookback time, adapted from Steidel *et al.* 1999. The number of stars formed at each time is proportional to the area under the curve. Redshifts corresponding to each lookback time are shown. Most of the stars in the universe appear to have been born in the first half of its history, at redshifts $1 \lesssim z \lesssim 5$.

Recent analyses suggest that the a large fraction of all stars—probably the majority—formed in the first half of the universe's history, at redshifts $1 \lesssim z \lesssim 5$ (e.g., Steidel *et al.* 1999; cf. figure 1). Observing *where* star formation occurs at these redshifts provides the most direct way to constrain empirically the relationship between structure formation and star formation in the universe. Chapter 1 describes simple and efficient strategies that can be used to locate large numbers of galaxies

at these redshifts from among the numerous foreground and background sources in deep optical images. These strategies have given us the first detailed view of star formation at $1 \lesssim z \lesssim 5$.

Because the selection strategies of Chapter 1 rely on observed-frame optical images, they can find only galaxies that are relatively bright in the rest-frame ultraviolet. But most star formation in the local universe is enshrouded by dust that only a small fraction of the ultraviolet photons emitted by newly formed stars are able to penetrate. The photons are usually absorbed instead, and the energy they carried finally emerges as far-infrared thermal radiation from the dust grains. The strong observed association of star formation and dust causes typical star-forming galaxies to emit the bulk of their luminosities in the far-infrared, not the ultraviolet. This has led many to argue that most high-redshift star formation occurred in dusty objects invisible at ultraviolet wavelengths, that only longer wavelength selection strategies can provide a reasonably complete census of galaxy formation (e.g., Barger, Cowie, & Richards 2000). Chapter 2 reviews what is known about dust in star-forming galaxies at low and high redshift, and shows why these arguments are wrong. Dust obscuration strongly affects the ultraviolet luminosities of high-redshift galaxies, but it does not obscure many of them completely.

With Chapter 3 our focus shifts away from the creation and towards the interpretation of high-redshift surveys. Our goal is not merely to find high-redshift galaxies but to place them into the larger context of structure formation in the universe. This remains an unsolved problem. One approach is to measure the spatial clustering of the observed galaxies in an attempt to link them with collapsed objects in the unobserved underlying distribution of dark matter. Numerical simulations and analytic calculations show that gravitational instability produces a strong correlation between the spatial clustering strength and the mass of collapsed "dark matter halos." One might expect the observed galaxies to be associated with dark matter halos that have

a similar spatial clustering strength. If this is the case, the clustering of Lyman-break galaxies at $z \sim 3$ suggests that there is a close connection between the mass of the halo and the star-formation rate it can support, as Chapter 3 explains.

Chapter 4 presents an attempt to understand the impact that young galaxies might have on the rest of the universe. In our picture of how the universe's baryons evolve, little is as poorly understood as the role that supernova explosions play. When observations fail to match simple theoretical predictions, supernovae are often blamed. Why did so small a fraction of baryons cool at early times despite the universe's high density? Supernova heating must have prevented it (White & Rees 1978). Why are there so few low mass galaxies in the local universe? Supernovae must have blown many of them apart (Cole et al. 1994). Why are observed disk galaxies so much bigger than the disk galaxies in simulations? Supernovae must break apart dense clumps of baryons that would otherwise lose angular momentum to the dark matter through dynamical friction (Mo & Mao 2002). Why does the observed relationship between X-ray temperature and luminosity in galaxy clusters deviate from simple self-similar predictions of hierarchical structure formation? Supernovae must heat clusters' gas and add an entropy floor that breaks the self similarity (e.g., Ponman, Cannon, & Navarro 1999). These examples are just a few among many. But is there any direct sign that supernovae influenced young galaxies and their environments as strongly as these arguments require? This is what we set out to observe. High-resolution spectra of high-redshift QSOs revealed where gas and metals are found at $z \sim 3$; low resolution spectra of color-selected galaxies near the QSO sight-line revealed the locations of galaxies; and the combination of the two let us search for putative supernova-driven winds from the young galaxies. As readers will see, we found tentative evidence for unexpectedly strong galactic winds.

The four chapters of this thesis described ways that we can improve our understanding of the universe's history by using distant objects to look back in time. Simple

color-selection criteria can be used to find galaxies at high redshifts; observations at other wavelengths can help us understand the physical nature of the detected galaxies; measurements of spatial clustering may show where galaxies form relative to perturbations in the underlying distribution of matter; and the combination of redshift surveys with QSO-absorption line studies may help us understand how star formation influences the large-scale distribution of baryons in the universe. But much was left undone. The observations covered only the ~ 5 billion years between redshifts $z \sim 5$ and $z \sim 1$, and even at $1 \lesssim z \lesssim 5$ we studied only star-forming galaxies. Little was said about how the young galaxies we observe might evolve into the largely old and inactive galaxies of the local universe; nothing was said about the first generations of stars and galaxies that reionized the universe at $z \gtrsim 6$. We tacitly assumed that the cosmological model and the nature of dark matter would be established by other observations. Understanding the evolution of the universe during the last thirteen billion years is a large, difficult, and shared enterprise. We hope to have established one line of attack; but the work presented is only a modest beginning.

Barger, A. J., Cowie, L. L., & Richards, E. A. 2000, *Astron. J.*, **119**, 2092.

de Bernardis, P. *et al.* 2000, *Nature*, **404**, 955.

Bromley, B. C. & Tegmark, M. 1999, *Astrophys. J. Lett.*, **524**, 79.

Cole, S., Aragón-Salamanca, A., Frenk, C. S., Navarro, J. F., & Zepf, S. E. 1994, *MNRAS*, **271**, 781.

Croft, R. A. C., Weinberg, D. H., Pettini, M., Hernquist, L., & Katz, N. 1999, *Astrophys. J.*, **520**, 1.

Mo, H.-J. & Mao, S. 2002, *Mon. Not. Roy. Astron. Soc.*, in press.

Ponman, T., Cannon, D., & Navarro, J. 1999, *Nature*, **397**, 135.

Steidel, C. C., Adelberger, K. L., Giavalisco, M., Dickinson, M., & Pettini, M. 1999, *Astrophys. J.*, **519**, 1.

White, S. D. M., Efstathiou, G., & Frenk, C. S. 1993, *Mon. Not. Roy. Astron. Soc.*, **262**, 1023.

White, S. D. M. & Rees, M. J. 1978, *Mon. Not. Roy. Astron. Soc.*, **183**, 341.

Contents

List of Tables

List of Figures

Chapter 1

Color-Selected Redshift Surveys at $1 < z < 4$

1.1 Introduction

As the photons from the microwave background stream towards earth they are gradually joined by other photons, first by those produced in the occasional recombinations of the neutral IGM, later by those cast off from cooling H_2 molecules, later still, after hundreds of millions of years, by increasing numbers of photons from quasars and galaxies, by bremsstrahlung from the hot gas in galaxy groups and clusters, and finally, shortly before reaching earth, by photons emitted by the Milky Way's own gas and stars and dust. All reach the earth together. These photons provide a record of the history of the universe throughout its evolution, but it is a confused record; two photons that simultaneously pierce the same pixel of a detector may have been emitted billions of years apart by regions of the universe that were in vastly different stages of evolution. One of the challenges in observational cosmology is to separate the layers of history that we on earth receive superposed.

A standard strategy is sort the incoming photons by energy. Photons emitted by

the surface of last scattering soon after the beginning of time can be easily distinguished from the much younger photons emitted by hot gas in X-ray clusters because their energies differ by nearly six orders of magnitude. More subtle spectral characteristics can be used to winnow out light from the galaxies at various redshifts that are the primary focus of this work. One example is the Lyman-break at 912Å, a ubiquitous feature in the spectra of star-forming galaxies that arises due to the absorption of ionizing radiation by the neutral hydrogen present in the atmospheres of stars and in interstellar and intergalactic space. At redshifts $z \gtrsim 3$ the Lyman-break is redshifted into the optical window, allowing star-forming galaxies at these redshifts to be separated from the dominant foreground and background populations in deep images by their broadband colors (see figure 1.1; cf. Steidel & Hamilton 1993; Steidel *et al.* 1999).

Much of this thesis will be devoted to analyzing a sample of galaxies at $z \sim 3$ selected with the Lyman-break technique, but $z \sim 3$ is not the only interesting redshift and the Lyman-break is not the only spectral feature that can be used to distinguish high-redshift galaxies. This chapter presents broadband techniques similar in spirit to the Lyman-break technique that can be used to locate star-forming galaxies at redshifts $z \lesssim 3$. In §1.2 color-selection criteria based on the 4000Å and Balmer-breaks are proposed and used to create a sample of $\sim$ 10000 galaxies at $z \sim 1$. In §1.3 color-selection criteria that exploit the *absence* of a break in the spectra of galaxies at certain redshifts are presented and used to construct a sample of galaxies at $z \sim 2$. Together with the Lyman-break technique, the techniques presented here allow the efficient creation of large samples of star-forming galaxies throughout the redshift range $1 \lesssim z \lesssim 5$ where recent analyses suggest the majority of stars in the universe were born (e.g., Steidel *et al.* 1999). §1.4 describes a statistical formalism that can be used to analyze the data in color-selected surveys.

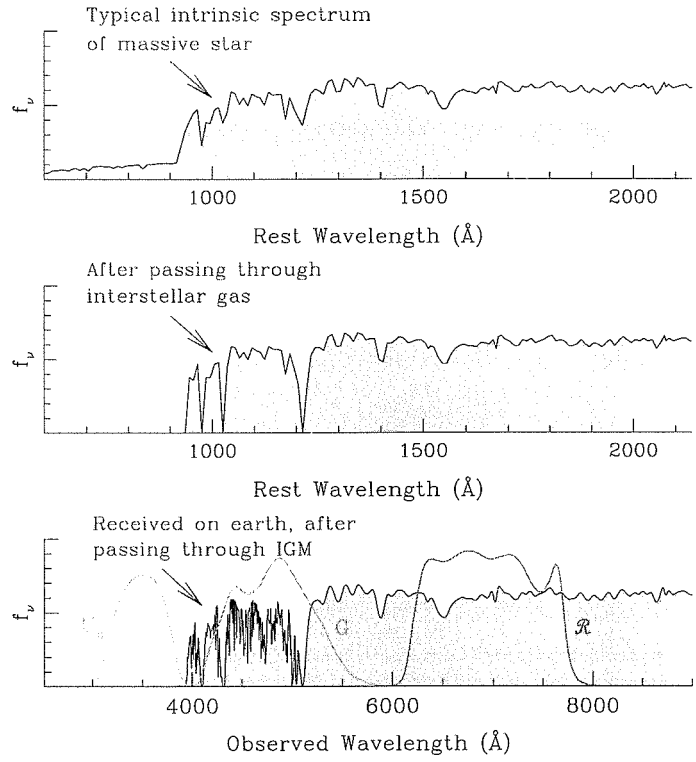

Figure 1.1 The Lyman-break technique. The rest-UV emission of star-forming galaxies is dominated by massive stars, whose spectra are roughly flat in the UV until a pronounced break at 912Å due to Lyman-continuum absorption in their atmospheres. As the light from these stars propagates towards earth, the "Lyman break" is strengthened, first by neutral hydrogen in the galaxy itself and then by neutral hydrogen in the intergalactic medium. The break is detectable from the ground for galaxies at $z \gtrsim 2.5$. Broadband imaging through filters that straddle the redshifted break (e.g., U_n and G at $z \sim 3$) provides an efficient way of locating the high-redshift galaxies among the numerous foreground and background sources in deep images. Obtaining additional images through a redder band (e.g., $\mathcal{R}$) helps distinguish high-redshift galaxies from intrinsically red objects in the more local universe.

1.2 Redshift $z \sim 1$

At redshifts $z \lesssim 3$ the Lyman-break is not detectable from the ground. Other spectral signatures must be used to locate galaxies at these redshifts. Most galaxies have second break in their spectrum at $\lambda_{\rm rest} \sim 4000$Å produced by a combination of Hydrogen Balmer-continuum absorption in the spectra of B, A, and F stars and CaII H&K

absorption in the spectra of F, G, and K stars. The relative strengths of the Balmer and 4000Å breaks depends upon mixture of stellar types in a galaxy—younger galaxies have stronger Balmer breaks and older galaxies have stronger 4000Å breaks—but most galaxies have a break of some sort near 4000Å. This break is especially well suited for locating galaxies at $z \sim 1$ because it falls between the $\mathcal{R}$ and i bandpasses at that redshift (figure 1.2).

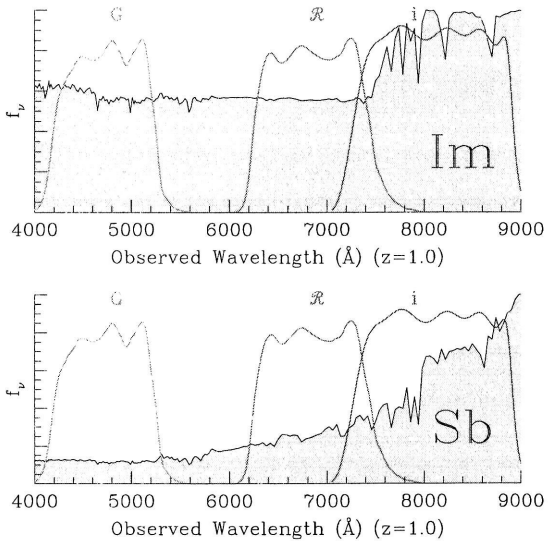

Figure 1.2 The Balmer and 4000Å breaks. Younger galaxies, represented by the "Im" model spectrum, have a Balmer break near $\sim$ 3700Å due to Hydrogen Balmer absorption in the spectra of B, A, and F stars; older galaxies, represented by the "Sb" model spectrum, have 4000Å CaII H&K breaks. These breaks give galaxies at $z \sim 1$ distinctive $G\mathcal{R}i$ colors.

Figure 1.2 suggests qualitatively that galaxies at $z \sim 1$ ought to have distinctive $G\mathcal{R}i$ colors, red in $\mathcal{R} - i$ and less red, often, in $G - \mathcal{R}$. Quantitative photometric selection criteria targeting these galaxies can be derived from plots similar to figure 1.3, which shows the $G\mathcal{R}i$ colors of model galaxies at various redshifts and of stars in our own galaxy. The figure shows the approximate expected colors for any object in deep $G\mathcal{R}i$ exposures; spectroscopic follow-up of objects with colors that are characteristic of $z \sim 1$ galaxies and distinct from the colors of other objects should

produce a redshift survey consisting primarily of objects at $z \sim 1$. These objects lie primarily to the right of the diagonal line in figure 1.3, suggesting

$$\mathcal{R} - i \geq (G - \mathcal{R})/2 + 0.2, \qquad G - \mathcal{R} \leq 1.8 \tag{1.1}$$

as reasonable criteria for identifying the $z \sim 1$ galaxies in deep $G\mathcal{R}i$ images. Because $z \sim 1$ galaxies are expected to have colors lying relatively close to this line, and because the typical uncertainty in our measured colors is ~ 0.2 magnitudes for faint objects, we might expect a significant fraction of galaxies at $z \sim 1$ to have measured colors lying just to the right of the selection window. Relaxing our photometric selection criteria, somewhat, to

$$\mathcal{R} - i \geq (G - \mathcal{R})/2, \qquad G - \mathcal{R} \leq 1.8, \tag{1.2}$$

will identify a larger fraction of the $z \sim 1$ galaxies in an image, but at the price of identifying a larger number of galaxies at lower and higher redshifts as well. We will use both equation 1.1 and 1.2 below.

Even if $z \sim 1$ galaxies had colors that matched our models perfectly, and even if we suffered no photometric errors, figure 1.3 makes it clear that some galaxies at $z \sim 1$ will not satisfy either of the selection criteria above. These are galaxies with extreme star-formation histories. At one extreme are galaxies whose present star-formation rates are much lower than their past average. Galaxies in this category, represented by the "E" tracks in figure 1.3, are rare at $z \sim 1$, and they host an even smaller fraction of the star-formation than their meager numbers would suggest. A survey of star-forming galaxies at $z \sim 1$ (such as ours) will be only negligibly affected by their omission. Of more concern are galaxies at the opposite extreme, galaxies with present star-formation rates much higher than the past average. The spectra of these galaxies are dominated by light from massive O stars—by stars whose atmospheres are too hot to contain significant amounts of neutral Hydrogen—and consequently they do not have Balmer breaks.

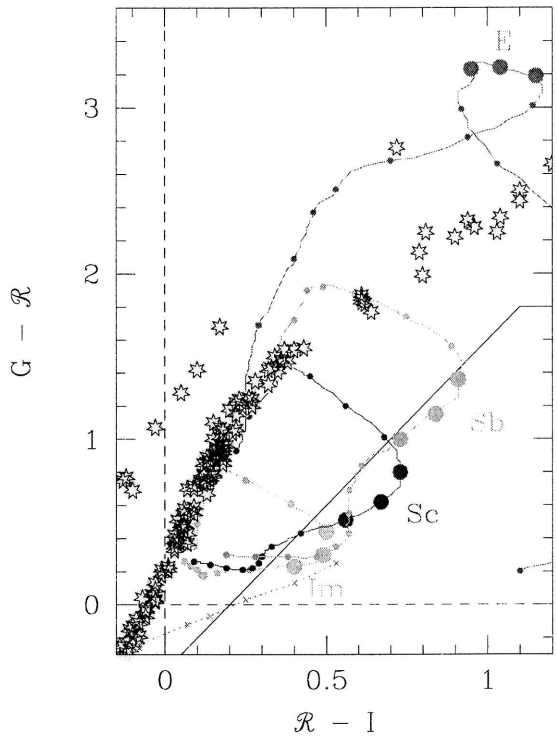

Figure 1.3 Expected locations of stars and galaxies on the two-color diagram. The stars are from Gunn & Stryker (1983). The curved tracks show the colors of model galaxies of different spectral types at various redshifts, starting at $z = 0$ and increasing clockwise. Circles mark redshift intervals of $dz = 0.1$; large circles mark $z = 0.9$, 1.0, 1.1. The galaxy templates are from Bruzual & Charlot (1996) and have been subjected to a dust reddening of $E(B - V) = 0.15$ that follows a Calzetti (1997) law. One would expect to find $z \sim 1$ galaxies and few interlopers to the right of the diagonal line. The dotted line connecting crosses shows the colors of a model galaxy at $z = 1.0$ that has been forming stars at a constant rate for 3, 10, 30, 100, 300, 1000 Myr; the galaxy becomes redder as it ages and begins to satisfy our selection criteria for $t \gtrsim 30$Myr.

How much higher than its past average must a galaxy's present star-formation rate be in order for it not to satisfy our photometric selection criteria? The ratio of past to present star-formation rate can be parametrized by calculating model spectra for a suite of galaxies that have been forming stars at a constant rate for the variable time t. As $t \to 0$, the ratio of past to present star-formation rate approaches infinity, while as $t \to \infty$ it approaches unity. The dotted line in figure 1.3 shows the expected

$G\mathcal{R}i$ colors of a galaxy at $z \sim 1$ for a range of times t, from $t = 3$ Myr (lower left) to $t = 1$ Gyr (upper right). Crosses mark $t = 3$, 10, 30, 100, 1000 Myr. A galaxy will have a ratio of A to O stars large enough to have a discernible Balmer break, and to satisfy our $z \sim 1$ selection criteria, if it has been forming stars at a constant rate for a few times the average lifetime of an O star, or $t \gtrsim 30$ Myr. If a large fraction of star formation at $z \sim 1$ occurred in episodes shorter than this, a Balmer-break survey like ours would be seriously incomplete.

Does a significant fraction of star formation at $z \sim 1$ occur in episodes shorter than 30Myr? This is a question that has to be addressed empirically, because theoretical models are too poorly developed to provide a robust answer, but the answer is likely to be "no." Most star formation in the local universe, for example, occurs among spiral galaxies and comparatively faint starbursts (e.g., Heckman 1997) which generally have dynamical times longer than 30Myr and are observed to contain stellar populations at least several hundreds of Myr old. Similarly most of the known star formation at $z \sim 3$ seems to have occurred in episodes lasting longer than 30Myr (e.g., Papovich, Dickinson, & Ferguson 2001; Shapley *et al.* 2001). Every $z \sim 3$ Lyman-break galaxy that has been observed in the near-IR appears to have a spectral energy distribution (SED) that would satisfy the Balmer-break selection criteria of equations 1.1 or 1.2. This can be shown by working out the best fit model SED to the optical and near-IR photometry of Lyman-break galaxies in the samples of Papovich *et al.* (2001) and Shapley *et al.* (2001), and then working out the $G\mathcal{R}i$ that these SEDs would have if placed at $z \sim 1$. The result is shown in figure 1.4. All of the galaxies lie to the right of the line $\mathcal{R} - i = (G - \mathcal{R})/2$ (equation 1.2), showing that the $z \sim 3$ galaxies selected through the Lyman-break technique could in principle have been identified equally successfully through the Balmer-break criteria that we propose.[1]

[1]Although, of course, Balmer-break selection at $z \sim 3$ is difficult in practice because the relevant parts of galaxy spectra are shifted into the near-IR where the night sky is bright.

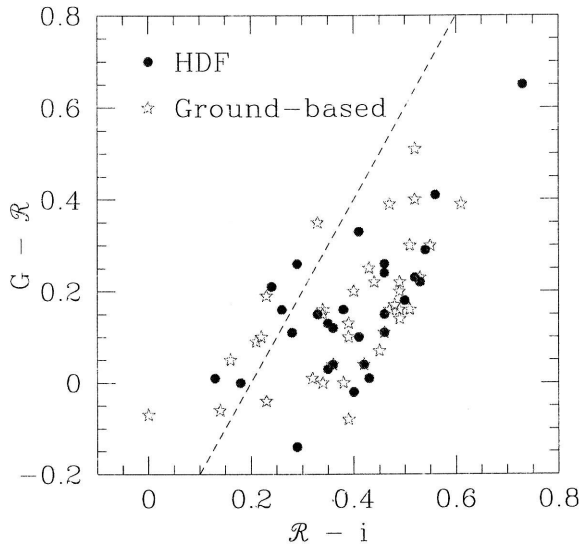

Figure 1.4 The colors of Lyman-break galaxies placed at $z \sim 1$. All of the galaxies lie to the right of the line $\mathcal{R} - i = (G - \mathcal{R})/2$, showing that the $z \sim 3$ galaxies selected through the Lyman-break technique could in principle have been identified equally successfully through the Balmer-break criteria that we propose.

These considerations suggest that Balmer-break selection ought to provide an efficient way of finding galaxies at $z \sim 1$. A more direct way to show this is to measure $G\mathcal{R}i$ colors for a large number of galaxies with redshifts previously measured in magnitude-limited surveys. Starting in August 1995, $G\mathcal{R}i$ images were obtained in four fields with completed or ongoing redshift surveys: the 00^h53 field of Cohen *et al.* (1999), the Hubble Deep Field (Williams *et al.* 1996; Cohen *et al.* 2000), the 14^h18 field of Lilly *et al.* (1995), and the 22^h18 field of Cowie *et al.* (1996) and Lilly *et al.* (1995). Spectroscopic redshifts have been published for 1312 objects in these fields combined. The published coordinates for these objects were sufficient for us to easily and unambiguously identify 1208 of them with objects in our images. Observed colors and redshifts for these 1208 objects are shown in figure 1.5. As expected, the bulk of the $z \sim 1$ galaxies in these surveys have $G\mathcal{R}i$ colors similar to our expectations from figure 1.3.

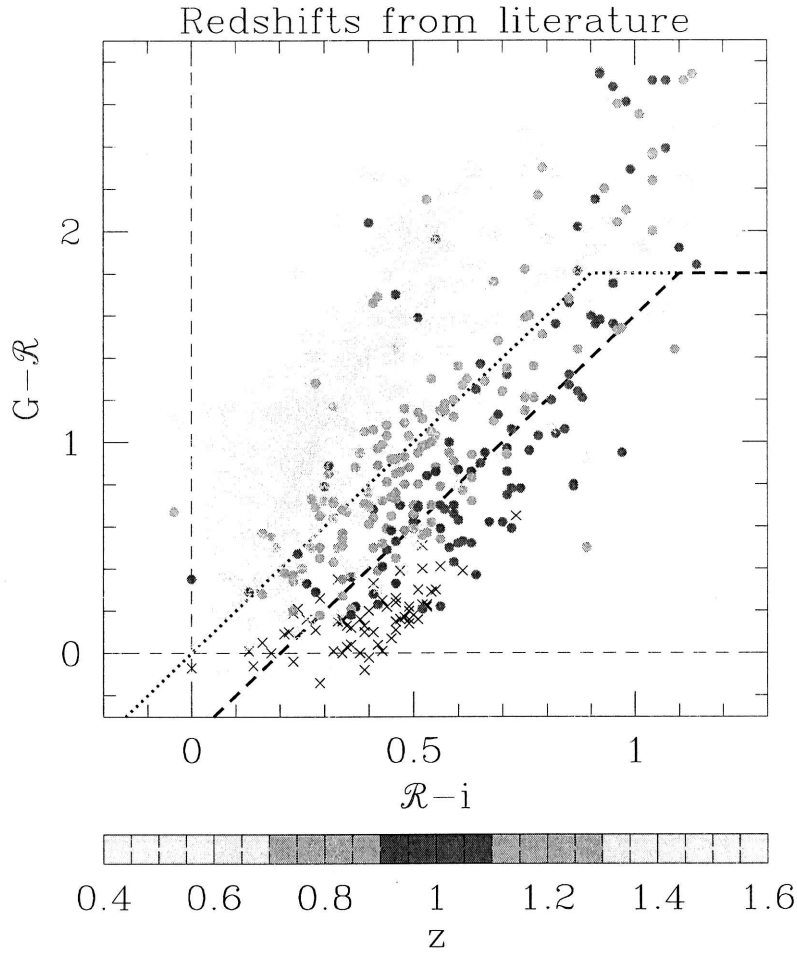

Figure 1.5 Observed $G\mathcal{R}i$ color as a function of redshift for galaxies in various magnitude limited surveys (see text). Known galaxies at $z \sim 1$ are observed to have $G\mathcal{R}i$ colors similar to our expectations from figure 1.3. Crosses show where Lyman-break galaxies would fall on this plot (cf. figure 1.4).

To quantify the performance of our $z \sim 1$ selection criteria, equations 1.1 and 1.2, we must establish two things. First, how large a fraction of $z \sim 1$ galaxies will not satisfy the criteria and be missing from our survey? And second, how large a fraction of the galaxies that satisfy our criteria will lie at redshifts lower or higher than the redshift of interest $0.9 < z < 1.1$? The first question can be answered by calculating a quantity α equal to the fraction of the luminosity of galaxies at $0.9 < z < 1.1$ that

is produced by objects satisfying our selection criteria. The second can be answered by calculating a quantity β equal to the fraction of the luminosity emitted by objects satisfying our criteria that is produced by galaxies at $0.9 < z < 1.1$. An ideal survey would have $\alpha = 1$ and $\beta = 1$, but this is not achievable in practice because of photometric errors and intrinsic variations in the spectra of galaxies. In general a high value of α is incompatible with a high value of β; the two variables make competing demands upon our selection criteria. If we wanted to make α as large as possible, for example, we would want to make our selection box very large so that it would include even galaxies with large photometric errors or abnormal spectral shapes. But this improvement in α would come at the price of admitting more galaxies at the wrong redshifts to our survey, and would therefore decrease β.

Table 1.1 lists α and β for galaxies satisfying equation 1.1 (α_f, β_f) and equation 1.2 (α_m, β_m). The numbers in the table are appropriate for luminosity in the G band, ~ 2500Å rest, but they would not be drastically different if we used $\mathcal{R}$ or i luminosities instead. Galaxies with $\mathcal{R} < 21$ were excluded from the calculation. Very few galaxies at $z \sim 1$ are so bright, and an object of this magnitude that satisfies our selection criteria is likely to be a low redshift galaxy with a very large emission line contribution to its broadband colors. The trade-off between α and β is clear, but the upshot of the table is that $\sim 90\%$ of the 2500Å luminosity density at $0.9 < z < 1.1$ is produced by objects that satisfy at least one of our selection criteria.

The galaxies at $0.9 < z < 1.1$ that do not satisfy our $G\mathcal{R}i$ selection criteria can be crudely grouped into three classes (cf. figure 1.5). First, there are the handful of galaxies with $\mathcal{R} - i \simeq 1.0$, $G - \mathcal{R} \sim 2.7$. These galaxies have rest-frame colors nearly identical to those of local ellipticals (cf. figure 1.3). They are objects that formed the bulk of their stars in the past and are no longer forming stars at a significant rate. Their absence from a color selected survey of star-forming galaxies is expected and harmless. Second, there are objects with colors identical to those of low redshift

Table 1.1 $z \sim 1$ Interloper Fraction and Completeness

Field	α_f	β_f	α_m	β_m	Ref.	N_f	N_m	$N_{\rm tot}$
00^h53	0.72	0.26	0.83	0.17	Cohen *et al.* 1999	22	46	168
HDF	0.47	0.70	0.87	0.35	Cohen *et al.* 2000	50	168	565
14^h18	0.50	0.66	0.94	0.45	Lilly *et al.* 1995	8	25	123
22^h18	0.72	0.57	0.93	0.25	Cowie *et al.* 1996	15	43	171
average	0.60	0.55	0.89	0.31				

galaxies but with reported spectroscopic redshifts $z \simeq 1.0$. Some of these objects may have abnormal star-formation histories, and some may have incorrectly measured spectroscopic redshifts. Third, there are objects with measured colors that place them just outside the Balmer-break color selection window. These galaxies may have been scattered out of our selection window by photometric errors, which are typically ~ 0.2 magnitudes in both $G - \mathcal{R}$ and $\mathcal{R} - i$. Their absence from a Balmer-break selected survey can be largely corrected with the statistical technique described in § 1.4 below.

In the spring of 1999 we began obtaining spectra of galaxies satisfying our selection criteria. Figure 1.6 shows the overall redshift histogram of the objects observed to date. The reduced portion of the Balmer-break survey currently contains 468 objects with spectroscopic redshifts $0.9 < z < 1.1$, 651 with $z > 0.9$, and nearly 10000 objects satisfying our photometric selection criteria spread over more than 0.6 square degrees. We might hope that this survey will teach us something about galaxies beyond what has been learned from the magnitude limited surveys mentioned above, which together contain 123 galaxies with $0.9 < z < 1.1$ and 209 objects with $z > 0.9$. But the author has neither the time nor the energy to say anything more here.

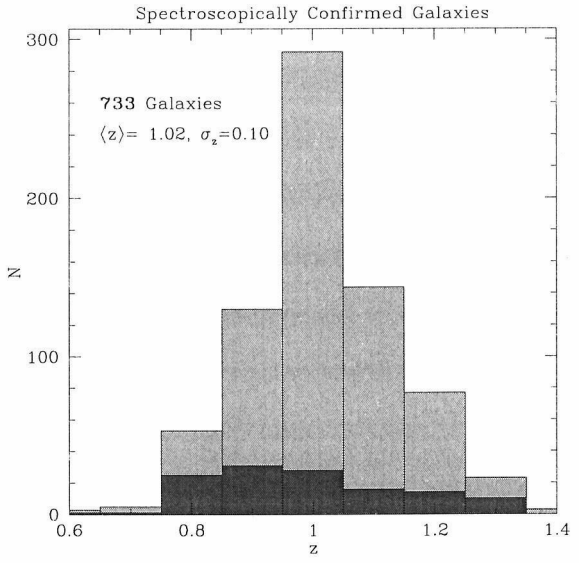

Figure 1.6 Redshift histogram of the reduced portion of the Balmer-break survey. Lighter bars are for objects satisfying equation 1.1; darker bars are for objects satisfying equation 1.2 but not 1.1.

1.3 Redshift $z \sim 2$

In principle selection criteria similar to those described in § 1.2 can be used to identify galaxies at any redshift where the Balmer/4000Å breaks are visible from the ground, but at $z \gtrsim 1.4$ these breaks are redshifted out of the optical window and into the near-IR where the sky is prohibitively bright. If we hope to use efficient optical imaging to locate galaxies at $z \gtrsim 1.4$, we will have to rely on a spectral feature other than the Balmer-break. At redshifts $z \gtrsim 2.5$ the Lyman-break becomes visible in the optical window, and it provides a natural feature to exploit in color-selected redshift surveys (e.g., Steidel & Hamilton 1993, Steidel *et al.* 1999), but what can we use to find galaxies at the intermediate redshift $z \sim 2$ where neither the Lyman nor Balmer break is easily detectable? Galaxy spectra contain no other pronounced break that is visible in the optical at this redshift. The lack of an easily detectable break at $z \sim 2$ has led many to assume that it will be a uniquely difficult redshift for galaxy detection. But let's be optimistic. Could the *lack* of a break in the optical perhaps

be itself a distinguishing characteristic that can be used for photometric preselection of galaxies at $z \sim 2$? As we shall shortly see, this idea, with a little refinement, can be made to work.

Let us begin by calculating the colors that typical Lyman-break galaxies would have if they were placed at $z \sim 2$ instead of $z \sim 3$. The rest wavelength probed by the $\mathcal{R}$ filter at $z \sim 2$ corresponds to an observed wavelength $\lambda_{\rm obs} \sim 9000$Å at $z \sim 3$, and so we will need to know the spectral shapes of $z \sim 3$ Lyman-break galaxies at wavelengths longer than i if we hope to constrain the $G - \mathcal{R}$ colors they would have if placed at $z \sim 2$. J band and redder magnitudes for several dozen Lyman-break galaxies have been measured by Papovich *et al.* (2001) and Shapley *et al.* (2001). The colors these galaxies would have if placed at $z \sim 2$ can be calculated by fitting a model spectrum to their observed photometry, blueshifting the model SED from $z \sim 3$ to $z \sim 2$, and applying a correction for the change in intergalactic reddening following the model of Madau (1995). The result is shown in figure 1.7. As we might have expected, compared to galaxies at $z \sim 3$, galaxies at $z \sim 2$ have slightly bluer $G - \mathcal{R}$ because the Lyman-α forest does not absorb in the G band and significantly bluer $U_n - G$ colors because the U_n band suffers Lyman-α forest rather than Lyman-continuum absorption. This is the part of $U_n G\mathcal{R}$ color–color space where we should look for galaxies at $z \sim 2$.

Unfortunately $z \sim 2$ galaxies are not the only occupants of this part of color–color space. Figure 1.7 shows that late-type galaxies at $z \lesssim 0.2$ and $z \gtrsim 1.1$ will have $U_n G\mathcal{R}$ colors similar to those of galaxies at $z \sim 2$. Optimal color-selection criteria for galaxies at $z \sim 2$ will have to be defined in a way that minimizes the unwanted contribution from galaxies at these lower redshifts. In an attempt to quantify the possible contribution from low redshift interlopers, we began in the fall of 1997 to obtain spectra of objects with colors similar to those expected for $z \sim 2$ galaxies. Figure 1.8 shows the result of this spectroscopy. As expected a significant fraction of

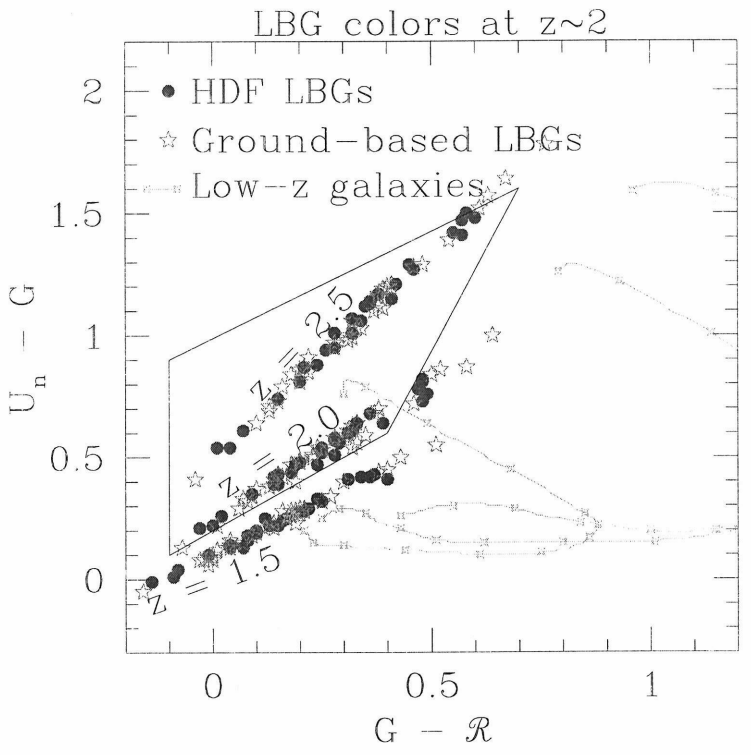

Figure 1.7 The colors of Lyman-break galaxies if placed at $z \sim 2$. Circles mark the estimated colors that the $z \sim 3$ Lyman-break galaxies in the samples of Papovich *et al.* 2001 and Shapley *et al.* 2001 would have if placed at $z = 1.5$, 2.0, 2.5. The tracks show the colors of galaxies at lower redshift as a function of z, beginning at $z = 0$ and increasing clockwise towards $z = 1.5$. Four pointed stars mark redshift intervals $dz = 0.1$. Bruzual & Charlot (1996) model galaxies of type Im, Sc, and Sb were assumed; each was reddened to $E(B-V) = 0.15$ with dust following a Calzetti law. These galaxies have colors similar to $z \sim 2$ galaxies for both $z \lesssim 0.3$ and $z \gtrsim 1.0$. The trapezoid marks our adopted selection region for $z \sim 2$ galaxies, as discussed below.

objects with $G - \mathcal{R} \sim 0.3$, $U_n - G \sim 0.8$ lies at $z \sim 2$, but a significant fraction lies at lower and higher redshifts as well.

An efficient $z \sim 2$ color-selection strategy should focus primarily on the regions of $U_n G\mathcal{R}$ color-color space where objects have the highest probability of lying at $z \sim 2$. Figure 1.9 shows the fraction of objects with different $U_n G\mathcal{R}$ colors that are found empirically to lie at $1.5 < z < 2.5$. The selection box defined by the equations

$$G - \mathcal{R} \; > \; -0.1$$

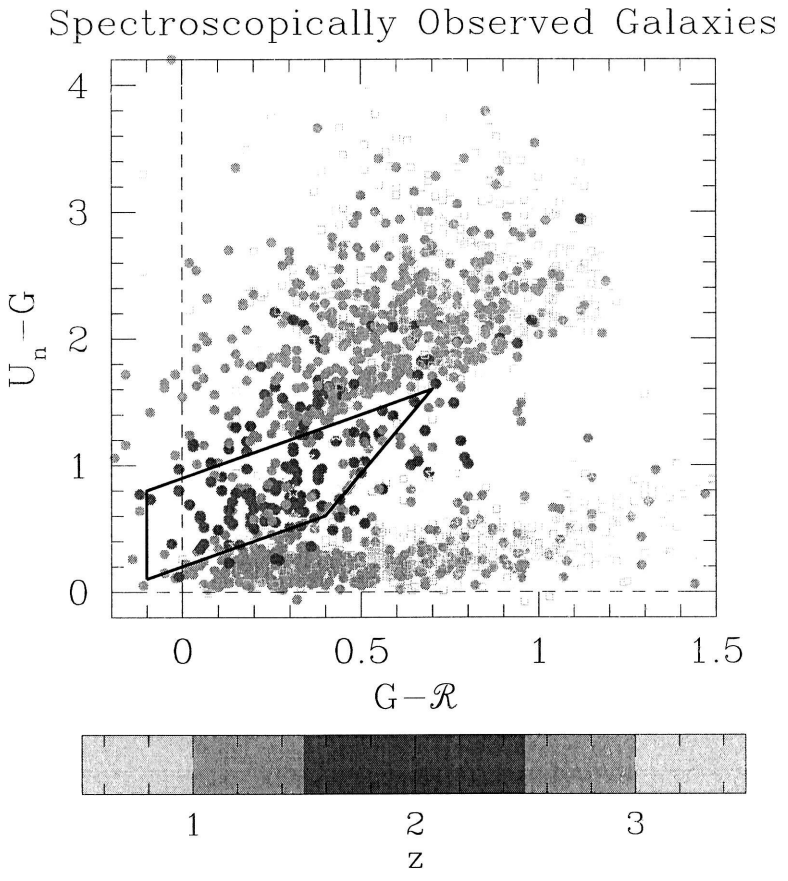

Figure 1.8 Galaxies at $z \sim 2$ will have colors that place them just below the Lyman-break selection box in the $U_n G\mathcal{R}$ color-color plane, but so do galaxies at other redshifts, as this plot shows.

$$\begin{aligned} U_n - G &> G - \mathcal{R} + 0.2 \\ G - \mathcal{R} &< \frac{3}{10}(U_n - G) + 0.2 \\ U_n - G &< G - \mathcal{R} + 0.9 \end{aligned} \tag{1.3}$$

roughly encompasses the region of color-color space with the highest fraction of galaxies at $z \sim 2$. A smaller selection region could be defined around the region $G - \mathcal{R} \simeq 0$,

$0 \lesssim U_n - G \lesssim 1$ that has the very highest fraction, but then only a very small percentage of $z \sim 2$ galaxies would satisfy our selection criteria and we would be systematically missing the $z \sim 2$ galaxies with the largest amounts of dust (cf. figure 1.7). The selection region of equation 1.3 is roughly as small as it can be while still maintaining a reasonable probability of containing all expected types of $z \sim 2$ galaxies' spectral shapes.

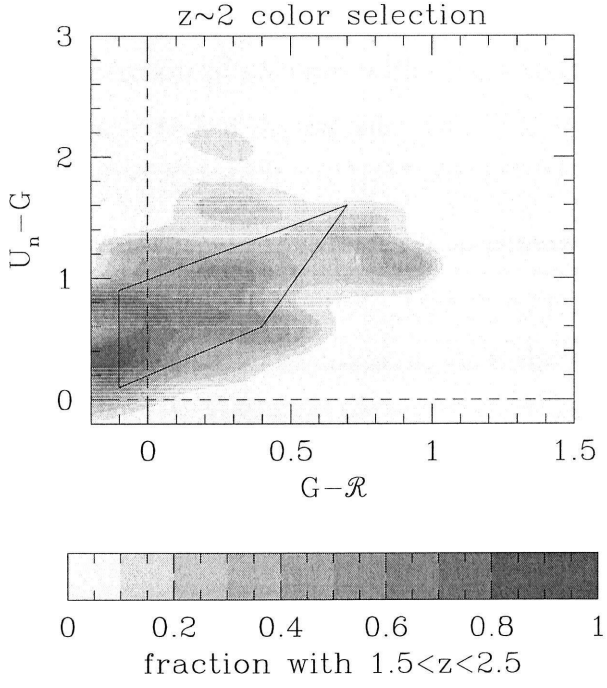

Figure 1.9 The fraction of objects in each segment of the $U_n G\mathcal{R}$ plane that lie at $1.5 < z < 2.5$. Efficient color-selection criteria should focus on the parts of color-color space where objects are most likely to lie at $z \sim 2$, but they should not be defined so restrictively that galaxies of certain spectral types cannot be detected at all. Overlain is the trapezoidal selection region we have adopted as a compromise.

Referring again to figure 1.7, one can see that objects satisfying these selection criteria will lie primarily at $2.0 \lesssim z \lesssim 2.5$ rather than our initially desired range of

$1.5 \lesssim z \lesssim 2.5$. The reason is that the $U_nG\mathcal{R}$ colors of galaxies at $z \sim 1.5$ are sufficiently similar to those of galaxies at $z \sim 1$ that they cannot easily be distinguished in realistically noisy $U_nG\mathcal{R}$ photometry, and so any selection strategy that aims to avoid galaxies at $z \sim 1$ will have to avoid those at $z \sim 1.5$ as well. It is only when the Lyman-α forest begins to cut significantly into the U_n band at $z \sim 2$ that the colors of galaxies begin to change rapidly with redshift. It is only then that the $U_nG\mathcal{R}$ colors of high-redshift galaxies become distinct enough for them to be reliably separated from the low redshift dross.

The redshift histogram of galaxies with colors that satisfy equation 1.3 is shown in figure 1.10. As expected, a significant fraction of the candidates, 52 of 197, lie at $z < 1.5$. But 132 of 197, or 67%, lie at the redshifts of interest $1.5 < z < 2.8$. In effect, one-third of the spectroscopic time spent on objects in this sample will be wasted on objects that are not of primary interest. This is unfortunate but hardly prohibitive. Our analysis does not support the common view that redshift surveys at $z \sim 2$ will be vastly more difficult than surveys at $z \sim 1$ or $z \sim 3$. Galaxies at $z \sim 1.5$ will not be well represented in a sample selected with the color criteria of equation 1.3, but if one wanted it would be easy to find these galaxies with a version of Balmer-break selection (§1.2) that pushes into the z band. In this way it will be possible to use two-color selection techniques to locate galaxies throughout the so-called "desert" at $1 < z < 3$.

1.4 Statistical analysis

The discussion in §§ 1.2 and 1.3 makes it clear that the definition of selection criteria used in color-selected redshift surveys are somewhat arbitrary. The goals in defining selection boxes are obvious—we would like to maximize the number of detected galaxies at the redshift of interest and minimize the number at other redshifts—but

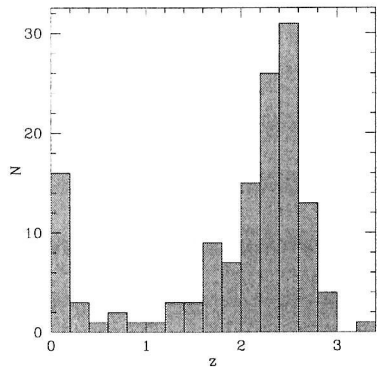

Figure 1.10 Redshift histogram of objects satisfying our $z \sim 2$ color selection criteria, equation 1.3.

the optimal compromise between these conflicting goals is not. Moreover even if an objectively optimal selection box could be derived, its details would depend upon the properties of the galaxies at the redshift of interest, which is something we do not know until the survey has begun. Color-selected redshift surveys will always be defined in a way that is somewhat less than optimal, and different researchers may well choose selection criteria that differ in their details even though they target the same redshift. The samples produced with different selection criteria will not be the same. Each will contain a different subset of the galaxies at the target redshift; each will have a different mix of galaxy spectral types and a different mean redshift. Is there some statistical technique we could use to analyze these different hypothetical data sets and realize that they were all drawn from the same underlying population? That is the subject of this section. Rather than attempting to derive optimal selection criteria, the focus will be on correcting color-selected redshift surveys for the effects of the suboptimal selection criteria that are inevitably employed.

The problem we face is called selection bias by statisticians. It can be understood intuitively by referring to figure 1.7. We have defined our selection box so that it will mainly contain galaxies at $2.0 < z < 2.5$. But it will not contain only galaxies at this redshift. Galaxies at $z \sim 1.5$ lie just outside the selection box, for example,

and many of them will have large enough photometric errors to be scattered into our selection box. And it will not contain equal numbers of galaxies at $z = 2.0$ and $z = 2.5$. Galaxies at $z = 2.0$ lie near the edge of the selection box, and photometric errors will scatter many more of them out of the box than galaxies at $z = 2.5$, which tend to lie near the center of the box. At each redshift a different mix of galaxy types will satisfy our selection criteria. At $z = 2.0$, for example, a larger fraction of intrinsically red galaxies lie outside the box than at $z = 2.5$. We will not be unable to detect the presence of the reddest galaxies, even though on average their colors place them outside of our selection box, because some will have large enough photometric errors to be scattered into the box, but they will make up a much smaller proportion of our observed sample than they ought. The mix of galaxy types and redshifts that we will find in our color-selected redshift survey is further affected by our magnitude limits at U_n, G, and $\mathcal{R}$ in ways that would be tedious to enumerate. At the end of the day we will be left with a sample of galaxies with complicated distributions of magnitudes and redshifts and spectral types, and, because of the numerous selection effects, we can be certain that the shape of none of these distributions will closely resemble the true distribution in the underlying population. Modifying our selection box would change each of the observed distributions. For example, raising the lower edge of the box would decrease the number of galaxies at $z = 2.0$, and moving the right edge towards the left would decrease the number of intrinsically red galaxies in the sample.

The goal of this section is to derive a statistical scheme for analyzing the data that will tell us about the properties of galaxies at high redshift, not about the properties of our selection box. It is a complicated problem, but it can be solved with the conceptually simple approach that we now describe. The approach will be applied to the Lyman-break sample at $z \sim 3$. It is trivial to generalize to our other samples.

1.4.1 Correcting selection bias: a simple example

Suppose we are asked to decide whether candidate A or B has won an election, and only have access to an unreliable ballot-counting machine. The machine returns a tally of n_A votes for A and n_B for B, but we know from experience that it is prone to error: some ballots marked A (for example) are incorrectly counted as votes for B, and some are ignored altogether. How can we estimate the total number of votes, μ, and the true fraction of votes for A, f_A, given only the machine's output n_A, n_B? A natural approach is to calibrate the machine after the fact by submitting a large number of ballots marked A, recording the fraction of these that are counted as votes for A ($p_{A\to A}$) and for B ($p_{A\to B}$), and then repeating the process with a large number of ballots marked B to calculate $p_{B\to A}$ and $p_{B\to B}$. (In general, $p_{A\to A} + p_{A\to B} < 1$ and $p_{B\to A} + p_{B\to B} < 1$ because some fraction of votes are ignored by the machine.) After calibrating the machine, we can calculate the expected machine tally $\bar{n}_A, \bar{n}_B$ for any values of μ and f_A by breaking $\bar{n}_A$ and $\bar{n}_B$ down into the expected contributions from votes marked A and B:

$$\bar{n}_A = \mu(f_A p_{A\to A} + f_B p_{B\to A}), \quad \bar{n}_B = \mu(f_A p_{A\to B} + f_B p_{B\to B}) \tag{1.4}$$

where $f_B \equiv 1 - f_A$. These expressions are all we need to evaluate the likelihood of the machine output, which is a product of two Poisson distributions:

$$\mathcal{L}(n_A n_B | \mu f_A) \propto \exp[-(\bar{n}_A + \bar{n}_B)] \bar{n}_A^{n_A} \bar{n}_B^{n_B}. \tag{1.5}$$

The likelihood contains all the information about true outcome of the election μ and f_A that we can hope to extract from the faulty machine count n_A and n_B. Maximizing the likelihood with respect to μ and f_A will give us our best estimates of the total number of voters and the fraction of voters who preferred candidate A. This is a general procedure that will extract the useful information about f_A for an arbitrarily configured machine. In the limiting case of a perfect machine ($p_{A\to A} = 1$, $p_{B\to B} = 1$,

$p_{A\to B} = p_{B\to A} = 0$), for example, this procedure sensibly returns $f_A = n_A/(n_A + n_B)$, while in the "reverse polarity" case ($p_{A\to B} = 1$, $p_{B\to A} = 1$, $p_{A\to A} = p_{B\to B} = 0$) it recognizes the switch and returns $f_A = n_B/(n_A + n_B)$. In the case of perfectly garbled output ($p_{A\to A} = p_{A\to B} = p_{B\to A} = p_{B\to B} = 1/2$) the likelihood $\mathcal{L}(n_A, n_B) \propto e^{-\mu}\mu^{n_A+n_B}$ has no dependence on f_A, informing us that all information about the voters' preference has unfortunately been lost.

Analyzing a color-selected redshift survey like ours is closely analogous to analyzing the output of a faulty vote-counting machine. Our procedure for counting galaxies at $z \sim 3$ is prone to missing some galaxies (e.g., red galaxies at higher redshifts, or faint galaxies at any redshift) and to misclassifying others (e.g., estimating $\mathcal{R} = 24.9$ for a galaxy whose true $\mathcal{R} = 25.2$), and we want to correct for this. The main difference is that now we want to estimate the fraction of galaxies in each of many different bins—for example, the fraction with $\mathcal{R} \simeq 24.0$ and $E(B-V) \simeq 0.15$ and $z \simeq 2.5$, with $\mathcal{R} \simeq 24.5$ and $E(B-V) \simeq 0.15$ and $z \simeq 2.5$, and so on, through all permutations of galaxy luminosity, reddening, and redshift—instead of only two. But the conceptual approach is identical.

1.4.2 Correcting selection bias: formal solution of the actual case

This, then, is the problem we face. We have data that consist of measured colors $U_n - G$ and $G - \mathcal{R}$, magnitudes $\mathcal{R}$, and (sometimes) redshifts z for the galaxies in our sample. From them we would like to determine the luminosity function of galaxies at $z \sim 3$ and the relative proportion of galaxies with different amounts of reddening $E(B-V)$, and we would like to see if either evolves over the redshift range we have probed. It is easy to work out the absolute luminosity and reddening implied by a galaxy's redshift, apparent magnitude, and colors, and trivial to place these values

into bins, but because of the selection bias described above we know that observed histograms of redshift, reddening, and luminosity are unlikely to closely resemble the true distributions in the underlying galaxy population. We would like some way of constraining the underlying distributions from the data in hand.

Let us specify the information we have about each galaxy with three numbers, the redshift z, the absolute luminosity L at $\lambda_{\rm rest} = 1600$Å, and the galaxy's spectral type E. E could in principle be anything that parametrizes the spectral shape of a galaxy—for example, an integer specifying a particular SED in a library—but in this example I will define E as the reddening $E(B-V)$ implied by the difference between each galaxy's observed colors and the colors of a dust-free model galaxy from Bruzual & Charlot (1996) that has been forming stars at a constant rate for 1Gyr. We will see below that this parametrization of E provides an adequate description of the $U_nG\mathcal{R}$ colors of every object in our sample at $z \sim 3$. Our goal is to work out the joint distribution of L, E, and z for galaxies in the underlying population from the joint distribution that we observe in our color-selected sample.

We can begin by making the hopeful assumption that galaxy luminosity, reddening, and redshift are intrinsically independent variables at the redshifts of interest, so that the average number of galaxies in the underlying sample with luminosity L, reddening E, and redshift z in a field of size $\Delta\Omega$ can be written

$$N(L,E,z)\frac{dV}{d\Omega dz}\Delta\Omega\, dL\, dE\, dz = \mu f(L)g(E)h(z)\frac{dV}{d\Omega dz}\Delta\Omega\, dL\, dE\, dz \qquad (1.6)$$

where the constant μ is related to the total comoving number density of galaxies, and the functions f, g, and h, are the underlying distributions of luminosity, reddening, and redshift normalized such that $\int_{L_{\rm min}}^{L_{\rm max}} dL f(L) = \int_{E_{\rm min}}^{E_{\rm max}} dE g(E) = \int_{z_{\rm min}}^{z_{\rm max}} dz h(z) = 1$. (This assumption is checked below and found to be adequate.)

In this case the analogs of equation 1.4 and 1.5 can be immediately written down. The expected number of galaxies in the observed sample with estimated luminosity

L, estimated reddening E, and estimated redshift z is

$$\bar{n}(L,E,z)\frac{dV}{d\Omega dz} = \mu \int dL'dE'dz' f(L')g(E')h(z')p_{L'E'z'\to LEz}\frac{dV}{d\Omega dz'}, \qquad (1.7)$$

and the likelihood of observing our data set (a list $\{L_iE_iz_i\}$ of the estimated luminosities, reddenings, and redshifts for each galaxy in the sample) is

$$\mathcal{L}(\{L_iE_iz_i\}) \propto \exp\left[-\mu\Delta\Omega \int dLdEdz\bar{n}(L,E,z)\frac{dV}{d\Omega dz}\right] \prod_i \bar{n}(L_i,E_i,z_i). \qquad (1.8)$$

Here $p_{L'E'z'\to LEz}$ is the probability that a galaxy with true luminosity L', reddening E', and redshift z' will be included in our sample and appear to have luminosity L, reddening E, and redshift z; it can be determined through Monte-Carlo simulations, as discussed below.

If we had good parametric models for the functions f, g, and h, we could determine their maximum likelihood shapes by numerically maximizing equation 1.8. In practice, however, it is hard to guess what shape these functions might have, and so the discrete versions of equations 1.6, 1.7 and 1.8 may be more useful. We can imagine dividing up each of the functions f, g, and h into a series of steps $\{f_i\}$, $\{g_j\}$, and $\{h_k\}$ whose height we want to determine. Set $\sum_i f_i = \sum_j g_j = \sum_k h_k = 1$, and let N_{ijk} and $\bar{n}_{ijk}$ represent the mean number of galaxies in a field of size $\Delta\Omega$ that any assumed values of $\{f_i\}$, $\{g_j\}$, and $\{h_k\}$ imply should lie in the i^{th} bin of luminosity, j^{th} bin of reddening, and k^{th} bin of redshift, for the underlying and observed samples respectively, and let n_{ijk} represent the observed number of galaxies in the same bin. Then equations 1.6, 1.7 and 1.8 become

$$N_{ijk} = \mu f_i g_j h_k V_k \Delta\Omega, \qquad (1.9)$$

$$\bar{n}_{ijk} = \mu\Delta\Omega \sum_{i'j'k'} f_{i'}g_{j'}h_{k'}V_{k'}p_{i'j'k'\to ijk}, \qquad (1.10)$$

and

$$\mathcal{L}(\{n_{ijk}\}) \propto \exp\left[-\sum_{ijk}\bar{n}_{ijk}\right] \prod_{ijk} \bar{n}_{ijk}^{n_{ijk}}, \qquad (1.11)$$

where V_k is the comoving volume per solid angle in the k^{th} bin of redshift.

The difference between using equation 1.11 and 1.8 is similar to the difference between using the luminosity function estimation methods of Sandage, Tammann, & Yahil (1979) and Efstathiou, Ellis, & Peterson (1988). In the first case one assumes a continuous shape for the luminosity function and works out the best parametric fit; in the second one models the luminosity function as a series of discrete segments and finds the best fit height for each.

In practice our data does not come from a single field, but from several. Because integration times, seeing, and crowding differ from one field to the next, the probabilities $p_{i'j'k'\to ijk}$ will as well. The likelihood is therefore the product of l terms similar to equation 1.11:

$$\mathcal{L}(\{n_{ijkl}\}) \propto \exp\left[-\sum_{ijkl} \bar{n}_{ijkl}\right] \prod_{ijkl} \bar{n}_{ijkl}^{n_{ijkl}}, \tag{1.12}$$

where

$$\bar{n}_{ijkl} = \mu\, \Delta\Omega_l \sum_{i'j'k'} f_{i'} g_{j'} h_{k'} V_{k'} p_{l,i'j'k'\to ijk} \tag{1.13}$$

and $p_{l,i'j'k'\to ijk}$ is the value of $p_{i'j'k'\to ijk}$ in the l^{th} field. When the data quality is similar from one field to the next, it is a good approximation to use equation 1.11 with $p_{i'j'k'\to ijk}$ replaced by

$$\bar{p}_{i'j'k'\to ijk} \equiv \sum_l \Delta\Omega_l p_{l,i'j'k'\to ijk} / \sum_l \Delta\Omega_l \tag{1.14}$$

instead of the more cumbersome equation 1.12.

Maximizing equation 1.12 is the formally correct way of estimating the underlying luminosity, reddening, and redshift distributions $\{f_i\}$, $\{g_j\}$, and $\{h_k\}$ from the data in our survey. But this approach is complicated, heavily reliant on computation rather than intuition, and not always easy to implement in practice. A simpler statistical approach would be desirable. Further discussion will be easier to understand if we first describe the way we calculate the "selection bias" coefficients $p_{i'j'k'\to ijk}$.

1.4.3 Quantifying selection bias in our sample

A $z \sim 3$ galaxy within one of our fields could be missed by our census for several reasons. It might be obscured by a nearby bright star, for example, or have measured colors which do not match our Lyman-break selection criteria, or simply have never been assigned a slit in one of our multislit masks. It is the job of the coefficients $p_{i'j'k' \to ijk}$ to quantify these (and other) selection effects in our sample.

In order to be included in our sample, a galaxy must be detected in our images and must have measured colors that satisfy the Lyman-break selection criteria

$$U_n - G \geq G - \mathcal{R} + 1.0, \qquad G - \mathcal{R} \leq 1.2, \qquad \mathcal{R} \leq 25.5. \tag{1.15}$$

It is easy to estimate the probability that this will occur. First, calculate the intrinsic $U_nG\mathcal{R}$ magnitudes that a galaxy with absolute luminosity L and reddening $E(B-V) = E$ would have if placed at redshift z. This requires applying the appropriate amount of dust reddening to a model spectrum of a star-forming galaxy, then subjecting the spectrum to intergalactic absorption (e.g., Madau 1995), and finally integrating the result through the $U_nG\mathcal{R}$ filter bandpasses. Recall that we have assumed that all Lyman-break galaxies have unreddened spectra similar to a Bruzual & Charlot (1996) model galaxy that has been forming stars at a constant rate for 1Gyr and that the dust reddening curve follows a Calzetti (1997) law. This assumption is consistent with the observed $U_nG\mathcal{R}$ colors of Lyman-break galaxies, as we will see below; Chapter 2 is concerned, in part, with whether the variations in spectral shapes observed in LBGs can be properly attributed to dust absorption in this way.

Now that the intrinsic $U_nG\mathcal{R}$ magnitudes of a galaxy with absolute luminosity L, reddening E, and redshift z are known, add large numbers of objects with those magnitudes to the $U_nG\mathcal{R}$ images of the Lyman-break survey, a few objects at a time, and try to detect them with the same photometric software used in the survey. Say the model galaxy's true properties place it in the i'th, j'th, k'th bin of L, E, z, and

say we have added it to the image of our lth field. Then the coefficients $p^{\rm phot}_{l,i'j'k'\rightarrow ijk}$ are equal to the number of galaxies that (a) were detected, (b) had measured colors that satisfied the Lyman-break selection criteria (equation 1.15), and (c) had measured colors that placed them in the ith, jth, kth bin of recovered properties, divided by the total number of galaxies with properties i', j', k' that were added to the image.

We have talked about the meaning of the i'th, j'th, k'th bins of intrinsic properties—they simply refer to the true absolute luminosity, reddening, and redshift of the model galaxies—but what do we mean by the ith, jth, kth bins of recovered properties? In principle they could index the *estimated* absolute luminosities, reddenings, and redshifts of the detected galaxies, but they do not have to; equation 1.12 does not care what i, j, and k stand for. In practice it is sometimes convenient to let them index properties closer to what we actually observe, say $\mathcal{R}$, $G-\mathcal{R}$, and z instead of L, E, z. $\mathcal{R}$ and $G-\mathcal{R}$ can be used to determine L and E, respectively, but only if we know the redshift z, and we would like the formalism to be able to do something with the large numbers of Lyman-break galaxies that have been photometrically detected but not spectroscopically observed. We will use both indexing schemes (measured L, E, z and $\mathcal{R}, G-\mathcal{R}, z$) below.

By adding sufficiently large numbers of objects with the full range of true L, E, z to each of our Lyman-break fields, we can determine all the coefficients $p^{\rm phot}_{l,i'j'k'\rightarrow ijk}$. These tell us everything we need to know about the selection bias that connects our photometric sample to the underlying population of galaxies at $z \sim 3$. But much of our analysis will rely on galaxies that have measured spectroscopic redshifts, and so we also need to understand the selection bias that connects the spectroscopic and photometric samples. This selection bias arose in two ways. First, spectroscopic targets were chosen from among the objects in the photometric sample in a partly subjective manner that is difficult to quantify in retrospect but clearly favored brighter sources. Roughly 50% of the photometric sample was targeted spectroscopically. Second, we

could not measure redshifts for many spectroscopic targets ($\sim$ 30%) due to the low signal to noise spectra. This introduced further bias against faint sources in the spectroscopic sample. The net effect is that the spectroscopic sample has a significantly different distribution of absolute magnitudes than the photometric sample. Because $P(\text{spect}|\text{exist}) = P(\text{spect phot}|\text{exist}) = P(\text{spect}|\text{phot})P(\text{phot}|\text{exist})$, the selection bias coefficients we want to use when analyzing the spectroscopic sample differ by a multiplicative factor $P(\text{spect}|\text{phot})$ from the photometric selection bias coefficients derived above. $P(\text{spect}|\text{phot})$ is, of course, the probability that a galaxy in the photometric Lyman-break galaxy will make it into the spectroscopic sample by virtue of (a) being chosen for spectroscopy, and (b) having an identifiable spectrum. I will assume here than $P(\text{spect}|\text{phot})$ depends only on the galaxy's apparent magnitude, though in principle it could depend on the galaxy's absolute magnitude, reddening, and redshift as well. This assumption can be checked by comparing results from the spectroscopic and photometric samples. One way to estimate $P(\text{spect}|\text{phot})$ is to calculate $\eta(\mathcal{R})$, the ratio of galaxies in our spectroscopic and photometric samples as a function of apparent magnitude. This provides a rough quantification of our bias against faint galaxies during spectroscopy, but it is not completely satisfactory. The main problem is that our spectroscopic bias against faint galaxies varies significantly from field to field. In some fields we spent only a small amount of time on spectroscopy, and as a result mainly only the brightest objects had measured redshifts. In other fields we doggedly continued the spectroscopy until we had redshifts for almost every object. In these fields there is much less spectroscopic bias against faint galaxies. One might imagine calculating $\eta(\mathcal{R})$ for each field separately, but this calculation would suffer badly from small number statistics in many of the fields, and in any case could not add anything to the information that is contained in the apparent magnitude distribution of the photometric sample itself. It would be difficult

to trust any determination of the luminosity function shape that relied on the coefficients $\bar{p}^{\rm spec}_{i'j'k'\to ijk}$; more robust luminosity function estimates will come from analysis of the photometric sample, which depends only upon the well determined coefficients $\bar{p}^{\rm phot}_{i'j'k'\to ijk}$. Nevertheless, we are forced to use the spectroscopic sample in some situations, e.g., determining the shape of the reddening distribution, because we can estimate $E(B-V)$ only for galaxies with measured redshifts. Fortunately the derived shape of the reddening distribution does not depend strongly on $P(\text{spect}|\text{phot})$, and it is an adequate approximation for this purpose to take

$$\bar{p}^{\rm spec}_{i'j'k'\to ijk} \simeq \eta(\mathcal{R}) \times p^{\rm phot}_{i'j'k'\to ijk} \tag{1.16}$$

with η equal to the ratio of galaxies in our spectroscopic and photometric samples as a function of apparent magnitude.

1.4.4 Correcting selection bias: approximate solutions

The goal of this subsection is to derive a way of estimating the distributions of L, E, z that is simpler and more intuitive than a brute force solution of equation 1.12.

Equation 1.12 simplifies substantially if we use the following approximation in addition to equation 1.14:

$$\bar{p}_{i'j'k'\to ijk} \simeq \bar{p}'_{ijk} \equiv \begin{cases} \sum_{lmn} \bar{p}_{i'j'k'\to lmn} & \text{if } i'=i,\ j'=j,\ k'=k \\ 0 & \text{otherwise} \end{cases} \tag{1.17}$$

Here ij should index each galaxy's inferred L, E rather than its measured $\mathcal{R}$, $G-\mathcal{R}$. In words, this approximation says that the true number of galaxies with L, E, z is roughly equal to the observed number with estimated luminosity, reddening, and redshift equal to L, E, z, divided by the number $\bar{p}'$, where $\bar{p}'$ is the fraction of simulated galaxies with L, E, z which were detected and recognized as Lyman-break galaxies in our Monte Carlo runs of § 1.4.3. The difference from our previous approach is

that now we are assuming that the estimated and true values L, E, z are always roughly equal. This is a reasonable approximation provided that our photometric uncertainties and biases are small compared to the bin sizes in L and E. This ought to be the case, or at least almost the case; it would be pointless to choose bin sizes that seriously violated that criterion.

Equation 1.12 can be brought to an even more convenient form if we know two of the three distribution functions $f(L)$, $g(E)$, and $h(z)$. We don't, of course, but it's not hard to make intelligent guesses. For example, we might be willing to assume that the true number density of Lyman-break galaxies does not change significantly over the redshift range of interest $2.5 \lesssim z \lesssim 3.5$, so that $h(z)$=const. Since the luminosity distance does not change by a large amount over the same redshift range, we might be willing to guess further that Lyman-break galaxies' luminosity function and apparent magnitude distributions have the same shape. With f and h known, and the selection bias coefficients $\bar{p}$ simplified by the diagonalization approximation 1.17, we can reduce equation 1.12 to

$$\mathcal{L}(\{n_{ijk}\}) \propto \exp\left[-\mu \sum_j g_j V_j^{\text{eff}}\right] \prod_j (g_j \mu)^{n_{\cdot j \cdot}} \tag{1.18}$$

where the

$$V_j^{\text{eff}} \equiv \Delta\Omega \sum_{ik} f_i h_k V_k \bar{p}'_{ijk} \tag{1.19}$$

are constants that can be calculated numerically once we have run the Monte-Carlo simulations and assumed forms for f_i and h_k, and

$$n_{\cdot j \cdot} \equiv \sum_{ik} n_{ijk} \tag{1.20}$$

is the number of galaxies in our sample with estimated reddenings that fall into the j^{th} bin of E.

Our best estimate of each g_j is the value that maximizes the likelihood 1.18, or

$$\mu g_j = n_{\cdot j \cdot} / V_j^{\text{eff}}. \tag{1.21}$$

We can see that the constant $V_j^{\rm eff}$ has a simple intuitive meaning: it is effective comoving volume in which our survey could have detected a galaxy with reddening that falls into the $j^{\rm th}$ bin of E. The effective volume of our survey is smaller for galaxies with $E(B-V) = 0.4$, which on average will satisfy our color-selection criteria over the redshift range $2.6 < z < 2.9$, than for galaxies with $E(B-V) = 0.15$ which satisfy our color-selection criteria throughout the redshift range $2.7 < z < 3.4$. Dividing the observed number of galaxies at each level of reddening by the appropriate effective volume provides a way to correct our survey for its selection bias against objects with certain spectral shapes.

Once we have estimates of the g_j, we can use them to refine our estimate of the luminosity function shape f_i. We assumed above that the luminosity distribution would have the same shape as the apparent magnitude distribution, but this cannot be completely correct; the Monte-Carlo simulations clearly show, for example, that we have problems detecting and measuring accurate colors for the fainter objects in our sample, and so they will be underrepresented in the observed apparent magnitude distribution. The approach just described can be used to derive the effective survey volume as a function of apparent magnitude by substituting the g_j determined above for the f_i in equation 1.19. These effective volumes will improve our estimate of the luminosity distribution shape, and we can then derive improved estimates of the effective volume as a function of reddening and improve our estimate of the reddening distribution shape, which can be used to improve our luminosity function yet again, and so on, until convergence is achieved. This was the approach used to derive the luminosity and reddening distributions that were presented in Steidel *et al.* (1999) with little explanation or justification.

The approach is appealingly simple and intuitive, but it is not entirely correct. The primary problem is with the assumptions behind approximation 1.17, which are violated in a number of ways. First, because the entire range of $G-\mathcal{R}$ colors observed

in galaxies at a single redshift, ~ 0.8 mag, is only ~ 4 times our typical photometric error in $G - \mathcal{R}$, we cannot in fact make our bins in the reddening distribution much larger than the uncertainty in the reddening. This means that significant numbers of galaxies that ought to fall in a particular bin of reddening will be scattered into neighboring bins by photometric errors. The problem would be inconsequential if each bin gained and lost equal numbers of members, but because the reddening distribution is peaked that will not be the case. Instead photometric errors will scatter galaxies away from the peak and into the wings of the distribution. This type of Malmquist bias cannot be corrected by any scheme that makes use of approximation 1.17. Second, it is not true that galaxies with true luminosity and reddening equal to L and E will on average have observed luminosity and reddening equal to L and E. The Monte-Carlo simulations show that our photometry is slightly biased; the $G - \mathcal{R}$ color is usually overestimated. This is due to the fact that our isophotes adjust themselves to include the maximum amount of light in the $\mathcal{R}$ band, where they are defined, but they are not allowed to similarly adjust themselves in G. This sort of photometric bias also cannot be corrected if we use approximation 1.17. Finally, photometric bias is especially acute for galaxies whose true L, E, and z would place them outside of our Lyman-break selection window on average. These galaxies will be included in our sample *only* if they have significant photometric errors, $L_{\rm meas} \neq L_{\rm true}$ and $E_{\rm meas} \neq E_{\rm true}$, so approximation 1.17 cannot be satisfied by them almost by definition.

These violations of approximation 1.17 are not disastrous, but they ought to be taken into account. One way to do this without resorting to a brute force solution of equation 1.12 is to follow the iterative approach above but use an expression for $\bar{n}_{ijk}$ that does not rely on approximation 1.17. One can begin by setting the f_i to the best fit values estimated above and assuming $h_k = \text{const}$. Then the maximum likelihood values of g_j can be estimated by numerically maximizing the likelihood as expressed in equations 1.11, 1.10, and 1.14. In this stage only the spectroscopic

sample is relevant, since we cannot estimate $E(B-V)$ for galaxies without measured redshifts[2], and so this is the sample we are analyzing it with the appropriate selection coefficients $p^{\rm spec}_{i'j'k'\to ijk}$.

Once the improved estimate of the reddening distribution g_j is in hand, we can use it to improve our estimate of the luminosity distribution. In this stage it is better to use the photometric sample, since then we can use selection bias coefficients that do not depend on the poorly understood way that we choose photometric candidates for spectroscopy. To use the photometric sample, we need a version of equation 1.12 appropriate for galaxies without measured redshifts. It is easy to guess what form this equation will take, but here is a formal derivation. Let $n_{ij.}$ be the number of galaxies we observe with $\mathcal{R}$ in the $i^{\rm th}$ bin of measured flux and $G-\mathcal{R}$ in the $j^{\rm th}$ bin of measured $G-\mathcal{R}$, and let $\mathcal{A}$ be the set of all matrices $\mathbf{x} = \{n_{ijk}\}$ such that each number n_{ijk} is a nonnegative integer and $\sum_k n_{ijk} = n_{ij.}$. Then, using the probability equality $P(A|C) = \sum_B P(AB|C)$, we can work out the likelihood of observing the measured numbers of galaxies $\{n_{ij.}\}$ in each $\mathcal{R}$, $G-\mathcal{R}$ bin for any given values of $\{f_i\}$, $\{g_j\}$, $\{h_k\}$:

$$\begin{aligned}
\mathcal{L}(\{n_{ij.}\}|\{f_i\}\{g_j\}\{h_k\}) &= \sum_{\mathbf{x}\in\mathcal{A}} \mathcal{L}(\{n_{ijk}\}|\{f_i\}\{g_j\}\{h_k\}) \\
&= \exp\Big[-\sum_{ij}\bar{n}_{ij.}\Big] \sum_{\mathbf{x}\in\mathcal{A}} \prod_{ijk} \frac{\bar{n}_{ijk}^{n_{ijk}}}{n_{ijk}!} \\
&= \exp\Big[-\sum_{ij}\bar{n}_{ij.}\Big] \prod_{ij} \frac{\bar{n}_{ij.}^{n_{ij.}}}{n_{ij.}!} \qquad (1.22)
\end{aligned}$$

where $\bar{n}_{ij.} \equiv \sum_k \bar{n}_{ijk}$ can be derived from our photometric selection bias coefficients $\bar{p}^{phot}_{i'j'k'\to ijk}$ and from equation 1.10. The last equality uses the Multinomial Theorem. Numerically maximizing 1.22 gives us an improved estimate of the luminosity function. The equation will automatically use whatever photometric redshift information

[2]because without the redshift we cannot account for the Lyman-α forest absorption in the G band, which is large and strongly redshift dependent.

is contained in each galaxy's color and magnitude to improve its guess at the distance modulus. This does not do us much good in the Lyman-break sample, where we have useful constraints on only a single color, $G - \mathcal{R}$, which is not strongly correlated with redshift, but it could prove important in other situations. We can then iterate through the estimation of the reddening and luminosity distributions until we reach convergence. This was the approach used to derive the luminosity function and reddening distribution presented without discussion in Adelberger & Steidel (2000) (Chapter 2).

1.4.5 Correlations among variables

We conclude by checking an assumption made near the beginning of this section. Starting with equation 1.6 we assumed that UV luminosity, reddening, and redshift were independent variables in galaxies at $z \sim 3$. If this were true, it would imply, for example, that the typical galaxy luminosity or reddening do not change with redshift for $2.5 \lesssim z \lesssim 3.5$ and that the brightest galaxies in the UV have the same distribution of reddening as the faintest. Is this assumption correct?

One way to check is to look for systematic differences between the number of galaxies n_{ijk} that are observed in a given bin of luminosity, reddening, and redshift and the number predicted by our best-fit values of f_i, g_j, h_k. The size of the differences can be quantified by calculating

$$\chi^2 = \sum_{ijk} \frac{(n_{ijk} - \bar{n}_{ijk})^2}{\bar{n}_{ijk}} \tag{1.23}$$

(e.g., Press *et al.* (1992, §14.4)) with $\bar{n}_{ijk}$ given by equations 1.10 and 1.14 above.

Another approach is to generate a large ensemble of simulated Lyman-break data sets from our selection-bias coefficients and best-fit $\{f_i\}$, $\{g_j\}$, $\{h_k\}$. The simulated data sets will be drawn from an underlying population with uncorrelated L, E, and z, but our selection biases will have introduced spurious correlation between the

variables. We can quantify the strength of these spurious correlations by calculating some statistic sensitive to correlation (e.g., Kendall's τ) for each of L, E, z against the others. Comparing the distribution of τ in the simulated data sets to the values observed in the real data can tell us whether our observations suggest that there is any correlation between L, E, and z beyond what our known selection biases would introduce.

Neither approach suggests that our observed data set is significantly different from the data sets we would obtain if L, E, and z were independent. Besides showing that L, E, and z cannot be strongly correlated in galaxies at $z \sim 3$, this demonstrates that the observed $U_n G\mathcal{R}$ colors of Lyman-break galaxies can be successfully reproduced by the SED parametrization we have adopted, a constant star-formation rate Bruzual & Charlot (1996) model subjected to varying amounts of dust reddening following a Calzetti (1997) law. But the color information we have is very limited. Most Lyman-break galaxies are undetected, or only marginally detected, in the U_n band, and so in most cases we have only asked our model SEDs to reproduce a single color, $G - \mathcal{R}$. It is hardly surprising the models succeeded; virtually any model with a single free parameter would. Establishing that the derived dust reddenings have a physical meaning will require us to observe high-redshift galaxies at wavelengths besides $U_n G\mathcal{R}$. That is the subject we turn to next.

Calzetti, D. 1997, *Astron. J.*, **113**, 162.

Cohen, J., Hogg, D., Pahre, M., Blandford, R., Shopbell, P., & Richberg, K. 1999, *Astrophys. J. Suppl.*, **120**, 171.

Cohen, J., Hogg, D., Blandford, R., Cowie, L., Hu, E., Songaila, A., Shopbell, P., & Richberg, K. 2000, *Astrophys. J.*, **538**, 29.

Cowie, L.L., Songaila, A., Hu, E.M., & Cohen, J.G. 1996, *Astron. J.*, **112**, 839.

Efstathiou, G., Ellis, R.S., & Peterson, B.A. 1988, *Mon. Not. Roy. Astron. Soc.*,

232, 431.

Gunn, J.E. & Stryker, L.L. 1983, *Astrophys. J. Suppl.*, **52**, 121.

Heckman, T. 1998, *Astron. Soc. Pac. Conf. Ser.*, **148**, 127.

Lilly, S.J., Hammer, F., Le Fevre, O., & Crampton, D. 1995, *Astrophys. J. Lett.*, **455**, 75.

Madau, P. 1995, *Astrophys. J.*, **441**, 18.

Papovich, C., Dickinson, M., & Ferguson, H. 2001, *Astrophys. J.*, **559**, 620.

Press, W. H., Flannery, B. P., Teukolsky, S. A., & Vetterling, W.T. 1992, in *Numerical Recipes in C* (Cambridge: Cambridge University Press.)

Sandage, A., Tammann, G.A., & Yahil, A. 1979, *Astrophys. J.*, **232**, 352.

Shapley, A.E., Steidel, C.C., Adelberger, K.L., Dickinson, M., Giavalisco, M., & Pettini, M. 2001, *Astrophys. J.*, **562**, 95.

Steidel, C. C., Adelberger, K. L., Giavalisco, M., Dickinson, M., & Pettini, M. 1999, *Astrophys. J.*, **519**, 1.

Steidel, C. C. & Hamilton, D. 1993, *AJ*, **105**, 2017.

Williams, R.E. *et al.* 1996, *Astron. J.*, **112**, 1335.

Chapter 2

Multiwavelength Observations of Dusty Star Formation at Low and High Redshift[1]

Abstract

If high-redshift galaxies resemble rapidly star-forming galaxies in the local universe, most of the luminosity produced by their massive stars will have been absorbed by dust and re-radiated as far-infrared photons that cannot be detected with existing facilities. This paper examines what can be learned about high-redshift star formation from the small fraction of high-redshift galaxies' luminosities that is emitted at accessible wavelengths. We first consider the most basic ingredient in the analysis of high-redshift surveys: the estimation of star-formation rates for detected galaxies. Standard techniques require an estimate of the bolometric luminosity produced by their massive stars. We review and quantify empirical correlations between bolometric luminosities produced by star formation and the UV, mid-IR, sub-mm, and radio luminosities of galaxies in the local universe.

[1]Previously published as Adelberger & Steidel 2000, *Astrophys. J.*, **544**, 218.

These correlations suggest that observations of high-redshift galaxies at any of these wavelengths should constrain their star-formation rates to within $\sim$ 0.2–0.3 dex. We assemble the limited evidence that high-redshift galaxies obey these locally calibrated correlations. The second part of the paper assesses whether existing surveys have found the galaxies that host the majority of star-formation at high redshift even though they directly detect only a small fraction of the luminosities of individual galaxies. We describe the characteristic luminosities and dust obscurations of galaxies at $z \sim 0$, $z \sim 1$, and $z \sim 3$. After discussing the relationship between the high-redshift populations selected in surveys at different wavelengths, we calculate the contribution to the 850μm background from each and argue that these known galaxy populations can together have produced the entire observed background. The available data show that a correlation between star-formation rate and dust obscuration $L_{\rm bol,dust}/L_{\rm UV}$ exists at low and high redshift alike. The existence of this correlation plays a central role in the major conclusion of this paper: most star-formation at high redshift occurred in galaxies with moderate dust obscurations $1 \lesssim L_{\rm bol,dust}/L_{UV} \lesssim 100$ similar to those that host the majority of star-formation in the local universe and to those that are detected in UV-selected surveys.

2.1 Introduction

The universe of galaxies beyond $z \sim 1$ has finally become relatively easy to observe. While only a handful of galaxies at $z \gtrsim 1$ were known five years ago, close to 2000 have spectroscopic redshifts today. Planned redshift surveys should increase the number by at least an order of magnitude in the next several years. Analyzing the large and rapidly growing samples of high-redshift galaxies will be a major challenge in the

coming decade.

Much of this analysis will rely on estimates of star-formation rates for the detected galaxies. These estimates are required to answer the most basic questions that high-redshift surveys can address—when did the stars in the universe form? how were the sites of star formation related to the evolving perturbations in the underlying distribution of matter?—but unfortunately no standard and widely accepted techniques exist for estimating star-formation rates from the data usually available in high-redshift samples. Researchers analyzing data taken at a variety of wavelengths with a variety of techniques have reached wildly discrepant conclusions about the star-formation history of the universe (e.g., Madau *et al.* 1996; Smail *et al.* 1997; Barger *et al.* 1998; Blain *et al.* 1999a; Blain *et al.* 1999c; Eales *et al.* 1999; Pettini *et al.* 1999; Steidel *et al.* 1999; Tan, Silk, & Balland 1999; Trentham, Blain, & Goldader 1999; Barger, Cowie, & Richards 2000, hereafter BCR).

The central problem is that the energy produced by star formation in young galaxies is emitted across more than six decades of frequency, from the far-UV to the radio, while most high-redshift surveys are based on observations at only a narrow range of frequencies. Standard methods for deriving a galaxy's star-formation rate require an estimate of the total energy emitted by its massive stars, but in existing surveys this is never directly observed. Radio surveys detect only the tiny percentage of the total energy that goes into accelerating electrons in supernova remnants, for example, while optical surveys detect the portion of massive stars' emission that is not absorbed by dust and sub-mm surveys detect a fraction of the portion that is. Large and uncertain corrections are needed to estimate the total emitted energy from the energy detected at any of these wavelengths. Differences in the adopted corrections are largely responsible for current discrepancies in estimates of the star-formation history of the universe.

In principle one could obtain a robust estimate of the energy emitted by massive

stars in a high redshift galaxy by observing it over a sufficiently wide range of wavelengths, but with current technology this is rarely possible. Star-forming galaxies at high redshift almost certainly emit the bulk of their luminosities at far-infrared wavelengths that are extremely difficult to detect. Although massive stars themselves radiate mainly in the far-UV, rapid star formation in the local universe occurs in dusty environments where most UV photons are quickly absorbed, and as a result most of the luminosity produced by massive stars tends to emerge in the far-IR where dust radiates. This is known to be true for a broad range of galaxies in the local universe, from the famous class of "Ultra Luminous Infrared Galaxies" (ULIRGs, galaxies with $L_{\rm FIR} \gtrsim 10^{12} L_{\odot}$) to the much fainter UV-selected starbursts contained in the IUE Atlas (e.g., Meurer, Heckman, & Calzetti 1999, hereafter MHC). The recent detection of a large extragalactic far-IR background (e.g., Fixsen et al. 1998) suggests that it is likely to have been true at high redshifts as well.

Because most of the energy produced by massive stars is likely radiated by dust in the far-IR, estimates of the bolometric dust luminosities of high redshift galaxies are required in order to estimate their star-formation rates. The bolometric dust luminosities usually cannot be directly observed—the earth's atmosphere is opaque in the far-IR and most high-redshift galaxies are too faint to have been detected by any far-IR satellite that has flown—but they can be inferred from known correlations between local galaxies' bolometric dust luminosities and their luminosities in the optical, mid-IR, sub-mm, and radio atmospheric windows.

The first part of this paper aims to present a unified framework for estimating the bolometric dust luminosities of high-redshift galaxies selected at different wavelengths. In § 2.2 we summarize and re-examine locally established correlations between bolometric dust luminosities and luminosities through atmospheric windows, quantifying their scatter in cases where it has not been done explicitly by previous

authors. In § 2.3 we present the limited available evidence that high-redshift galaxies obey these correlations. Published estimates of the cosmic star-formation history derived from observations through one atmospheric window have often been accompanied by claims that most of the star-formation could not have been detected with observations through other atmospheric windows. In the second part of this paper, § 2.4, we use the results of §§ 2.2 and 2.3 to evaluate whether this is true. After reviewing the properties of star-forming galaxies in the local universe, we discuss the properties of high-redshift galaxies selected in surveys at different wavelengths and estimate the contribution to the far-IR background from galaxies similar to those detected in optical, mid-IR, and sub-mm surveys. Our conclusions are presented in § 2.5.

Throughout this paper we shall denote luminosities by L when they have units of energy time^{-1}, by l_ν when they have units of energy time^{-1} frequency^{-1}, and by l_λ when they have units of energy time^{-1} wavelength^{-1}; and observed fluxes by f_ν (units of energy time^{-1} frequency-1 area^{-1}) or f_λ (units of energy time^{-1} wavelength^{-1} area^{-1}).

2.2 Dust-obscured star formation in the local universe

The energy produced by massive stars emerges from galaxies over a wide range of wavelengths. Figure 2.1 shows typical spectral shapes of this emission for rapidly star-forming galaxies in the local universe. Massive stars radiate predominantly in the far-UV, but as galaxies become dustier an ever larger fraction of their luminosity is absorbed by dust and re-radiated in the far-IR. In typical cases most of the energy released by massive stars emerges in the far-IR. This section describes how the dust's

bolometric luminosity can be estimated from observations through the atmospheric windows indicated on the x-axis of Figure 2.1.

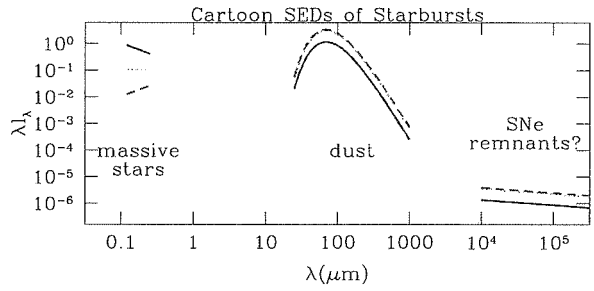

Figure 2.1 Schematic spectra of a starburst with fixed star-formation rate and varying dust opacity. These spectra illustrate the empirical correlations between UV, far-IR, and radio properties of actively star-forming galaxies in the local universe. Increasing the dust obscuration makes the UV continuum redder and fainter while boosting the far-IR luminosity; increases in far-IR luminosity are accompanied by increases in radio luminosity. The range of obscurations shown ($A_{1600} \sim 0.5$, solid line; $A_{1600} \sim 2.5$, dotted line; $A_{1600} \sim 4.5$, dashed line) roughly span the range observed in local starbursts. At $A_{1600} \sim 2.5$ most of the luminosity of massive stars is absorbed by dust. Further increases in dust opacity do not significantly increase the absorbed energy, and so the dotted and dashed lines nearly overlap in the far-IR and radio. Dust emission in the far-IR is typically the dominant component in rapidly star-forming galaxies bolometric luminosities, but most of this emission cannot be detected through atmospheric windows (shaded regions on the lower abscissa).

2.2.1 Sub-mm constraints on dust luminosity

Although a galaxy's total dust luminosity at $10\mu m \lesssim \lambda \lesssim 1000\mu m$ cannot be directly measured from the ground, narrow atmospheric windows in the sub-millimeter (Figure 2.1) allow a small fraction of it to reach the earth's surface. If dust in all galaxies radiated with the same known spectral energy distribution (SED)—say a 50K blackbody—then a galaxy's bolometric dust luminosity could be reliably estimated by simply scaling the flux measured through a sub-mm atmospheric window.[2] Unfortunately dust SEDs vary considerably from one galaxy to the next and are more complex than simple blackbodies. Obtaining a reasonable fit to a galaxy's measured

[2]provided, of course, that the galaxy's redshift and luminosity distance are known.

dust SED usually requires at least two "modified" blackbodies of the form

$$f_\nu \propto \frac{\nu^{3+\epsilon}}{\exp(h\nu/kT) - 1} \tag{2.1}$$

where $\epsilon \sim 1.5$, the emissivity index, is sometimes treated as a free parameter in addition to the temperatures and amplitudes of the modified blackbodies (e.g., Klaas *et al.* 1997). The required parameters in these fits vary among galaxies in a way that is not quantitatively understood.

Because of the significant variation in the shape of galaxies' dust SEDs, measuring a galaxy's flux in one of the narrow sub-mm atmospheric windows cannot precisely determine its bolometric dust luminosity. Nevertheless, sub-mm fluxes provide some useful information; galaxies with large fluxes through the sub-mm atmospheric windows tend also to have large bolometric dust luminosities. To quantify how well sub-mm flux measurements can constrain the bolometric dust luminosities of actively star-forming galaxies in the local universe, we have assembled from the literature a sample of these galaxies with published IRAS fluxes at 25μm, 60μm, and 100μm, as well as at least one flux measurement at a wavelength 200μm $< \lambda <$ 1000μm to constrain the temperature of the cool dust component and the slope of its (modified) Rayleigh-Jeans tail. This sample consists of 27 galaxies: the ULIRGs IRAS05189-2524, IRAS08572+3915, UGC5101, IRAS12112+0305, Mrk231, Mrk273, IRAS14348-1447, and IRAS15250+3609 detected at 800μm (and sometimes 450μm) by Rigopoulou *et al.* (1996); the LIRGs NGC1614, NGC3110, NGC4194, NGC4418, NGC5135, NGC5256, NGC5653, NGC5936, Arp193, and Zw049 detected at 850μm by Lisenfeld *et al.* 1999; the interacting galaxies NGC6240, Arp220, and Arp244 observed at 25μm $< \lambda <$ 200μm by Klaas *et al.* (1997); the UV-selected starbursts NGC6090, NGC7673, NGC5860, IC1586, and Tol1924-416 detected at 150μm and 205μm by Calzetti *et al.* (1999); and the nearby starburst M82 (Hughes, Robson, & Gear 1990 and references therein).

The dust SEDs of these galaxies are shown in Figure 2.2. For clarity we have connected measurements of individual galaxies at different wavelengths with spline fits (continuous lines). These fits were calculated in $\log \lambda - \log f_\lambda$ space and should roughly capture the expected power-law shape of dust SEDs in their (modified) Rayleigh-Jeans tails. Measurements from all galaxies were normalized to have the same total luminosity under the fits.

This plot can be used to estimate a rapidly star-forming galaxy's bolometric dust luminosity on the basis of its luminosity at a single observed wavelength:

$$L_{\rm bol,dust} \sim \left\langle \frac{L_{\rm bol,dust}}{\lambda l_\lambda} \right\rangle \lambda l_\lambda \equiv \mathcal{K}(\lambda) \lambda l_\lambda \tag{2.2}$$

where the expectation value is taken over all dust SEDs in the figure. Table 2.1 lists the values $\mathcal{K}$ at various wavelengths. Ideally one would calculate $\mathcal{K}$ by fitting two modified blackbodies to each dust SED, as discussed above, but most of the galaxies in our sample have measured fluxes at only 4 relevant wavelengths (25μm, 60μm, 100μm, and 850μm) and this fit has more than 4 free parameters. Instead, we estimated $\mathcal{K}$ from the log-log spline interpolations shown in Figure 2.2. This spline fitting does not take proper account of uncertainties in the measured fluxes, but the uncertainties are almost always far smaller than the intrinsic differences in dust SEDs among the galaxies in our sample. The observed spread among these galaxies in $L_{\rm bol,dust}/\lambda l_\lambda$ at a given wavelength provides a measure of how reliably a flux measurement at that wavelength can constrain a galaxy's bolometric dust luminosity. The RMS spread in $\log_{10} \mathcal{K}$, also listed in Table 2.1, suggests sub-mm estimates of $L_{\rm bol,dust}$ will be accurate to about a factor of 2.

According to Sanders & Mirabel (1996) and Dunne *et al.* (2000), the shapes of galaxies' dust SEDs are correlated with their bolometric luminosities, and so one might hope to estimate $L_{\rm bol,dust}$ more accurately by using different values of $\mathcal{K}$ for galaxies with different absolute sub-mm luminosities. Unfortunately, this trend does

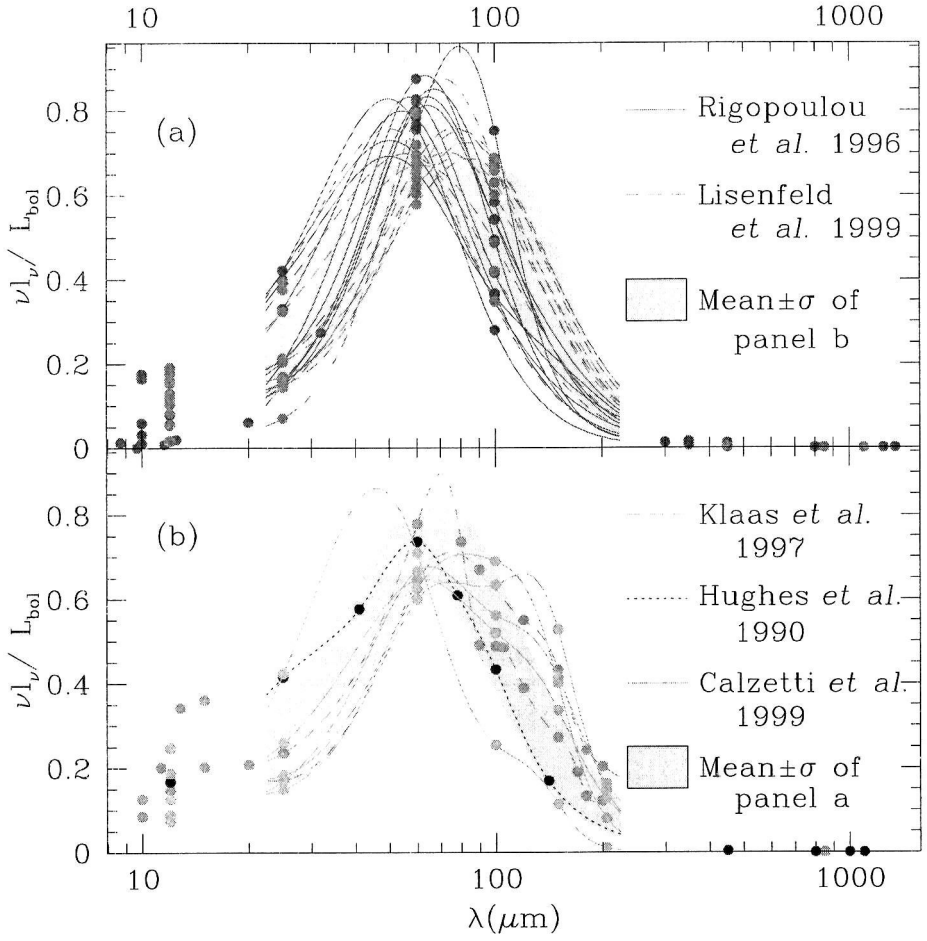

Figure 2.2 The far-IR spectral energy distributions of plausible local analogs to rapidly star-forming high-redshift galaxies. The points show measurements (see text for references) and the lines show spline fits to these measurements. Each SED has been scaled to have the same total luminosity within the range of the spline fit. Panel (a) shows the dust SEDs of galaxies with unusually large IR luminosities (LIRGs and ULIRGs). Panel (b) shows galaxies where more detailed dust SED measurements are available; these are mainly less luminous UV-selected galaxies. The dust SEDs of these two samples are not drastically different, as the shaded regions show. Because of the range in $\nu l_\nu / L_{\rm bol}$ at each wavelength, measuring a galaxy's flux at only one far-IR/sub-mm wavelength cannot pin down precisely its bolometric dust luminosity. This statement is quantified in § 2.2.1 and Table 2.1.

not appear to be strong enough among rapidly star-forming galaxies to substantially reduce the scatter in $\mathcal{K}$ (i.e., to substantially improve estimates of $L_{\rm bol,dust}$ derived

Table 2.1 Dust SEDs of local starbursts

$\lambda(\mu\mathrm{m})$	$\langle 1/\mathcal{K}_\lambda \rangle$	$\sigma_{\mathcal{K}}(\mathrm{dex})$	N_{objects}
25	0.25	0.21	27
50	0.64	0.08	27
75	0.69	0.06	27
100	0.53	0.12	27
125	0.38	0.17	27
150	0.26	0.22	27
175	0.17	0.25	27
200	0.11	0.30	27
225	0.076	0.30	21
250	0.055	0.31	21
275	0.041	0.32	21
300	0.030	0.32	21
325	0.023	0.32	21
350	0.017	0.32	21
375	0.013	0.32	21
400	0.010	0.32	21
425	0.0080	0.33	21
450	0.0063	0.33	21
500	0.0040	0.33	21
550	0.0026	0.33	21
600	0.0017	0.33	21
650	0.0012	0.33	21

from photometry in a single sub-mm window). Illustrating this point, Figure 2.3 shows $\mathcal{K}(200\mu\mathrm{m})$ ($\equiv L_{\mathrm{bol,dust}}/\lambda l_\lambda$ at $\lambda = 200\mu\mathrm{m}$) versus $L_{\mathrm{bol,dust}}$ for each galaxy in our sample. Although LIRGs clearly have systematically different $\mathcal{K}(200\mu\mathrm{m})$ values than ULIRGs, the trend disappears at lower luminosities. Including an absolute luminosity dependence in $\mathcal{K}(\lambda)$ seems unlikely to significantly improve sub-mm constraints on $L_{\mathrm{bol,dust}}$.

Measuring the luminosity of a galaxy in two sub-mm bands instead of only one provides additional information about the shape of the dust SED that could in principle be used to estimate $L_{\mathrm{bol,dust}}$ more accurately. Unfortunately, the major sub-mm

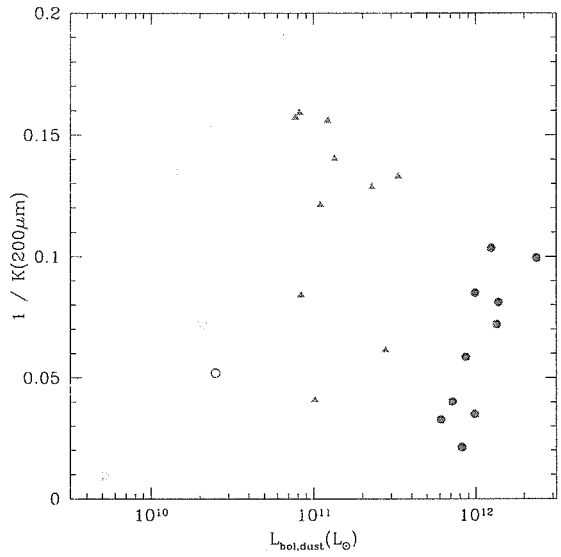

Figure 2.3 Dust SED shapes at different bolometric dust luminosities. The quantity $\mathcal{K}(200\mu\mathrm{m}) \equiv L_{\mathrm{bol,dust}}/\nu l_\nu(200\mu\mathrm{m})$ is sensitive to differences in the shapes of galaxies' dust SEDs; its value will be important to us below when we discuss 850μm fluxes from galaxies at $z \sim 3$. Shown are the values of $1/\mathcal{K}(200\mu\mathrm{m})$ for local galaxies spanning a range of bolometric dust luminosities: ULIRGs (filled circles), LIRGs (triangles), "interacting galaxies" (filled stars), UV-selected starbursts (open stars), and M82 (open circle). More complete descriptions of these local samples are presented in the text. The bolometric luminosities assume that each galaxy is at a distance of $cz/(75\mathrm{km/s/Mpc})$, except for M82 where we used 3.2 Mpc (Freedman & Madore 1988). Brighter galaxies tend to have hotter dust temperatures and larger values of $\mathcal{K}(200\mu\mathrm{m})$, but this trend has a great deal of scatter and cannot easily be used to improve estimates of galaxies' bolometric dust luminosities derived from observations at $\sim 200\mu$m rest.

atmospheric windows at 450μm and 850μm both lie in the Rayleigh-Jeans tail of typical dust SEDs at $z \lesssim 3$. Measuring both 450μm and 850μm fluxes of a galaxy at these redshifts therefore reveals little about the temperature of the cold dust component and almost nothing at all about the possible presence of other dust components at higher temperatures. At larger redshifts measuring both fluxes provides better constraints on the shape of the dust SED, but even then two flux measurements cannot uniquely determine the shape of dust SEDs that typically require more than four free parameters for a reasonable fit. In any case accurate fluxes in more than one sub-mm

band are seldom available for the faint high-redshift galaxies that are our primary concern. Obtaining these additional sub-mm fluxes may ultimately prove useful for more accurate estimation of galaxies' bolometric dust luminosities, but we will not consider this possibility further.

2.2.2 Mid-Infrared constraints on dust luminosity

At wavelengths $\lambda \lesssim 15\mu$m the dust emission from galaxies tends to rise significantly above the modified blackbody fits discussed in § 2.2.1. This excess emission is thought to originate from very small grains transiently heated by single UV-photons to high non-equilibrium temperatures; much of it emerges in a few discrete polycyclic aromatic hydrocarbon (PAH) lines at 3.3, 6.2, 7.7, 8.6, and 11.3μm (see, e.g., Xu *et al.* 1998 and references therein). 7.7μm is often the strongest of these lines and the easiest to detect at high redshift. In this subsection we will attempt to quantify the constraints that observations through a 6–9μm filter can place on a galaxy's bolometric dust luminosity. We will need this information in § 2.3.3 below.

The sample we will use consists of 11 starbursts and 53 star-formation–dominated ULIRGs observed in the mid-IR by Rigopoulou *et al.* (2000) and the starburst NGC6090 observed in the mid-IR by Acosta-Pulido *et al.* (1996).

In analogy to § 2.2.1 we will define a constant of proportionality $\mathcal{K}_{\rm MIR}$ between bolometric dust luminosity and luminosity at $6\mu{\rm m} < \lambda < 9\mu$m:

$$L_{\rm bol,dust} = \mathcal{K}_{\rm MIR} \int_{6\mu{\rm m}}^{9\mu{\rm m}} d\lambda \, l_\lambda. \tag{2.3}$$

After excluding two outliers with anomalously low $\sim 8\mu$m luminosities, IRAS00199-7426 and IRAS20100-4156, the mean value of $\mathcal{K}_{\rm MIR}$ among the galaxies in this sample is 52, the mean value of $1/\mathcal{K}_{\rm MIR}$ is 0.025, and the rms dispersion in $\log_{10}\mathcal{K}_{\rm MIR}$ is 0.22 dex. Each galaxy's bolometric dust luminosity was estimated from its measured IRAS 60μm and 100μm luminosities with the relationship $L_{\rm bol,dust} \simeq 1.47 L_{FIR}$, where

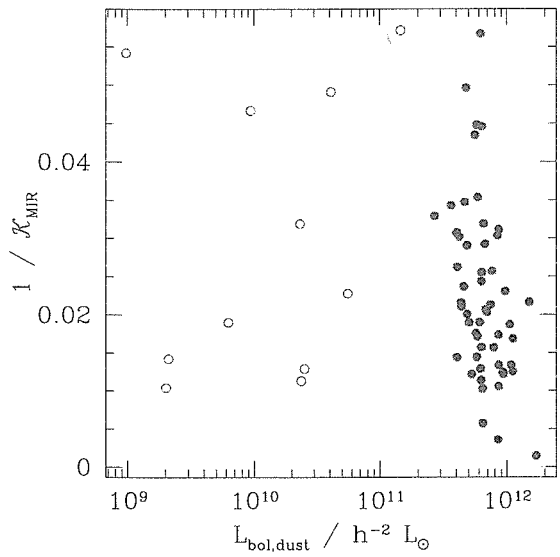

Figure 2.4 The ratio of $6 < \lambda < 9\mu$m PAH luminosity to bolometric dust luminosity ($\mathcal{K}_{\rm MIR} \equiv L_{\rm bol,dust} / \int_{6\mu m}^{9\mu m} d\lambda l_\lambda$) for rapidly star-forming galaxies in the local universe. Open and solid circles represent starbursts and star-formation–dominated ULIRGs observed by Rigopoulou *et al.* (2000). The star represents the starburst NGC6090 observed by Acosta-Pulido *et al.* (1996). Similar values of K_{MIR} are observed in rapidly star-forming galaxies with a large range of bolometric luminosities.

$L_{FIR} \equiv 0.65L_{60} + 0.42L_{100}$, $L_{60} \equiv \nu l_\nu$ at $\nu = c/60\mu$m, and $L_{100} \equiv \nu l_\nu$ at $\nu = c/100\mu$m (e.g., Helou *et al.* 1988). The adopted relationship between $L_{\rm bol,dust}$ and L_{FIR} is satisfied by the galaxies in the sample of § 2.2.1 with an rms scatter of 7%. The estimated mean and rms of $\mathcal{K}_{\rm MIR}$ are not significantly altered by restricting our analysis either to galaxies with flux measurements in the sub-mm as well as at 60 and 100μm or to the galaxies with the least noisy mid-IR spectra. Similar values of $\mathcal{K}_{\rm MIR}$ are observed in galaxies with a wide range of bolometric luminosities, as shown in Figure 2.4.

2.2.3 UV constraints on dust luminosity

The methods of estimating $L_{\rm bol,dust}$ discussed so far rely on fitting an average dust SED through the observed dust emission at a single wavelength. $L_{\rm bol,dust}$ can also be estimated without observing any dust emission at all. Many standard methods of estimating the dust content of galaxies rely on the absorption signature of dust in the UV/optical rather than its emission in the far-IR. We will focus our attention on one of these methods, which has been shown (see, e.g., MHC) to predict reasonably well the observed dust emission of local starburst galaxies.

The idea behind this technique is simple. Because dust absorbs shorter wavelengths more strongly than longer wavelengths, the UV continua of starbursts should become redder on average as the galaxies become dustier and the ratio of far-IR to far-UV luminosity increases. According to MHC, there is surprisingly little scatter in this trend among starburst galaxies in the local universe; the bolometric dust luminosities of the 57 starburst galaxies in their sample obey

$$L_{\rm bol,dust} = 1.66(10^{0.4(4.43+1.99\beta)} - 1)L_{1600}, \tag{2.4}$$

where $L_{1600} \equiv \nu l_\nu$ evaluated at $\nu = c/1600\text{Å}$ and β is the observed spectral slope ($l_\lambda \propto \lambda^\beta$) at $1200 \lesssim \lambda \lesssim 2000\text{Å}$, with a scatter of 0.3 dex. This correlation is illustrated in Figure 2.1.

2.2.4 Radio constraints on dust luminosity

Observations through the radio atmospheric window can also constrain $L_{\rm bol,dust}$. Increases in far-IR luminosity are accompanied, in local galaxies, by increases in radio emission with a typical spectral slope at $\nu \sim c/20\text{cm}$ of $f_\nu \propto \nu^{-0.8}$ (Condon 1992). The radio emission is thought to be synchrotron radiation from electrons in supernova remnants; it is proportional to $L_{\rm bol,dust}$ presumably because supernovae occur in

the same population of massive stars responsible for heating the dust. According to Condon (1992), galaxies without active nuclei in the local universe satisfy

$$L_{\rm bol,dust} \simeq 7.9 \times 10^5 L_{20}, \tag{2.5}$$

where $L_{20} \equiv \nu l_\nu$ at $\nu = c/20{\rm cm}$, with a scatter of 0.2 dex. This relationship is usually expressed in terms of the quantity L_{FIR}; the constant of proportionality in equation 2.5 assumes $L_{\rm bol,dust} \simeq 1.47 L_{FIR}$, as discussed in § 2.2.2.

The local radio/far-IR relation (equation 2.5) is unlikely to hold to arbitrarily high redshifts. At some redshift the energy density of the cosmic microwave background, increasing as $(1+z)^4$, will become comparable to the magnetic energy density in star-forming galaxies, and relativistic electrons in supernova remnants will begin to cool through inverse Compton scattering rather than synchrotron emission. For magnetic energy densities comparable to those observed among rapidly star-forming galaxies in the local universe, this will occur at $z \gtrsim$ 3–6 (e.g., Carilli & Yun 1999).

We conclude this section with a brief digression. Carilli & Yun (1999) have recently proposed the ratio $\eta \equiv f_\nu(850\mu{\rm m})/f_\nu(20{\rm cm})$ as a photometric redshift estimator. Results in this section allow us to quantify the estimator's likely accuracy. Equations 2.2 and 2.5 imply

$$\eta \simeq \frac{3400(1+z)^{-1-\alpha}}{\mathcal{K}(850\mu{\rm m}/1+z)}, \tag{2.6}$$

where $\alpha \simeq -0.8$ is the spectral index of the radio emission and $\mathcal{K}(\lambda)$ can be interpolated from table 1. Calculating the mean expected η and its uncertainty as a function of redshift is complicated by the logarithmic uncertainties and by the presence of $\mathcal{K}$ in the denominator of equation 2.6. To calculate the mean expected value of η we used $\bar{\eta} = 3400(1+z)^{-\alpha-1}\langle 1/\mathcal{K}(850\mu{\rm m}/1+z)\rangle$, where $\langle 1/\mathcal{K}\rangle$ is the mean value of $1/\mathcal{K}$ among the galaxies in § 2.2.1; to calculate the (asymmetrical) 1σ uncertainties in η we assumed that $\log_{10}(\eta)$ was symmetrically distributed around $\mu \equiv \log_{10}(\bar{\eta}) - \sigma^2_{\rm dex}\log_e 10/2$, where $\sigma_{\rm dex}$, the logarithmic spread in η for galaxies at

a given redshift, is the quadrature sum of the logarithmic uncertainty in $\mathcal{K}(\lambda)$ (from Table 2.1) and the 0.2 dex scatter in the radio/far-IR correlation. If the uncertainty in $\log_{10}(\eta)$ has a Gaussian distribution—as is roughly the case—this choice of μ correctly reproduces the desired mean $\bar{\eta}$. We will handle denominator terms and logarithmic uncertainties similarly throughout this paper unless stated otherwise.

Figure 2.5 shows the expected range of η for star-forming galaxies as a function of redshift; redshift has been placed on the ordinate to allow redshift constraints to be easily read off this figure given a measured value of η. This figure can be used to estimate redshifts of a star-forming galaxies on the basis of their 850μm and 20cm fluxes, but the estimates will be accurate only if these galaxies obey the local radio to far-IR correlation (equation 2.5) and have similar dust SEDs as the local sample of § 2.2.1. Our next section is concerned, in part, with whether this is true (see also Carilli & Yun 2000).

2.3 Observations at high redshift

With very few exceptions, galaxies at high redshift are too faint to have been detected over the wavelength range $20\mu\text{m} \lesssim \lambda \lesssim 200\mu\text{m}$ by any satellite that has flown. Their bolometric dust luminosities therefore cannot be directly measured; they can only be indirectly estimated with the correlations we have just described between $L_{\text{bol,dust}}$ and luminosities at accessible wavelengths. Unfortunately the underlying physics responsible for these empirical correlations is poorly understood, and so there is no particular theoretical reason to expect them to exist in identical form at high-redshift. Nor can their existence be directly established empirically, for without measuring high-redshift galaxies' fluxes at several wavelengths $20\mu\text{m} \lesssim \lambda \lesssim 200\mu\text{m}$ it is impossible to show directly that their bolometric dust luminosities are correlated in the expected way with their fluxes through various atmospheric windows. It might therefore appear that the

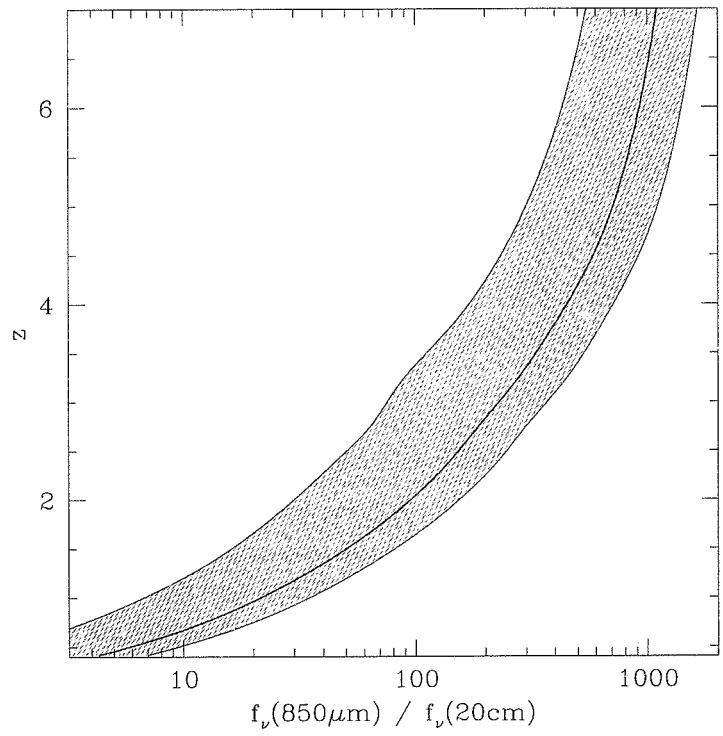

Figure 2.5 The ratio of sub-mm to radio flux as a redshift indicator. The shaded region shows 1σ limits on the ratio $f_\nu(850\mu\text{m})/f_\nu(20\text{cm})$ for rapidly star-forming galaxies at different redshifts; the solid line shows the mean ratio. The error bars are skewed for reasons discussed in § 2.2.4. See also Carilli & Yun (1999, 2000).

assumptions required to estimate high-redshift galaxies' bolometric dust luminosities (and therefore star-formation rates) are not only questionable but also untestable; but this is not entirely true. If a galaxy's fluxes in the rest-UV, mid-IR, sub-mm, and radio are each correlated with its bolometric dust luminosity, then they should also be correlated with each other in a way that is straightforward to calculate. Observing high-redshift galaxies at more than one of these wavelengths therefore provides an indirect test of standard methods for estimating $L_{\text{bol,dust}}$. These indirect tests are the subject of this section.

Because our ultimate goal is to estimate the 850μm fluxes of known UV-selected

high-redshift populations from their UV colors, our emphasis in this section will be on testing whether high-redshift galaxies have the mid-IR, sub-mm, and radio fluxes that their UV-colors and the correlations in § 2.2 would predict. This should not give the false impression that we are testing solely whether MHC's β/far-IR relation is satisfied by high-redshift galaxies. Without directly measured bolometric dust luminosities, it is impossible to test for the existence of any one of the correlations of § 2.2 independently of the others; they can only be tested in pairs. If $z \sim 3$ galaxies are found to have radio fluxes at odds with our predictions from their far-UV properties, for example, it might mean that they do not obey the local β/far-IR relation, but it could equally well mean that they do not obey the local radio/far-IR relation. What we are really testing in this section is whether high-redshift star-forming galaxies are sufficiently similar to their low redshift counterparts for their bolometric dust luminosities and star-formation rates to be reliably estimated in the absence of complete photometry at rest wavelengths $20\mu\mathrm{m} \lesssim \lambda \lesssim 200\mu\mathrm{m}$.

The observations required for these tests are extremely difficult with current technology, and even though the data analyzed in this section are among the best available, much of the evidence presented is rather marginal. We have included even inconclusive evidence below when it illustrates what can (and cannot) be learned from currently feasible observations.

2.3.1 SMMJ14011

The lensed galaxy SMMJ14011+0252 at $\alpha(\mathrm{J2000}) = 14^{\mathrm{h}}01^{\mathrm{m}}04\overset{\mathrm{s}}{.}97$, $\delta(\mathrm{J2000}) = +02^{o}52'24\overset{''}{.}6$, $z = 2.565$ (Smail *et al.* 1998, Frayer *et al.* 1999) is the only sub-mm-selected object robustly confirmed to be a high redshift galaxy without an obviously active nucleus (e.g., Ivison *et al.* 2000). 450μm, 850μm, and 20cm fluxes for this object were obtained by Ivison *et al.* (2000). We obtained rest-UV photometry through the G and $\mathcal{R}$ filters (Steidel & Hamilton 1993) with COSMIC (Kells *et al.* 1998)

on the Palomar 200 inch Hale telescope in March 1999. Our optical photometry of SMMJ14011 is presented in Table 2.2.

Table 2.2 Photometry of two 850μm sources

Object	G	R	i	J	H	K_s
SMMJ14011 J1+J2	21.94	21.25	-	19.33	18.44	17.69
West MMD11	25.09	24.05	23.84	21.28	20.12	19.44

Predicting SMMJ14011's radio and sub-mm fluxes from its UV photometry requires an estimate of the slope of its UV continuum, β (in $f_\lambda \propto \lambda^\beta$; see § 2.2.3). Estimating β from UV photometry is not entirely trivial for two reasons. First, the observed UV continua of high-redshift galaxies have been reddened by the intergalactic absorption of the Lyman-α forest, and this must be corrected before we can estimate their intrinsic continuum slopes β. Second, the UV continua of starburst galaxies are not exactly power laws, and so fitting their continua over different wavelength ranges can produce different estimates of the best fit slope β. MHC calculated β for galaxies in their local sample by fitting these galaxies' fluxes through ten "windows" spanning the wavelength range 1260Å $< \lambda <$ 2600Å; nine of these windows were bluer than 1950Å. The available photometry of high-redshift galaxies rarely covers an identical wavelength range. At SMMJ14011's redshift of $z = 2.565$, for example, the G and $\mathcal{R}$ filters sample $\sim$ 1350Å and $\sim$ 1950Å rest. To estimate β for SMMJ14011 in a way that took some account of these complications, we first subjected a GISSEL96 model of an actively star-forming galaxy (Bruzual & Charlot 1996) to the appropriate intergalactic absorption (Madau 1995), and then reddened the resulting spectrum with increasing dust extinction following a Calzetti (1997) law until this synthetic spectrum had the same G and $\mathcal{R}$ colors as SMMJ14011. Finally we fit this synthetic spectrum through the ten windows of MHC with a power-law of

the form $l_\lambda \propto \lambda^\beta$. The best fit β we find—which is rather insensitive to the details of this procedure—is $\beta = -0.74$, with a 1σ uncertainty due to photometric errors of ± 0.25.

Equations 2.2, 2.3, and 2.4 can now be used to predict SMMJ14011's radio and sub-mm fluxes from its UV photometry. Defining the constants

$$\mathcal{K}_{850}(z) \equiv L_{\rm bol,dust}/\nu l_\nu \quad \text{at} \quad \nu = c(1+z)/850\mu\text{m}, \tag{2.7}$$

$$\mathcal{K}_{450}(z) \equiv L_{\rm bol,dust}/\nu l_\nu \quad \text{at} \quad \nu = c(1+z)/450\mu\text{m}, \tag{2.8}$$

$$\mathcal{K}_L(z,\alpha) \equiv L_{\rm bol,dust}/\nu l_\nu \simeq 7.9\times10^5(1+z)^{-(1+\alpha)} \quad \text{at} \quad \nu = c(1+z)/20\text{cm}, \tag{2.9}$$

and

$$\mathcal{K}_\mathcal{R}(z,\beta) \equiv L_{1600}/\nu l_\nu \simeq (4.3/1+z)^{\beta+1} \quad \text{at} \quad \nu = c(1+z)/6900\text{Å}, \tag{2.10}$$

where $\alpha \simeq -0.85 \pm 0.16$ (Richards 2000) is the slope of the synchrotron emission (in $f_\nu \propto \nu^\alpha$), β is the slope of the UV-continuum, as defined above, and 6900Å is approximately the central wavelength of the $\mathcal{R}$ filter, and using $f_\nu = 10^{-0.4(m_{\rm AB}+48.60)}$ ergs/s/cm^2/Hz, we find, after substituting into equations 2.2, 2.4, and 2.5, and changing from l_ν to f_ν with the equation $l_{\nu_1}/l_{\nu_2} = f_{\nu_1}/f_{\nu_2}$, the following relationships between the observed-frame optical, sub-mm, and radio fluxes of star-forming galaxies at $z \sim 3$:

$$f_{\nu,\rm obs}(850\mu\text{m}) \sim 10^{-0.4(\mathcal{R}-22.17)}\left(\frac{\mathcal{K}_\mathcal{R}(z,\beta)}{1.}\right)\left(\frac{\mathcal{K}_{850}(z)}{10.}\right)^{-1}(10^{0.4(4.43+1.99\beta)}-1) \quad \text{mJy} \tag{2.11}$$

$$f_{\nu,\rm obs}(450\mu\text{m}) \sim 10^{-0.4(\mathcal{R}-22.98)}\left(\frac{\mathcal{K}_\mathcal{R}(z,\beta)}{1.}\right)\left(\frac{\mathcal{K}_{450}(z)}{2.5}\right)^{-1}(10^{0.4(4.43+1.99\beta)}-1) \quad \text{mJy} \tag{2.12}$$

$$f_{\nu,\rm obs}(1.4\text{GHz}) \sim 10^{-0.4(\mathcal{R}-23.86)}\left(\frac{\mathcal{K}_\mathcal{R}(z,\beta)}{1.}\right)\left(\frac{\mathcal{K}_L(z,\alpha)}{6.0\times10^5}\right)^{-1}(10^{0.4(4.43+1.99\beta)}-1) \quad \mu\text{Jy} \tag{2.13}$$

with no dependence on cosmology. The redshift dependence is contained in the K-corrections $\mathcal{K}_{450}$, $\mathcal{K}_{850}$, $\mathcal{K}_\mathcal{R}$, and $\mathcal{K}_L$; the default values of $\mathcal{K}_{850} = 10$, $\mathcal{K}_{450} = 2.5$,

$\mathcal{K}_{\mathcal{R}} = 1$, $\mathcal{K}_L = 6.0 \times 10^5$ in this equation, derived from equations 2.7, 2.8, 2.9, and 2.10 and from Table 2.1, are roughly appropriate for $z \simeq 3.0$. The uncertainty in these equations is large. Equation 2.4 is able to predict $L_{\rm bol,dust}$ from starbursts' UV luminosities and spectral slopes with an uncertainty of about 0.3 dex. At fixed $L_{\rm bol,dust}$ there is (as argued in § 2.2.1) an additional uncertainty of 0.1 dex in l_ν at $100\mu{\rm m} \simeq 450\mu{\rm m}/1+z$, 0.3 dex at $200\mu{\rm m} \simeq 850\mu{\rm m}/1+z$, and 0.2 dex at 6cm $\simeq$ 20cm$/1+z$. If these logarithmic uncertainties add in quadrature, we would expect equations 2.11, 2.12, and 2.13 to be able to predict sub-mm and radio fluxes from UV fluxes to within 0.3–0.4 dex, if high-redshift galaxies resembled local starbursts exactly.

For a galaxy at $z = 2.565$ with $\beta = -0.74$, the appropriate K-correction constants for equations 2.11, 2.12, and 2.13 are $\mathcal{K}_{\mathcal{R}} = 1.05$, $\mathcal{K}_L = 6.13 \times 10^5$, and, interpolating between the values listed in Table 2.1, $\mathcal{K}_{850} = 15.3$ and $\mathcal{K}_{450} = 2.6$. These equations then predict 850μm, 450μm, 20cm fluxes for SMMJ14011 of 23^{+14}_{-9} mJy, 70^{+43}_{-28} mJy, $150^{+95}_{-67}\mu$Jy. The quoted uncertainties reflect only the uncertainty in β from photometric errors. An additional uncertainty of ~ 0.4 dex applies to each predicted flux, and so these predicted fluxes agree well with the measured fluxes (Ivison *et al.* 2000) $f_\nu(850\mu{\rm m}) = 15 \pm 2$mJy, $f_\nu(450\mu{\rm m}) = 42 \pm 7$mJy, $f_\nu(20{\rm cm}) = 115 \pm 30\mu$Jy (see Figure 2.6). SMMJ14011 evidently exhibits the same relationship between its UV, far-IR, and radio properties as rapidly star-forming galaxies in the local universe.

2.3.2 Lyman-break galaxies

Sub-mm

Although it is encouraging that one galaxy at $z \sim 3$, SMMJ14011+0252, appears similar to local galaxies in the correlations of its rest-frame UV, sub-mm, and radio fluxes, ideally we would like to establish that this holds true for entire populations of galaxies

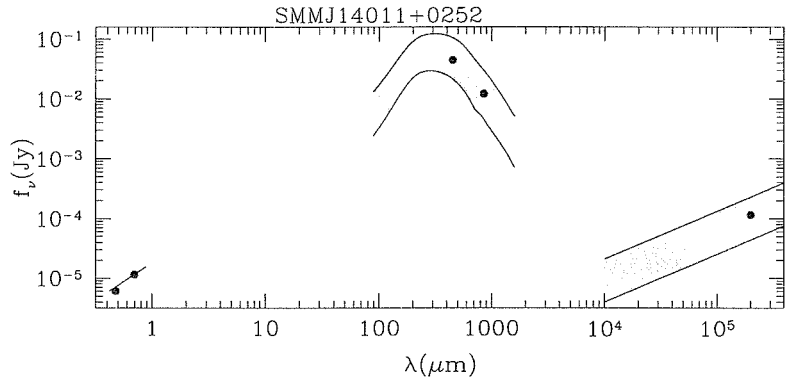

Figure 2.6 The optical to radio SED of the lensed star-forming galaxy SMMJ14011+0252 at $z = 2.565$. Circles show measured fluxes (see text for references). G and $\mathcal{R}$ photometry were used to estimate the slope of this galaxy's (rest) far-UV continuum (solid line). This slope was then used to predict the far-IR and radio properties of SMMJ14011 as described in sections 2 and 3.1. The measured sub-mm and radio fluxes fall within the $\pm 1\sigma$ predicted region (shaded), suggesting that SMMJ14011 follows the same relation between its UV, far-IR, and radio properties as local starburst galaxies.

at $z \sim 3$. Unfortunately, this is exceedingly difficult with current technology. None of the $\sim$ 800 spectroscopically confirmed $z \sim 3$ galaxies in the UV-selected sample of Steidel *et al.* (2000), for example, has an $\mathcal{R}$ magnitude as bright as SMMJ14011's $\mathcal{R} = 21.25$, and $\sim 95\%$ of the galaxies in that sample are more than ten times fainter. Even if these galaxies were as heavily obscured as SMMJ14011, we would expect their 850μm fluxes to be at least ten times lower than SMMJ14011's, or $\lesssim$ 1mJy, well below SCUBA's detection limit. (SCUBA, on the James Clerk Maxwell Telescope, is the current state-of-the-art sub-mm bolometer array; see Holland *et al.* 1999). This suggests that (typical) individual Lyman-break galaxies are unlikely to be detected with SCUBA, and tests of whether these galaxies have the bolometric dust luminosities predicted from their UV spectral slopes will be at best statistical.

The faintness of typical Lyman-break galaxies makes their sub-mm and radio fluxes difficult to predict as well. Predicted bolometric dust luminosities depend sensitively on the UV spectral slope β, and this slope is difficult to estimate accurately

for faint objects with relatively large photometric errors. For example, if a galaxy at $z = 2.6$ had $G - \mathcal{R} = 0.75$, we would estimate (using the method of § 2.3.1) $\beta = -0.60$ and $L_{\rm bol,dust} \simeq 31 \times L_{1600}$, while if it had $G - \mathcal{R} = 0.95$ we would estimate $\beta = -0.07$ and $L_{\rm bol,dust} = 85 \times L_{1600}$. A photometric error of 0.2 in $G - \mathcal{R}$ is not unusual for Lyman-break galaxies, especially at fainter magnitudes (e.g., Adelberger *et al.* 2002), and so photometric errors can easily affect our predicted sub-mm and radio fluxes by a factor of ~ 3.

The situation is worsened by the fact that the only Lyman-break galaxies likely to be detectable in the sub-mm or radio are those with reddest UV slopes and highest dust obscurations. Sub-samples of Lyman-break galaxies selected for follow-up observations at these wavelengths will have to be chosen from among the reddest members of the population. Because highly reddened Lyman-break galaxies are much rarer than their less reddened counterparts (cf. Figure 2.14, discussed below), and because the typical photometric errors on Lyman-break galaxies are large, there is a reasonable chance that a Lyman-break galaxy which appears to be heavily reddened is actually a less reddened galaxy with photometric errors. These sub-samples will therefore suffer from significant Malmquist bias.

For these reasons, observing Lyman-break galaxies in the sub-mm does not appear to be an especially promising way to test whether these galaxies obey the β/far-IR correlation. Nevertheless, Chapman *et al.* (2000) have attempted the observations. Their results are shown in Figure 2.7.

In order to calculate predicted sub-mm fluxes for these galaxies in a way that accounted for the significant photometric uncertainty and Malmquist bias discussed above, and for the expected intrinsic scatter in the UV/850μm relationship (equation 2.11), we proceeded as follows. We first generated a large ensemble of simulated Lyman-break galaxies with $\mathcal{R}$ magnitudes drawn at random from the $z \sim 3$ LBG luminosity function shown in Figure 2.14, UV slopes β drawn at random from the

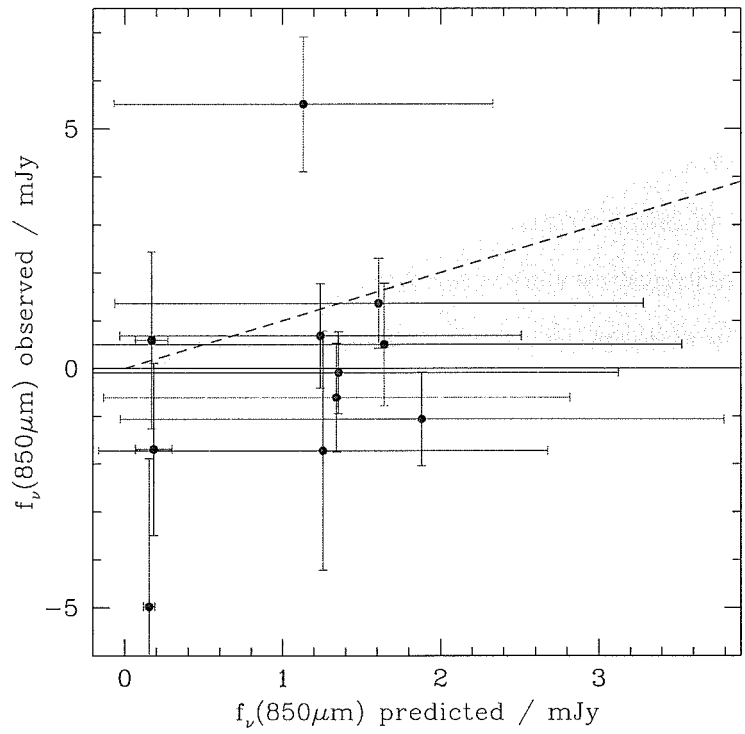

Figure 2.7 The predicted and observed 850μm fluxes of 11 LBGs observed by Chapman *et al.* (2000). The shaded region shows the 90% credible interval on the slope of the line $f_{850,\mathrm{observed}} = b \times f_{850,\mathrm{predicted}}$. The large error bars on the predicted fluxes, which arise for reasons discussed in § 2.3.2, are plotted symmetrically about the mean for simplicity, though in fact they are very skewed. Monte-Carlo simulations suggest that most Lyman-break galaxies will have observed fluxes smaller than the predicted mean and that a small fraction will have observed fluxes significantly larger.

distribution in Figure 2.14 (cf. Steidel *et al.* (1999), Adelberger *et al.* (2000)), and redshift z drawn at random from the interval $2.5 < z < 3.5$. Each of these galaxies was assigned a G magnitude by inverting the procedure of § 2.3.1, and an 850μm flux using equation 2.11. The 850μm fluxes were then changed randomly to reflect the scatter in the β/far-IR relation and in $\mathcal{K}_{850}(z)$. Finally, we placed each simulated galaxy at a random location in our G and $\mathcal{R}$ images and attempted to detect it and

measure its photometry with the same software used to find real Lyman-break galaxies in these images. This produced a long list of the $\mathcal{R}$ magnitudes and $G-\mathcal{R}$ colors we would expect to measure for Lyman-break galaxies with known redshifts and 850μm fluxes if the galaxies obeyed the local β/far-IR relation and had dust SEDs similar to their local analogs. In order to predict the 850μm fluxes shown in Figure 2.7, we binned together the 850μm fluxes of simulated galaxies with magnitudes, colors, and redshifts similar to those of each galaxy in the sample of Chapman *et al.* (2000). As our best guess of the predicted 850μm flux for each galaxy in the Chapman *et al.* sample, we took the sample mean of the 850μm flux among simulated galaxies in its bin; for the uncertainty in the predicted flux we took the standard deviation of the 850μm fluxes of these same simulated galaxies.

For simplicity we have indicated in Figure 2.7 the uncertainties in the predicted fluxes with the convention mean $\pm$ rms, but in fact these uncertainties are very skewed. The Monte Carlo simulations just described suggest that most Lyman-break galaxies should have 850μm fluxes lower than the mean value and that some will have 850μm fluxes significantly larger (how else could we have mean $\sim$ rms with the predicted fluxes bounded below by zero?), and so the observations are more consistent with the predictions than Figure 2.7 might suggest at first glance.

One way to quantify the agreement of the observations with our predictions is to calculate χ^2. Denoting the predicted fluxes by x and the observed by y, the relevant χ^2 figure of merit,

$$\chi^2 \equiv \sum_{i=1}^{N} \frac{(x_i - y_i)^2}{\sigma_{x,i}^2 + \sigma_{y,i}^2} \tag{2.14}$$

(e.g., Press *et al.* 1992 §15.3) is equal to 14.5. There are 11 data points and no free parameters in this fit, and so the data are at least not grossly inconsistent with our expectations. It is difficult to make a more quantitative statement with this approach, however, because the error bars on the predicted flux are very skewed, and χ^2 is therefore not drawn from the usual distribution derived for Gaussian uncertainties.

An alternate approach is to ask what these data say about slope b of the line $f_{\rm observed} = b f_{\rm predicted}$. If Lyman-break galaxies obeyed the β/far-IR correlation and had dust SEDs similar to those of local galaxies, we would expect the data to be consistent with $b = 1$. A Bayesian approach can quantify the constraints on b in a way that takes proper account of our skewed uncertainties. This approach requires us to calculate the likelihood of the data as a function of b. In the brief derivation below, f_m and σ denote measured 850μm fluxes and uncertainties for the galaxies in Chapman *et al.* (2000), f_t denotes these galaxies' (unknown) true fluxes that would be measured if we had perfect data, $f_t' \equiv f_t/b$ denotes the true 850μm fluxes of the *simulated* Lyman-break galaxies, calculated above under the assumption $b = 1$, and I is shorthand for the background knowledge (such as the luminosity and β distributions of Lyman-break galaxies, and the scatter in the β/far-IR relation, and so on) that went into our Monte Carlo simulations. Our data set consists of the redshifts $\{z\}$, apparent magnitudes $\{\mathcal{R}\}$, colors $\{G-\mathcal{R}\}$, and 850μm fluxes $\{f_m\}$ of each galaxy in the sample of Chapman *et al.* (2000). The likelihood of observing these data given b is equal to the product of the likelihoods of observing each galaxy individually:

$$P\Big(\{G-\mathcal{R}\}\{\mathcal{R}\}\{z\}\{f_m\} \,|\, \{\sigma\} b I\Big) = \prod_i^N P\Big((G-\mathcal{R})_i \mathcal{R}_i z_i f_{m,i} \,|\, \sigma_i b I\Big). \qquad (2.15)$$

These individual likelihoods can be evaluated by integrating over the unknown true 850μm flux of each galaxy:

$$P\Big((G-\mathcal{R})\mathcal{R} z f_m \,|\, \sigma b I\Big) = \int_0^\infty df_t \; P\Big(f_t \,|\, b I\Big) P\Big((G-\mathcal{R})\mathcal{R} z \,|\, f_t I\Big) P\Big(f_m \,|\, f_t \sigma\Big). \quad (2.16)$$

We have simplified this equation by omitting irrelevant variables from the conditional probabilities and by writing $P(AB)$ as $P(A)P(B)$ when A and B are independent. $P\Big(f_m \,|\, f_t\sigma\Big)$ can be calculated by assuming that the uncertainties in the measured fluxes are Gaussian, which is roughly true. The remaining probabilities in the integral can be estimated from the Monte Carlo simulations. Writing the total number of

galaxies in the simulations as $N_{\rm tot}$, and the number of galaxies in the simulations with both properties A and B as $n(A,B)$, we have $P\Big(f_t \,|\, bI\Big) \simeq n(f_t')/N_{\rm tot}$ and $P\Big((G-\mathcal{R})\mathcal{R}z \,|\, f_t I\Big) \simeq n(G-\mathcal{R},\mathcal{R},z,f_t')/n(f_t')$. Substituting into equation 2.15 yields the likelihood, given b, of observing a single galaxy at redshift z with UV photometry $\mathcal{R}$ and $G-\mathcal{R}$ and 850μm flux f_m:

$$P\Big((G-\mathcal{R})\mathcal{R}z f_m \,|\, \sigma b I\Big) \propto \int_0^\infty df_t'\; n(G-\mathcal{R},\mathcal{R},z,f_t') \exp\Big[-\frac{1}{2}\Big(\frac{bf_t'-f_m}{\sigma}\Big)^2\Big]. \quad (2.17)$$

The maximum likelihood value of b, calculated numerically using equations 2.15 and 2.17, is $b = 0.45$. For a uniform prior, the 68% and 90% highest posterior density regions are $0.22 \leq b \leq 0.87$ and $0.09 \leq b \leq 1.2$. The sub-mm fluxes of Lyman-break galaxies therefore appear to be somewhat lower than we would have expected. This could indicate that Lyman-break galaxies do not quite satisfy MHC's β/far-IR correlation, or that their dust SEDs are different from those of the local galaxies described in § 2.2.1; but the inconsistency with $b = 1$ is only marginally significant and we will not speculate further about its possible cause. All we can say with much confidence is that the sub-mm fluxes of Lyman-break galaxies are unlikely to be either much higher or more than an order of magnitude lower than our predictions.

Our interpretation of these data differs quantitatively from that of Chapman *et al.* (2000). This is because those authors ignored the uncertainties in the predicted fluxes in most of their analyses, and assumed that the dust SEDs of all Lyman-break galaxies would be well approximated by a single modified black-body (equation 2.1) with $T = 50$K and $\epsilon = 1.5$, rather than by the range of empirical SEDs estimated in § 2.2.1.

Radio

Radio observations of Lyman-break galaxies can in principle provide another indirect test of standard methods for estimating these galaxies' bolometric dust luminosities.

Extremely deep radio images are required, however, if we hope to put interesting limits on the radio fluxes of typical $z \sim 3$ galaxies: equation 2.13 implies that the vast majority of Lyman-break galaxies in the sample of Steidel *et al.* (2000) will have 20cm fluxes of only a few μJy or less. One of the deepest existing radio images is Richards' (2000) 20cm VLA map of the Hubble Deep and Flanking Fields, which reaches a 1σ noise limit of 8μJy/beam. Unfortunately, even this image does not appear sufficient for a meaningful test. Of the 46 Lyman-break galaxies in our spectroscopic sample that lie within this 20cm image, only 2 are predicted (using the Monte-Carlo method of § 2.3.2) to have marginally detectable fluxes $f_\nu > 10\mu$Jy. These two, with predicted fluxes of $12 \pm 15\mu$Jy and $19 \pm 17\mu$Jy, have observed fluxes of $4 \pm 12\mu$Jy and $-6 \pm 12\mu$Jy—not exactly in line with our predictions, but not damning either. (Our method of estimating the observed fluxes is described in § 2.3.3 below.) Nine galaxies have marginally significant observed fluxes of $f_\nu > 10\mu$Jy, and none of these nine were predicted to be especially bright; but six galaxies have measured fluxes $f_\nu < -10\mu$Jy, and so even the marginally significant detections may simply reflect the noise characteristics of Richards' (2000) image. Statistical tests based on the sample as a whole are as inconclusive as the object-by-object tests we have just described: the total observed and predicted 20cm fluxes from these 46 galaxies are $105 \pm 81\mu$Jy and $114 \pm 36\mu$Jy, respectively, and the formal 90% credible interval on $b \equiv f_{\rm observed}/f_{\rm predicted}$, estimated using the Monte Carlo simulations and Bayesian approach of § 2.3.2, is $0 < b < 2.1$.

2.3.3 Balmer-break galaxies

Galaxies at redshifts as high as $z \sim 3$ are hardly ideal for testing whether the UV-properties of high-redshift galaxies can be used to predict their bolometric dust luminosities, because large luminosity distances and unfavorable K-corrections make them extremely faint in the optical, mid-IR, and radio (cf. Figure 2.1). A better redshift is

$z \sim 1$. At this redshift galaxies are much brighter in these atmospheric windows, and their far-UV spectral slopes β can still be measured with ground-based photometry. In this section we will use galaxies drawn from the $z \sim 1$ "Balmer-break" sample of Adelberger *et al.* (2000) to test whether actively star-forming galaxies at $z \sim 1$ follow the correlations between UV, mid-IR, and radio properties observed among galaxies in the local universe. This color-selected sample consists of ~ 700 star-forming galaxies with spectroscopic redshifts $0.9 \lesssim z \lesssim 1.1$ and apparent magnitudes $\mathcal{R} \lesssim 25.5$.

One warning is due before we begin. The β/far-IR correlation of MHC (equation 2.4) has been shown to hold only for starburst galaxies in the local universe. It is not known whether less rapidly star-forming galaxies such as the Milky Way satisfy this correlation, and post-starburst galaxies, whose red UV slopes reflect age rather than dust content, almost certainly do not. At $z \sim 3$ galaxies are bright enough to satisfy the Lyman-break criteria of Steidel *et al.* (1999) only if they are forming stars rapidly ($\gtrsim 30 M_{\odot}$/yr with typical dust obscurations, for $h = 0.7$, $\Omega_M = 0.3$, $\Omega_\Lambda = 0.7$), and so these galaxies might reasonably be expected to obey the β/far-IR correlation (see MHC for further discussion of the Lyman-break galaxy/starburst connection). But at $z \sim 1$ post-starburst galaxies and slowly star-forming galaxies like the Milky Way can both satisfy our Balmer-break selection criteria, in addition to the starburst galaxies that are expected to obey the β/far-IR correlation. There is therefore good reason to suspect *a priori* that some galaxies in our Balmer-break sample will not obey this correlation.

In principle one might be able to select the starburst analogs from among a Balmer-break sample on the basis of their photometric or spectroscopic signatures, but a proper treatment is beyond the scope of this paper. Fortunately slowly star-forming galaxies will be far too faint in the radio and mid-IR to be detected in current data, and so their presence in our Balmer-break sample will not significantly affect the conclusions of this subsection. A crude way of partially excluding post-starbursts,

which we shall adopt below, is to impose an additional selection criterion $U_n - G < 0.5$ on the Balmer-break sample. This limits the Balmer-break sample to the same range of β observed among starburst galaxies in the local universe and among Lyman-break galaxies at $z \sim 3$ by excluding the galaxies that are reddest in the far-UV, whose slopes might reflect age rather than their dust content. We will discuss this further elsewhere (Adelberger *et al.* 2000).

Mid-Infrared

Because of the strength of the 7.7μm PAH feature, 15μm observations provide a particularly promising way of observing dust emission from galaxies at $z \sim 1$. Seventy-one Balmer-break galaxies from our spectroscopic sample lie within the 15μm (LW3) ISO image of the CFRS 1415+52 field obtained by Flores *et al.* (1999); six of them are listed as optical counterparts to 15μm sources in these authors' 3σ catalog.

Equations 2.3 and 2.4 imply the following relationship between the UV and mid-IR photometry of galaxies at $z \sim 1$:

$$f_{\nu,\mathrm{obs}}(15\mu\mathrm{m}) \sim 10^{-0.4(U_n-25.22)}\left(\frac{\mathcal{K}_U(z,\beta)}{1}\right)\left(\frac{\mathcal{K}_{15}}{20}\right)^{-1}(10^{0.4(4.43+1.99\beta)}-1) \quad \mu\mathrm{Jy}, \quad (2.18)$$

where

$$\mathcal{K}_{15} \equiv L_{\mathrm{bol,dust}}/\nu\bar{l}_\nu \quad \text{at} \quad \nu = c(1+z)/15\mu\mathrm{m}, \quad (2.19)$$

$$\mathcal{K}_U(z,\beta) \equiv L_{1600}/\nu l_\nu \simeq \left(\frac{1+z}{2.3}\right)^{\beta+1} \quad \text{at} \quad \nu = c(1+z)/3700\text{Å}, \quad (2.20)$$

$\bar{l}_\nu$ is the mean luminosity density at rest frequencies $c(1+z)/18\mu\mathrm{m} < \nu < c(1+z)/12\mu\mathrm{m}$, and 3700Å is roughly the central wavelength of the U_n filter after accounting for atmospheric absorption and instrumental throughput. In most cases the observed 15μm fluxes of $z \sim 1$ galaxies are dominated by emission from the 7.7 and 8.6μm PAH lines, and $\mathcal{K}_{15}$ depends very weakly on redshift near $z \sim 1$. It is well approximated by $\mathcal{K}_{\mathrm{MIR}}/2.4 \simeq 22$ for all the redshifts we will consider here ($\mathcal{K}_{\mathrm{MIR}}$ is defined in § 2.2.2.

To estimate β for these galaxies, we used their $U_n - G$ colors, which sample rest wavelengths $\sim$ 1850Å and $\sim$ 2350Å, and a procedure analogous to the one described in § 2.3.1. Photometric errors are less of a concern for these optically bright galaxies than for the faint $z \sim 3$ galaxies of § 2.3.2. Instead of taking the elaborate Monte-Carlo approach of § 2.3.2, we estimated the predicted 15μm fluxes for these galaxies by assuming that their true U_n magnitudes and $U_n - G$ colors were equal on average to the measured values; for the uncertainty in the predicted fluxes we simply propagated through the uncertainties in the $U_n - G$ and U_n fluxes determined from the Monte-Carlo simulations. The total uncertainty in the predicted fluxes, 0.5 dex, arises from the scatter in the β/far-IR correlation (0.3 dex), from the expected scatter in $\mathcal{K}_{15}$ (0.2 dex), from photometric uncertainties in U_n magnitudes (0.1 dex), and from the uncertainty in β due to photometric errors in $U_n - G$ (0.3 dex).

Figure 2.8 shows the predicted and observed 15μm fluxes of these 71 Balmer-break galaxies. The majority of these galaxies do not appear in the 3σ catalog of Flores *et al.* (2000), and so we know only that their fluxes were less than $\sim$ 150μJy; these sources are indicated with downward pointing arrows. The detections are indicated by points with error bars.

These data appear encouragingly consistent with our UV-based predictions: the large number of galaxies with predicted flux significantly lower than the detection limit are not detected, while the majority of those with predicted fluxes close to (or above) the detection limit are. The only apparently serious discrepancy between predicted and observed fluxes, ISO138 with $f_{\rm predicted} \sim 4$, $f_{\rm observed} \sim 250$, may result from a misidentification of the optical galaxy responsible for the 15μm emission; according to Flores *et al.* (2000) there is a 27% chance of misidentification for this object, compared to a median 3% chance for the other five detections.

Readers who do not find Figure 2.8 persuasive may wish to consider the following. The seven galaxies that we predicted to be brightest have the following ranks in

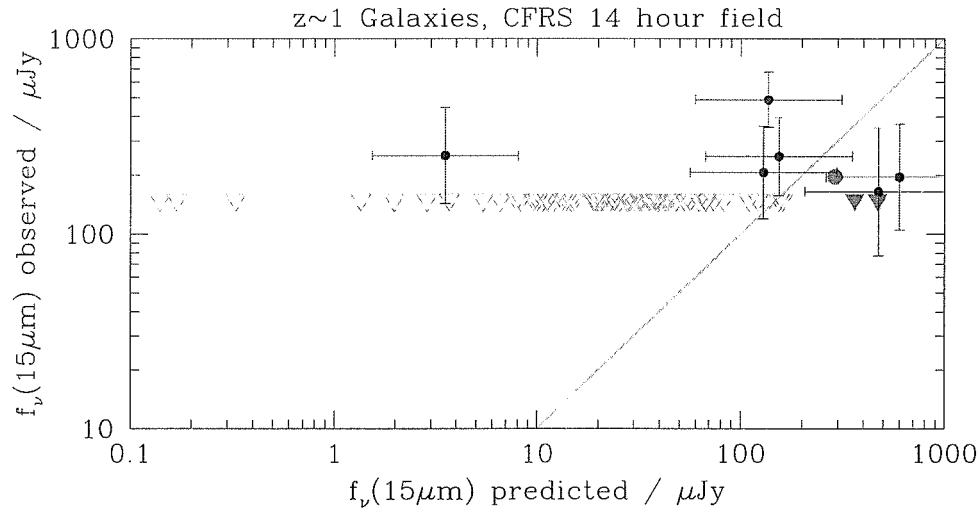

Figure 2.8 The predicted and observed 15μm fluxes of Balmer-break galaxies at $z \sim 1$. The majority of these galaxies are undetected at a 3σ limit of 150μJy; uncertainties on the predicted fluxes of these galaxies have been omitted for clarity, and the upper limits to their observed fluxes are indicated with downward pointing triangles. The six detections are indicated by points with error bars in both x and y; the one with $f_{15,\mathrm{predicted}} \ll f_{15,\mathrm{observed}}$ has a significant separation between its optical and mid-IR centroids and may be a misidentification. Three Balmer-break galaxies in this field are too red in the far-UV to satisfy the active star-formation criterion discussed in § 2.3.3; their locations on this plot are indicated by smaller triangles for the non-detections and by a point without error bars for the detection.

observed flux: 5, 6, >6, 3, >6, 1, 4, where undetected objects are assigned the rank ">6" because we know only that they are fainter than the six detected objects. Over 90% of the Balmer-break galaxies in the 15μm image have the observed rank ">6"; if our UV-predicted 15μm fluxes were unrelated to the observed fluxes, we would have expected $\sim$ 90% of the seven objects predicted to be brightest to have the rank ">6", but that is not the case. This type of reasoning can be quantified with a version of Kendall's τ generalized for censored data sets by Oakes (1982): of 500 simulated data sets we have made by scrambling the observed rank assigned to each predicted rank, only 2 had a generalized τ as large or larger than the real data set. The predicted and observed fluxes of these galaxies evidently display a significant positive correlation; and moreover the fact that the handful of detections have observed fluxes broadly in

line with their predicted fluxes suggests that this correlation is consistent with the expected linear correlation $\langle f_{\rm predicted} \rangle = \langle f_{\rm observed} \rangle$.

Radio

Eighty-nine of the Balmer-break galaxies from the spectroscopic sample of Adelberger *et al.* (2000) lie within the deep 1.4GHz image of the Hubble Deep Field recently published by Richards (2000). We estimated rough 1.4GHz fluxes for this sample by summing the flux within a 2.″0 radius aperture surrounding the optical centroid of each object. The measured fluxes are shown in Figure 2.9. For the 1σ uncertainty we took $\sim 12\mu$Jy, the observed rms when we estimated fluxes in a similar manner for random locations in Richards' (2000) image. The predicted fluxes were estimated using

$$f_{\nu,\rm obs}(20\rm cm) \sim 10^{-0.4(U_n - 24.19)} \left(\frac{\mathcal{K}_U(z,\beta)}{1} \right) \left(\frac{\mathcal{K}_L}{6.9 \times 10^5} \right)^{-1} (10^{0.4(4.43+1.99\beta)} - 1) \quad \mu\rm Jy, \tag{2.21}$$

which follows from equations 2.4, 2.5, 2.9, and 2.20. Otherwise the predicted radio fluxes were derived in an identical manner to the predicted mid-IR fluxes in § 2.3.3. The uncertainty in the predicted fluxes arises from the scatter in the β/far-IR correlation (0.3 dex), from the scatter in the far-IR/radio correlation (0.2 dex), from photometric uncertainties in U_n magnitudes (0.1 dex), and from the uncertainty in β due to photometric errors in $U_n - G$ (0.4 dex). Added in quadrature these amount to a ~ 0.5 dex uncertainty in the predicted 20cm flux for each object.

Because of the large uncertainties in the predicted and observed fluxes, these data can hardly provide a rigorous test of whether $z \sim 1$ galaxies obey the correlations between far-UV, far-IR, and radio properties observed in rapidly star-forming galaxies in the local universe. However, despite the unimpressive appearance of Figure 2.9, the data do strongly suggest that the predicted and observed fluxes of Balmer-break

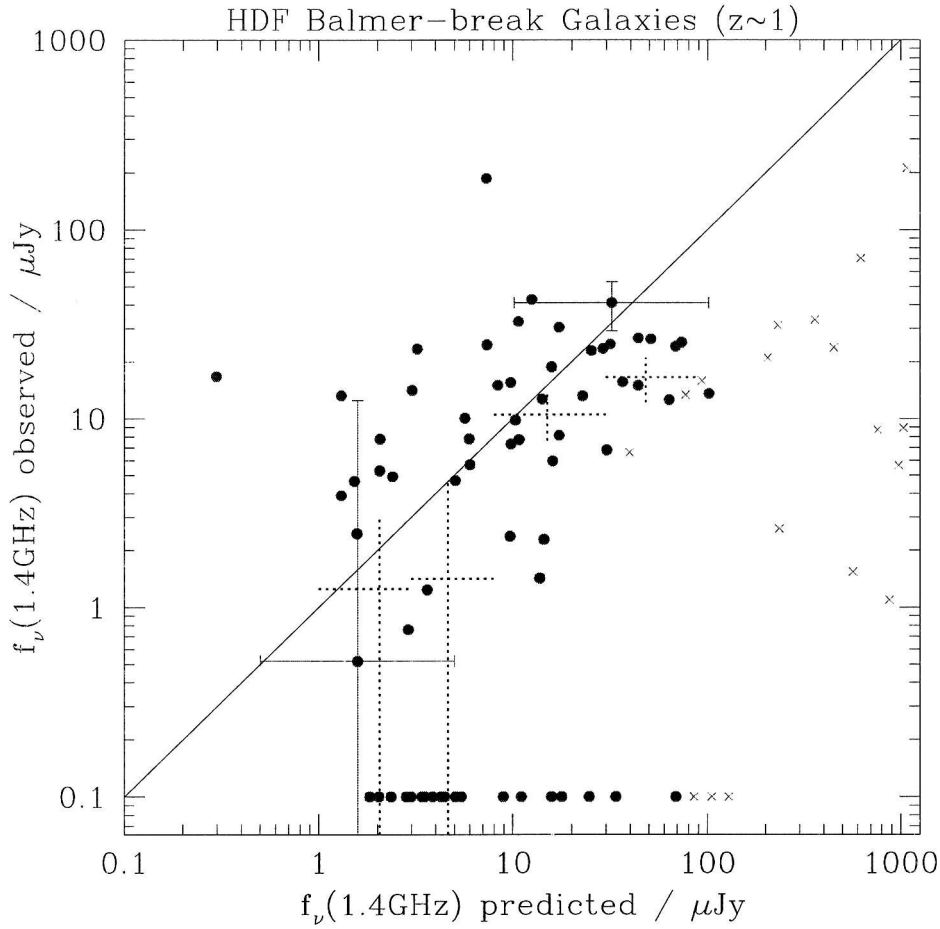

Figure 2.9 The predicted and observed 20cm fluxes of Balmer-break galaxies at $z \sim 1$. For clarity uncertainties are shown for only a few representative points. Galaxies with observed fluxes lower than 0.1μJy are shown on the plot at 0.1μJy. The locations of Balmer-break galaxies too red to satisfy the active star-formation criterion of § 2.3.3 are indicated with solid crosses. The larger dotted crosses indicate the mean observed flux and standard deviation of the mean for galaxies in different bins of predicted flux. One outlier was excluded from the calculation of the mean and standard deviation in its bin of predicted flux, the galaxy with $f_{\rm pred} \simeq 7.5$, $f_{\rm obs} \simeq 200$, which likely has a significant AGN contribution to its measured flux.

galaxies are at least positively correlated: fewer than 1% of simulated data sets generated by randomly shuffling the observed and predicted fluxes had a Kendall's τ as large as the observed data set. The trend of higher measured fluxes for objects

with higher predicted fluxes is illustrated by the dotted crosses in Figure 2.9, which show the mean measured flux ($\pm$ the standard deviation of the mean) for objects in different bins of predicted flux. Although objects with higher predicted fluxes clearly tend to have higher observed fluxes, it appears that the measured 20cm fluxes may be somewhat lower than our predictions, especially for the brightest objects. The significance of this result is difficult to assess without running Monte-Carlo simulations similar to those discussed in § 2.3.2. These simulations are not yet available.

2.3.4 HR10

The $z = 1.44$ galaxy HR10 initially attracted the attention of Hu & Ridgway (1994) because of its unusually red optical-to-infrared color. Those authors suggested that HR10 was a high-redshift elliptical galaxy, but subsequent observations provided hints that HR10 was actively forming stars and suggested that its red colors might result from extreme dust reddening rather than from an aged stellar population (Graham & Dey 1996). This interpretation has received strong support from the recent detection of HR10 at 450μm and 850μm. HR10 is now considered the prototypical example of an extremely dusty star-forming galaxy at high redshift. Its photometry is presented in Figure 2.10 (Dey *et al.* 1999, Haynes *et al.* 2002).

Because of the large uncertainties in its rest-frame far-UV colors, we cannot reliably measure β for HR10, but we can use its observed ratio of far-UV to far-IR luminosity to estimate the value of β required for this object to satisfy MHC's β/far-IR relation. This slope, shown in Figure 2.10, is not obviously inconsistent with the data.

Although it is unclear if HR10 satisfies the β/far-IR relation, we can say with confidence that its ratio of far-IR to UV luminosity far exceeds that of any other galaxy discussed in this section. Despite the large star-formation rate implied by its

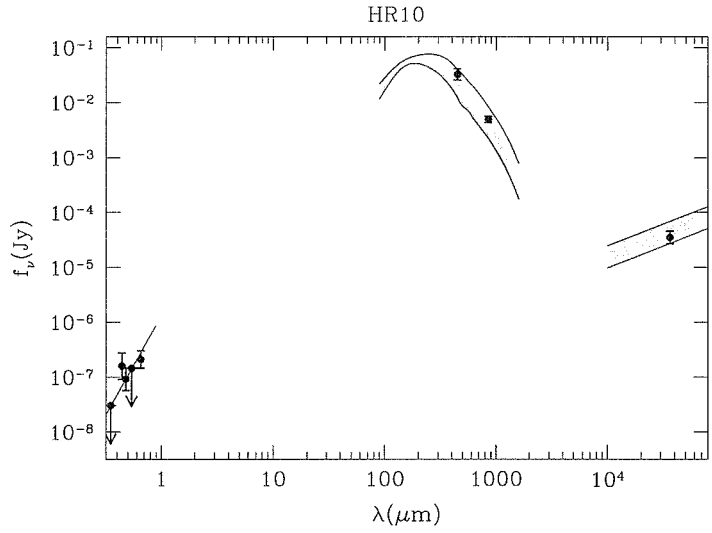

Figure 2.10 The far-UV to radio SED of HR10. The shaded regions, adjusted vertically to match the observed 450μm, 850μm, and 3.6cm photometry, show $\pm 1\sigma$ uncertainties on the shape of this galaxy's far-IR and radio emission under the assumption that it obeys the local FIR/radio correlation and has a dust SED similar to those of actively star-forming galaxies in the local universe. The very uncertain (rest) far-UV photometry for this galaxy does not allow us to estimate its far-UV spectral slope β; the solid line in the UV indicates the slope that MHC's β/far-IR relation would predict. HR10 has a far higher ratio of far-IR to far-UV luminosity than the other galaxies we have considered, and would not be included in most UV-selected surveys despite its large star-formation rate.

850μm flux, HR10 would not be included in most optically selected high-redshift surveys. Placed at $z = 3.0$, for example, HR10 would be too faint and too red to satisfy commonly used "Lyman-break" photometric selection criteria (e.g., Steidel, Pettini, & Hamilton 1995). If most of the star formation in the universe occurred in objects like HR10, rather than in the relatively UV-bright Balmer-break and Lyman-break galaxies previously discussed, then UV-selected high-redshift surveys will provide a seriously incomplete view of star formation in the universe. But this seems an unlikely

possibility to us, as we will now explain.

2.4 UV-selected populations, sub-mm sources, and the far-IR background

In § 2.3 we tried to assess whether the star-formation rates of known high-redshift galaxies can be estimated from their fluxes through various atmospheric windows. Our conclusions were uncertain but hopeful: the meager available evidence is at least consistent with the idea that ground-based observations can be used together with locally calibrated correlations to provide rough constraints on high-redshift galaxies' star-formation rates. But estimating moderately accurate star-formation rates is only one step towards the ultimate goal of high-redshift surveys, producing a reasonably complete census of star-formation at high redshift that can be used to constrain our empirical and theoretical understanding of the early stages of galaxy formation. In this section we will set aside the object-by-object comparisons of star-formation rates estimated from photometry at different wavelengths, and turn our attention instead to the larger question of whether existing surveys are approaching the reasonably complete view of high-redshift star formation that we desire.

There is good reason to be concerned that the view of high-redshift star-formation provided by these surveys is far from complete. Few star-forming galaxies in the local universe would be included in existing surveys if they were placed at high redshift. This is illustrated by Figure 2.11, which shows the ratio of dust to ultraviolet luminosity for local galaxies with various star-formation rates. For this plot we have adopted $L_{1600} + L_{\rm bol,dust}$ as a crude measure of star-formation rate, though in some cases 1600Å luminosities and dust luminosities can be powered by processes other than star formation. Because of the different constants of proportionality in the conversions of

L_{1600} and $L_{\rm bol,dust}$ to star-formation rates, the quantity $1.66L_{1600} + L_{\rm bol,dust}$ (cf. equation 2.4; see also MHC) would likely provide a better measure of star-formation rate, but in almost all cases L_{1600} is small compared to $L_{\rm bol,dust}$ and our adoption of the simpler $L_{1600} + L_{\rm bol,dust}$ will not appreciably affect the subsequent discussion.

Solid circles on Figure 2.11 denote UV-selected starbursts from the sample of MHC, discussed earlier in the text; § symbols denote nearby spirals[3], selected randomly from among the objects present in both the Carnegie Atlas of Sandage & Bedke (1994) and the far-UV catalog of Rifatto, Lango, & Capaccioli (1995); open squares denote three LIRGs (NGC4793, NGC5256, and NGC6090) from the catalog of Sanders, Scoville, & Soifer (1991) which had UV fluxes estimated by Kinney *et al.* (1993) or Rifatto *et al.* (1995); and open stars denote the ULIRGs VII Zw 031, IRAS F12112+0305, and IRAS F22691-1808 observed in the far-UV by Trentham, Kormendy, & Sanders (1999). Bolometric dust luminosities were estimated from these galaxies' 60μm and 100μm IRAS fluxes as discussed in § 2.2.4. The adopted conversion from IRAS fluxes to bolometric dust luminosities is more appropriate for the starbursts, LIRGs, and ULIRGs in Figure 2.11 than for the spirals, but the resulting errors in the spirals' estimated dust luminosities will not affect our conclusions significantly.

Taken together the galaxies in this plot are representative of those that host the majority of star-formation in the local universe: according to Heckman (1998), starbursts and spirals account for roughly equal shares of the bulk of star-formation in the local universe, while LIRGs and ULIRGs (galaxies with $L_{FIR} \gtrsim 10^{11} L_{\odot}$) account for perhaps 6% (Sanders & Mirabel 1996).

The curved lines on this plot show the $z = 3.0$ completeness limits ($\Omega_M = 0.3$,

[3]NGC247, NGC1232, NGC1313, NGC1398, NGC2403, NGC2683, NGC2976, NGC3556, NGC3623, NGC3726, NGC3877, NGC4178, NGC4216. NGC4254, NGC4303, NGC4307, NGC4321, NGC4522, NGC4559, NGC4565, NGC4592, NGC4595, NGC4653, NGC5055, NGC5248, NGC5457, NGC5806, NGC5879, NGC5907, NGC6946

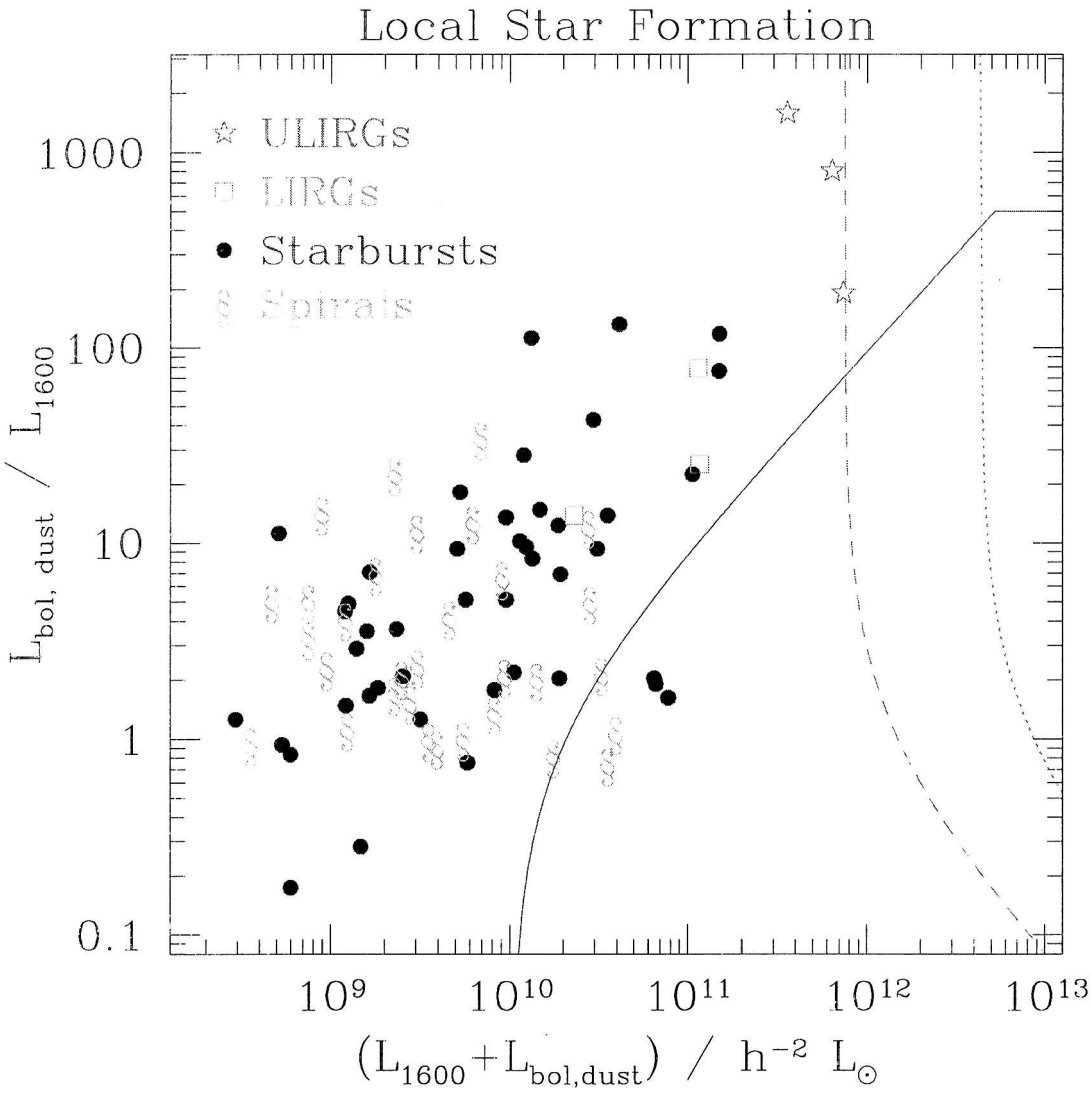

Figure 2.11 Star formation in the local universe. The sum $L_{1600} + L_{\rm bol,dust}$, on the abscissa, provides a crude measure of star formation rate; the ratio $L_{\rm bol,dust}/L_{1600}$, on the ordinate, provides a rough measure of dust obscuration. Star formation in the local universe occurs among galaxies with a wide range of luminosities and dust obscuration, and more rapidly star-forming galaxies tend to be more heavily obscured. See text for a description of the four local galaxy samples (spiral, starburst, LIRG, ULIRG) shown. Galaxies similar to those in this plot would not be included in existing optical, sub-mm, or radio surveys at $z \sim 3$, which can detect objects lying to the right of the solid, dashed, and dotted lines.

$\Omega_\Lambda = 0.7$) for existing surveys at optical (solid line), sub-mm (dashed line), and radio (dotted line) wavelengths. These lines assume an optical flux limit of $f_\nu(1600\text{Å} \times (1+z)) \gtrsim 0.2\mu\text{Jy}$ ($\mathcal{R}_{\text{AB}} \lesssim 25.5$), roughly appropriate for the Lyman-break survey of Steidel *et al.* (1999), a sub-mm flux limit of $f_\nu(850\mu\text{m}) \gtrsim$ 2mJy, the confusion limit of SCUBA on the JCMT, and a radio flux limit of $f_\nu(20\text{cm}) \gtrsim 50\mu\text{Jy}$, the completeness limit of Richards' (2000) catalog of HDF sources. Observations with lower flux limits have been obtained in each of these bands, especially the optical—the flux limit in the Hubble Deep Field is nearly an order of magnitude fainter than the 0.2μJy optical limit we have adopted—but the flux limits above are roughly appropriate for the bulk of existing "deep" observations at each wavelength. Sub-mm and radio flux limits were converted into dust luminosity limits under the assumption that high-redshift galaxies follow the empirical correlations described in § 2.2. The minimum luminosity for sub-mm detection is roughly independent of redshift, because K-corrections largely cancel out changes in luminosity distance, but the minimum luminosity for optical and radio detection would be (respectively) 7.4 and 13 times fainter at $z \sim 1$ (cf. Figures 2.12 and 2.13), and 2.2 and 3.1 times brighter at $z \sim 5$. Evidently only a small fraction of star-forming galaxies in the local universe would be detected in existing surveys if they were placed at $1 \lesssim z \lesssim 5$.

Nevertheless large numbers of high-redshift galaxies have been found. Figure 2.12 shows the location on the star-formation rate versus dust obscuration plot of the majority of known galaxies at $z \sim 1$. Solid circles represent optically selected Balmer-break galaxies at $0.8 < z < 1.2$ from the sample of Adelberger *et al.* (2000), open stars represent 15μm ISO sources at $0.8 < z < 1.2$ from the HDF sample discussed in § 2.4.2 below, open squares (triangles) represent radio and sub-mm sources with estimated redshifts $z < 2$ from the optically detected (undetected) sample of BCR, and the open circle represents HR10. Each object's dust luminosity was estimated from its available ground-based photometry through the empirical correlations described in

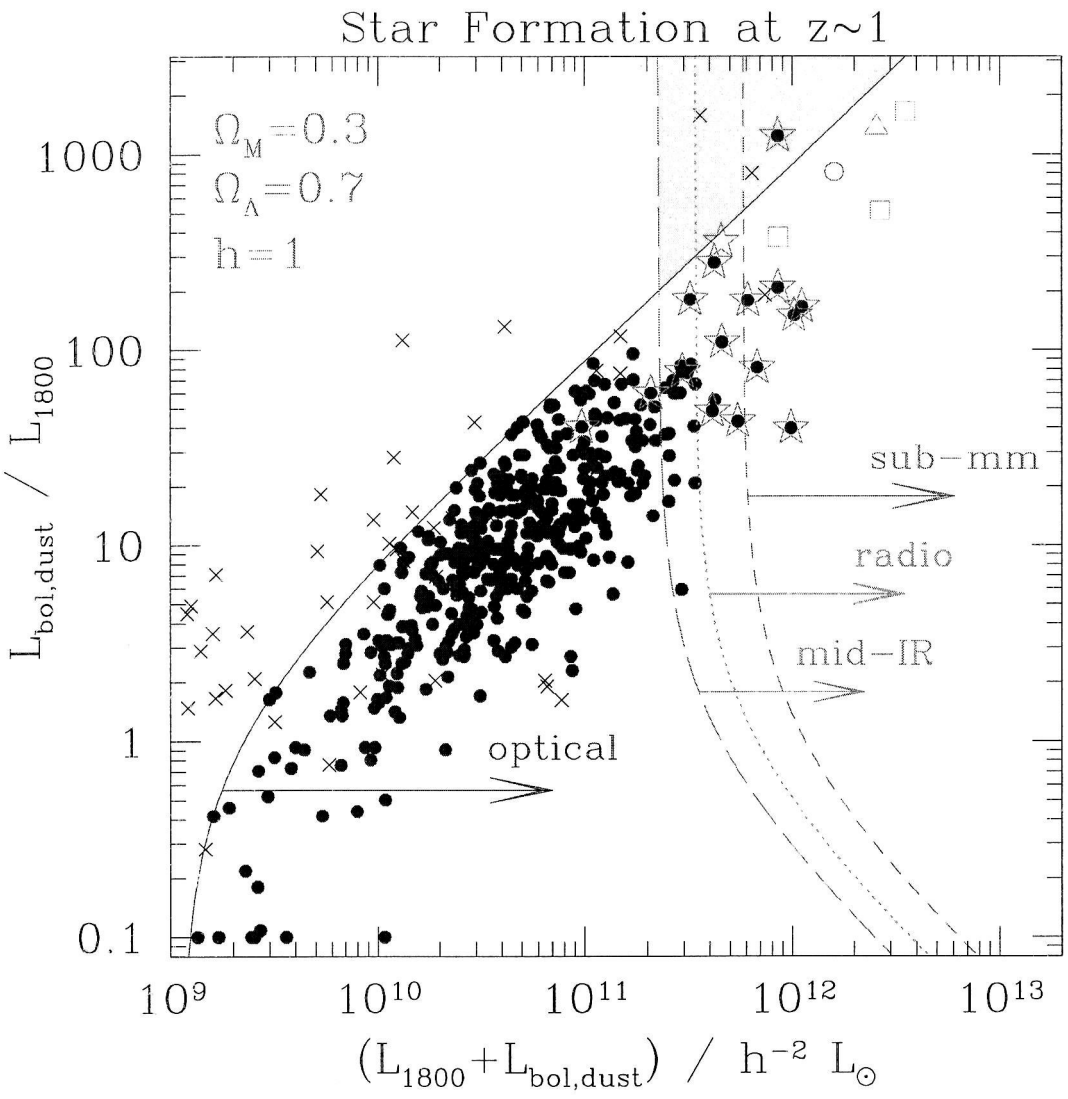

Figure 2.12 Star-formation at $z \sim 1$. The abscissa and ordinate are as in Figure 2.11. Solid circles represent optically selected Balmer-break galaxies at $z \sim 1$, stars represent $z \sim 1$ ISO 15μm sources (15/16 of which are also Balmer-break galaxies), open squares (triangles) represent 850μm/radio sources with estimated redshifts $z < 2$ from BCR that have detected (undetected) optical counterparts, and the open circle represents HR10. Crosses mark the positions of the local starbursts, LIRGs, and ULIRGs from Figure 2.11. Galaxies at $z \sim 1$ exhibit a similar correlation of luminosity and dust obscuration as local galaxies. The lines show $z = 1.0$ completeness limits for existing surveys at various wavelengths. Objects in the shaded region of the plot can be detected only through their dust emission.

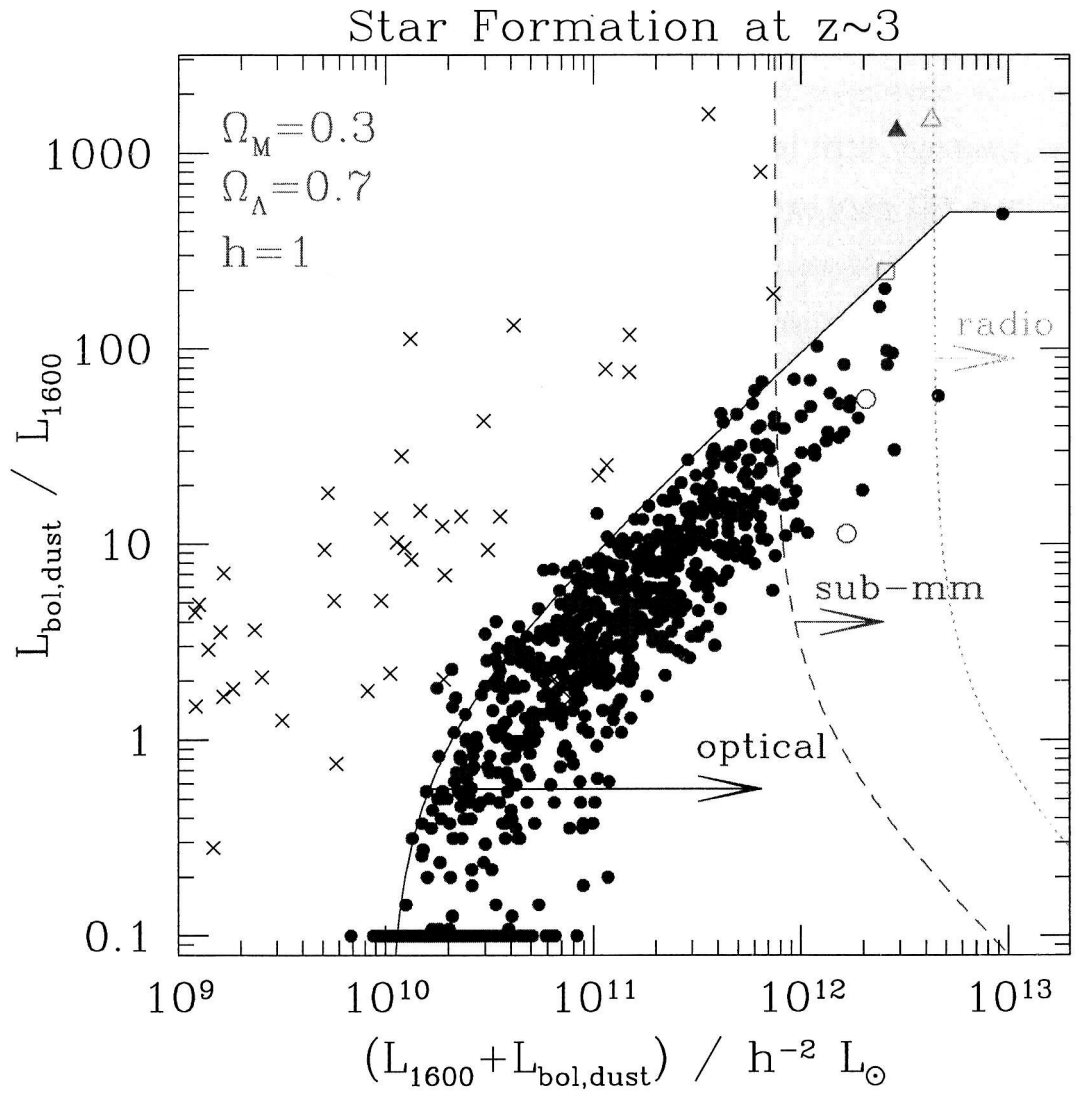

Figure 2.13 Star-formation at $z \sim 3$. The abscissa and ordinate are as in Figure 2.11. Solid circles represent optically selected Lyman-break galaxies, open circles represent the optically identified $z \sim 3$ 850μm sources SMMJ14011+0252 and west MMD11, open squares (triangles) represent 850μm/radio sources with estimated redshifts $z > 2$ from BCR that have detected (undetected) optical counterparts, and the solid triangle represents the optically undetected sub-mm source SMMJ00266+1708. Crosses represent local starbursts, LIRGs, and ULIRGs. Solid, dashed, and dotted lines show the approximate $z = 3.0$ completeness limits of existing optical, sub-mm, and radio surveys. Besides a 1600Å flux limit, the optical line assumes a $G - \mathcal{R}$ color limit of 1.2; the probability that a $z \sim 3$ galaxy will be blue enough to satisfy standard LBG selection criteria declines steadily for $L_{\rm bol,dust}/L_{1600} \gtrsim 20$ and reaches zero by $L_{\rm bol,dust}/L_{1600} \sim 500$—assuming that these galaxies obey MHC's β/far-IR relationship. See Steidel *et al.* (1999) and Adelberger *et al.* (2000) for a more complete discussion. Any galaxies in the shaded region of this diagram would be detectable in blank-field sub-mm surveys but not in standard optical surveys.

§ 2.2. In cases where an object's dust luminosity could have been estimated with more than one of the empirical correlations, we took an estimate from the object's flux in only one wavelength range, with the following order of preference: 850μm, 15μm, 20cm, UV. The dust luminosities of ISO sources in the HDF, for example, were estimated from their 15μm fluxes (§ 2.2.2) rather than from their UV spectral slopes (§ 2.2.3) or radio fluxes (§ 2.2.4). The curved lines in Figure 2.12 show typical $z = 1.0$ detection thresholds for observations at different wavelengths. The optical, sub-mm, and radio thresholds assume the flux limits discussed above; the mid-IR limit assumes a 15μm flux limit of 75μJy, which is roughly appropriate for the HDF catalog of Aussel *et al.* (1999). Because the objects in this plot do not lie at precisely $z = 1.0$, and because small amounts of data exist with flux limits deeper than the typical values adopted here, some detected objects have star-formation luminosities $L_{1800} + L_{\rm bol,dust}$ lower than the indicated thresholds.

Figure 2.13 is a similar plot for galaxies at $z \sim 3$. The solid circles represent optically selected Lyman-break galaxies from the sample of Steidel *et al.* (2000), open circles represent the sub-mm sources SMMJ14011+0252 and west MMD11, the open squares (triangles) represent radio/sub-mm sources with estimated redshifts $z > 2$ from the optically detected (undetected) sample of BCR, and the solid triangle is the optically undetected sub-mm source SMMJ00266+1708 with an estimated redshift $z \sim 3.5$ (Frayer *et al.* 2000). In this plot (and in Figure 2.19 below) the gravitational lensing magnification of SMMJ14011+0252 and SMMJ00266+1708 was roughly corrected by dividing their observed luminosities by 2.75 (Frayer *et al.* 1999) and 2.4 (Frayer *et al.* 2000) respectively.

At each of these redshifts, $z \sim 0$, $z \sim 1$, and $z \sim 3$, star-forming galaxies appear to have a similar range of dust obscuration $0.1 \lesssim L_{\rm bol,dust}/L_{\rm UV} \lesssim 1000$, and to follow a similar correlation of dust obscuration and star-formation rate, but the bolometric star-formation luminosities of detected galaxies increase steadily from $z \sim 0$ to $z \sim 1$

to $z \sim 3$. This is partly a selection effect, but it also reflects a genuine increase in the number density of rapidly star-forming galaxies at higher redshifts (e.g., Lilly *et al.* 1996, Steidel *et al.* 1999, BCR). Although existing high-redshift surveys are not deep enough (for the most part) to detect star-forming galaxies similar to those in the local universe, the observed increase in bolometric star-formation luminosity with redshift suggests that these surveys may nevertheless have detected a substantial fraction of high-redshift star formation.

The goal of this section is to estimate how large a fraction of high-redshift star formation they have detected. Have these surveys detected the majority of high-redshift star formation, or only the relatively small fraction that comparison to the local universe might make us expect? Although we will be primarily concerned with the possibility that dust obscuration has hidden large amounts of star formation from existing surveys, other physical effects—surface brightness dimming (e.g., Lanzetta *et al.* 1999) is an obvious example—can make high-redshift star formation undetectable as well. The results in this section will provide a rough limit on the amount of high-redshift star formation that is undetected in existing surveys.

This limit can be estimated because the brightness of the 850μm background provides an upper limit on the total amount of star formation at high redshift. Since K-corrections at 850μm largely cancel out changes in luminosity distance, a galaxy with given bolometric dust luminosity will appear almost equally bright at 850μm for any redshift in the range $1 \lesssim z \lesssim 5$ (e.g., Blain & Longair 1993). Taken together with the observation that star-forming galaxies emit the majority of their luminosities in the far-IR (cf. Figures 2.11, 2.12, and 2.13), this implies that a flux-limited 850μm survey is nearly equivalent to star-formation limited survey at $1 \lesssim z \lesssim 5$, and that the integrated 850μm background provides upper limit to the total amount of star-formation at high redshift. It is an upper limit, rather than a measurement, because some fraction of the 850μm background is known to be produced by objects other

than star-forming high-redshift galaxies (e.g., AGN and low-redshift galaxies: Edge *et al.* 1999; Ivison *et al.* 2000).

Our strategy for placing limits on the amount of undetected star-formation at high redshift will be to calculate the contribution to the 850μm background from the various known high-redshift populations represented in Figures 2.12 and 2.13, and see if there is significant shortfall between the background contribution from these galaxies and the total background that is observed.

2.4.1 Sub-mm sources

We begin by reviewing the contribution to the 850μm background from resolved sub-mm sources. According to Barger, Cowie, & Sanders (1999), 20–30% of the 850μm background is produced by objects brighter than SCUBA's 2mJy confusion limit. Understanding the nature of these objects is difficult, because the large diffraction disk of SCUBA on the JCMT means that most have several plausible optical counterparts, but multi-wavelength observational programs (e.g., Frayer *et al.* 1999, Dey *et al.* 1999, BCR, Chapman *et al.* 2000, Frayer *et al.* 2000, Ivison *et al.* 2000) have established robust optical counterparts for a handful of them. This work has shown that approximately half of the detected 850μm sources are associated with AGN (Ivison *et al.* 2000). Of the sources which do not appear to be AGN, three—SMMJ14011+0252 (Frayer *et al.* 1999), HR10 (Dey *et al.* 1999), and west MMD11 (Chapman *et al.* 2000)—are robustly associated with high-redshift star-forming galaxies. These galaxies, shown in Figures 2.12 and 2.13, have relatively large dust obscurations $30 < L_{\rm bol,dust}/L_{\rm UV} < 1000$ and large implied star-formation rates, but their UV luminosities are comparable to those of typical optically selected galaxies at similar redshifts. BCR have shown that the brightest 850μm sources tend to be even more heavily obscured: their analysis suggests that $\sim$ 75% (6/8) of 850μm sources brighter than 6mJy have extreme dust obscurations $300 < L_{\rm bol,dust}/L_{\rm UV} < 3000$

(cf. Figures 2.12 and 2.13). The ratio of dust to UV luminosity for these sources is very uncertain because their redshifts (and consequently luminosity distances) are unknown, but BCR's radio/sub-mm photometric redshifts (cf. § 2.2.4) would have to be seriously in error to bring their estimated dust obscurations into a less extreme range. Despite the large star-formation rates implied by their sub-mm fluxes, objects similar to those in the sample of BCR account for only a tiny fraction, $\sim 5\%$ (Barger, Cowie, & Sanders 1999), of the measured 850μm background (Fixsen *et al.* 1998).

The large dust obscurations observed in 850μm sources have excited the interest of numerous authors (e.g., Smail *et al.* 1998; Hughes *et al.* 1998; Eales *et al.* 1999; Barger, Cowie, & Sanders 1999; Sanders 1999; BCR), who have rightly noted that if fainter high-redshift galaxies had similar levels of dust obscuration, the majority of high-redshift star formation would have occurred in objects that could not be detected in any existing survey (cf. Figures 2.12 and 2.13). This popular argument for "hidden" star-formation at high redshift is based on analysis of galaxies responsible for only a small fraction of the 850μm background, however, and it ignores the strong correlation of dust obscuration and luminosity that is observed at low and high redshift alike (cf. Figures 2.11, 2.12, and 2.13). Compelling arguments for or against the existence of hidden high-redshift star formation will require observations of galaxies with typical star-formation rates, not merely those with the extreme star-formation rates characteristic of the objects discussed in this subsection. Although some progress can be made at 850μm through observations of lensed sources (e.g., Smail *et al.* 1998; Ivison *et al.* 2000), the best constraints currently come from observations at other wavelengths.

2.4.2 Mid-IR sources

At $z \sim 1$, 15μm observations can provide a deeper view of dusty star-formation than the sub-mm observations we have just discussed (cf. Figure 2.12). The deepest

existing large-area 15μm image, a $\sim$ 20 square arcmin region centered on the Hubble Deep Field, was obtained by the ISO satellite in 1997. In this subsection we will review the properties of the dusty galaxies at $z \sim 1$ detected in the PRETI reduction (Aussel *et al.* 1999) of this data.

The primary (high significance) catalog of Aussel *et al.* (1999) contains 46 15μm sources. As discussed by Aussel *et al.* (1999) and Cohen *et al.* (2000), the majority of these sources ($\gtrsim$ 80%) can be reasonably associated with relatively bright optical counterparts ($R \lesssim 23$). Although some of the ISO sources may lie close to optically bright galaxies by chance, the fact that so many lie close to optically bright galaxies cannot be a coincidence. Spectroscopic redshifts for 40 of these optical counterparts are provided by Aussel *et al.* (1999) and Cohen *et al.* (2000); an additional redshift, $z \simeq 0.94$ for HDF-PM3-22, was obtained by Adelberger *et al.* (2000). Of the optical counterparts,[4] 16 lie at redshifts $0.8 < z < 1.2$.

These 16 galaxies provide a reasonably complete sample of the $z \sim 1$ galaxies in this part of the sky that have the largest dust luminosities. The limiting dust luminosity for this sample is roughly a factor of three lower than the limit of blank-field SCUBA surveys. The sample is not exactly dust-luminosity limited, because of the scatter in the $L_{MIR}/L_{\rm bol,dust}$ relationship (§ 2.2.2), and it is not 100% complete, because redshifts have not been obtained for some of the 15μm sources in this field[5], but it is as close an approximation to a complete, dust-luminosity sample at high redshift as currently exists.

The bolometric luminosities and dust obscurations of the galaxies in this sample are indicated in Figure 2.12. Their typical dust obscurations, $L_{\rm bol,dust}/L_{UV} \sim 100$, are lower than those of the brighter sub-mm sources at similar redshifts. This trend

[4]HDF-PM3-1, HDF-PM3-6, HDF-PM3-8, HDF-PM3-9, HDF-PM3-10, HDF-PM3-11, HDF-PM3-19, HDF-PM3-20, HDF-PM3-21, HDF-PM3-22, HDF-PM3-25, HDF-PM3-31, HDF-PM3-34, HDF-PM3-37, HDF-PM3-39 and HDF-PM3-45

[5]If the 15μm sources without redshifts have the same redshift distribution as those with redshifts, then perhaps two additional 15μm sources in this field lie at the redshifts of interest $0.8 < z < 1.2$.

of lower dust obscuration in fainter sources is also observed in the local universe (Figure 2.11).

For the most part, the $z \sim 1$ ISO sources in the HDF appear to be drawn from among the same population of $z \sim 1$ galaxies that is routinely studied in the optical. Most of the sources are included in the (optical) magnitude-limited HDF survey of Cohen *et al.* (2000), for example, and 15 of 16 satisfy the Balmer-break photometric selection criteria of Adelberger *et al.* (2000) and are included in that $z \sim 1$ optical survey as well. They are not typical of the galaxies in optical populations, as the non-detection at 15μm of most optically selected HDF galaxies shows, but Figure 2.12 suggests that the $z \sim 1$ ISO population can be naturally interpreted as the high luminosity, high obscuration tail of known $z \sim 1$ optical populations. Optically selected galaxies are thought to possess a wide range of dust obscurations, and the analysis of § 2.4.3 (below) suggests that $10^{+7}_{-4}\%$ have the obscurations $L_{\rm bol,dust}/L_{UV} \gtrsim 30$ characteristic of ISO sources in the HDF. For $\Omega_M = 0.3$, $\Omega_\Lambda = 0.7$ the comoving number density of Balmer-break galaxies to $U_n(AB) \sim 25.5$ (roughly the faintest U_n magnitude for HDF ISO sources) is $\sim 3 \times 10^{-2} h^3$ Mpc^{-3}, and so optical observations would lead us to expect that $\sim 3.0^{+2.0}_{-1.2} \times 10^{-3}$ galaxies per comoving h^{-3} Mpc^3 would have dust obscurations $L_{\rm bol,dust}/L_{UV} \gtrsim 30$ similar to those observed among ISO sources. This is roughly equal to the observed comoving number density of $z \sim 1$ ISO sources in the HDF (16 galaxies with $0.8 < z < 1.2$ in ~ 20 square arcmin, or $2.4 \times 10^{-3} h^3$ Mpc^{-3} for $\Omega_M = 0.3$, $\Omega_\Lambda = 0.7$), showing that the $z \sim 1$ ISO population can be consistently interpreted as the dustiest part of the optical population.

A worrisome aspect of Figure 2.12 is that 10 of the $z \sim 1$ ISO sources are predicted to have detectable radio fluxes $f_\nu(20{\rm cm}) \gtrsim 50\mu$Jy, while only 2 were detected at this level by Richards (2000). Other $z \sim 1$ ISO sources are detected in Richards' 20cm image at lower flux levels, but the total observed 20cm flux for the $z \sim 1$ ISO sources, after excluding HDF-PM3-6 and HDF-PM3-20 which have optical spectra suggesting

the presence of an AGN (Cohen *et al.* 2000), is $\sim$ 360μJy, roughly a factor of 4 lower than the total predicted from the local correlations described in § 2.2. The implication is that the bolometric dust luminosities of the ISO sources may be on average a factor of $\sim$ 4 lower than indicated in Figure 2.12, presumably because the ratio of mid-IR luminosity to total dust luminosity is systematically higher at $z \sim 1$ than in the local universe. This possibility only strengthens the main point we aimed to make in this section, that ISO sources have lower dust luminosities $L_{\rm bol,dust}$ and lower dust obscurations $L_{\rm bol,dust}/L_{UV}$ than the brighter SCUBA sources, and does not significantly affect the mid-IR/far-UV comparison of § 2.3.3 which exploited the ranks of observed 15μm fluxes rather than their absolute values; but it does suggest that estimates of the 850μm background contribution of ISO sources will be subject to significant uncertainty.

The 850μm background contribution of galaxies similar to ISO sources can be crudely estimated as follows. If we adopt a version of the mid-IR/$L_{\rm bol,dust}$ relationship (§ 2.2.2) that correctly predicts the radio fluxes of $z \sim 1$ ISO sources in the HDF, and use the sub-mm/$L_{\rm bol,dust}$ relationship of § 2.2.1, then the total predicted 850μm flux from the 16 $z \sim 1$ ISO sources in the HDF is $\sim$ 8mJy, or 0.4mJy / arcmin^2, roughly 3% of the background measured by Fixsen *et al.* (1998). This number applies only to galaxies in the redshift range $0.8 < z < 1.2$, where ISO 15μm observations are particularly sensitive due to the PAH features. Because little is known about the number density evolution of bright and highly obscured galaxies similar to ISO sources, it is difficult to estimate the contribution from galaxies outside this redshift interval, but a similar population of galaxies distributed uniformly between $z = 1$ and $z = 5$ would contribute $\sim$ 40% ($\Omega_M = 0.3$, $\Omega_\Lambda = 0.7$) of the total 850μm background.

Because of the substantial overlap between ISO sources and galaxies in optical surveys, much of the 850μm background contribution attributed above to ISO sources

will be included as well in our calculation of the background contribution from optically selected galaxies, which we now describe.

2.4.3 Optical sources

Relatively few high-redshift galaxies have been detected by their dust emission, and the few that have apparently account for less than half of the 850μm background. The vast majority of known high-redshift galaxies have been found in optical surveys. Can the large numbers of optically selected galaxies account for the remainder of the 850μm background?

Figures 2.12 and 2.13 illustrate the relationship between optically selected galaxies and the 850μm and 15μm sources we have just discussed. The solid circles in Figure 2.12 represent $z \sim 1$ galaxies from the spectroscopic Balmer-break sample of Adelberger *et al.* (2000). Except in cases where their dust emission has been directly measured, the handful of Balmer-break galaxies with estimated dust obscurations $L_{\rm bol,dust}/L_{UV} > 100$ were omitted from this plot due to the large uncertainties in their dust luminosities (cf. § 2.3.3). Balmer-break galaxies with $U_n(AB) > 25.5$ were also omitted, because at these faint magnitudes the Balmer-break sample suffers from severe selection effects. The solid circles in Figure 2.13 represent Lyman-break galaxies from the spectroscopic sample of Steidel *et al.* (2000). As described in the introduction to § 2.4, the dust luminosities of the optically selected galaxies in Figures 2.12 and 2.13 were estimated from their dust emission in the few cases where it was measured, and from their UV photometry in the typical cases where it was not.

These figures support the common view (e.g., Eales *et al.* 1999; BCR; Frayer *et al.* 2000) that galaxies detected in the UV are typically far less luminous and less obscured than those detected in the IR. In the next sections we will see if UV-selected populations can make up in number what they lack in luminosity and still produce a significant contribution to the 850μm background.

The 850μm luminosity function of Lyman-break galaxies

As a first step we will estimate the contribution to the 850μm background from the best understood population of UV-selected high-redshift galaxies: the Lyman-break galaxies at $z \sim 3$. Figure 2.14 shows these galaxies' apparent magnitude and β distributions (Steidel *et al.* 1999, Adelberger *et al.* 2000). Adelberger *et al.* (2000) find no significant correlation between apparent magnitude and β for Lyman-break galaxies in their ground-based sample ($\mathcal{R} \leq 25.5$; a scatter plot of UV-luminosity versus dust obscuration in $z \sim 3$ galaxies is presented in Figure 2.19 and discussed in § 2.4.4 below) and so it is relatively simple to turn these two distributions into an 850μm luminosity function. The result is shown in Figure 2.15. To produce this plot in a way that accounted for the various uncertainties, we first generated a large number of random realizations of Lyman-break galaxies' apparent magnitude and β distributions, consistent to within the errors with the distributions of Figure 2.14. We then picked at random a β distribution and an apparent magnitude distribution from among these realizations, generated a long list of $\mathcal{R}$, β pairs, with $\mathcal{R}$ drawn randomly from the best Schechter-function fit to the apparent magnitude distribution and β from the β distribution, assigned to each $\mathcal{R}$, β pair in the list an 850μm flux with equation 2.11, and adjusted each of these 850μm fluxes at random by an amount reflecting the uncertainty in their predicted values (see § 2.3). Binning this list and dividing by the appropriate volume produced one realization of the 850μm luminosity function shown in Figure 2.15. We repeated the process, choosing a different realization of the β and apparent magnitude distributions each time, until we had many binned realizations of the expected 850μm luminosity function. The points shown in Figure 2.15 are the mean values among these many binned realizations; the uncertainties are the standard deviations. Also shown in Figure 2.15 are two related luminosity functions estimated in a similar manner: the expected 60μm luminosity function of Lyman-break galaxies (similar in shape to their bolometric dust luminosity function) and the

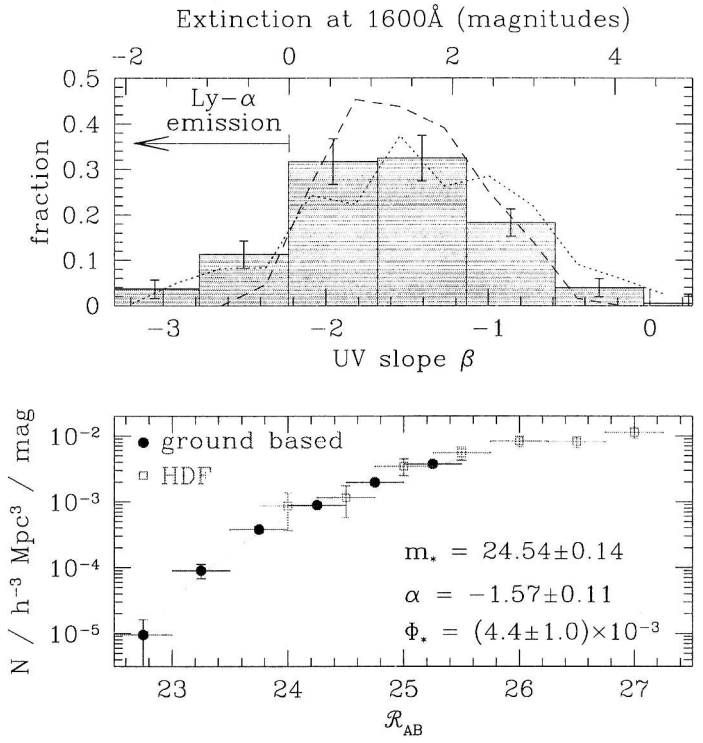

Figure 2.14 The apparent magnitude and β distributions of Lyman-break galaxies at $z \sim 3$, from Steidel *et al.* (1999) and Adelberger *et al.* (2000). The shaded β distribution is our current best estimate. Systematic uncertainties is the shape of this distribution are probably larger than the random uncertainties denoted by the error bars. This is illustrated by the dotted and dashed lines, which show, respectively, a previous estimate of the β distribution (derived by Steidel *et al.* (1999) with a crude treatment of photometric errors and incompleteness) and the β distribution derived by correcting for spectroscopically observed Lyman-α emission but not for our photometric errors and incompleteness. The small differences between these distributions in their red tails have significant consequences; see below. The number density in the luminosity function assumes $\Omega_M = 0.3$ and $\Omega_\Lambda = 0.7$.

"dust corrected" UV luminosity function (derived by taking $A_{1600} = 4.43 + 1.99\beta$ for the extinction in magnitudes at 1600Å, as suggested by MHC). The shapes of these two luminosity distributions, both essentially equivalent to the star-formation rate distribution, are similar to what is predicted by the simplest hierarchical models of galaxy formation (Adelberger 2000, Adelberger *et al.* 2000).

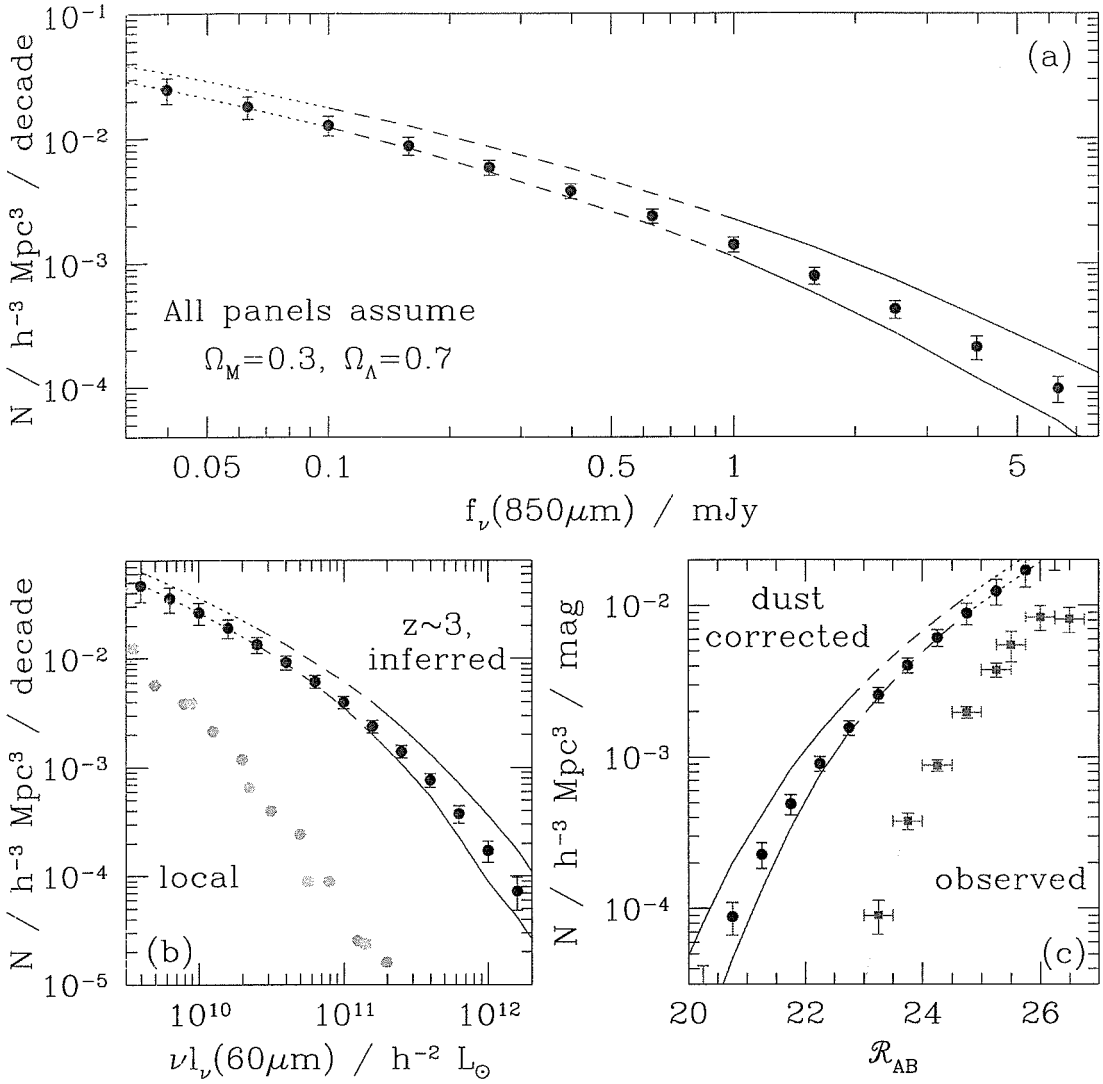

Figure 2.15 (a) The 850μm flux distribution of Lyman-break galaxies as inferred from their UV properties. The points in the flux distribution show our best estimate; their error bars include the random uncertainties discussed in the text. The curved envelope surrounding these points shows the much larger uncertainty in the 850μm flux distribution due to possible systematic errors in our derived β distribution. At the faintest fluxes (dotted envelope) the expected contribution from sources with $\mathcal{R} > 27$ accounts for most of the estimated 850μm flux distribution. At slightly higher fluxes (dashed envelope) the contribution from sources with $\mathcal{R} > 25.5$ dominates. The inferred flux distribution is most secure at the brightest fluxes (solid envelope) that are dominated by the contribution from galaxies with $\mathcal{R} < 25.5$. (b) Comparison of the local 60μm luminosity function (Lawrence *et al.* 1986; Soifer *et al.* 1987) to the inferred 60μm luminosity function of Lyman-break galaxies at $z \sim 3$. Symbols are as in (a). (c) The observed and dust corrected far-UV luminosity functions of Lyman-break galaxies at $z \sim 3$. The observed luminosity function is from Steidel *et al.* (1999); the dust corrected luminosity function was estimated as described in the text. Symbols are as in (a).

The systematic uncertainties in these luminosity functions are far larger than the random uncertainties. The most obvious systematic uncertainty is in the validity of our underlying assumption that the β/far-IR correlation will hold at high redshift. This uncertainty is difficult to treat quantitatively. If the β/far-IR correlation does not hold these results are meaningless; the data in § 2.3 give us hope that it may hold; there is little else to say.

A second source of systematic uncertainty is the unknown shape of the apparent magnitude distribution at magnitudes fainter than $\mathcal{R} \sim 27$. Galaxies so faint in the UV may still have large star-formation rates if they are sufficiently dusty, and so our estimate of the number density of high star-formation rate galaxies depends to some degree on the unknown number density of these faint galaxies. In our calculation above we assumed that the $\alpha \sim -1.6$ faint-end slope of the apparent magnitude distribution would continue to arbitrarily faint magnitudes. This extrapolation has a significant effect on our conclusions only at the faintest luminosities; Figure 2.15 shows the luminosities below which most of the estimated luminosity density comes from objects with $\mathcal{R} > 27$. These parts of the luminosity functions should be viewed with considerable scepticism.

A related source of systematic uncertainty is our assumption that the β distribution of Lyman-break galaxies is the same at all apparent magnitudes. This is known to be true only for $\mathcal{R} < 25.5$ (Adelberger *et al.* 2000), and so the faintest points in our inferred luminosity functions are subject to further systematic uncertainties which are difficult to quantify. This source of systematic uncertainty is negligible only at the brightest luminosities, where most of the estimated luminosity density comes from galaxies with $\mathcal{R} < 25.5$; see Figure 2.15.

The final source of significant systematic uncertainty is the shape of the β distribution. Deriving this distribution from our data is difficult. It requires (among other things) a quantitative understanding of the selection biases that result from our

photometric selection criteria and of the effects of photometric errors and Lyman-α emission/absorption on our measured broadband colors. Our current best estimate of the β distribution is shown in Figure 2.14 (Adelberger *et al.* 2000). To give some idea of the systematic uncertainty in this distribution, we also show our previously published estimate (adapted from Steidel *et al.* 1999) and the β distribution we would derive if we neglected photometric errors and incompleteness corrections altogether and simply corrected the measured broadband colors for the spectroscopically observed Lyman-α equivalent width. The most important difference between these three distributions (for our present purposes) is the shape of their red tails. The true shape almost certainly falls within the range they span; it is unlikely to be redder than the distribution of Steidel *et al.* (1999), and, since all known selection biases cause the Lyman-break technique to miss the reddest objects at $z \sim 3$, it cannot be bluer than the distribution that neglects completeness corrections. The luminosity functions that we would infer given these two limiting β distributions are show in Figure 2.15 by curved lines. The systematic uncertainty in the β distribution means that the mean extinction at 1600Å for Lyman-break galaxies, a factor of 6 in our best estimate, could lie between a factor of 5 and a factor of 9.

UV-selected populations and the 850μm background

In this section we will extend the preceding calculation to derive a crude estimate of the total contribution to the 850μm background from known UV-selected populations at $1 < z < 5$. § 2.4.3 described the uncertainties affecting our calculation of $z \sim 3$ Lyman-break galaxies' contribution to the 850μm background. Because relatively little is known about UV-selected populations at redshifts other than $z \sim 3$, the uncertainties in the present calculation will be much larger still. As a first approximation we can assume that these galaxies will have the same $\sim$ 1800Å luminosity distribution, the same β distribution, and the same lack of correlation between β and $\sim$ 1800Å

luminosity as Lyman-break galaxies at $z \sim 3$. This is clearly an over-simplification, but the available data suggest that it might not be seriously incorrect. For example, Lyman-break galaxies at $z \sim 4$ appear to have approximately the same luminosity distribution and (possibly) β distribution as Lyman-break galaxies at $z \sim 3$ (Steidel *et al.* 1999); Balmer-break galaxies at $z \sim 1$ have far-UV spectral slopes β that lie mainly in the range $-2.2 < \beta < -0.5$ observed in Lyman-break galaxies at $z \sim 3$ (Adelberger *et al.* 2000); and, like Lyman-break galaxies at $z \sim 3$, Balmer-break galaxies at $z \sim 1$ exhibit no significant correlation of β with apparent magnitude at rest-frame $\sim$ 1800Å (Adelberger *et al.* 2000; cf. Figure 2.19, which we discuss below). The available data suggest further that the comoving star-formation density in UV-selected populations is roughly constant for $1 < z < 5$ (Steidel *et al.* 1999), and so the contribution to the 850μm background from UV-selected high-redshift populations can probably be crudely approximated as the contribution that would arise from Lyman-break–like populations distributed with a constant comoving number density at $1 < z < 5$.

To estimate this contribution we simulated an ensemble of $\sim 10^6$ Lyman-break–like galaxies at $1 < z < 5$. Each galaxy was assigned a UV slope β drawn randomly from the (shaded) β distribution shown in Figure 2.14; a redshift z_i drawn randomly from the interval $1 < z < 5$ with probability proportional to dV/dz (where dV/dz is the comoving volume per arcmin^2 per unit redshift in an $\Omega_M = 0.3$, $\Omega_\Lambda = 0.7$ cosmology); an apparent magnitude at rest-frame 1600Å, m_{1600}, drawn randomly from the apparent magnitude distribution in Figure 2.14 shifted by the ($\Omega_M = 0.3$, $\Omega_\Lambda = 0.7$) distance modulus between z_i and $z = 3.0$ and truncated at $m_{1600} = 27$; and an observed-frame 850μm flux with a version of equation 2.11 appropriate to redshift z_i. Finally each 850μm flux was adjusted at random by an amount reflecting the uncertainty in its predicted value (§ 2.3).

Figure 2.16 was produced by placing these simulated galaxies into bins of 850μm

flux and dividing by the appropriate area. The top panel shows the estimated contribution to the 850μm background per logarithmic interval in f_ν, $f_\nu^2 n(f_\nu)$, where $n(f_\nu)$ is the number of sources per mJy per square degree. The overall background expected from UV-selected populations in this crude calculation, $4.1 \times 10^4 \mathrm{mJy/deg}^2$, is close to the measured background of 4.4×10^4 (Fixsen *et al.* 1998). The closeness of the agreement is not especially meaningful, because the uncertainties in the calculation are so large, but nevertheless it is clear that the known UV-selected galaxies at high redshift could easily have produced the $\sim$ 75% of the 850μm background that has not currently been resolved into discrete sources by SCUBA. There is little need to invoke large amounts of hidden high-redshift star-formation in order to account for the brightness of the 850μm background.

If the bulk of the 850μm background is produced by galaxies similar to those in UV-selected surveys, as we have argued, then the shape of the 850μm number counts should be similar to what our calculation suggests UV selected populations would produce. This appears to be the case. The bottom panel of Figure 2.16 compares the cumulative 850μm number counts $N(> f_\nu)$ ($\equiv$ the number of objects per square degree brighter than f_ν) measured by Blain *et al.* (1999b) to the number counts that would be produced by the UV-selected high-redshift galaxies in our calculation. Although there are clear differences at the brightest end, where the observed number counts receive contributions from AGN, from low-redshift galaxies, and from extremely luminous high-redshift galaxies that may differ from the more normal galaxies detected in the UV, the observed number counts are remarkably close to what UV-selected populations would produce in the range $0.3 < f_\nu < 3$mJy that dominates the 850μm background.

Figure 2.17 shows the expected contribution to the 850μm background from objects with different apparent magnitudes at rest-frame 1600Å. This gives a rough idea of the apparent magnitudes we would expect to measure for sub-mm sources

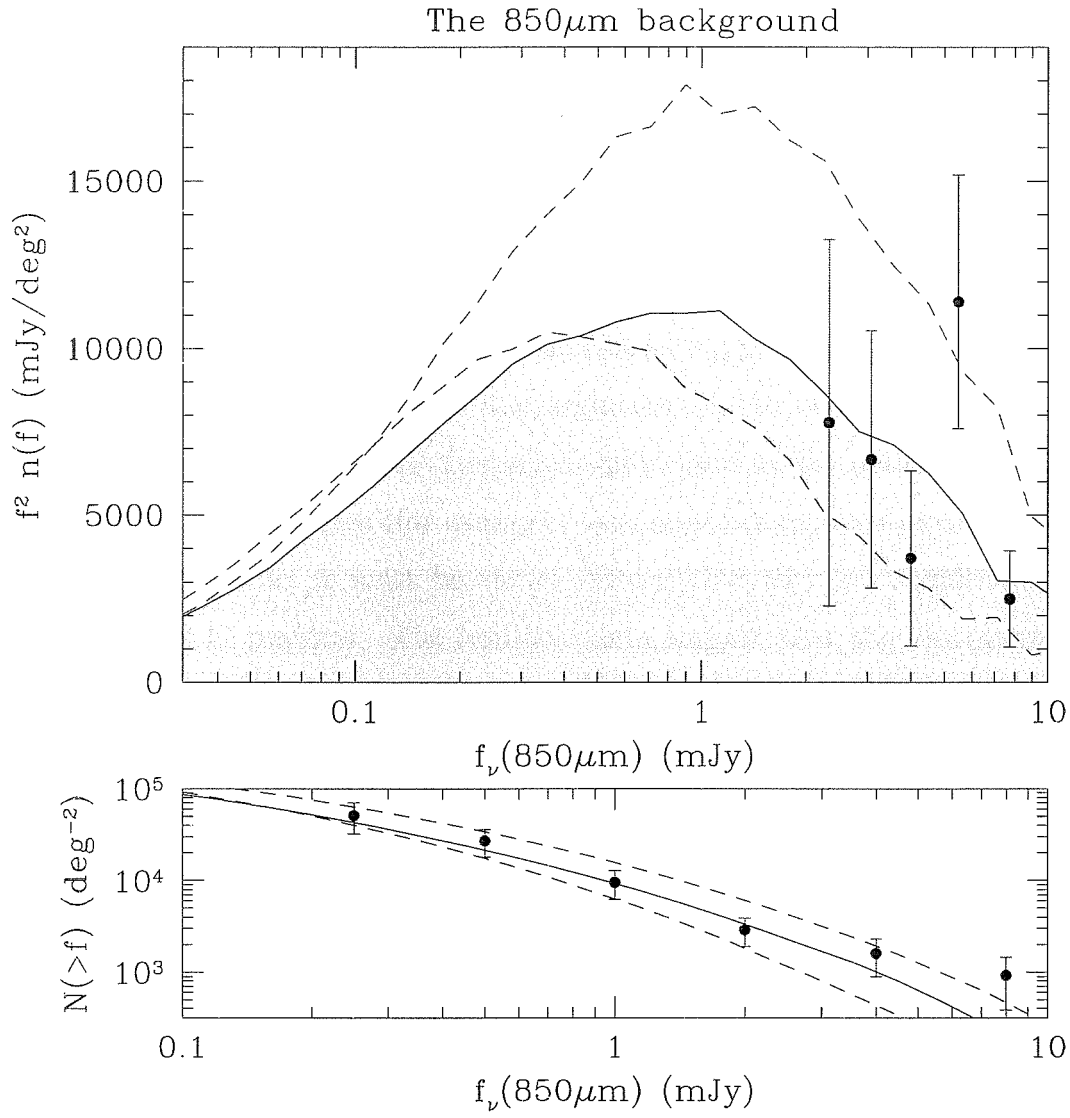

Figure 2.16 Top panel: The 850μm background contribution $f_\nu^2 n(f_\nu)$ from sources with different fluxes. Points with error bars show observed values, derived from data in Barger, Cowie, and Sanders (1999); the smooth curves show the background known UV-selected populations at $1 \lesssim z \lesssim 5$ would produce given the simple assumptions described in the text. The solid curve is appropriate to our best estimate of the β distribution. Dashed lines illustrate the uncertainty due to possible systematic errors in our adopted β distribution. This is certainly not the largest source of systematic uncertainty; is it merely the easiest to quantify. The total background for our best fit β distribution (shaded region) is 4.1×10^4 mJy/deg^2. The measured 850μm background is 4.4×10^4 mJy/deg^2 (Fixsen *et al.* 1998). Bottom panel: The cumulative 850μm number counts. Symbols are as in the top panel. The observed number counts are from Blain *et al.* (1999).

with various fluxes if rest-frame UV-selected populations obeying the local correlations between far-UV and far-IR fluxes produced the bulk of the 850μm background. At any given 850μm flux density, objects are expected to have a wide range of redshifts and dust obscurations, and consequently of optical magnitudes, but even at the brightest 850μm fluxes most objects are expected to be relatively faint ($m_{1600} > 24$) in the optical. The observed faintness of optical counterparts to 850μm sources is sometimes thought to show that the 850μm background is produced by objects not present in rest-UV-selected surveys, but this argument has to be made carefully: UV-selected high-redshift galaxies are themselves quite faint in the optical, and as a result it is not sufficient to show (for example) that most optical counterparts are fainter than $24^{\rm th}$ magnitude; it must be shown instead that they are significantly fainter than Figure 2.17 predicts. The available data suggest that the sources responsible for brightest 850μm number counts, $f_\nu \gtrsim 6$mJy, are in fact significantly fainter than the predictions of Figure 2.17 (e.g., BCR; Frayer *et al.* 2000), and this is hardly surprising since our calculation shows that UV-selected populations cannot by themselves account for the brightest 850μm number counts. Objects with larger obscurations $L_{\rm bol,dust}/L_{UV} \sim 1000$ are required and have been found. Measuring the optical magnitudes of $\sim$ 1mJy sources would provide a better test of whether UV-selected populations contribute significantly to the far-IR background, but with current technology this is possible only for lensed sources and adequate data do not yet exist.

Also shown in Figure 2.17 is the contribution to the 850μm background that would be produced by galaxies with $27 < m_{1600} < 29$ if the $\alpha = -1.6$ faint-end slope of the luminosity function continued past the faintest observed magnitude of $m_{1600} \simeq 27$ and if dust obscuration and reddening remained uncorrelated at the faintest magnitudes. Due to the steep faint-end slope, objects with $m_{1600} > 27$ might

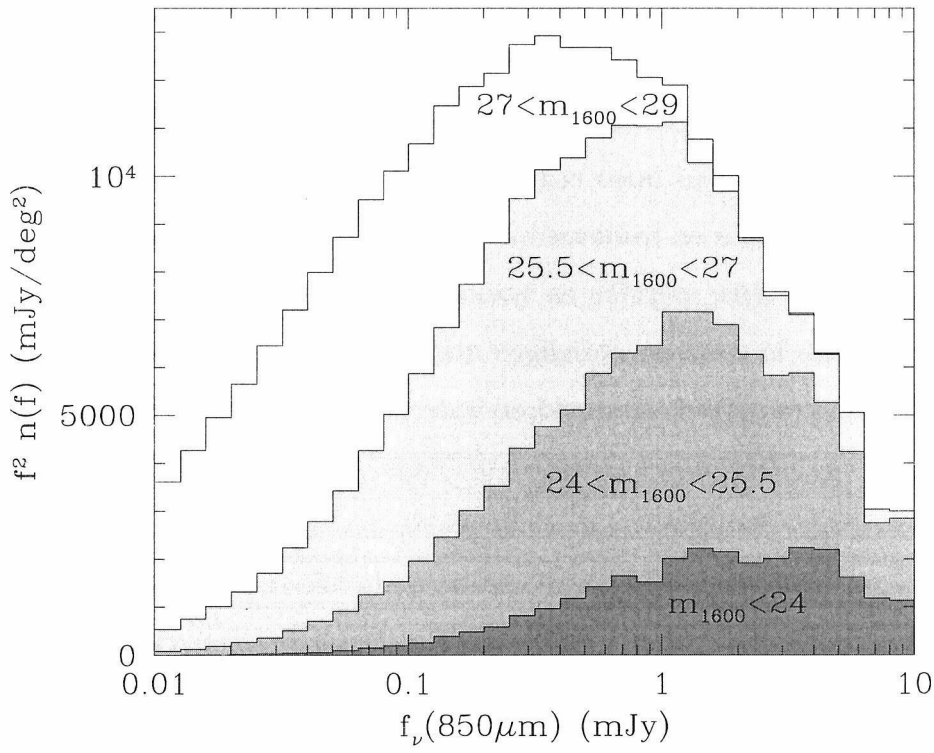

Figure 2.17 The expected contribution to the 850μm background from UV-selected sources with different apparent magnitudes at 1600Å rest. Even if UV-selected populations were solely responsible for the 850μm background, we would expect most of the sub-mm sources brighter than 2mJy at 850μm to be fainter than $m_{AB} = 24$ at 1600Å rest. Also shown is the contribution to the background which would be produced by galaxies with $27 < m_{AB} < 29$ if the $\alpha = -1.6$ faint end slope of the assumed luminosity function continued past the faintest observed magnitude of $m_{1600} \simeq 27$. These galaxies were excluded from the calculation whose results are shown in Figure 2.16; see text.

be expected to contribute significantly to the 850μm background. MHC have presented evidence, however, from Lyman-break galaxies with $25.5 \lesssim m_{1600} < 27$ in the HDF, that galaxies fainter in the UV tend to have lower dust extinctions. Because

apparent magnitude and dust obscuration are not correlated among $z \sim 3$ Lyman-break galaxies with $m_{1600} < 25.5$, we assumed when producing Figures 2.16 and 2.17 that they would remain uncorrelated at fainter magnitudes as well. MHC's analysis suggests that this assumption is incorrect: galaxies with $25.5 < m_{1600} < 27$ are probably somewhat less dusty than we have assumed and galaxies with $m_{1600} > 27$ are probably significantly less dusty. When estimating the total background contribution from UV-selected populations (Figure 2.16), we assumed as a compromise that galaxies with $25.5 < m_{1600} < 27$ would be as dusty as galaxies with $m_{1600} < 25.5$, and that galaxies with $m_{1600} > 27$ would contain negligible amounts of dust. This is obviously a very crude solution to a complicated problem; the background contribution from objects with $m_{1600} > 25.5$ is a significant source of systematic uncertainty in Figures 2.16 and 2.17.

Figure 2.17 would be more useful for observational tests if we showed the predicted magnitudes at fixed observed-frame wavelengths, say the i band, rather than a fixed rest-frame wavelength, but this requires us to estimate K-corrections for these galaxies and we have not found an adequate model for their UV/optical SEDs. The problem is illustrated by Figure 2.18, which shows the measured rest-frame UV/optical SEDs of two Lyman-break galaxies detected at 850μm, SMMJ14011+0252 (Smail *et al.* 1998) and west MMD11 (Chapman *et al.* 2000). The optical data were obtained as described in § 2.3.1 and in Steidel *et al.* (2000); the near-IR photometry was obtained with NIRC (Matthews & Soifer 1994) on Keck I with excellent seeing ($\lesssim 0\farcs5$) in May 1999. Neither SED is fit well by a model of a continuously star-forming galaxy subjected to varying amounts of dust following a standard extinction law. Moreover, even though SMMJ14011+0252 and west MMD11 have essentially indistinguishable SEDs in the UV—both are consistent with the same value of β—their optical SEDs are significantly different. The shapes of galaxies' UV/optical SEDs are strongly dependent on their star-formation histories, and perhaps the simplest conclusion to

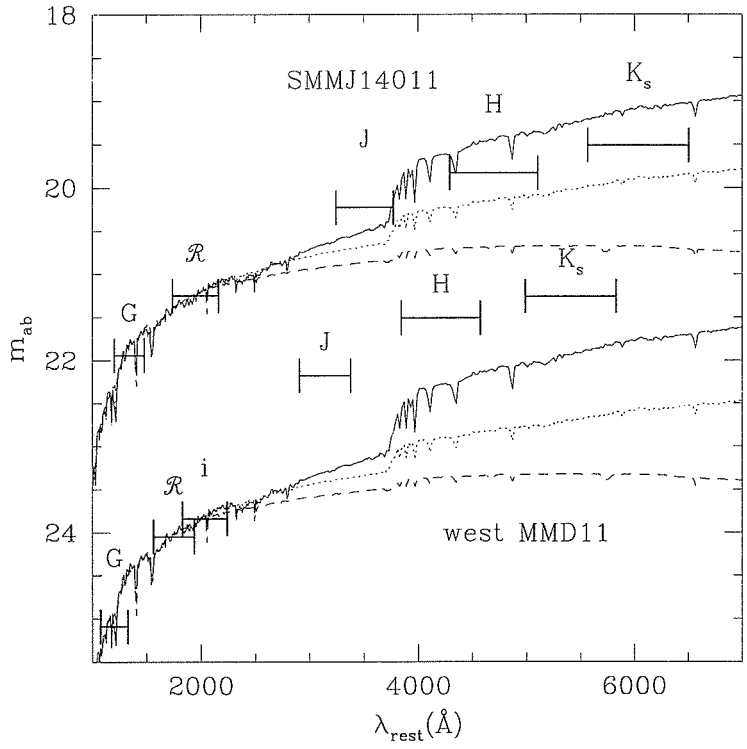

Figure 2.18 The UV to optical photometry of two $z \sim 3$ galaxies detected at 850μm. The bars show measured AB magnitudes, and the lines Bruzual & Charlot (1996) model galaxies after 1Myr (dashed), 40 Myr (dotted), and 1Gyr (solid) of star formation at a constant rate. The model SEDs were reddened with dust following Calzetti's (1997) extinction law as required to match the observed $G-\mathcal{R}$ color; for both galaxies this required $A_{1600} = 3.2$ for the 1Gyr SED, $A_{1600} = 3.9$ for the 40Myr SED, and $A_{1600} = 4.5$ for the 1Myr SED. The value of A_{1600} adopted in the text was derived from the empirical correlation between UV spectral slope β and the ratio $L_{\rm bol,dust}/L_{1600}$, not from an assumed SED and dust reddening law.

draw from Figure 2.18 is that the star-formation histories of high-redshift galaxies are complicated and diverse. We have found no obvious way to predict their optical photometry from their UV photometry. See Shapley *et al.* (2000) for a more complete discussion.

This is a good place to remind readers that our UV-based estimates of high-redshift galaxies' bolometric dust luminosities are not derived from an assumed intrinsic SED and dust reddening law; they are derived instead from the empirical (and somewhat

mysterious) correlation between β and $L_{\rm bol,dust}/L_{1600}$ described in § 2.2.3. The diversity of observed SEDs makes it difficult to understand why this correlation should exist, but local (§ 2.2) and (less convincingly) high redshift (§ 2.3) observations suggest that it does.

2.4.4 Discussion

The major result of this section is our calculation showing that galaxies similar to those detected in UV-selected surveys probably produced a large fraction of the measured 850μm background. Recent analyses of 850μm surveys have reached the opposite conclusion (e.g., Smail *et al.* 1998, Hughes *et al.* 1998, Eales *et al.* 1999, Barger, Cowie, & Sanders 1999, Sanders 1999, BCR). Skeptical readers may wonder if our calculation is robust given its apparently heavy reliance on the poorly tested assumption (§ 2.3) that high-redshift galaxies' dust luminosities can be estimated from their UV fluxes with the correlations of § 2.2.

Although the details of our calculation certainly depend upon the assumption that high-redshift galaxies obey MHC's β/far-IR relationship, the overall background contribution from UV-selected galaxies depends primarily upon the adopted mean value of $L_{\rm bol,dust}/L_{UV}$. MHC's relationship implies that $\langle L_{\rm bol,dust}/L_{UV}\rangle \sim 6$ for galaxies at $z \sim 3$, and our calculation in § 2.4.3 showed that this factor of 6 is sufficient for UV-selected galaxies to have produced the bulk of the 850μm background. High-redshift galaxies may not satisfy MHC's relationship, but the adopted $\langle L_{\rm bol,dust}/L_{UV}\rangle \sim 6$ is still a plausible estimate of their mean dust obscuration. This mean obscuration is hardly unrealistically high; it is roughly equal to mean obscuration among the Lyman-break galaxies observed in the sub-mm by Chapman *et al.* (2000), for example, and it is significantly lower than the mean obscuration (~ 15) in the local starburst sample of MHC. Even the local spirals in the sample discussed before § 2.4.1 have $\langle L_{\rm bol,dust}/L_{UV}\rangle \sim 5$; given the correlation of dust obscuration and star-formation

rate that appears to exist at all redshifts (cf. Figures 2.11, 2.12, and 2.13), it is hard to imagine that a rapidly star-forming population at any redshift could have values of $L_{\rm bol,dust}/L_{UV}$ significantly lower than spirals in the local universe.

But the fundamental difference between our analysis and the analyses of previous authors who reached opposite conclusions is not simply the value of $\langle L_{\rm bol,dust}/L_{UV}\rangle$ adopted for UV-selected galaxies; it is instead the assumed dependence of dust obscuration on luminosity among high-redshift galaxies. Arguments for large amounts of hidden star-formation at high redshift generally assume that dust obscuration and luminosity are independent. Data from low and high redshifts lead us to believe that $L_{\rm bol,dust}/L_{UV} \overset{\propto}{\lesssim} L_{\rm bol,dust}$ is a better approximation (cf. Figures 2.11, 2.12, 2.13 and 2.19). This correlation between dust obscuration and luminosity means that the $f_\nu(850\mu{\rm m}) \sim 1{\rm mJy}$ sources that produce most of the 850μm background are likely to be significantly less obscured than the brighter sources currently detectable in the sub-mm. For example, if the $\sim$ 10mJy sources studied by BCR have $200 \lesssim L_{\rm bol,dust}/L_{UV} \lesssim 2000$ (cf. Figures 2.12 and 2.13), then the correlation of dust obscuration and luminosity would suggest the 1mJy sources responsible for most of the 850μm background have $20 \lesssim L_{\rm bol,dust}/L_{UV} \lesssim 200$. These sources would be dustier than typical optically selected galaxies, but they would nevertheless be as easy to detect in the optical as in the sub-mm. More generally, the correlation of dust obscuration with luminosity means that heavily obscured sources are not necessarily any harder to detect in the rest-frame UV than less obscured sources. Their higher UV obscurations are largely cancelled out by their higher intrinsic luminosities. This is illustrated by Figure 2.19, which shows the observed UV luminosities of sources with different dust obscurations at low and high redshift. Observed UV luminosities are similar for galaxies with dust obscurations $L_{\rm bol,dust}/L_{UV}$ spanning four orders of magnitude.

How robust is the claimed existence of the correlation between dust obscuration

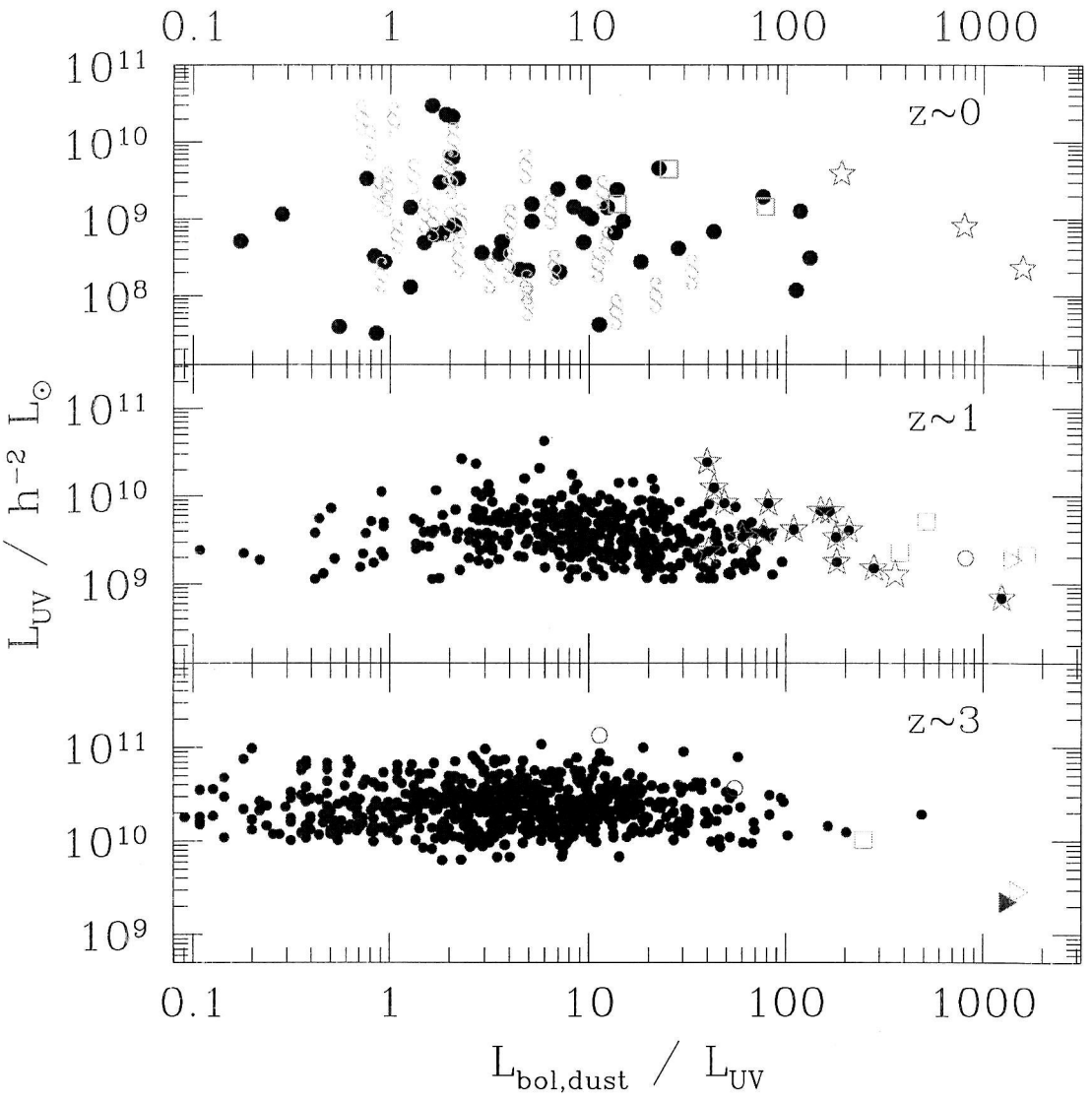

Figure 2.19 Far-UV luminosity versus dust obscuration for star-forming galaxies at $z \sim 0$ (top panel), $z \sim 1$ (middle panel), and $z \sim 3$ (bottom panel). Symbols are as in Figures 2.11, 2.12, and 2.13. Dust absorbs UV photons, but dustier galaxies tend to have higher star-formation rates and larger intrinsic UV luminosities, and as a result the observed UV luminosities of star-forming galaxies are largely independent of their dust obscuration. There are exceptions, but in general extremely dusty galaxies are no fainter in the far-UV than relatively dust-free galaxies. The 1600Å luminosities assume $\Omega_M = 0.3$, $\Omega_\Lambda = 0.7$. Objects represented by open squares, open triangles, and solid triangles do not have spectroscopic redshifts, and their placement on this plot is very uncertain. The lower limits to the UV luminosities of optically selected galaxies at $z \sim 1$ and $z \sim 3$ reflect the flux limits of existing surveys. The apparent increase of UV luminosities with redshift is partly but not solely a selection effect. The color-selection criteria used in constructing the $z \sim 1$ and $z \sim 3$ optical samples result in a selection bias against the bluest objects at $z \sim 1$ and the reddest objects at $z \sim 3$. When selection effects are corrected (as they have been in § 2.4 but not in this figure), the observed dust obscuration distributions in optical populations at $z \sim 1$ and $z \sim 3$ are similar.

and luminosity? At low redshift, where objects' dust luminosities are well constrained by IRAS measurements, its existence is indisputable. At higher redshifts, dust luminosities can only be estimated with the uncertain empirical correlations described in § 2.2, and its existence is somewhat less secure. But even if none of the empirical correlations of § 2.2 hold at high redshift, it is difficult to escape the conclusion that dust obscuration and luminosity are correlated. Without the correlations of § 2.2 we would not know precisely where on the x-axis to place any object in Figure 2.19, for example, but we would still know that ISO sources are typically more luminous and more obscured than optical sources, and that SCUBA sources are typically more luminous and more obscured than ISO sources[6]; and that is enough to establish the existence of the correlation.

A final and more direct argument that UV-selected galaxies contribute significantly to the 850μm background comes from the work of Peacock *et al.* (2000), who showed that positive background fluctuations in a deep 850μm image of the HDF (Hughes *et al.* 1998) tend to be coincident with the locations of UV-selected high-redshift galaxies. Their detailed analysis suggests that UV-selected populations must have produced at least one quarter, and probably at least one half, of the total 850μm background.

Taken together the preceding arguments make a reasonably strong case that the majority of high-redshift star formation is detectable in the deepest optical surveys. But this does not imply that IR/sub-mm observations are unnecessary. Although many of the results that have emerged from sub-mm surveys could have been inferred from UV data alone—the brightness of the 850μm background, for instance, or the domination of the 850μm background by $\sim$ 1mJy sources (e.g., Blain *et al.* 1999b; cf. Figure 2.16), or the $\sim$ thousand-fold increase in number density of ULIRGs from

[6]For example, typical optical sources at $z \sim 1$ are fainter at 15μm and 20cm than ISO sources at $z \sim 1$; typical $z \sim 1$ ISO sources must be fainter than typical SCUBA sources, or else they would over-produce the 850μm number counts.

$z \sim 0$ to $z \gtrsim 3$ (e.g., Sanders 1999; cf. Figure 2.15)—some could not. For example, there was little indication from UV-selected surveys that extremely dusty galaxies with $L_{\rm bol,dust}/L_{UV} \gg 100$ even existed (cf. Figure 2.14), let alone that they hosted significant fraction ($\gtrsim 5\%$) of high-redshift star-formation. Observations in the IR will continue to play a central role in studies of high-redshift star formation, both as tests of the dust corrections that UV-selected surveys require and as the most efficient way to find the dustiest and most rapidly star-forming galaxies.

2.5 Summary

The available evidence strongly suggests that dust in high-redshift galaxies will have absorbed most of the UV radiation emitted by their massive stars. Dust certainly absorbs most of the UV radiation emitted by rapidly star-forming galaxies in the local universe, and the ratio of the far-IR to optical backgrounds shows that the situation must have been similar throughout the history of the universe. Estimating the bolometric dust luminosities of high-redshift galaxies is therefore a crucial step in deriving their star-formation rates. The first part of this paper was primarily concerned with ways bolometric dust luminosities can be estimated even though most of the dust emission is blocked by the earth's atmosphere before it can be detected on the ground.

We began in § 2.2 by describing correlations between local galaxies' bolometric dust luminosities and luminosities at more accessible far-UV, mid-IR, sub-mm, and radio wavelengths. These correlations provide the basis for attempts to estimate high-redshift galaxies' bolometric dust luminosities. Much of this section was simply a review of previously published results; the minor new contribution was a quantification of the uncertainties involved in estimating bolometric dust luminosities from observations at a single rest wavelength $25\mu{\rm m} \lesssim \lambda \lesssim 600\mu{\rm m}$ or $\lambda \sim 8\mu{\rm m}$. The data

suggest that radio, sub-mm, mid-IR, and far-UV estimates of local galaxies' bolometric dust luminosities are all subject to a comparable uncertainty of 0.2–0.3 dex.

§ 2.3 was concerned with establishing whether the bolometric dust luminosities of high-redshift galaxies can be estimated from their fluxes through various atmospheric windows with the correlations of § 2.2. The evidence presented was of uneven quality. The galaxy with the highest quality observations, SMMJ14011+0252 at $z = 2.565$, obeyed the expected correlations nicely. The observations of more typical $z \sim 3$ galaxies had extremely low signal to noise ratios ($\lesssim 1$), and were largely inconclusive, though at least consistent with the expected correlations. Galaxies in our $z \sim 1$ sample were bright enough in the mid-IR and radio for us to show with high significance (>99%) that their predicted and observed fluxes in each of these bands were positively correlated. The data suggested moreover that this positive correlation was at least broadly consistent with the expected linear correlation $\langle f_{\rm observed} \rangle = \langle f_{\rm predicted} \rangle$. Taken together the data in this section make a plausible but still unconvincing case that the bolometric dust luminosities of high-redshift galaxies can be estimated with the expected accuracy using correlations calibrated in the local universe.

Our most important results were presented in the second part of this paper, § 2.4, where we estimated the contributions to the far-IR background from different high-redshift populations. The brightness of the 850μm background provides a rough measure of the total amount of star-formation at high redshift, and a significant shortfall between the background contribution from known populations and the measured background would show that existing surveys have not detected the majority of star-formation at high redshift. We did not find any evidence for a shortfall. The extremely luminous objects currently detectable in the sub-mm can account for $\sim 25\%$ of the far-IR background; the somewhat fainter galaxies detected in the mid-IR by ISO can account for perhaps an additional $\sim 15\%$; and the galaxies detected in optical surveys can account for the remainder. Attributing the far-IR background to

different galaxy populations in this way obscures the fact that there is substantial overlap between galaxy populations selected at different wavelengths, especially the mid-IR and optical, but the important point is that the brightness of the 850μm background is similar to what known high-redshift populations would produce if they obeyed the local correlations of § 2.2. This casts doubt on recent claims that the majority of high-redshift star formation is hidden from existing surveys (e.g., Lanzetta *et al.* 1999; BCR).

The analysis of § 2.4 suggested that the bulk of the 850μm background was produced by moderately obscured galaxies ($1 < L_{\rm bol,dust}/L_{UV} < 100$) similar to those that host most of the star formation in the local universe and to those that are detected in UV-selected high-redshift surveys. The brightness of the 850μm background is sometimes cited as evidence that most of the star formation in the universe occurred in dusty objects missing from UV-selected surveys, but this is a mistaken conclusion: the bright 850μm background shows only that a large fraction of star formation occurred in dusty objects, not that it occurred in the extremely dusty objects ($L_{\rm bol,dust} \gtrsim 100 L_{UV}$) that are easier to detect in the sub-mm than the far-UV. If we assumed that star formation at high redshift occurred only in known UV-selected populations and asked how dusty these galaxies would have to be to produce the observed 850μm background, we would find that the mean required extinction at 1600Å was a factor of ~ 6—precisely the value that is generally inferred for UV-selected galaxies at $z \sim 1$ and $z \sim 3$ and similar to the values observed in spirals and UV-selected starbursts at $z \sim 0$. The brightness of the 850μm background does not by itself require any star formation at all to have occurred in galaxies dustier than the moderately obscured ones ($1 < L_{\rm bol,dust}/L_{UV} < 100$) known to contain most of the star formation in the local universe.

This is not to say that extremely dusty galaxies ($L_{\rm bol,dust}/L_{UV} > 100$) do not exist. Some clearly do (e.g., Dey *et al.* 1999; BCR; Frayer *et al.* 2000). Part of the

far-IR background is produced by them. Our argument is simply that if high-redshift galaxies are similar to local galaxies in either their typical dust obscurations or their correlation of dust obscuration with luminosity, then UV-selected populations at high redshift must have contributed significantly to the 850μm background (see § 2.4.4). The fundamental difference between our analysis and the analyses of previous authors who reached opposite conclusions is the assumption made about the correlation between luminosity and dust obscuration. We have assumed that a correlation exists; they have assumed that it does not. The assumed existence of this correlation strongly affects the amount of high-redshift star-formation that is detectable in the optical, since it implies first that the $0.3 < f_\nu(850\mu\mathrm{m}) < 3\mathrm{mJy}$ sources which dominate the 850μm background are likely to be less obscured than the brighter sources detectable with SCUBA, and second that the dustiest, most rapidly star-forming galaxies at high redshift are not necessarily any harder to detect in the UV than the less obscured sources forming stars at more moderate rates. A correlation similar to the one we have assumed is known to exist in the local universe, and in § 2.4 we presented evidence that it exists at $z \sim 1$ and $z \sim 3$ as well. As illustrated by Figure 2.19, the high-redshift galaxies that have been detected by their dust emission are (with few exceptions) no fainter in the UV than the less obscured UV-selected galaxies at comparable redshifts.

Although we have argued that the majority of high-redshift star-formation is detected in UV-selected surveys, and that many of the recent results from far-IR/submm observations could have been predicted from UV observations alone (e.g., the brightness of the 850μm background, the shape of the 850μm number counts, the $\sim$ thousand-fold increase in the number density of ULIRGs at high redshift), we do not want to suggest that IR observations are unnecessary. Our arguments imply on the contrary that they are indispensable. Large corrections for dust extinction will be necessary in the interpretation of UV-selected surveys, and only IR observations

can show whether the currently adopted corrections are valid or suggest alternatives if they are not. And the fact remains that IR/sub-mm surveys are the most efficient way to find the extremely luminous and dusty galaxies known to produce at least 5% of the 850μm background.

It is commonly assumed that star formation at high redshift occurs in two distinct populations of galaxies, one relatively unaffected by dust and the other completely obscured. We favor a different view. High-redshift galaxies exhibit a continuum of dust properties. Some contain little dust, and some contain so much dust that they are nearly invisible in the optical; but the majority of star formation occurs in galaxies between these two extremes, in galaxies with $1 < L_{\rm bol,dust}/L_{UV} < 100$. The galaxies in this dominant population are undeniably dusty—most emit a larger fraction of their bolometric luminosities in the far-IR than in the far-UV—but with current technology they are easiest to detect in the rest-frame UV. Because in most cases only a small fraction of their luminosities emerge in the far-UV, large corrections for dust obscuration are required when estimating their star formation rates. A major purpose of this paper was to show that these corrections are tractable and produce sensible results. Although the validity of UV-derived dust corrections has not been convincingly demonstrated on an object-by-object basis, and further observations in the infrared are clearly required, our analysis suggests that the majority of high-redshift star formation occurs in objects which can at least be detected in existing UV-selected surveys. This is good news for those attempting to understand galaxy formation at high redshift, since it is likely that UV-selected surveys will continue to provide the most statistically robust information for at least the next decade.

Acosta-Pulido, J. A. *et al.* 1996, *Astron. Astrophys. Lett.*, **315**, 121.

Adelberger, K. L. 2000, in Clustering at High Redshifts, eds. A. Mazure, O. Le Fèvre, & V. Le Brun, *Astron. Soc. Pac. Conf. Ser.*, **200**, 13.

Aussel, H., Cesarsky, C. J., Elbaz, D., & Starck, J. L. 1999, *Astron. Astrophys.*, **342**, 313.

Barger, A. J., Cowie, L. L., Sanders, D. B., Fulton, E., Taniguchi, Y., Sato, Y., Kawara, K., & Okuda, H. 1998, *Nature*, **394**, 248.

Barger, A. J., Cowie, L. L., & Richards, E. A. 2000, *Astron. J.*, **119**, 2092 (BCR).

Barger, A. J., Cowie, L. L., & Sanders, D. B. 1999, *Astrophys. J. Lett.*, **518**, 5.

Barger, A. J., Cowie, L. L., Smail, I., Ivison, R. J., Blain, A. W., & Kneib, J.-P. 1999, *Astron. J.*, **117**, 2656.

Blain, A. W. & Longair, M. S. 1993, *Mon. Not. Roy. Astron. Soc.*, **264**, 509.

Blain, A. W. 1999, *Mon. Not. Roy. Astron. Soc.*, **309**, 955.

Blain, A. W., Smail, I., Ivison, R. J., & Kneib, J.-P. 1999a, *Mon. Not. Roy. Astron. Soc.*, **302**, 632.

Blain, A. W., Kneib, J.-P., Ivison, R. J., & Smail, I. 1999b, *Astrophys. J. Lett.*, **512**, 87.

Blain, A. W., Jameson, A., Smail, I., Longair, M., Kneib, J.-P., & Ivison, R. 1999c, *Mon. Not. Roy. Astron. Soc.*, **309**, 715.

Calzetti, D. 1997, *Astron. J.*, **113**, 162.

Calzetti, D., Armus, L., Bohlin, R. C., Kinney, A. L., Koornneeff, J., & Storchi-Bergmann, T. 2000, *Astrophys. J.*, **533**, 682.

Carilli, C. L. & Yun, M. S. 1999, *Astrophys. J. Lett.*, **513**, 13.

Carilli, C. L. & Yun, M. S. 2000, *Astrophys. J.*, **530**, 618.

Chapman, S., Scott, D., Steidel, C. C., Borys, C., Halpern, M., Morris, S. L., Adelberger, K. L., Dickinson, M., Giavalisco, M., & Pettini, M. 2000, *Mon. Not. Roy. Astron. Soc.*, **319**, 318.

Cohen, J., Hogg, D., Blandford, R., Cowie, L., Hu, E., Songaila, A., Shopbell, P., & Richberg, K. 2000, *Astrophys. J.*, **538**, 29.

Condon, J. J. 1992, *Ann. Rev. Astron. Astrophys.*, **30**, 575.

Cowie, L. L. & Barger, A. J. 2000, *Astron. Soc. Pac. Conf. Ser.*, **193**, 213.

Dey, A., Graham, J. R., Ivison, R. J., Smail, I., Wright, G. S., & Liu, M. C. 1999, *Astrophys. J.*, **519**, 610.

Dunne, L., Eales, S., Edmunds, M., Ivison, R., Alexander, P., & Clements, D. L. 2000, *Mon. Not. Roy. Astron. Soc.*, **315**, 115.

Eales, S., Lilly, S., Gear, W., Dunne, L., Bond, J. R., Hammer, F., Le Fèvre, O., & Crampton, D. 1999, *Astrophys. J.*, **515**, 518.

Edge, A. C., Ivison, R. J., Smail, I., Blain, A. W., & Kneib, J.-P., 1999, *Mon. Not. Roy. Astron. Soc.*, **306**, 599.

Fixsen, D. J., Dwek, E., Mather, J. C., Bennett, C. L., & Shafer, R. A. 1998, *Astrophys. J.*, **508**, 123.

Flores, H. *et al.* 1999, *Astrophys. J.*, **517**, 148.

Frayer, D. T., Ivison, R. J., Scoville, N. Z., Evans, A. S., Yun, M., Smail, I., Barger, A. J., Blain, A. W., & Kneib, J.-P. 1999, *Astrophys. J. Lett.*, **514**, 13.

Freedman, W. & Madore, B. 1988, *Astrophys. J. Lett.*, **332**, 63.

Genzel, R. *et al.* 1998, *Astrophys. J.*, **498**, 579.

Graham, J. R. & Dey, A. 1996, *Astrophys. J.*, **471**, 720.

Haynes, T. *et al.* 2002, *Mon. Not. Roy. Astron. Soc.*, submitted.

Heckman, T. 1998, *Astron. Soc. Pac. Conf. Ser.*, **148**, 127.

Helou, G., Khan, I. R., Malek, L., & Boehmer, L. 1988, *Astrophys. J. Suppl.*, **68**, 151.

Holland, W. S. *et al.* 1999, *Mon. Not. Roy. Astron. Soc.*, **303**, 659.

Hu, E. M. & Ridgway, S. E. 1994, *Astron. J.*, **107**, 1303.

Hughes, D. H., Gear, W. K., & Robson, E. I., 1990, *Mon. Not. Roy. Astron. Soc.*, **244**, 759.

Hughes, D. H. *et al.* 1998, *Nature*, **394**, 241.

Ivison, R. J. *et al.* 2000, *Mon. Not. Roy. Astron. Soc.*, **315**, 209.

Kells, W., Dressler, A., Sivaramakrishnan, A., Carr, D., Koch, E., Epps, H., Hilyard, D., & Pardeilhan, G. 1998, *Proc. Astron. Soc. Pac.*, **110**, 1489.

Klaas, U., Haas, M., Heinrichsen, I., & Schulz, B. 1997, *Astron. Astrophys. Lett.*, **325**, 21.

Lanzetta, K. M., Chen, H.-W., Fernandez-Soto, A., Pascarelle, S., Yahata, N., & Yahil, A., 1999, *Astron. Soc. Pac. Conf. Ser.*, **193**, 544.

Lawrence, A., Walker, D., Rowan-Robinson, M., Leech, K. J., & Penston, M. V. 1986, *Mon. Not. Roy. Astron. Soc.*, **219**, 687.

Lilly, S. J., Le Fèvre, O., Hammer, F., & Crampton, D. 1996, *Astrophys. J. Lett.*, **460**, 1.

Lisenfeld, U., Isaak, K. G., & Hills, R. 2000, *Mon. Not. Roy. Astron. Soc.*, **312**, 433.

Madau, P. 1995, *Astrophys. J.*, **441**, 18.

Madau, P., Ferguson, H. C., Dickinson, M. E., Giavalisco, M., Steidel, C. C., & Fruchter, A. 1996, *Mon. Not. Roy. Astron. Soc.*, **283**, 1388.

Matthews, K. & Soifer, B. T. 1994, in *Infrared Astronomy with Arrays* (Dordrecht: Kluwer, ed. I. McLean) 239.

Meurer, G. R., Heckman, T. M., & Calzetti, D. 1999, *Astrophys. J.*, **521**, 64 (MHC).

Oakes, D. 1982, *Biometrics*, **38**, 451.

Peacock, J. A. *et al.* 2000, *Mon. Not. Roy. Astron. Soc.*, **318**, 535p.

Pettini, M., Kellogg, M., Steidel, C. C., Dickinson, M., Adelberger, K. L., & Giavalisco, M. 1998, *Astrophys. J.*, **508**, 539.

Press, W. H., Flannery, B. P., Teukolsky, S. A., & Vetterling, W. T. 1992, in *Numerical Recipes in C* (Cambridge: Cambridge University Press.)

Richards, E. A. 2000, *Astrophys. J.*, **533**, 611.

Rifatto, A., Longo, G., & Capaccioli, M. 1995, *Astron. Astrophys. Suppl.*, **114**, 527.

Rigopoulou, D., Lawrence, A., & Rowan-Robinson, M. 1996, *Mon. Not. Roy. Astron.*

Soc., **278**, 1049.

Rigopoulou, D., Spoon, H. W. W., Genzel, R., Lutz, D., Moorwood, A. F. M., & Tran, Q. D. 1999, *Astron. J.*, **118**, 2625.

Sandage, A. & Bedke, J. 1994, in *The Carnegie Atlas of Galaxies* (Washington: The Carnegie Institution of Washington.)

Sanders, D. B., Scoville, N. Z., & Soifer, B. T. 1991, *Astrophys. J.*, **370**, 158.

Sanders, D. B. & Mirabel, I. F., 1996, *Ann. Rev. Astron. Astrophys.*, **34**, 749.

Sanders, D. B. 1999, *Astrophys. Spac. Sci.*, **269**, 381.

Smail, I., Ivison, R. J., & Blain, A. W. 1997, *Astrophys. J. Lett.*, **490**, 5.

Smail, I., Ivison, R. J., Blain, A. W., & Kneib, J.-P., 1998, *Astrophys. J. Lett.*, **507**, 21.

Smail, I., Ivison, R. J., Kneib, J.-P., Cowie, L. L., Barger, A. J., Owen, F. N., & Morrison, G. 1999, *Mon. Not. Roy. Astron. Soc.*, **308**, 1061.

Soifer, B. T., Sanders, D. B., Madore, B. F., Neugebauer, G., Danielson, G. E., Elias, J. H., Lonsdale, C. J., & Rice, W. L. 1987, *Astrophys. J.*, **320**, 238.

Steidel, C. C., Adelberger, K. L., Giavalisco, M., Dickinson, M., & Pettini, M. 1999, *Astrophys. J.*, **519**, 1.

Steidel, C. C., Pettini, M., & Hamilton, D. 1995, *Astron. J.*, **110**, 2519.

Steidel, C. C. & Hamilton, D. 1993, *Astron. J.*, **105**, 2017.

Tan, J. C., Silk, J., & Balland, C. 1999, *Astrophys. J.*, **522**, 579.

Trentham, N., Blain, A. W., & Goldader, J. 1999, *Mon. Not. Roy. Astron. Soc.*, **305**, 61.

Trentham, N., Kormendy, J., & Sanders, D. B. 1999, *Astron. J.*, **117**, 2152.

Xu, C. *et al.* 1998, *Astrophys. J.*, **508**, 576.

Chapter 3

A Counts-in-cells Analysis of Lyman-break Galaxies at Redshift $z \sim 3$[1]

Abstract

We have measured the counts-in-cells fluctuations of 268 Lyman-break galaxies with spectroscopic redshifts in six $9' \times 9'$ fields at $z \sim 3$. The variance of galaxy counts in cubes of comoving side length 7.7, 11.9, 11.4 h_{100}^{-1} Mpc is $\sigma^2_{\rm gal} \sim 1.3 \pm 0.4$ for $\Omega_M = 1$, 0.2 open, 0.3 flat, implying a bias on these scales of $\sigma_{\rm gal}/\sigma_{\rm mass} = 6.0 \pm 1.1$, 1.9 ± 0.4, 4.0 ± 0.7. The bias and abundance of Lyman-break galaxies are surprisingly consistent with a simple model of structure formation which assumes only that galaxies form within dark matter halos, that Lyman-break galaxies' rest-UV luminosities are tightly correlated with their dark masses, and that matter fluctuations are Gaussian and have a linear power-spectrum shape at $z \sim 3$ similar to that determined locally ($\Gamma \sim 0.2$). This conclusion is largely independent of cosmology or spectral normalization σ_8. A measurement of the masses

[1]Previously published as Adelberger, Steidel, Giavalisco, Dickinson, Pettini, & Kellogg, 1998, Astrophys. J., 505, 18

of Lyman-break galaxies would in principle distinguish between different cosmological scenarios.

3.1 Introduction

Much of observational cosmology depends upon the assumption that the spatial distribution of galaxies is related in a simple way to the underlying distribution of matter. At first it was hoped that the galaxy distribution might simply be a Poisson realization of the matter distribution; but as this model became difficult to reconcile with large scale peculiar velocities, the amplitude of microwave background fluctuations, the different clustering strengths of different galaxy types, and theoretical prejudice for $\Omega_M = 1$, cosmologists began to assume an unspecified constant of proportionality b between galaxy and mass fluctuations: $\delta_{\rm gal} = b\delta_{\rm mass}$. Though many physical processes could in principle give rise to a relationship of this form (e.g., Dekel & Rees 1987), most were poorly understood, and, if invoked, would make it difficult to use galaxy observations to constrain the cosmological mass distribution. An important exception was gravitational instability. This is relatively well understood, and if it were dominant in determining where galaxies formed—if galaxies formed within virialized "halos" of dark matter, and if the poorly understood physics of star formation, supernova feedback, and so on were important only in determining the properties of galaxies within dark matter halos—then the large scale distribution of galaxies would still be related in a simple way to the underlying distribution of matter; the value of the "bias parameter" b in $\delta_{\rm gal} = b\delta_{\rm mass}$ would be straightforward to calculate (White & Rees 1978, Kaiser 1984, Bardeen *et al.* 1986, Mo & White 1996). Because it maintains a simple relationship between galaxies and mass, agrees with our limited knowledge of the relevant physics, and seems consistent with numerical simulations, this "dark halo" model has become increasingly popular, and is now the basis of the modern

understanding of galaxy formation. It is assumed in most analytic treatments, in semi-analytic models, and in numerical simulations which include only gravity; and yet it remains a conjecture that has never been thoroughly tested. One prediction of the dark halo model is that galaxies of a given mass should form first in regions where the density is highest, and since such regions are expected to be strongly clustered (e.g., Kaiser 1984), a natural test is to measure the clustering of galaxies in the young universe.

The Lyman-break technique (e.g., Steidel, Pettini, & Hamilton 1995) provides a way to find large numbers of star-forming galaxies at $z \sim 3$. Star-forming galaxies have pronounced breaks in their spectra at 912 Å (rest) from a combination of absorption by neutral hydrogen in their interstellar media and the intrinsic spectra of massive stars. At $z \gtrsim 3$ this "Lyman break," strengthened from additional absorption by hydrogen in the unevolved intergalactic medium, is redshifted sufficiently to be observed with ground-based broadband photometry. By taking images through filters that straddle the redshifted Lyman break, and looking for objects that are much fainter in images at wavelengths shortward of the break than longward of the break, one can efficiently separate high-redshift galaxies from the many foreground objects. In our implementation of the technique, we have used deep photometry in the custom U_n, G, $\mathcal{R}$ filter system of Steidel & Hamilton (1993) to assemble a sample of over 1300 probable $z \sim 3$ galaxies, of which more than 400 have been spectroscopically confirmed with the Low-Resolution Imaging Spectrograph (Oke *et al.* 1995) on the W. M. Keck telescopes.

After initial spectroscopy in one $9' \times 18'$ field, we argued, on the basis of a single large concentration of galaxies, that these $z \sim 3$ Lyman-break galaxies were much more strongly clustered than the mass, with an inferred bias parameter $b \equiv \sigma_{\rm gal}/\sigma_{\rm mass}$ of $b \gtrsim 6$, 2, 4 for $\Omega_M = 1$, 0.2 open, and 0.3 flat (Steidel *et al.* 1998a). Qualitatively this strong biasing was consistent with the idea that galaxies form first in the (strongly

clustered) densest regions of the universe, but there appeared to be quantitative problems. In the dark matter halo model there is an inverse relationship between the abundance and bias of a population of halos, with the rarest, most massive halos being the most strongly clustered (i.e., most "biased"). As emphasized by Jing & Suto (1998), for halos to be as strongly clustered as Lyman-break galaxies, they would have to be very rare indeed. Yet Lyman-break galaxies are not that rare; for $\Omega_M = 1$ their comoving number density to $\mathcal{R} = 25.5$ is $n \gtrsim 8 \times 10^{-3}$ per h_{100}^{-3} Mpc^3, comparable to the number density of L_* galaxies today. As we will see below, in standard ($\Omega_M = 1$, $\sigma_8 = 0.6$, $\Gamma = 0.50$) CDM, halos at $z \sim 3$ with the same abundance as observed Lyman-break galaxies have a bias of $b \sim 4$, substantially lower than the implied galaxy bias. For $\Omega_M < 1$ the disagreement is less severe, because both the estimated bias and the comoving abundance of observed Lyman-break galaxies are lower. It appeared then from preliminary analyses that our data were consistent with the dark halo model only for $\Omega_M < 1$; but it was unclear how seriously to take conclusions based on a single feature in a single field. Moreover other authors soon analyzed the overdensity differently and argued that it was consistent with models in which galaxies are significantly less clustered than we claimed, with b low enough to remove the inconsistencies with the abundances for $\Omega_M = 1$ (e.g., Bagla 1997, Governato *et al.* 1998, Wechsler *et al.* 1998).

In this paper we present a counts-in-cell analysis of the clustering of 268 Lyman-break galaxies (all with spectroscopic redshifts) in six $9' \times 9'$ fields. This sample contains four times as many galaxies over an area three times as large as our original analysis. Since in addition it takes into account all galaxy fluctuations in the data, and not just a single over-density, one might hope it would provide a more definitive measurement of the strength of clustering.

3.2 Data

Many relevant details of our survey for Lyman-break galaxies are presented elsewhere (Steidel *et al.* 1996, Giavalisco *et al.* 1998a, Steidel *et al.* 1998a, Steidel *et al.* 1998b), and in this section we give only a brief review. We initially identify $z \sim 3$ galaxy candidates in deep U_n, G, $\mathcal{R}$ images taken (primarily) at the Palomar 5m Hale telescope with the COSMIC prime focus camera. In images of our typical depths (1σ surface brightness limits of 29.1, 29.2, 28.6 AB magnitudes per arcsec^2 in U_n,G, and $\mathcal{R}$) approximately 1.25 objects per arcmin^2 meet our current selection criteria of

$$\mathcal{R} \leq 25.5, \quad G - \mathcal{R} \leq 1.2, \quad U_n - G \geq G - \mathcal{R} + 1, \quad U_n - G \geq 1.6.$$

A subset of these photometric candidates is subsequently observed spectroscopically at the W. M. Keck telescope through multislit masks which accommodate $\sim$ 20 objects each. To date we have obtained spectra of 540 objects satisfying the above photometric criteria; 376 of these have been identified as galaxies (of which a very small fraction show evidence of AGN activity), with a redshift distribution shown in Figure 3.1; 18 are stars; and the remainder have not been identified because of inadequate signal to noise ratio. In this paper we restrict our analysis to the 268 Lyman-break galaxies in our six most densely sampled $\sim 9' \times 9'$ fields, including more complete data in the "SSA22" field analyzed in Steidel *et al.* 1998a. The redshift histograms of these six fields are shown in Figure 3.2; each field is treated independently in the analysis that follows, although in two cases (SSA22 and DSF2237) pairs of $9'$ fields are adjacent on the plane of the sky.

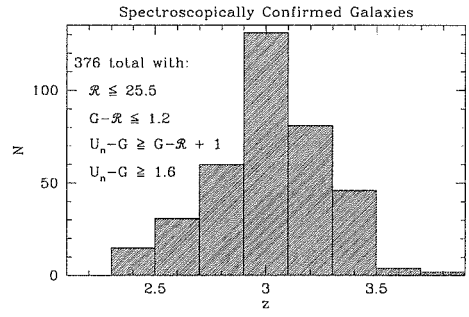

Figure 3.1 The redshift distribution of objects satisfying the Lyman-break criteria adopted in this letter. Only the 70% of candidates that have been confirmed to be galaxies are shown; 25% of our spectroscopic sample has not been identified because of low signal-to-noise ratio, and 5% of our objects are stars.

3.3 Statistical analysis

The strength of clustering can be estimated by placing galaxies into spatial bins ("cells") and looking at the fluctuations in galaxy counts from cell to cell. A convenient measure of the clustering strength is

$$\sigma^2_{\rm gal} \equiv \frac{1}{V^2_{\rm cell}} \int \int_{V_{\rm cell}} dV_1 dV_2 \xi_g(r_{12})$$

where $\xi_g(r)$ is the galaxies' two-point correlation function. If there were large numbers of galaxies in each cell, so that shot noise were negligible, $\sigma^2_{\rm gal}$ would just be equal to the relative variance of galaxy counts in cells of volume $V_{\rm cell}$: $\sigma^2_{\rm gal} =< (N-\mu)^2 > /\mu^2$, where N is the observed and μ the mean number of galaxies in a cell. In practice shot noise makes a significant contribution to the variance of cell counts, and this contribution must be removed to estimate $\sigma^2_{\rm gal}$:

$$\sigma^2_{\rm gal} = (< (N-\mu)^2 > -\mu)/\mu^2$$

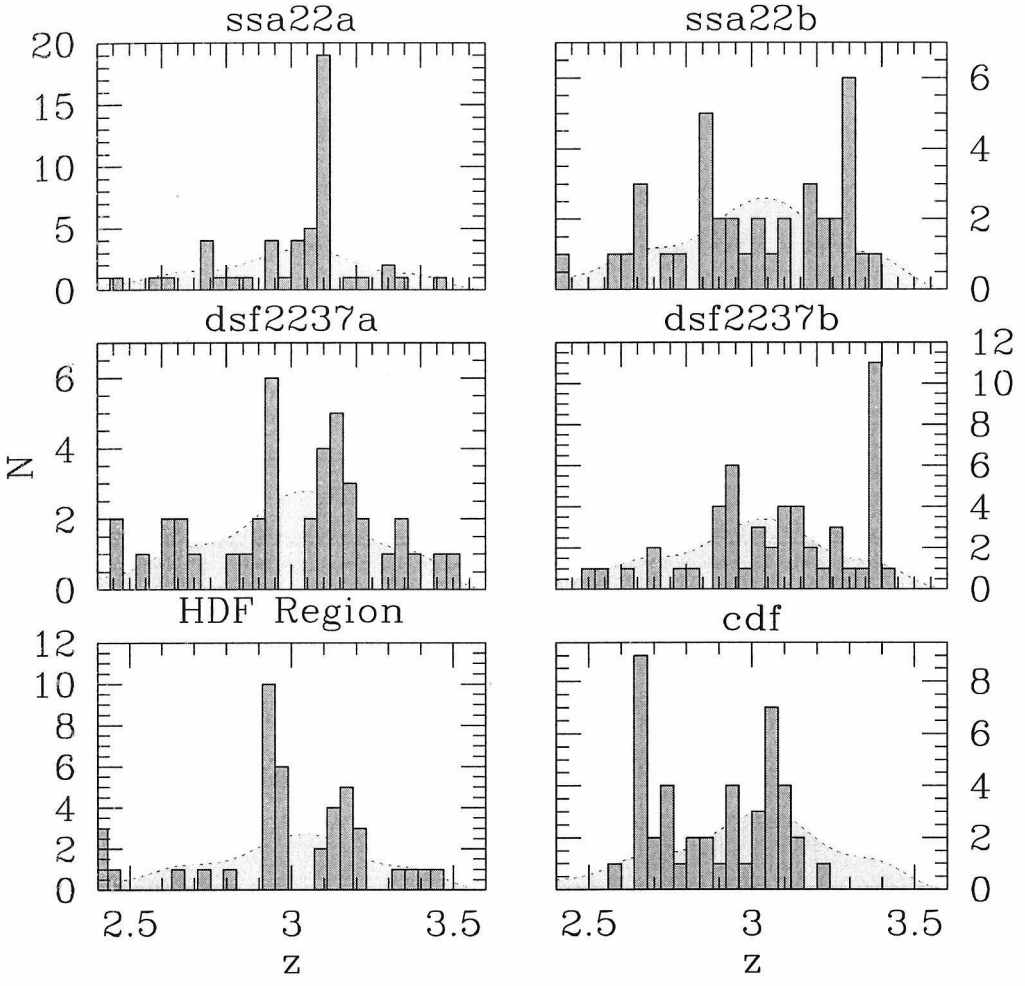

Figure 3.2 Redshift distributions in the six fields. The smooth curve is our estimated selection function, produced by fitting a spline to the coarsely binned redshifts of all candidates matching our selection criteria. The superimposed histograms are the measured redshifts in each field. The actual binning used in our analysis is somewhat different from the binning presented here. The average number of redshifts per field is about 44, with field to field variations due mainly to different levels of spectroscopic completeness.

(Peebles 1980, §36). For any cell the expected number of galaxies can be estimated accurately as $\mu \simeq N_{\rm tot}\phi(z)\Delta z$, where $\phi(z)$ is our selection function, determined by

fitting a spline to the coarsely binned redshifts of all $\sim$ 400 Lyman-break galaxies which satisfy our current color criteria and have redshifts, and $N_{\rm tot}$ is the number of galaxies in the field with redshifts. ($N_{\rm tot}$ varies from field to field because of differing spectroscopic completeness.) In general the uncertainty in cell count N will dominate the uncertainty in μ. If we neglect the relatively small uncertainty in μ, we can estimate $\sigma^2_{\rm gal}$ from the number of counts N in a single cell as

$$\mathcal{S} = ((N-\mu)^2 - \mu)/\mu^2.$$

If μ were perfectly known, $\mathcal{S}$ would have expectation value $<\mathcal{S}>=\sigma^2_{\rm gal}$ and variance

$$<\mathcal{S}^2> - <\mathcal{S}>^2 = 2\sigma^4_{\rm gal} + 4\sigma^2_{\rm gal}/\mu + (2+7\sigma^2_{\rm gal})/\mu^2 + 1/\mu^3 \qquad (3.1)$$

where we have used results in Peebles (1980, §36) and neglected the integrals over the three- and four-point correlation functions. In fact $\mathcal{S}$ will be a slightly biased estimator of $\sigma^2_{\rm gal}$, since our estimate of μ depends weakly on N (through its contribution to $N_{\rm tot}$), but this bias should be small compared to the variance--which is itself only approximately equal to the RHS of equation 3.1. With $\mathcal{S}$ we can estimate $\sigma^2_{\rm gal}$ from the observed number of counts in a single cell; by combining the estimates $\mathcal{S}$ from every cell in our data with inverse-variance weighting, we arrive at our best estimate of $\sigma^2_{\rm gal}$. (The variance depends on the unknown $\sigma^2_{\rm gal}$, of course, but the answer converges with a small number of iterations.)

Placing our counts into a dense grid of roughly cubical cells whose transverse size is equal to the field of view ($\sim 9'$), we estimate $\sigma^2_{\rm gal} = 1.3 \pm 0.4$ in cells of approximate length 7.7, 11.9, 11.4 h^{-1}_{100} Mpc for $\Omega_M = 1$, 0.2 open, 0.3 flat. The uncertainty is the standard deviation of the mean of $\mathcal{S}$ estimated in the fields individually.

This approach with the estimator $\mathcal{S}$ has the advantage of being relatively model independent, but statisticians have long argued that an optimal data analysis must use the likelihood function (e.g., Birnbaum 1962). If we had a plausible model for

the probability density function (PDF) of galaxy fluctuations $P(\delta_{\rm gal}|\sigma^2_{\rm gal})$, we might hope to produce a better estimate of $\sigma^2_{\rm gal}$ by finding the value that maximizes the likelihood of the data. An exact expression for the galaxy PDF has not been found, but it should be sufficient to use a reasonable approximation. The main requirement for this approximate PDF is that it be skewed, since a galaxy fluctuation $\delta_{\rm gal} \equiv (\rho_{\rm gal} - \bar{\rho}_{\rm gal})/\bar{\rho}_{\rm gal}$ can be arbitrarily large but cannot be less than -1. A particularly simple distribution with the necessary skew, the lognormal, provides a good fit to the PDF of mass fluctuations and of linearly biased galaxies in N-body simulations (e.g., Coles & Jones 1991, Coles & Frenk 1991, Kofman *et al.* 1994). The lognormal probability of observing a galaxy fluctuation $\delta_{\rm gal}$ given $\sigma^2_{\rm gal}$ is

$$P_{LN}(\delta_{\rm gal}|\sigma^2_{\rm gal}) = \frac{1}{2\pi x}\exp\left[-\frac{1}{2}\left(\frac{\log(1+\delta_{\rm gal})}{x}+\frac{x}{2}\right)^2\right]$$

where $x \equiv \sqrt{\log(1+\sigma^2_{\rm gal})}$, and so in this model, assuming Poisson sampling, the likelihood of observing N galaxies in a cell when μ are expected is

$$P(N|\mu\sigma^2_{\rm gal}) = \int_{-1}^{\infty} d\delta_{\rm gal} P_{LN}(\delta_{\rm gal}|\sigma^2_{\rm gal})\exp[-(1+\delta_{\rm gal})N](1+\delta_{\rm gal})^N\mu^N/N!.$$

The analytical solution to this integral is unknown, but it presents no numerical challenge. If the cells are large enough to be nearly uncorrelated, we can find the maximum likelihood value of $\sigma^2_{\rm gal}$ by maximizing the product of the likelihoods from individual cells. Figure 3.3 shows the product of the likelihoods for $\sigma^2_{\rm gal}$ from all cells in all six fields for $\Omega_M = 1$. The plots for $\Omega_M = 0.2$ open and $\Omega_M = 0.3$ flat are similar, with small differences arising because our desire for cubical cells forces us to use different redshift binning for different cosmologies. For each cosmology the overall maximum likelihood value is close to $\sigma^2_{\rm gal} \sim 1.3$; the 68.3% credible intervals are 0.8 to 1.6, 0.7 to 1.4, and 1.1 to 2.1 for $\Omega_M = 1$, $\Omega_M = 0.2$ open, and $\Omega_M = 0.3$ flat, in reasonable agreement with our estimate from $\mathcal{S}$.[2] We will take the maximum likelihood estimates as our best estimates of $\sigma^2_{\rm gal}$ hereafter.

[2]This approach to estimating $\sigma^2_{\rm gal}$ is very similar to that of Peacock (1999).

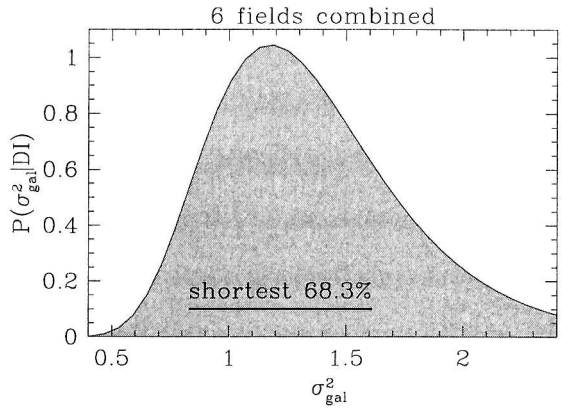

Figure 3.3 The posterior probability of our data as a function of clustering strength $\sigma^2_{\rm gal}$. A uniform prior in $\sigma^2_{\rm gal}$ is assumed, and the shortest 68% credible interval is shown.

A more common measure of the clustering strength is the characteristic length r_0 in a correlation function of assumed form $\xi_g(r) = (r/r_0)^{-\gamma}$. For spherical cells r_0 and $\sigma^2_{\rm gal}$ are related through $\sigma^2_{\rm gal} = 72(r_0/R_{\rm cell})^\gamma/[(3-\gamma)(4-\gamma)(6-\gamma)2^\gamma]$ (Peebles 1980 §59), and so approximating our cubical cells as spheres with equal volume, and assuming $\gamma = 1.8$, we arrive at a rough estimate of $r_0 \simeq 4 \pm 1$, 5 ± 1, 6 ± 1 comoving h_{100}^{-1} Mpc for $\Omega_M = 1$, 0.2 open, 0.3 flat. These values are large, comparable to the correlation lengths of massive galaxies today.

The correlation lengths for $\Omega_M = 1$ and $\Omega_M = 0.2$ open are larger, by about 2σ, than those recently derived by Giavalisco *et al.* (1998a, "G98a" hereafter) from the angular clustering of Lyman-break galaxies. This discrepancy could be resolved in several ways. The correlation lengths would agree at the 1σ level if a large fraction of the objects whose spectra we cannot identify (about 25% of the spectroscopic sample) were lower redshift interlopers diluting the angular clustering signal. The discrepancy would also be reduced if γ were larger than 1.8, although γ would have to

be equal to ~ 2.6, contradicting the results of G98a, to make the correlation lengths agree at the 1σ level. Because the spectroscopic subsample is somewhat brighter than the sample as a whole, one would expect (from arguments we develop below) the galaxies analyzed here to be somewhat more strongly clustered than those analyzed in G98a, but this would change r_0 by only $\sim$ 10-20% (these numbers follow from the formalism presented below, and will be explained more fully in Giavalisco *et al.* (1998b)). Inferring r_0 from observed angular clustering depends upon the assumed cosmological geometry, because (for example) projection effects must be corrected, and an intriguing possibility is that the correlation lengths disagree because G98a assumed an incorrect geometry when deriving r_0 from the angular clustering. According to G98a, the quantity $A^{1/\gamma}$ (for a correlation function of the assumed form $\omega(\theta) = A\theta^{1-\gamma}$) is well constrained by their observations. If we take $A^{1/\gamma}$ and $\sigma^2_{\rm gal}$ as two cosmology-independent parameters fixed by observation (which is not quite true; see above), then the correlation length derived from $\omega(\theta)$ scales with cosmological parameters roughly as $r_{0,\omega} \propto (g(\bar{z})/f^{1-\gamma}(\bar{z}))^{1/\gamma}$, where $g \equiv dl/dz$ is the change in proper distance with redshift and f is the angular diameter distance, while the correlation length derived from $\sigma^2_{\rm gal}$ roughly obeys $r_{0,\sigma^2} \propto f(\bar{z})$. The ratio of these correlation lengths therefore depends on the geometry as $r_{0,\omega}/r_{0,\sigma^2} \propto (g/f)^{1/\gamma}$, and so if we assume $f = f_f$ and $g = g_f$ when the correct values are $f = f_t$ and $g = g_t$, we will find correlation lengths from counts-in-cell and $\omega(\theta)$ analyses which differ by a factor $\eta \equiv r_{0,\omega}/r_{0,\sigma^2} = (f_t g_f / f_f g_t)^{1/\gamma}$. For $\gamma = 1.8$ in an $\Omega_M = 0.2$ flat cosmology, we would find $\eta = 0.88$ if we mistakenly assumed $\Omega_M = 0.2$ open, and $\eta = 0.84$ if we assumed $\Omega_M = 1$. This does not go far towards reconciling the discrepant correlation lengths, but it does suggest an interesting variant of Alcock & Paczynski's (1979) classic cosmological test. Finally, G98a found differences of 30% in r_0 when measuring the angular clustering with different estimators, and this implies that the systematics in that sample may not be fully understood. While these effects taken

together could easily reconcile the results presented here with those of G98a, the differences are significant and will likely only be convincingly resolved by better data. Because the largest corrections we have proposed apply to the estimates of r_0 from angular clustering, we will take the counts-in-cell result as our best estimate of the clustering strength in our subsequent discussion.

3.4 The bias and abundance of Lyman-break galaxies

A large bias for high-redshift galaxies is a prediction of models that associate galaxies with virialized dark matter halos (e.g., Cole & Kaiser 1989), and on the face of it the strong clustering of Lyman-break galaxies seems a significant success for them. But these models explain strong clustering by associating high-redshift galaxies with rare events in the underlying Lagrangian density field, and would be ruled out if Lyman-break galaxies were too common to be so strongly clustered. In this section we examine the consistency of clustering strength and abundance in more detail; but before we can do so we need to estimate the Lyman-break galaxies' bias. Our definition of bias is the ratio of rms galaxy fluctuation to rms mass fluctuation in cells of our chosen size: $b \equiv \sigma_{\rm gal}/\sigma_{\rm mass}$. The mean square mass fluctuation in a cell at $z \sim 3$ can be calculated with a numerical integration: $\sigma^2_{\rm mass} = (2\pi)^{-3} \int d^3k |\delta_k|^2 |W_k|^2$ (e.g., Padmanabhan 1993), where W_k is the Fourier transform of the cell volume and $|\delta_k|^2$ is the power-spectrum of density fluctuations. By most accounts the shape of the power-spectrum is close to that of a CDM-like model with "shape parameter" $\Gamma \sim 0.2$ (Vogeley *et al.* 1992, Peacock & Dodds 1994, Maddox *et al.* 1996; we use Bardeen *et al.* 1986 equations G2 and G3 with $q = k/\Gamma h$ and an $n = 1$ long-wavelength limit as an approximation to the spectral shape). The normalization of the power-spectrum

can be determined at $z = 0$ from the abundance of X-ray clusters, and on large scales of interest here can be reliably extrapolated back to $z = 3$ with linear theory.

One complication prevents us from simply dividing our measured $\sigma_{\rm gal}$ by the calculated $\sigma_{\rm mass}$ to estimate the bias: we have measured the relative variance of galaxy counts in cells defined in redshift space, and this variance is boosted relative to the real-space galaxy variance of interest by coherent infall towards overdensities, and reduced by redshift measurement errors.[3] Both effects must be corrected before we can estimate the bias. Fortunately, neither effect is large for highly biased galaxies in cells of this size, and the correction is straightforward. Following Peacock & Dodds (1994), we estimate b by numerically inverting

$$\sigma^2_{\rm gal} = \frac{b^2}{(2\pi)^3} \int d^3k |\delta_k|^2 |W_k|^2 (1 + f k_z^2/k^2 b)^2 \exp(-k_z^2 \sigma_v^2)$$

where $f \simeq \Omega_M^{0.6}(z)$ and $\sigma_v \simeq 300 \frac{\rm km}{\rm s}(1+z)/H(z)$ is the adopted uncertainty in a galaxy's position from redshift measurement errors (see Steidel *et al.* 1998a). This expression is a modified version of the usual integral relationship between the variance and the power-spectrum; the factor of $1 + f k_z^2/k^2 b$ in the integrand accounts for the increase in redshift-space power (relative to real-space power) due to coherent infall (e.g., Kaiser 1987), and the Gaussian models our redshift uncertainties. Corrections for the non-linear growth of perturbations on scales much smaller than our cell (described, for example, in the same Peacock & Dodds reference) have been neglected. The results of this bias calculation are shown in Figure 3.4. With $\Gamma = 0.2$ we find $b = 6.0 \pm 1.1$, 1.9 ± 0.4, and 4.0 ± 0.7 for $\Omega_M = 1$, 0.2 open, and 0.3 flat. This estimate of the bias is inversely proportional to the somewhat-uncertain power-spectrum normalization σ_8; for concreteness we have chosen $\sigma_8 = 0.5$, 1.0, 0.9 for $\Omega_M = 1$, 0.2 open,

[3] We are assuming that these errors dominate the pair-wise velocity dispersion ("finger of god" effect). A large pairwise velocity dispersion decreases the size of redshift-space fluctuations for a fixed size of real-space fluctuations, and so by neglecting the dispersion we will underestimate the bias. But the effect is not large; the pairwise velocity dispersion would have to be ~ 800 km/s to change our estimated bias by 1σ.

and 0.3 flat, close to the cluster normalization of Eke, Cole, & Frenk (1996), but our most important conclusions below, about the bias/abundance relationship, are insensitive to the normalization. Varying the spectral shape over the plausible range $\Gamma = 0.1$–0.5 changes our estimate of the bias by about $\pm$ 10% for $\Omega_M = 1$ and by a negligible amount for the other cosmologies (see figure 3.4), assuming the Γ dependence of σ_8 is negligible (e.g., White, Efstathiou, & Frenk 1993).

We can test the idea that Lyman-break galaxies form within dark matter halos by comparing their inferred bias to the predicted bias of dark matter halos with similar abundance. Simple statistical arguments (e.g., Kaiser 1984, Mo & White 1996) show that the main factor controlling the clustering strength of a population of halos with mass M is their "rareness" $\nu \equiv \delta_c/\sigma(M)$, where $\sigma(M)$ is the rms relative mass fluctuation in the density field smoothed by a spherical top-hat enclosing average mass M, and $\delta_c \simeq 1.7$ is the linear overdensity corresponding to spherical collapse. To first order,

$$b \simeq 1 + (\nu^2 - 1)/\delta_c \tag{3.2}$$

(Mo & White 1996). The abundance of these same halos is approximately given by the Press-Schechter (1974) formula

$$n(\nu)d\nu = \frac{\bar{\rho}}{M(\nu,\Gamma)}\sqrt{\frac{2}{\pi}}\exp(-\nu^2/2)d\nu \tag{3.3}$$

where we have written the halo mass as $M(\nu,\Gamma)$ to emphasize that it depends upon both the halos' rareness and the shape of the matter power-spectrum, as discussed below. This relation is easy to understand: $\bar{\rho}/M$ is the maximum possible number density of collapsed objects on mass scale M, given the finite average density of the universe $\bar{\rho}$, and $\sqrt{2/\pi}\exp(-\nu^2/2)$—which follows from the assumed Gaussian distribution of the linear density field—is the fraction of this maximum number that has just reached the threshold for collapse. From the Press-Schechter formula is it clear that the clustering strength of a population of given abundance will depend upon

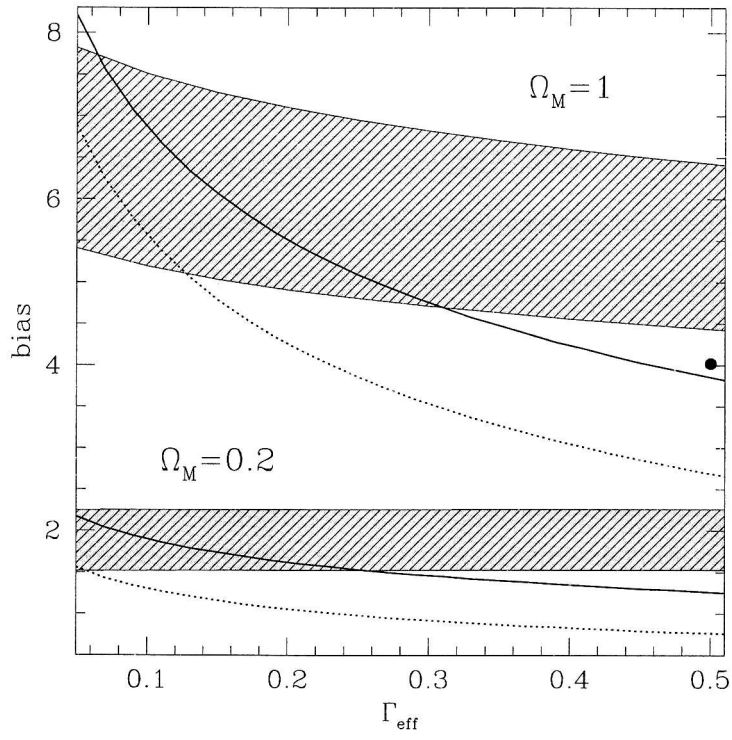

Figure 3.4 The spectrum-dependence of bias for objects of fixed abundance. Rarer (high-ν) halos are more strongly clustered, but the details of the bias–abundance relationship depend upon the fluctuation power-spectrum. Spectra with more small scale power (higher Γ) have a lower bias for objects of given abundance. The solid curves show the predicted bias of dark halos as abundant as Lyman-break galaxies, and the dotted lines show the bias for halos ten times more abundant. Our 68% credible intervals on the bias are shaded. The results for $\Omega = 0.3$ flat, discussed in the text, have been suppressed for clarity. The observations are consistent with all cosmologies considered ($\Omega_M = 1$, 0.2 open, 0.3 flat) if the spectral shape Γ is treated as a free parameter, though the preferred values $\Gamma \lesssim 0.3$ arise more naturally if $\Omega_M < 1$. Standard CDM, with $\Omega_M = 1$ and $\Gamma = 0.5$, seems to disagree with our data at about the 2σ level—but this is hardly the worst of its problems. The analytic approximations used are rather crude, and the point to the right of the plot, drawn from the $\Gamma = 0.5, \Omega_M = 1$ N-body simulation of Jing & Suto (1998), gives some idea of their reliability. The N-body estimate of the bias has been scaled to the values of σ_8 we adopt ($\sigma_8 = 0.5$ for $\Omega_M = 1$, $\sigma_8 = 1$ for $\Omega_M = 0.2$).

the shape of the power-spectrum: if the fluctuation spectrum has more small-scale power, then the process of collapse will have advanced to larger mass scales, $\bar{\rho}/M$ will be smaller, and ν (and therefore b, by equation 3.2) will also have to be smaller to

match the observed abundance.

If we were free to specify the shape of the fluctuation spectrum, then we could (almost) always argue that our observation of a galaxy population with abundance n and bias b was consistent with the idea that galaxies form within dark matter halos, by simply adjusting the level of small-scale power until halos of abundance n were predicted to have bias b;[4] but if we restrict ourselves to spectral shapes that are not grossly inconsistent with local constraints, we find what is summarized in Figure 3.4.

Figure 3.4 shows the linear bias (equation 3.2) as a function of spectral shape Γ for dark halos with abundance equal to the observed abundance of Lyman-break galaxies.[5] Decreasing the amount of small scale power (i.e., decreasing Γ) increases the predicted bias of these halos; the inferred bias of Lyman-break galaxies begins to match the predicted bias of dark halos at $\Gamma \sim 0.2$, the locally favored spectral shape, as would be expected if these galaxies formed within the most massive dark matter halos at $z \sim 3$. At $\Gamma = 0.2$ the number density of Lyman-break galaxies implies typical masses of 6×10^{10}, 1.4×10^{12}, $8 \times 10^{11} h_{100}^{-1} M_{\odot}$ for $\Omega_M = 1$, $\Omega_M = 0.2$ open, and $\Omega_M = 0.3$ flat. Though (in the dark-halo model) measuring the number density and bias of a population of objects reveals little about cosmology other than the shape of the power-spectrum, measuring in addition the *masses* of the objects pins down the spectral normalization and provides a sensitive cosmological probe. Limited

[4]Varying the *normalization* of the power-spectrum changes our inferred bias and the theoretical bias of the dark halos by almost the same factor, and therefore has little effect on the consistency of our observations with the dark halo model. This means that our conclusions will not be very sensitive to the assumed cosmological model, as Figure 3.4 shows.

[5]The bias of a population of halos depends upon its mass distribution, since more massive halos are more strongly clustered than less massive halos. We do not know this distribution for Lyman-break galaxies. If we assumed the Lyman-break technique detected one galaxy in each halo more massive than some limit M_0, and no galaxies in halos less massive, we could determine M_0 from the abundance of the galaxies by integrating the Press-Schechter formula (equation 3.3). In fact, the technique is likely to find galaxies in halos less massive than M_0 as well as in halos more massive, and so M_0 defined this way is perhaps close to the typical halo mass. The bias shown in Figure 3.4 is for halos of mass M_0, and as such is only an approximation to the bias of the observed population. A more sophisticated treatment will be presented elsewhere.

near-infrared spectroscopy on Lyman-break galaxies (Pettini *et al.* 1998) has so far placed only weak constraints on their masses; we look forward to the availability of near-IR spectrographs on 8m-class telescopes.

If it is in fact true that Lyman-break galaxies form within dark halos, then other conclusions follow from the data. For example, we have assumed so far that Lyman-break galaxies—the brightest $z \sim 3$ galaxies in the rest UV—reside only within the most massive dark halos, but this need not be true; it is easy to imagine that the galaxies brightest in the UV are those with the least dust, or with the most recent burst of star formation, and that halo mass is only a secondary consideration. In this case there could be a large spread in the UV luminosities of galaxies within halos of a given mass. Because low-mass halos are so much more numerous than high-mass halos, if the spread were large enough our observed sample would be dominated by low-mass halos which happened to be UV bright. The strong clustering we observe shows that there cannot be a large population of low-mass (and thus weakly clustered) interlopers in our sample, and this limits the allowed spread in UV luminosities for halos of a given mass. The dotted lines in Figure 3.4, showing the bias of halos ten times more abundant than Lyman-break galaxies, illustrate the point. These halos have masses only 4, 8, 5 times lower than halos as abundant as Lyman-break galaxies for $\Omega_M = 1$, 0.2 open, 0.3 flat, but if even 10% of them contained galaxies bright enough to be included in our sample, the clustering strength would be diluted to well below what we observe. The implication is that lower mass halos are fainter in the UV not just on average, but (nearly) on a halo-by-halo basis. If Lyman break galaxies really were sub-galactic fragments, rapidly fading after bursts of star formation triggered by chance interactions with other fragments (e.g., Lowenthal *et al.* 1997), one might not expect so tight a correlation between UV luminosity and dark

halo mass. Similar arguments can be used to undermine the claim that the Lyman-break technique misses a large fraction of the galaxies in massive halos at $z \sim 3$.[6] The uncertainty in the bias is still large, and our analytic approximations rather crude, so it would be premature to make too much of arguments such as these; but they show the kind of conclusions that can be drawn from our sample in the context of the dark halo model. These ideas will be developed further elsewhere (Adelberger *et al.* 1998).

3.5 Summary

We have estimated the variance of Lyman-break galaxy counts in cubes of side length 7.7, 11.9, 11.4 h_{100}^{-1} Mpc as $\sigma^2_{\rm gal} \sim 1.3 \pm 0.4$ for $\Omega_M = 1$, 0.2 open, 0.3 flat. This variance implies that Lyman-break galaxies have a bias $b \equiv \sigma_{\rm gal}/\sigma_{\rm mass}$ of $b = 6.0 \pm 1.1$, 1.9 ± 0.4, 4.0 ± 0.7 for the same cosmologies. The bias is in good agreement with a simple model, first proposed by White & Rees (1978), in which galaxies form within virialized halos of dark matter. The agreement of our data with this model depends on cosmology primarily through the shape of the power-spectrum, rather than through the growth rate of matter perturbations as might have been expected. Given the abundance of Lyman-break galaxies and the locally determined power-spectrum shape, one could have predicted a priori from this model the clustering strength we have observed (e.g., Mo & Fukugita 1996). The agreement is surprisingly good, for it assumes not only that galaxies form within dark halos—which is plausible enough—but that galaxies UV-bright enough for us to detect reside almost exclusively within the most massive halos. UV luminosity depends so strongly on the age of a starburst and on the importance of dust extinction that one might have expected halo mass to play a comparatively minor role in Lyman-break galaxies' UV luminosities; but this appears

[6]The opposite possibility—that there is more than one Lyman-break galaxy per massive halo—could in principle help reconcile our observations with standard CDM, but is inconsistent with the small number of close galaxy pairs in our sample (Giavalisco *et al.* 1998a).

not to be the case. The observed abundance and clustering properties of Lyman-break galaxies suggest instead an almost one-to-one correspondence of massive halos to *observable* galaxies, and this implies, for example, that the most massive halos essentially always exhibit star formation at detectable levels (i.e., that the duration of star formation is close to the time interval over which the galaxies in the sample are observed), and that halos only slightly less massive rarely do. The simple analytic approach adopted in §4 cannot justify more precise statements here; these will be presented elsewhere (Adelberger *et al.* 1998).

While we have argued that our data can be understood through an appealingly simple model for galaxy formation in which galaxies form within dark-matter halos, the UV luminosities of young galaxies are tightly correlated with their masses, and the power-spectrum of mass fluctuations at $z \sim 3$ has a shape similar to that determined locally, this does not of course rule out other models. We look forward to learning how well our data agree with competing scenarios for galaxy formation. In the meantime, one prediction of the scenario we favor is that fainter samples of Lyman-break galaxies in the same redshift range should exhibit weaker clustering; existing data will allow us to test this observationally (Giavalisco *et al.* 1998b).

Alcock, C. & Paczynski, B. 1979, *Nature*, **281**, 358.

Bagla, J. S. 1998, *Mon. Not. Roy. Astron. Soc.*, **297**, 251.

Bardeen, J. M., Bond, J. R., Kaiser, N., & Szalay, A.S. 1986, *Astrophys. J.*, **304**, 15.

Birnbaum, A. 1962, *Jour. Am. Stat. As.*, **45**, 164.

Cole, S. & Kaiser, N. 1989, *Mon. Not. Roy. Astron. Soc.*, **237**, 1127.

Coles, P. & Jones, B. 1991, *Mon. Not. Roy. Astron. Soc.*, **248**, 1.

Coles, P. & Frenk, C. S. 1991, *Mon. Not. Roy. Astron. Soc.*, **253**, 727.

Dekel, A. & Rees, M. J. 1987, *Nature*, **326**, 455.

Eke, V. R., Cole, S., & Frenk, C. S. 1996, *Mon. Not. Roy. Astron. Soc.*, **282**, 263.

Giavalisco, M., Steidel, C. C., Adelberger, K. L., Dickinson, M. E., Pettini, M., & Kellogg, M. 1998, *Astrophys. J.*, **503**, 543.

Governato, F., Baugh, C. M., Frenk, C. S., Cole, S., Lacey, C. G., Quinn, T., & Stadel, J. 1998, *Nature*, **392**, 359.

Jing, Y. P. & Suto, Y. 1998, *Astrophys. J. Lett.*, **494**, 5.

Kaiser, N. 1984, *Astrophys. J. Lett.*, **284**, 9.

Kaiser, N. 1987, *Mon. Not. Roy. Astron. Soc.*, **227**, 1.

Kofman, L., Bertschinger, E., Gelb, J., Nusser, A., & Dekel, A. 1994, *Astrophys. J.*, **420**, 44.

Maddox, S. J., Efstathiou, G., & Sutherland, W. J. 1996, *Mon. Not. Roy. Astron. Soc.*, **283**, 1227.

Mo, H. J. & Fukugita, M., 1996, *Astrophys. J. Lett.*, **467**, 9.

Mo, H. J. & White, S. D. M., 1996, *Mon. Not. Roy. Astron. Soc.*, **282**, 347.

Oke, J. B. et al. 1995, *Proc. Astron. Soc. Pac.*, **107**, 3750.

Padmanabhan, T. 1993, in *Structure Formation in the Universe* (New York: Cambridge University Press.)

Peacock, J. A. & Dodds, S. J. 1994, *Mon. Not. Roy. Astron. Soc.*, **267**, 1020.

Peacock, J. A. 1999, in *The Most Distant Radio Galaxies: Proceedings of the KNAW colloquium* (Amsterdam: Reidel, eds. Röttgering, H.J.A, Best, P.N., & Lehnert, M.D.) 377.

Peebles, P. J. E. 1980, in *The Large Scale Structure of the Universe* (Princeton: Princeton University Press.)

Pettini, M., Kellogg, M., Steidel, C. C., Dickinson, M., Adelberger, K. L., & Giavalisco, M. 1998, *Astrophys. J.*, **508**, 539.

Press, W. H. & Schechter, P. 1974, *Astrophys. J.*, **187**, 425.

Steidel, C. C., Adelberger, K. L., Dickinson, M., Giavalisco, M., Pettini, M., & Kellogg, M. 1998a, *Astrophys. J.*, **492**, 428.

Steidel, C. C., Adelberger, K. L., Dickinson, M., Giavalisco, M., Pettini, M., & Kellogg, M. 1998b, in *The Young Universe* (San Francisco: ASP, eds. A. Fontana, S. d'Odorico, & E. Giallongo) 428.

Steidel, C. C., Giavalisco, M., Pettini, M., Dickinson, M., & Adelberger, K. L. 1996, *Astrophys. J. Lett.*, **462**, 17.

Steidel, C. C., Pettini, M., & Hamilton, D. 1995, *AJ*, **110**, 2519.

Steidel, C. C. & Hamilton, D. 1993, *AJ*, **105**, 2017.

Vogeley, M. S., Park, C., Geller, M. J., & Huchra, J. P. 1992, *Astrophys. J. Lett.*, **391**, 5.

Wechsler, R. H., Gross, M. A. K., Primack, J. R., Blumenthal, G. R. & Dekel, A. 1998, *Astrophys. J.*, **506**, 19.

White, S. D. M., Efstathiou, G., and Frenk, C. S. 1993, *Mon. Not. Roy. Astron. Soc.*, **262**, 1023.

White, S. D. M. & Rees, M. J. 1978, *Mon. Not. Roy. Astron. Soc.*, **183**, 341.

Chapter 4

Galaxies and Intergalactic Matter at Redshift $z \sim 3$[1]

Abstract

We present the first results from a survey of the relative spatial distributions of galaxies, intergalactic neutral hydrogen, and intergalactic metals at high redshift. We obtained high-resolution spectra of 8 bright QSOs at $3.1 < z < 4.1$ and spectroscopic redshifts for 431 Lyman-break galaxies (LBGs) at slightly lower redshifts. Comparing the locations of galaxies to the absorption lines in the QSO spectra shows that the intergalactic medium contains significantly less neutral hydrogen than the global average within $r \lesssim 0.5h^{-1}$ co-moving Mpc of LBGs and significantly more than average at slightly larger distances $1 \lesssim r \lesssim 5h^{-1}$ co-moving Mpc. The intergalactic medium within the largest over-densities at $z \sim 3$, which will presumably evolve into the intracluster medium by $z \sim 0$, contains gas with a surprisingly high neutral fraction. The lack of HI absorption at small distances from LBGs appears unlikely to be produced solely by the Lyman continuum radiation they emit. The excess HI absorption on

[1]Submitted to Astrophys. J. as Adelberger, Steidel, Shapley, & Pettini 2002

larger scales appears inconsistent with standard models of the intergalactic medium which assume that the intergalactic HI density is primarily controlled by the local density of dark matter. We argue that both the deficit of HI near LBGs and the strength of the correlation of HI and galaxies on larger scales can be explained if supernova-driven winds in LBGs maintain their measured outflow velocities of $\sim 600\mathrm{km\,s^{-1}}$ for a few hundred million years and reach radii approaching $1h^{-1}$ comoving Mpc. Simple calculations show that the galaxies' supernovae should emit enough energy to set these winds in motion; simple models of wind evolution show that the winds could reach this radius before stalling. The strong observed association of galaxies with intergalactic metals supports the idea that winds enrich galaxies' surroundings. The existence of superwinds from massive galaxies at $z \sim 3$ could have profound implications for our understanding of the intergalactic medium and of galaxy formation.

4.1 Introduction

The large-scale distribution of matter in the universe is well understood only at the earliest times, a few hundred thousand years after the big bang, when primordial photons strained against the opacity of matter and drove small acoustic waves throughout space. But though this era was appealingly simple, elegantly predicted, magnificently observed, and so on, it was nevertheless brief. Particles slowed as the universe cooled. Electrons became unable to outrun the Coulombic pull of nuclei and vanished into atomic orbits. The universe became transparent; the photons of the microwave background hurtled through history; and the baryons left behind, freed from the regulating pressure of light, began to evolve according to their own complicated rules. Many acoustic waves had not even completed their first oscillation when the universe ceased

to be described by the simple physics of linear fluid dynamics. Baryons fell towards overdensities in the matter distribution. They crashed together and became shock heated. They cooled. Nuclear reactions ignited. Black holes formed. Intense radiation filled the universe. The final result of this chaos is known only because we can survey the wreckage that surrounds us. A small fraction of baryons in the universe were crushed into stars that now huddle together in galaxies, burning through their measure of fuel, dying one by one. Most of the remainder were blasted to $T \sim 10^5$–10^7 K, temperatures they had not experienced since shortly after the big bang, and were left to drift for a sterile eternity in the vast stretches of intergalactic space. Few goals in cosmology are more fundamental than understanding the physical processes that transformed the large-scale distribution of baryons in this way.

Attempts to reason backwards from observations of the recent universe suggest that the violence of galaxy formation must have had a profound impact on the rest of the universe. It has long been known that young galaxies and their nuclei emitted enough radiation to re-ionize the universe, but the data suggest that this may have been only a small part of their influence. Elliptical galaxies contain little interstellar material (Mathews & Baker 1971), for example, but tend to be enveloped by intracluster gas that is rich in metals (de Young 1978), as if the numerous supernova explosions that accompanied their formation expelled much of their matter far into their surroundings. The surprising scarcity of faint galaxies in the local universe may show that only the most massive galaxies could resist being destroyed in this way (e.g., Cole et al. 1994). Local starburst galaxies send large amounts of gas careering towards intergalactic space (e.g., Heckman et al. 2000) even though they are often more massive and less rapidly star-forming than their high-redshift counterparts. Metals produced in stars have been found far from known galaxies at high redshift (e.g., Cowie et al. 1995; Ellison et al. 2000; Mushotzky & Loewenstein 1997). Extreme releases of heat from supernovae may be required to explain the small fraction

of baryons that cooled at early times despite the universe's high density (e.g., White & Rees 1978). The faintness of the soft X-ray background (Pen 1999) and the broken self-similarity of the cluster X-ray luminosity/temperature relationship (Kaiser 1991; Ponman, Cannon, & Navarro 1999) appear to indicate that something imparted ~ 1 keV of energy to each of the young universe's nucleons. These observations and others are often thought to show that supernova explosions significantly altered the evolution of the universe's baryons.

But this conclusion seems to be contradicted by numerical simulations that attempt to model the behavior of baryons after recombination (early examples include Cen et al. 1994, Zhang et al. 1995, and Hernquist et al. 1996). In these simulations most of the baryons in the universe settle into thermal equilibrium soon after reionization; their energy gain from photoionization, $\Gamma \propto n_{\rm HI} \propto n_{\rm H}^2 T^{-0.7}$, is balanced by their energy loss from expansion cooling, $\Lambda \propto n_{\rm H} T$, and a simple relationship $T \propto n_{\rm H}^{0.6}$ between their temperature and density is established.[2] The characteristics of the intergalactic Lyman-α absorption observed in the spectra of high-redshift QSOs appear to be reproduced in the simulations with astonishing accuracy (see Weinberg, Katz, & Hernquist 1998 and references therein). Because the time for gas to reach equilibrium through expansion cooling is long, roughly the age of the universe, any disturbance of the intergalactic medium would not soon be erased. The similarities of the observed intergalactic medium at high redshift to the quiescent medium of the simulations has been claimed to show that the intergalactic medium was not much affected by the violence of star-formation in galaxies, that galaxies influence the evolution of baryons in the universe solely through the ionizing radiation they emit.

The tension between these two views of history inspired us to observe the relative distribution of galaxies and intergalactic material in young universe, at redshift $z \sim 3$, roughly two billion years after the demise of the acoustic waves and one billion years

[2]See Hui & Gnedin (1997) for a more refined derivation of the temperature–density relationship.

after the reionization of hydrogen by the first generations of stars and black holes. This was a time when the amount of star formation in the universe was near its peak (e.g., Steidel et al. 1999) and the number density of galaxies with extremely large star-formation rates was $\sim$ 3 orders of magnitude larger than in the local universe (e.g., Adelberger & Steidel 2000 §4), yet when comparison of the Lyman-α absorption in numerous QSO spectra to predictions of numerical simulations suggests that most baryons remained undisturbed. Our goal was to place constraints on the possible influence of rapidly star-forming galaxies upon their surroundings. Our observation strategy and the data we obtained are described in §2. In §3 we present an overview of the observed association of galaxies and intergalactic material, showing first that the intergalactic medium within $\sim$ 0.5 comoving Mpc of Lyman-break galaxies appears to contain little neutral hydrogen, and second that galaxy overdensities on larger spatial scales ($\lesssim$ 10 comoving Mpc) tend to contain an excess of neutral hydrogen. In §4 we argue that our data on scales $\lesssim$ 1 comoving Mpc are consistent with the idea that winds from Lyman-break galaxies have significantly disturbed the intergalactic medium in their vicinity. In §5 we argue that the unexpectedly tight correlation of galaxy and HI overdensities on $\sim$ 10 Mpc scales is not easily compatible with the idea that the intergalactic medium is in thermal equilibrium and obeys the resulting simple relationship between the densities of neutral hydrogen and matter. §6 presents the raw auto- and cross-correlation functions of galaxies with galaxies, with CIV systems, and with Lyman-α forest flux decrements. They may help readers draw their own conclusions. Our conclusions are summarized in §7 and criticized in §8. At times the discussion required derivations that we judged to be distractingly long. These have been placed in a series of appendices that most readers may wish to skip.

4.2 Data

4.2.1 Observations

Our strategy was to use the Lyman-break technique to locate star-forming galaxies at $z \simeq 3.0 \pm 0.25$ in fields surrounding background QSOs whose spectra were suitable for measuring Lyman-α absorbing gas at $z \sim 3$. Two criteria were used to select fields. First, we wanted the QSO to lie at $3.3 \lesssim z \lesssim 3.6$ and to be bright enough for high-resolution spectroscopy. The lower redshift limit was set to maximize the number of Lyman-break galaxies at redshifts where HI absorption was probed by absorption in the QSO spectra; the upper limit was chosen to minimize the impact of Lyman-continuum and (especially) Lyman-β absorption at higher redshifts upon the $z \sim 3$ Lyman-α forest in each QSO spectrum. Second, we wanted the fields to have as little 100μm cirrus flux from the Galaxy as possible, to minimize the attenuation of Lyman-break galaxies' light from dust in our own galaxy.

We were able to obtain data in six fields satisfying these criteria (Table 4.1); one field contains two QSOs. Our sample was augmented by including data from the "SSA22" field where previous Lyman-break observations (Steidel *et al.* 1998) had discovered a QSO at $z = 3.352$.

High resolution ($R \sim 40000$; see table 4.1) spectra of Q0256-0000, Q0302-0019, Q0933+2845, Q1422+2309[3], and Q2233+1341 were obtained with the HIRES echelle spectrograph (Vogt 1994) on Keck I between 1996 and 2000. Two overlapping echelle grating angles were chosen to provide complete wavelength coverage through the $z \sim 3$ Lyman-α forest. SSA22D13 was observed with the Echellette Spectrograph and Imager (ESI; Sheinis et al. 2000) on Keck II in echellette mode ($R \sim 6000$) in June and August 2000. An ESI spectrum was also obtained for Q1422+2309b, a faint QSO that we discovered $\sim 40''$ from Q1422+2309. The HIRES spectra were reduced

[3]The beautiful spectrum of this QSO was taken and generously shared by W. Sargent

Table 4.1 QSO/LBG Fields

QSO	α^a_{2000}	δ^a_{2000}	$z^a_{\rm QSO}$	$G^b_{\rm QSO}$	$R^c_{\rm spec}$	$\Delta\Omega^e$	N^f_1	N^g_2
Primary:								
Q0256-0000	$02^h59^m05.6$	$+00°11'22''$	3.364	18.2	44000	$8\farcm5\times 8\farcm5$	45	38
Q0302-0019	$03^h04^m49.9$	$-00°08'13''$	3.281	17.8	44000	$6\farcm5\times 6\farcm9^h$	47	23
Q0933+2845	$09^h33^m37.3$	$+28°45'32''$	3.428	17.5	33000	$8\farcm9\times 9\farcm3^h$	65	32
Q1422+2309[i]	$14^h24^m38.1$	$+22°56'01''$	3.620	16.5	44000	$7\farcm3\times 15\farcm6$	111	62
Q1422+2309b	$14^h24^m40.6$	$+22°55'43''$	3.629	23.4	6000			
SSA22D13	$22^h17^m22.3$	$+00°16'41''$	3.352	21.6	6000	$8\farcm7\times 17\farcm4$	79	54
Q2233+1341	$22^h36^m27.2$	$+13°57'13''$	3.210	20.0	44000	$9\farcm2\times 9\farcm3$	47	29
Supplemental:								
Q0000-2620	$00^h03^m22.9$	$-26°03'17''$	4.098	19.4		$3\farcm7\times 5\farcm1$	18	1
Q0201+1120	$02^h03^m46.7$	$+11°34'45''$	3.610	20.1	44000	$8\farcm7\times 8\farcm7$	19	11

[a]QSO coordinates [b]QSO AB magnitude [c]Spectral resolution [d]Spectral integration time (sec) [e]Angular size of surrounding region with known $z \sim 3$ galaxies [f]Number of Lyman-break galaxies with spectroscopic redshifts [g]Number of Lyman-break galaxies with $z_{{\rm Ly}\beta} < z < z_{\rm QSO} - 0.05$ and $2.6 < z < 3.4$ [h]Region with spectroscopic follow-up; images cover a larger area [i]Sum of lensed components A and C (see, e.g., Rauch, Sargent, & Barlow 1999)

in the usual way with Tom Barlow's Makee package. Their continua were fit using an interactive program kindly provided by R. Simcoe. The ESI spectra were reduced and continuum fit with the "Dukee" suite of custom IRAF scripts and C programs written by KLA and M. Hunt.

$U_nG\mathcal{R}$ images were obtained in each field, with COSMIC (Kells *et al.* 1998) on the Palomar 5m Hale Telescope for Q0256-0000, Q0933+2845, Q2233+1341, and two adjacent pointings in SSA22, and with the Prime Focus Imager on the William Herschel Telescope for Q0302-0019 and Q1422+2309. The Palomar images of Q0933+2845 and WHT images of Q0302-0019 were supplemented with data obtained for another project with MOSAIC on the Kitt Peak 4m Mayall telescope. The images were reduced and photometric catalogs were constructed as described in Steidel *et al.* (1999). The typical reduced image depths were $\sim$ 29.1, 29.2, 28.6 AB magnitudes per arcsec^2 in U_n,G, and $\mathcal{R}$, and approximately 2.2 objects per square arcminute in each field

were found to satisfy the Lyman-break selection criteria

$$U_n - G \geq G - \mathcal{R} + 1.0, \qquad G - \mathcal{R} \leq 1.2, \qquad \mathcal{R} \leq 25.5. \tag{4.1}$$

In Q1422 exceptionally deep data let us extend our sample to $\mathcal{R} = 26$.

Low resolution spectra for a subset of these Lyman-break candidates were obtained with LRIS (Oke *et al.* 1995) on the Keck I and II telescopes between 1995 and 2001. Each field was observed through at least 4 multislit masks that accommodated ~ 20 objects each. Spectra were obtained for Lyman-break candidates throughout the regions observed in $U_nG\mathcal{R}$, except in the case of Q0302 and Q0933 where spectra were obtained only in a $\sim 7 - 9'$ region surrounding the QSO rather than throughout the larger imaged fields. The field sizes and number of useful redshifts obtained in each field are listed in Table 4.1.

These five fields make up the primary sample used in most of our analysis below. In a few cases we also used data in fields surrounding two additional QSOs, Q0000-2620 and Q0201+1120. $U_nG\mathcal{R}$ images for Q0000-2620 were obtained with EMMI on the 3.6m NTT telescope in 1994; images for Q0201+1120 were obtained with COSMIC on the Palomar 5m Hale telescope in 1995. Our echelle spectrum of Q0000-2620 is a combination of a HIRES spectrum taken by W. Sargent with the UVES (Dekker et al. 2000) spectrum made public after the instrument's commissioning. P. Molaro kindly provided us with the reduced UVES spectrum. A HIRES spectrum of Q0201+1120 was obtained in 1999 and reduced as described above. LRIS on Keck I was used in 1995 and 1996 to measure redshifts for a few objects in each field whose $U_nG\mathcal{R}$ colors satisfied equation 4.1. We excluded these two fields from most of the analysis for a number of reasons. Their images are shallow. Few spectroscopic redshifts were measured. The $U_nG\mathcal{R}$ filters used for observing Q0000-2620 differed somewhat from those used in the rest of the observations, leading to significant changes in the redshift distribution of spectroscopically observed galaxies. Moreover Q0000-2620 is

at so high a redshift that most of the interesting CIV lines are buried in the Lyman-α forest and most of the Lyman-α forest close to our galaxies is badly affected by absorption from Lyman series lines from gas at higher redshifts. The spectrum of Q0201+1120 contains large gaps between echelle orders in the red that prevented us from detecting CIV systems in a uniform way. Nevertheless in two cases below—figures 4.7 and 4.10—we were able to make some use of these data.

4.2.2 Redshifts

Initial wavelength calibration

Our raw data are arrays of numbers listing the number of photoelectrons in each potential well of the CCD detector. Of the many steps required to reduce these data, one of the most crucial is the wavelength calibration, the estimate of which wavelengths of light were cast on each pixel by the optics of the spectrograph. This section describes how we calibrated our LRIS data. The HIRES and ESI calibrations were similar.

The most robust approach to wavelength calibration is to use the spectrum of the object itself, measuring the pixel numbers of a large number of sky lines that have well known wavelengths, then using an interpolant (e.g., a $\sim$ 5th order Legendre polynomial fit to the wavelength vs. pixel-number relation) to estimate the wavelengths of light that fell on the numerous pixels without sky lines. Unfortunately our spectra usually showed few (if any) detectable sky lines with $\lambda < 5577$Å, the wavelengths where most features in the spectra of $z \sim 3$ galaxies lie. We were forced to rely on the spectrograph's arc lamps for the wavelength calibration. The primary disadvantage of arc lamps is that gravitational deformation of the instrument alters the wavelength of light that falls on each pixel by a small but (sometimes) significant amount as the telescope moves around the sky, and the wavelength solution appropriate to the arc

lamp exposure may not be appropriate for the galaxies exposure. To minimize changes in the instrument's deformation, our arc lamp exposures for each multislit mask were taken immediately after the galaxies were observed, at the same telescope position as the final galaxies exposure. Deformation of the instrument during the series of exposures of the galaxies was corrected (when present) by linearly translating each exposure's data until its sky lines lined up with the final exposure's. The individual spectra of each galaxy on the mask were then added together, and a wavelength was assigned to each pixel in the co-added spectra by a fifth-order Legendre polynomial fit to the pixel-number vs. wavelength relationship of the slit's arc lamp exposure. Owing (presumably) to changes in the spectrograph's gravitational deformation between the final galaxies exposure and the arc lamp exposure, we sometimes found that sky lines in the co-added spectra had been assigned wavelengths that were systematically too large or too small by up to ~ 1Å. This was corrected by translating the co-added spectrum in the wavelength direction until sky lines fell at the proper wavelength. In the resulting spectra, the mean difference between the true and estimated sky line wavelengths was negligible and the 1σ scatter was ~ 0.25Å.

Vacuum heliocentric correction

The procedure above yields a reasonably accurate estimate of the wavelengths of the photons as they passed through the spectrograph[4]. But this is a poor coordinate system for spectral calibration. The $\sim 30\mathrm{km\,s^{-1}}$ motion of the earth about the sun causes the observed wavelength of any feature in an object's spectrum to oscillate slightly from one season to the next, while the refraction of light by the earth's atmosphere subtly alters the relative spacing of features in a spectrum. An accurate determination of the relative redshifts of objects requires the spectra to be put into

[4]or, more correctly, of the wavelength the photons would have had if the air were dry and had a temperature of 15°C and a pressure of 760mm Hg, the same conditions assumed in the tabulated wavelengths of the arc lamp's lines

the vacuum-heliocentric frame.

Standard formulae were used to correct our spectra for the earth's motion and place them into the heliocentric frame. A tolerably good first-order fit to the relationship between air[5] and vacuum wavelengths in angstroms is provided by the formula

$$\lambda_{\rm vac} = 1.000266732\lambda_{\rm air} + 0.0619. \tag{4.2}$$

The maximum error in equation 4.2 does not exceed 0.01Å anywhere in the optical window $3200 < \lambda < 9500$Å. This formula was used to convert our ESI quasar spectra and LRIS galaxy spectra into the vacuum frame. The HIRES spectra were converted to the vacuum frame by the Makee reduction package (Barlow 2001, private communication) using a similar but higher-order fit.

Correction for galactic winds

The $\sim$ 30 km s^{-1} velocity of the earth about the sun perturbs our redshifts by $\Delta z \sim 0.0001$. The gravitational flexure of the spectrograph and the slowing of light by the earth's atmosphere perturb them by larger amounts $\Delta z \sim 0.001$. Larger still are the perturbations due to the chaotic motions of material within Lyman-break galaxies themselves. The various emission and absorption lines within the spectrum of a single Lyman-break galaxy seldom have the same redshift. Absorption lines from the cool interstellar gas tend to have the lowest redshifts; nebular emission lines from the hot gas close to stars tend to have slightly higher redshifts; and Lyman-α almost always has the highest redshift (e.g., Pettini et al. 2002; Pettini et al. 2001). The redshift range spanned by the interstellar lines and Lyman-α often exceeds $\Delta z = 0.01$ ($\sim$ 750kms^{-1}; cf. figure 4.1). This reflects velocity differences within the galaxy itself—the observed redshift differences are qualitatively consistent with the idea that a typical Lyman-break galaxy is expelling some fraction of its interstellar

[5]dry, 15°C, 760mm Hg

gas in a supernovae-driven wind (cf. figure 4.2; see also Tenorio-Tagle et al. 1999)—but if the redshift differences were erroneously assumed to be caused by the Hubble flow, the implied comoving distance between the reddest and bluest features would be $\sim 7h^{-1}$ Mpc ($z = 3$, $\Omega_M = 0.3$, $\Omega_\Lambda = 0.7$). The challenge is to estimate from our data the redshift of each Lyman-break galaxy's stars, to pick out where each Lyman-break galaxy lies within the $\sim 7h^{-1}$ Mpc range that our observations would seem to allow.

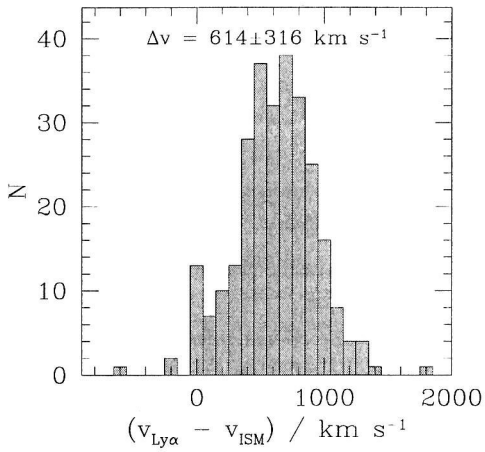

Figure 4.1 The distribution of velocity differences between Lyman-α emission and interstellar absorption in the spectra of Lyman-break galaxies.

Our approach was guided by the assumption that the redshift of a galaxy's nebular lines (e.g., [OII]λ3727, Hβ, [OIII]$\lambda\lambda$4959, 5007) ought to be nearly equal to the redshift of its stars, that the gas responsible for nebular emission should always lie close to hot stars. Because nebular lines are redshifted to the near-IR, where spectroscopy is extraordinarily difficult, we were unable to measure their redshifts for the vast majority of galaxies in our sample. Instead we searched for correlations between nebular-line redshifts and UV spectral characteristics among the 27 Lyman-break galaxies that have measured nebular redshifts, then used these correlations to estimate the systemic redshift of each galaxy in our larger sample from its rest-frame UV spectrum. The near-IR data for 14 of these 27 galaxies were taken from Pettini et al.

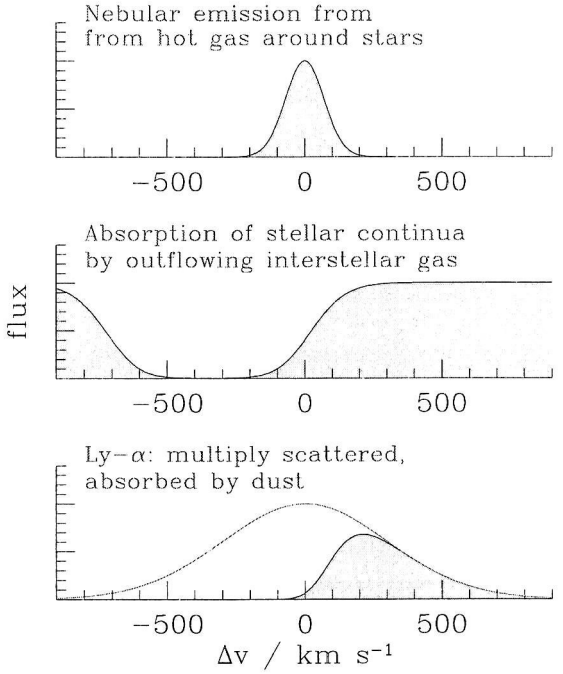

Figure 4.2 Schematic view of the different redshifts in the spectrum of a single Lyman-break galaxy. Narrow ($\sigma_{1D} \sim 70$ km s^{-1}) nebular emission lines have been detected through the near-IR spectroscopy of 27 Lyman-break galaxies. These emission lines presumably lie near the galaxy's systemic redshift. Wide interstellar absorption lines are usually seen blueward of the nebular lines. Lyman-α emission of varying widths lies redward. The relative redshifts can be understood through a simple wind model for the gas in Lyman-break galaxies. Absorption of stellar continua is produced by outflowing (i.e., blueshifted) gas lying between the observer and the stars. Resonant scattering sends Lyman-α photons on long random walks through the dusty outflow. The few photons that escape without being absorbed by dust are those that were scattered along unusually short paths out of the galaxy; most of these photons scattered off the redshifted back of the outflow and along the steep velocity gradient towards us.

(2001); our NIRSPEC (McLean et al 1998) spectra of the remaining galaxies will be presented elsewhere.

The following four relationships were found to hold for the 27 galaxies with nebular redshifts. Each resulted from a singular-value decomposition solution of a linear least-squares equation (e.g., Press et al. 1994, §15.4).

Among the galaxies with detectable Lyman-α emission, the velocity of Lyman-α

relative to the nebular lines roughly satisfied

$$v_{\mathrm{Ly}\alpha} \simeq 700 - 9.9 W_\lambda \quad \mathrm{km\,s^{-1}} \tag{4.3}$$

where W_λ is the rest-frame equivalent width of Lyman-α in Å[6]. The rms scatter about this mean relationship was $170 \mathrm{km\,s^{-1}}$. The sense of this correlation is consistent with the idea that dust absorption of resonantly scattered photons is responsible for driving Lyman-α to the red; the reddest Lyman-α lines ought to be the weakest.

Averaging equation 4.3 over the distribution of W_λ among galaxies with detectable Lyman-α emission but no detectable absorption lines leads to the mean relationship

$$v_{\mathrm{Ly}\alpha} \simeq 340 \quad \mathrm{km\,s^{-1}}. \tag{4.4}$$

This equation can provide an estimate of a Lyman-α–emitting galaxy's systemic redshift when W_λ has not been measured, but the redshift's precision ($\sigma_v \sim 250$ km s^{-1}) suffers. Note that equation 4.4 is applicable only to data of similar quality as ours, since the adopted distribution of W_λ was appropriate for galaxies with detectable Lyman-α emission and no detectable interstellar metal lines, and this classification is affected by the signal to noise ratio of our typical spectra.

Among galaxies that had both measurable Lyman-α and interstellar-absorption redshifts, the mean of the Lyman-α and interstellar redshifts was larger than the nebular redshift by an amount

$$v_{\mathrm{mid}} \simeq -0.014 \Delta v - 7.1 W_\lambda + 320 \quad \mathrm{km\,s^{-1}} \tag{4.5}$$

if W_λ was used in the fit or

$$v_{\mathrm{mid}} \simeq 0.114 \Delta v + 270 \quad \mathrm{km\,s^{-1}} \tag{4.6}$$

[6]Here W_λ refers to the equivalent width of only the part of the Lyman-α line that is observed in emission. It is therefore non-negative by definition. Because the lines often have P-Cygni profiles, the values W_λ we measure from our spectra according to this definition will generally differ from the equivalent widths one would derive from (e.g.) a narrow-band image; we would record a positive (emission) value for W_λ if we saw a weak Lyman-α emission line at the red edge of a deep Lyman-α absorption trough, while narrow-band photometry would reveal only that Lyman-α appeared dominantly in absorption.

if W_λ was ignored. Here Δv is the observed velocity difference between Lyman-α and the absorption lines. The rms scatter about equations 4.5 and 4.6 was 150 and 210km s^{-1} respectively. The physical origins of correlations 4.5 and 4.3 are similar. Correlation 4.6 presumably reflects the fact that vagaries of the gas and dust geometry can drive the Lyman-α redshift quite far from the systemic redshift, while the maximum difference between the absorption and systemic redshifts is constrained by the wind velocity a typical Lyman-break galaxy can generate. As a consequence the absorption redshift tends to lie closer than the Lyman-α redshift to the systemic redshift in cases where the interstellar absorption and Lyman-α emission are widely separated.

The mean velocity difference between the interstellar lines and nebular lines for galaxies with measurable interstellar redshifts was

$$v_{\rm abs} \simeq -170 \quad {\rm km\,s^{-1}} \tag{4.7}$$

with an rms scatter of 160km s^{-1}. The qualitative picture of figure 4.2 suggests that taking account of the velocity widths of the interstellar absorption lines might improve the accuracy of equation 4.7, but in practice the resolution of galaxy spectra, set by the seeing to $\sim$ 300–600 km s^{-1} (FWHM), was unusably coarse.

Two anomalous galaxies were excluded when calculating each of these fits and their scatter. The large residuals of the excluded galaxies could be traced back to their unusual spectra. One had two Lyman-α emission lines separated by $\sim$ 1000 km s^{-1}; the other had interstellar absorption at two redshifts separated by more than 1500km s^{-1}. As far as we could tell nothing about the UV spectra of these objects would have allowed us to predict their nebular redshifts with much precision. We chose to give up on the 2 pathological cases and optimize our fits for the 25 normal galaxies where we had some chance of success. Readers should be aware that for perhaps 1 galaxy among 10 the equations above will lead to an estimated redshift

that is incorrect by several times the quoted rms.

Equations 4.3 or 4.4, 4.5 or 4.6, and 4.7 were used to estimate the systemic redshifts of galaxies in our sample that had, respectively, detectable Ly-α emission only, both detectable Ly-α emission and interstellar absorption, and only detectable interstellar absorption. Lyman-α equivalent widths were measured only for galaxies within $60''$ of a QSO sightline, because only for these galaxies did the moderately improved precision of equations 4.3 and 4.5 relative to 4.4 and 4.6 make a significant difference.

We can check the accuracy of our redshift estimates by noting that that the cross-correlation function of galaxies and intergalactic material will be isotropic in an isotropic universe. On average the intergalactic medium ought to be symmetric when reflected in the z direction about the true location of each Lyman-break galaxy. The same is not true for reflection about the measured interstellar or Lyman-α redshift of the galaxies, because these redshifts are influenced only by material that lies between the galaxies' stars and us, and so the symmetry is broken.

Figure 4.3 shows the mean Ly-α transmissivity of the intergalactic medium for all pixels of our QSO spectra that lay within an apparent distance of $4h^{-1}$ and $6h^{-1}$ comoving Mpc of a Lyman-break galaxy. Also shown is the mean transmissivity we would have measured had our estimated galaxy redshifts been systematically higher or lower by an amount ranging from $\Delta z = -0.02$ to $\Delta z = +0.02$. The three panels correspond (from top to bottom) to galaxies with only detectable absorption, both detectable absorption and emission, and only detectable emission. In each case the curves of mean transmissivity vs. Δz are roughly symmetrical about $\Delta z = 0$, which suggests that the systemic redshifts assigned through equations 4.3, 4.6, and 4.7 are accurate on average. The mean redshift offset of the emission and/or absorption lines for each class is marked by the vertical bars.

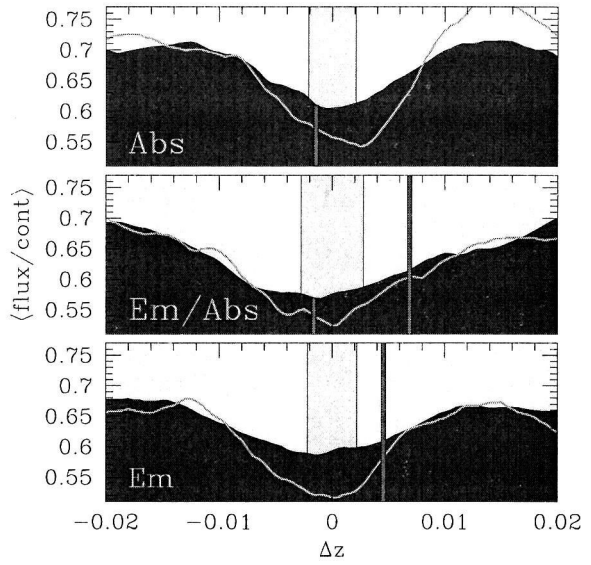

Figure 4.3 The mean transmissivity of all parts of the QSO spectra that lie within $4h^{-1}$ (solid line) or $6h^{-1}$ (shaded region) comoving Mpc of a Lyman-break galaxy. The height of these curves at $\Delta z = 0$ shows our best estimate from the redshift assignment described in § 4.2.2; the height of the curves at other values of Δz shows the mean transmissivity we would have measured had we applied an additional redshift adjustment of Δz to each galaxy. Large systematic errors in our redshift estimates would show up as asymmetries about $\Delta z = 0$ in this plot, but in fact $\Delta z = 0$ lies near the minimum of each curve. The sample was divided into classes defined by the type of features we could detect in each object's spectrum. The mean redshift of the detected features relative to our assigned redshift is marked with vertical bars, short for absorption lines and tall for emission lines. The size of our estimated uncertainty ($\pm 1\sigma$) in a single galaxy's redshift is indicated by the rectangular strip surrounding $\Delta z = 0$.

4.3 Overview of the galaxy/forest cross-correlation

We are now ready to begin looking at the relative spatial distributions of galaxies and intergalactic material and $z \sim 3$. This section will present a brief overview of our results; more detailed treatments can be found in the sections that follow.

4.3.1 Large-scale association of galaxies and HI

One of the most striking aspects of our data is the fact that the transmissivity of the Lyman-α forest tends to be low in volumes that contain a large number of Lyman-break galaxies. Figure 4.4 shows the Lyman-α forest along skewers through the $\sim 10 \times 10 \times 10h^{-3}$ comoving Mpc^3 cubes that contain the two most significant galaxy overdensities and the two most significant galaxy underdensities in our sample. The mean transmissivity is much lower through the galaxy overdensities. The trend is observed throughout the range of galaxy densities, not merely at the extremes. This can be seen in figure 4.5, which shows the mean galaxy overdensity in 3-dimensional cells surrounding the QSO sightlines in our primary sample as a function of the mean flux $\bar{f}_{0.02}$ on the $\Delta z = 0.02$ sightline segment enclosed by the cell. Each cell was a right rectangular parallelepiped with depth $\Delta z = 0.02$ and transverse dimensions equal to its CCD image's (table 4.1); in comoving units each was roughly a cube with side-length $13h^{-1}$ comoving Mpc ($\Omega_M = 0.3$, $\Omega_\Lambda = 0.7$). The mean galaxy overdensity associated with Lyman-α forest spectral segments with mean transmissivity in the range $\bar{f}_{0.02} \pm \delta\bar{f}$ was calculated by summing the observed number of galaxies in every cell with a mean transmissivity in that range, then dividing by the sum of the number of galaxies that would have been expected in those cells if Lyman-break galaxies were distributed uniformly in space:

$$\langle \delta_{\rm gal} \rangle \equiv \frac{\sum_i^{\rm cells} N_i}{\sum_i^{\rm cells} \mu_{g,i}} - 1, \tag{4.8}$$

where N_i is the observed number of galaxies in the ith cell and $\mu_{g,i}$ is the expected number in the absence of clustering. $\mu_{g,i}$ was estimated by scaling our average selection function by the number of galaxies with spectroscopic redshifts in the appropriate field. See appendix 4.C for a justification for this estimator. In order to (slightly) reduce the shot noise, the centers of adjacent cells were separated by $\Delta_z = 0.004$, so that we oversampled our data by a factor of 5. The QSO spectra were used over

the redshift range $(1+z_q)\lambda_{\mathrm{Ly}\beta}/\lambda_{\mathrm{Ly}\alpha} - 1 < \lambda/\lambda_{\mathrm{Ly}\alpha} - 1 < z_q - 0.05$, where z_q is the QSO redshift, in order to avoid contamination of the Lyman-α forest by material associated with the QSO or by Lyman-β absorption from gas at higher redshifts. Segments of the QSO spectra with $2.91 < \lambda/\lambda_{\mathrm{Ly}\alpha} - 1 < 2.98$ in SSA22 and with $3.214 < \lambda/\lambda_{\mathrm{Ly}\alpha} - 1 < 3.264$ in Q0933 were removed from the analysis to avoid damped Lyman-α systems.

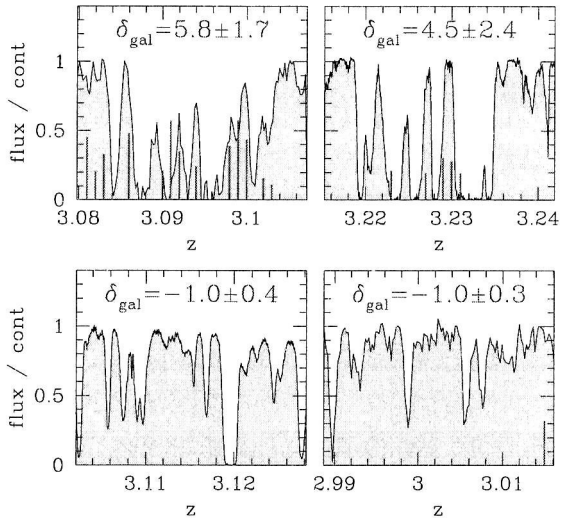

Figure 4.4 The Lyman-α forest through the $\sim 10 \times 10 \times 10h^{-3}$ comoving Mpc^3 cells that contain the two most significant galaxy overdensities (top panel) and underdensities (bottom panel). Galaxy redshifts are indicated with vertical lines. The height of each line is proportional to the galaxy's distance to the QSO sightline; a line reaching flux/cont = 1 represents a galaxy 10′ away. The galaxy overdensity in the upper right panel is the "spike" in SSA22 (e.g., Steidel et al. 1998; Steidel et al. 2000), the largest galaxy overdensity in the entire Lyman-break galaxy sample and our best candidate for a proto-Abell cluster. These data suggest that the intercluster medium contained a relatively large amount of neutral hydrogen at early times.

The correlation apparent in figure 4.5 is surprisingly linear. It is also surprisingly tight. The tightness of the correlation can be quantified through the correlation

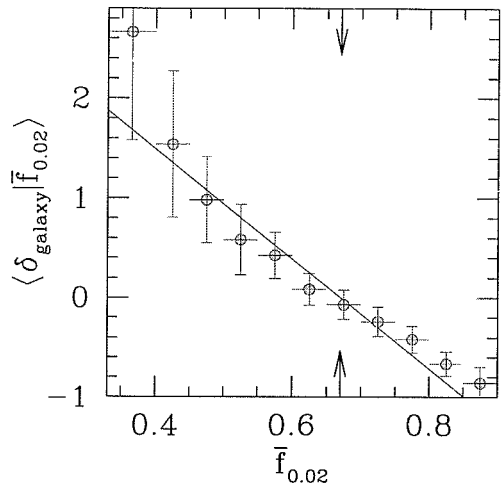

Figure 4.5 The mean galaxy density in a $\sim 13h^{-1}$ comoving Mpc cubical cell as a function of the mean Lyman-α forest transmissivity along the $\Delta z = 0.02$ sightline skewer through the cell. Galaxy overdensities contain large amounts of neutral hydrogen; galaxy voids contain less. Arrows indicate the mean value of $\bar{f}_{0.02}$ among all sightline segments in our sample.

coefficient (see, e.g., appendix 4.A), which we estimate with the statistic

$$r \equiv \frac{\sum_i^{\rm cells}(N_i - \mu_{g,i})(f_i - \mu_{f,i})}{\left(\sum_i^{\rm cells}(N_i - \mu_{g,i})^2 - \mu_{g,i}\right)^{1/2}\left(\sum_i^{\rm cells}(f_i - \mu_{f,i})^2\right)^{1/2}} \tag{4.9}$$

where f_i is the mean Lyman-α transmissivity along the segment of sightline through the ith cell and $\mu_{f,i}$ is the global mean transmissivity at the redshift of the ith cell (equation 4.10 below). N and f are treated differently in the denominator of equation 4.9 because N suffers from significant shot noise while f does not. Summing over all pixels in all fields, we arrive at a best estimate for the correlation coefficient of $\langle r_{\rm line} \rangle = -0.63$. The standard deviation of the mean of $r_{\rm line}$ estimated separately in each field is 0.07. The best fit regression line implied by this correlation coefficient, $\langle \delta_{\rm gal}/\sigma_{\rm gal} \rangle = r_{\rm line}\delta_{\rm line}/\sigma_{\rm line}$, shown in Figure 4.5, has a slope similar to what we would have derived from this figure itself, showing that our estimator 4.9 has produced a reasonable estimate of the correlation coefficient. We will have more to say about the

tightness of the correlation in § 4.5.

Some may be surprised that this trend extends to the largest galaxy overdensities, which are likely to evolve into rich clusters by $z = 0$. The comoving volume between $z = 2.7$ and $z = 3.3$ that we have observed, $\sim 3.7 \times 10^5 h^{-3}$ Mpc^3 for $\Omega_M = 0.3$, $\Omega_\Lambda = 0.7$, is large enough to contain ~ 3 structures that are destined to become clusters with X-ray temperatures $kT > 2.5$keV, and we have no better candidates for the protoclusters than the two overdensities shown in figure 4.4 or (more generally) than the large galaxy overdensities associated with the lowest $\bar{f}_{0.02}$ bins in figure 4.5. A number of arguments suggest that the intracluster medium was heated at early times, before the cluster itself had formed, and this has led some to speculate that young clusters at $z \sim 3$ might contain far less neutral hydrogen than the universal average (e.g., Theuns, Mo, & Schaye 2001). Figures 4.4 and 4.5 show that the opposite is true. The large Lyman-α opacities of (presumed) intracluster media at early times do not imply that preheating has not happened, however, as we argue in appendix 4.F: putative shocks traveling outward from high-redshift galaxies and heating the young intracluster medium could easily increase the mean HI content in the volumes they affect.

4.3.2 CIV

The notion that the intergalactic material within galaxy overdensities may have already been preheated receives some support from its observed abundance of metals. The association of Lyman-break galaxies and metals can be quantified in any number of ways, and will receive more attention below; but the qualitative point we wish to make here is adequately illustrated by figure 4.6. This figure shows the redshifts of the Lyman-break galaxies and CIV systems in the field of Q1422+2309, the QSO with the best spectrum in our sample. The top panel shows the number of galaxies and CIV systems in redshifts bins of width $\Delta z = 0.025$; the bottom panel shows

the result of smoothing the raw redshifts by a Gaussian with width $\sigma_z = 0.008$ and then dividing by the selection function. The selection function used for the galaxies, shown in the top panel of the figure, is a spline fit to a coarsely binned histogram of every Lyman-break galaxy redshift in our sample. The selection function for CIV systems was approximated as constant with redshift. Though obscured somewhat by shot noise, the connection between galaxy density and CIV density is in fact surprisingly strong; Pearson's correlation coefficient between the two curves in the bottom panel of figure 4.6 is 0.61. It is interesting that the amplitudes of the CIV and galaxy fluctuations are comparable. The figure suggests that a volume of the universe which is overdense in galaxies by a factor of $1 + \delta \sim 3$ (e.g.) will tend to be overdense in CIV systems by a factor of ~ 3 as well. But because Lyman-break galaxies are biased tracers of the mass distribution (e.g., Adelberger et al. 1998), the baryonic overdensity of the same volume will be significantly smaller. This shows that there is more detectable CIV absorption per baryon in galaxy overdensities than elsewhere. One of several possible interpretations is that the intergalactic metallicity is enhanced near galaxies at $z \sim 3$—though a similar trend might also result from the density-dependence of carbon's ionization state (§ 4.H).

The carbon we observe was presumably fused within galaxies and dispersed into intergalactic space by supernova explosions. Since the spectra of Lyman-break galaxies strongly suggest that they are expelling some fraction of their baryons (e.g., § 4.2.2 above; Pettini et al. 2002), it is interesting to search the intergalactic medium closest to Lyman-break galaxies for hints that these galaxies may themselves be enriching their surroundings with metals. Figure 4.7 shows the distribution of HI and CIV absorption along the QSO sightline segments that approach Lyman-break galaxies most closely. The angular separation of the galaxy from the sightline is marked in each panel. At $z = 3$ one arcminute corresponds to roughly $1.3h^{-1}$ comoving Mpc

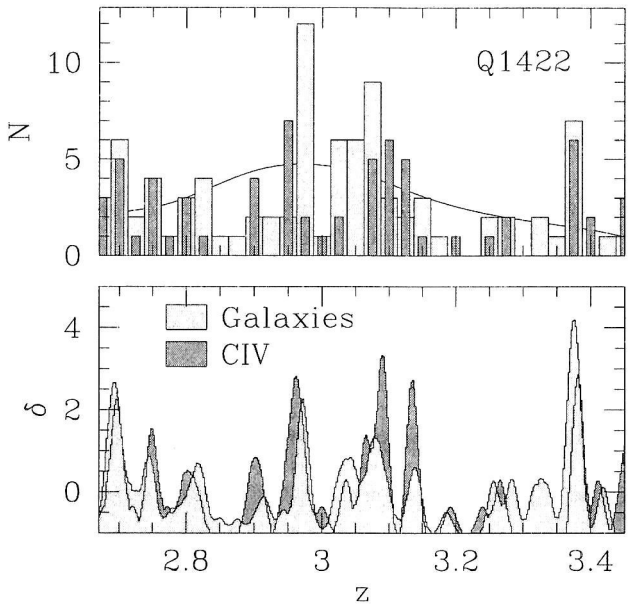

Figure 4.6 The redshift distributions of galaxies and CIV absorbers in the field of Q1422+2309. The top panel shows the number of objects observed at each redshift. The bottom panel shows the implied overdensity as a function of redshift for Gaussian smoothing in the redshift direction. The good correspondence of features in the lower panel shows that CIV systems are preferentially found within galaxy overdensities.

for $\Omega_M = 0.3$, $\Omega_\Lambda = 0.7$, and so at closest approach these sightlines probe the intergalactic medium at ~ 0.3 to $1.3h^{-1}$ comoving Mpc from the galaxy. The shaded curves show the Lyman-α forest transmissivity. The symbol β appears next to the impact parameter in each panel if Lyman-β absorption from gas at higher redshifts affects the appearance of the Lyman-α forest at the galaxy's redshift. The horizontal line marks the mean transmissivity at the galaxy's redshift. When the forest was not contaminated by Lyman-β absorption, its the mean transmissivity was taken to be

$$\bar{f}(z) = 0.676 - 0.220(z - 3), \tag{4.10}$$

a fit to the relationship between mean transmissivity $\bar{f}$ and redshift presented by McDonald et al (2000). The mean transmissivity of the forest contaminated by Lyman-β

and higher lines is roughly independent of redshift because the increased absorption in the blue due to high Lyman-series lines is largely canceled out by the gradual thinning of the forest towards lower redshifts. The mean transmissivity in this case was found to roughly obey the formula

$$\bar{f} = 0.633 - 0.40(z_{\rm QSO} - 3.5) \tag{4.11}$$

where $z_{\rm QSO}$ is the QSO's redshift. Circles mark the locations of detectable CIV absorption. The size of each circle is related to the CIV column density; a tripling of a circle's area corresponds to a factor of ten increase in column density. Due to significant gaps in our echelle spectrum of Q0201, we did not attempt to make a catalog of the CIV systems in this field. The short and tall vertical bars mark the observed redshifts of interstellar absorption and Lyman-α emission, respectively, in each galaxy's spectrum. Wide shaded boxes mark the 1σ confidence interval on each galaxy's systemic redshift, estimated from the appropriate equation among 4.3, 4.5, and 4.7. The figure gives the qualitative impression that CIV systems in QSO spectra often lie at or near the systemic redshift of galaxies within $\sim 1h^{-1}$ comoving Mpc of the QSO sightline. In a few cases the ratio of CIV to HI column densities in the gas near to the galaxies is large enough to show that the gas must have a metallicity well above the global average (§ 4.H). These results will be discussed more fully in §§ 4.4.2 and 4.6 below.

4.3.3 A lack of HI near Lyman-break galaxies

We would now like to draw readers' attention to another interesting aspect of figure 4.7. Although the intergalactic medium within $\sim 10h^{-1}$ comoving Mpc of galaxy overdensities appears to contain large amounts of neutral hydrogen, often little neutral hydrogen is observed along the small segments of the QSO sightline that pass within $\sim 1h^{-1}$ comoving Mpc of a Lyman-break galaxy. This is illustrated most clearly in

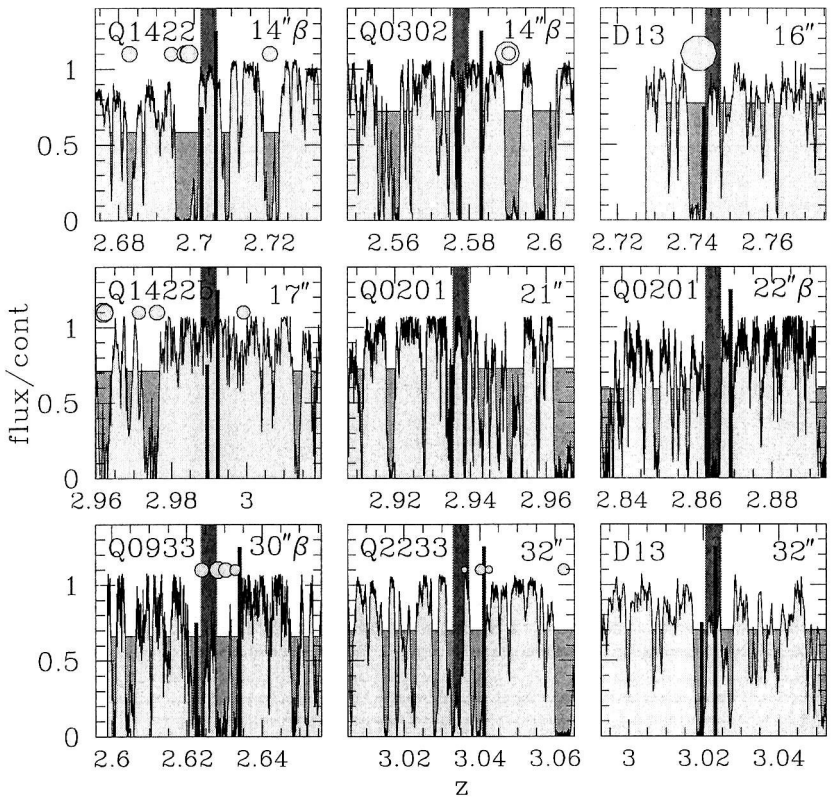

Figure 4.7 The distribution of neutral hydrogen and CIV absorption along the segments of the QSO spectra that pass closest to a Lyman-break galaxy. The shaded curve shows the Lyman-α forest. The horizontal line marks the mean transmissivity at this redshift in the QSO's spectrum. Circles mark the redshifts of detectable CIV absorption. Larger circles correspond to larger CIV column densities; a tripling in the circle's area corresponds to a factor of 10 increase in column density. Numerical values for the HI and CIV column densities of the absorbing gas near to one of these galaxies can be found in the last entry of table 4.2. The wide vertical region shows our estimated redshift for each galaxy. Narrower vertical bars mark the redshifts of Lyman-α (tall bar) or interstellar absorption (short bar) in each galaxy's spectrum. The distance from each galaxy to the QSO sightline is indicated. $10''$ corresponds to roughly $200h^{-1}$ comoving kpc. A β next to the distance indicates that the Lyman-α forest at this redshift is contaminated by Lyman-β (or higher) absorption from gas at larger redshifts.

figure 4.8, which shows the mean Lyman-α transmissivity of the intergalactic medium as a function of apparent comoving distance to a Lyman-break galaxy. Only parts of

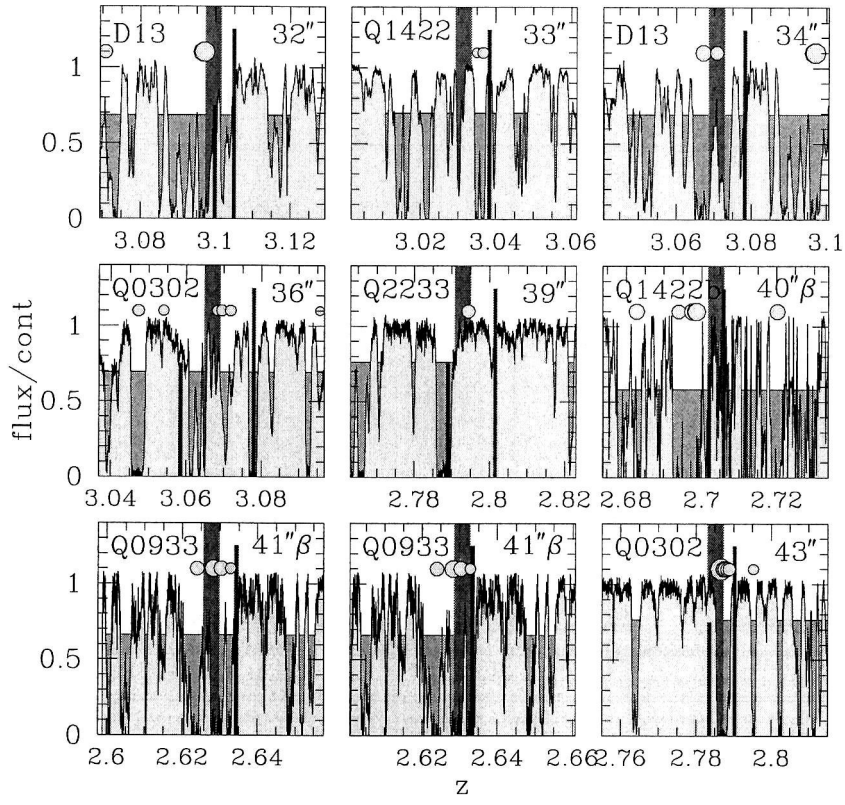

Figure 4.7 continued.

the QSO spectra uncontaminated by Lyman-β absorption from gas at higher redshifts or by damped Lyman-α systems were used. The mean Lyman-α transmissivity at a distance $0.5 < r < 1.0h^{-1}$ Mpc (say) from a single Lyman-break galaxy can be estimated with the ratio A_i/B_i, where $A_i \equiv \sum_j^{\rm pixels} f_{ij}\Delta l_{ij}$ is the sum of transmissivity f_{ij} times pixel size Δl_{ij} for all pixels in the QSO spectrum with an apparent distance r to the galaxy satisfying $0.5 < r < 1.0h^{-1}$ Mpc, and $B_i \equiv \sum_j^{\rm pixels} \Delta l_{ij}$ is the total path length of the same pixels. The mean transmissivities in figure 4.8 were set equal to $\sum_i^{\rm galaxies} A_i / \sum_i^{\rm galaxies} B_i$. Points with error bars show our measurements; crosses show the mean transmissivity we measured in a large ensemble of fake data sets generated by adding a Gaussian deviate with $\sigma_z = 0.075$ ($\sim 50h^{-1}$ comoving Mpc for $\Omega_M = 0.3$,

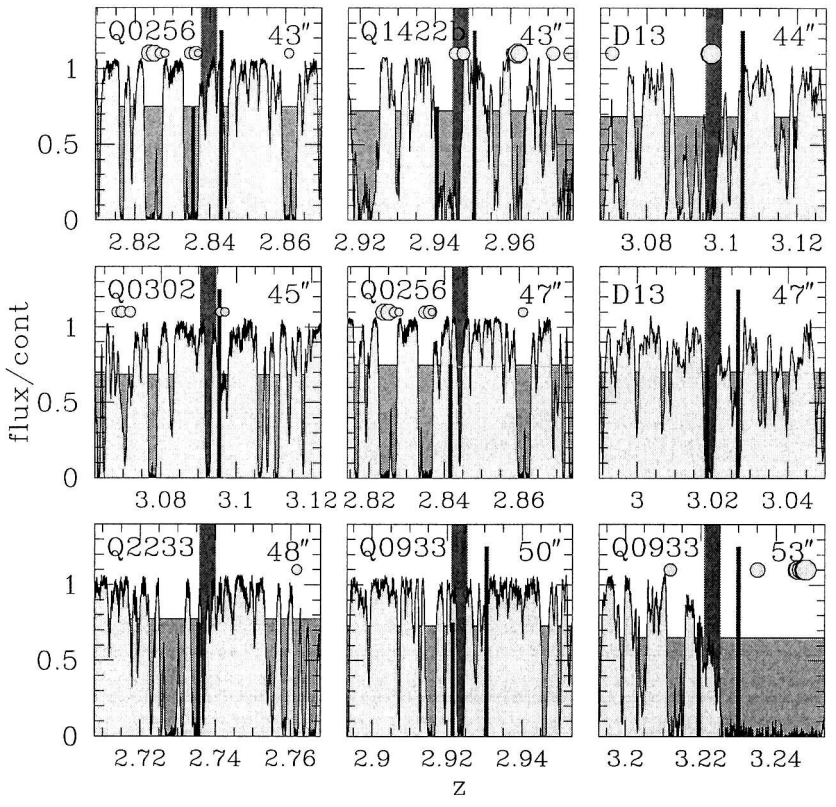

Figure 4.7 continued.

$\Omega_\Lambda = 0.7$) to the redshift of each galaxy in our sample. These fake data sets play the role of a control sample; they will resemble the true data set in most ways, except any possible correlation of galaxies and the Lyman-α forest on scales $\lesssim 50h^{-1}$ comoving Mpc will be erased. The error bars on our measurements were set to equal the 1σ scatter about the mean among our fake data sets. They may be underestimates of the true uncertainty, as discussed below.

Figure 4.8 shows again the result discussed above (cf. figures 4.4 and 4.5): on scales of ~ 1 to $\sim 5h^{-1}$ comoving Mpc Lyman-break galaxies are associated with an excess of neutral hydrogen. But on the smallest scales the trend appears to reverse. Little neutral hydrogen is found within $\sim 0.5h^{-1}$ comoving Mpc of Lyman-break galaxies.

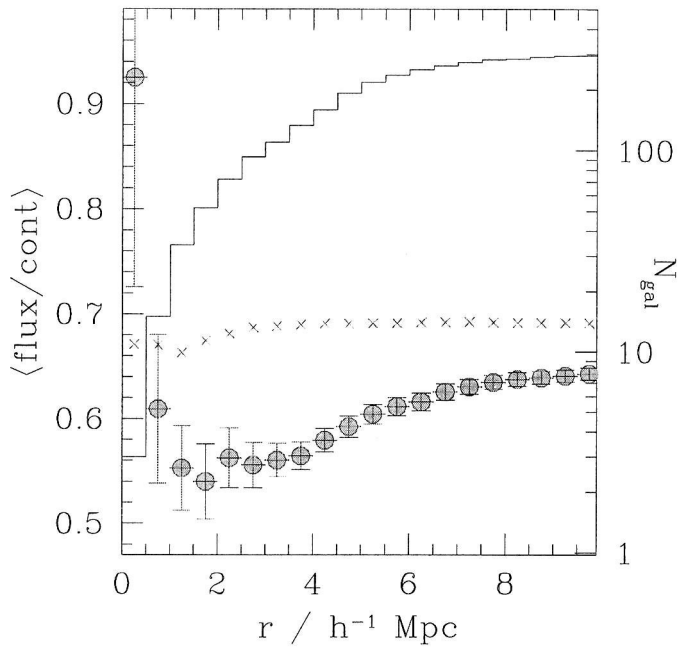

Figure 4.8 Mean intergalactic Lyman-α transmissivity as a function of comoving distance from Lyman-break galaxies. Points with error bars mark our measurements; crosses without error bars show the result if we randomize our redshifts. Refer to the left axis for the scale. Lyman-break galaxies are associated with significant neutral hydrogen overdensities (i.e., flux decrements) on scales extending to several Mpc, and with significant HI underdensities on the smallest spatial scales. The number of galaxies in our sample within each radius is shown with the continuous line (right axis).

Figure 4.9 shows that the change in mean transmissivity with distance derives from spatial variations in the relative proportion of lightly and heavily obscured pixels in the Lyman-α forest spectra: few pixels with transmissivities less than 0.5 are found within $\sim 1h^{-1}$ comoving Mpc of a Lyman-break galaxy, while a significant excess of saturated pixels with transmissivity ~ 0 are found within $\sim 4h^{-1}$ Mpc of Lyman-break galaxies.

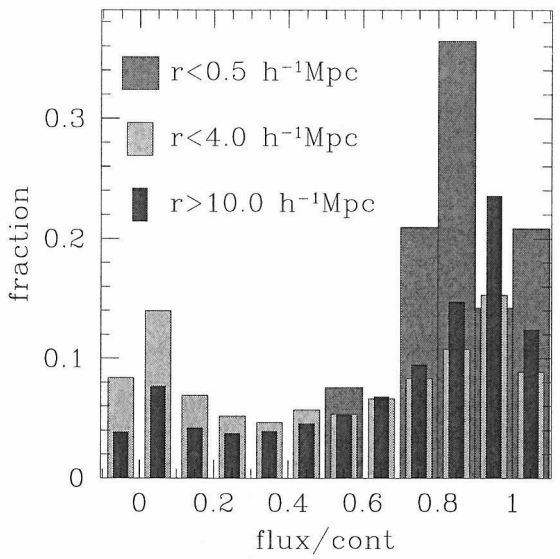

Figure 4.9 Histogram of pixel transmissivities at different distances from Lyman-break galaxies. The shape of figure 4.8 derives from a relative lack of low transmissivity pixels within $r \sim 0.5h^{-1}$ comoving Mpc of Lyman-break galaxies and an excess with $1 \lesssim r \lesssim 5h^{-1}$ comoving Mpc.

4.3.4 Damped Lyman-α systems

When estimating the mean transmissivity of the intergalactic medium as a function of distance to a Lyman-break galaxy, we deliberately excluded damped Lyman-α systems from the analysis. For completeness we will now briefly describe the association of Lyman-break galaxies with the four damped systems (table 4.2) in our sample. Figure 4.10 compares the mean overdensity of Lyman-break galaxies within cells centered on damped systems to the mean overdensity of Lyman-break galaxies within cells centered on other Lyman-break galaxies. Each cell was a cylinder with height $\Delta z = 0.025$ ($\sim 16.7h^{-1}$ comoving Mpc for $\Omega_M = 0.3$, $\Omega_\Lambda = 0.7$) and radius equal to value of $\Delta\theta$ shown on the figure's abscissa. Even at the largest value of $\Delta\theta$ (265″, or $r \sim 5.7h^{-1}$ Mpc comoving), each cylinder's diameter is significantly smaller than its height. This helped ensure that galaxies correlated with the central object would fall into the surrounding cell even in the presence of substantial redshift errors. If

Lyman-break galaxies and damped systems were similar objects, the mean density of Lyman-break galaxies around damped systems would be similar to the mean density of Lyman-break galaxies around other Lyman-break galaxies, but this is not the case. The observed number of Lyman-break galaxies close to the damped systems in our sample is instead roughly what one would expect if the two populations were independently distributed; we see no evidence for an excess of Lyman-break galaxies near damped systems. In contrast the overdensity of Lyman-break galaxies near other Lyman-break galaxies is large, as the filled circles in figure 4.10 show. Table 4.2 compares the observed number of Lyman-break galaxies near each damped system with the number one would have expected if damped systems and Lyman-break galaxies were the same objects. If they were the same objects, we would have expected to find 5.96 Lyman-break galaxies within $\Delta\theta = 265''$, $\Delta z = 0.0125$ of the damped systems. In fact we found 2. A Poisson distribution with true mean 5.96 will yield 2 or fewer counts about 6.4% of the time, so the significance of this result is slightly better than 90%. The significance can be assessed in a more empirical way by exploiting the fact that our spectroscopic sampling density in Q0933+2841 and SSA22D13 is very similar to the density in the rest of the Lyman-break galaxy sample. We selected at random from our Lyman-break galaxy catalogs many sets of two galaxies, one galaxy at roughly the redshift of the damped system in Q0933+2841, the other at roughly the redshift of the damped system in SSA22D13. We then counted the number of other Lyman-break galaxies in cylindrical cells surrounding the two galaxies in each set, and compared to the number of Lyman-break galaxies in cells surrounding the damped systems. The curve in figure 4.10 shows the frequency $P(> n)$ with which a set of two random galaxies had more galaxy neighbors than the set of two damped systems. The lack of Lyman-break galaxies within $\sim 5.7h^{-1}$ comoving Mpc ($\Delta\theta < 265''$) of these two damped systems lets us conclude with $\sim 90\%$ confidence again that Lyman-break galaxies and damped systems do not reside in similar parts

of the universe. Taken together, the data in figure 4.10 suggest that the statistical association between damped systems and Lyman-break galaxies is weak; the data are consistent with the idea that damped systems tend to reside in small potential wells that are much more uniformly distributed in space than the massive wells that presumably host Lyman-break galaxies (cf. Gawiser et al. 2001).

Table 4.2 Damped Ly-α systems [+1]

QSO	z	$\log(N_{HI}/\mathrm{cm}^{-2})$	$\log(N_{CIV}/\mathrm{cm}^{-2})$	N^a_{obs}	N^b_{exp}
Q0000-2620	3.3902	21.3	14.7	1	0.67
Q0201+1120	3.3864	21.3	13.9	0	0.45
Q0933+2845	3.2352	20.3	12.8	1	2.23
SSA22D13	2.9408	20.7	13.1	0	2.61
SSA22D13[c]	2.7379	15.1	14.4		

[a]Observed number of Lyman-break galaxies with $\Delta\theta < 265''$, $\Delta z < 0.0125$ [b]Expected number of Lyman-break galaxies if the DLA-LBG cross-correlation function were the same as the LBG-LBG correlation function [c]Not a damped system. This is the gas within $\Delta\theta = 16''$ ($90h^{-1}$ proper kpc), $\Delta z < 0.007$ of a Lyman-break galaxy in SSA22 (cf. figure 4.7). Its HI and CIV column densities are listed for comparison.

4.3.5 HeII

Heap et al. (2000) obtained a spectrum at wavelengths $1140 \lesssim \lambda_{\mathrm{obs}} \lesssim 1300$Å of one of the QSOs in our sample, Q0302-0019. This spectrum revealed that the HeII Lyman-α ($\lambda_{\mathrm{rest}} \simeq 304$Å) optical depth of the intergalactic medium in front of the QSO was large and surprisingly variable. The observed range of optical depths in the spectrum, $\tau_{\mathrm{HeII}} \sim 1$ to $\tau_{\mathrm{HeII}} \gtrsim 5$, apparently implies that the hardness of the ionizing background and the ratio of HI to HeII number density must vary significantly in the intergalactic medium at $z \sim 3$. Figure 4.11 shows that the observed variations in intergalactic HeII opacity appear to be spatially correlated with the locations of galaxies and CIV systems. Excluding the region $z > 3.24$, which is presumably affected by radiation

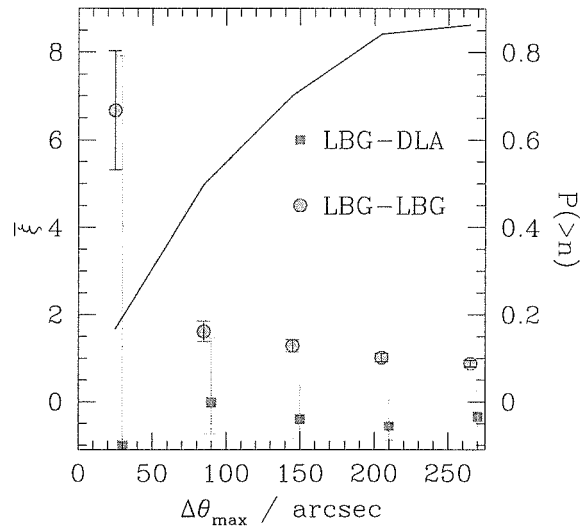

Figure 4.10 The spatial association of Lyman-break galaxies and damped Lyman-α systems. Square points show the mean overdensity of Lyman-break galaxies in cylinders of constant depth $\Delta z = 0.025$ and variable radius $\Delta\theta$ surrounding the four damped systems in our survey. Circular points show the mean overdensity of Lyman-break galaxies in similar parallelepipeds centered on other Lyman-break galaxies. Their error bars assume Poisson statistics. The line shows how frequently randomly chosen Lyman-break galaxies at similar redshifts to the two DLAs in our primary sample have more galaxy neighbors than the DLAs. Damped systems do not appear to trace out the same large-scale structure as galaxies.

from Q0302-0019 itself (e.g., Hogan et al. 1997), and the region $2.987 < z < 3.016$, which is contaminated by geocoronal Lyman-α emission, we calculate $r_s \sim 0.21, 0.27$ for the value of Spearman's rank correlation coefficient between the smoothly varying galaxy, CIV overdensities shown in figure 4.11 and the HeII absorption spectrum. The galaxy and CIV overdensities were calculated as described above, near figure 4.6. A correlation strength $r_s > 0.21$ was found for roughly 13% of randomized galaxy catalogs that we correlated with the HeII spectrum; $r_s > 0.27$ was found for roughly 6% of the CIV catalogs. Though the formal significance of the measured correlation ($\sim$ 87–94%) is hardly overwhelming, it is easy to think of reasons that the HeII opacity of the intergalactic medium might decrease near galaxies or CIV systems.

The most obvious is that the reionization of HeII should happen first in the dense regions where galaxies, metal line absorbers, and AGN reside. But this is unlikely to be the full explanation; the HeII optical depth at the mean density at $z \sim 3$ would be of order 1000 if HeII were the dominant ionization state, and so the small but significant fraction of the QSO's light that is detectable at $\lambda \lesssim 1310$Å shows that HeII must already be highly reionized almost everywhere. A more likely explanation may be that the spatial clustering bias of galaxies and AGN causes the number of HeII-ionizing photons per baryon to be largest in overdensities where galaxies and AGN tend to be found. Because the mean free path of 4Ryd photons at $z \sim 3$ is likely to be ~ 1500 km s^{-1} (Miralda-Escudé, Haehnelt, & Rees 2000), or roughly the size of independent bins in figure 4.11, we might reasonably expect to see this effect in the figure. We should also add that much of the evidence for a correlation between HeII transmissivity and galaxy or CIV density comes from redshifts $z \lesssim 2.9$. If the decrease in HeII opacity at these redshifts reflects a global change in the hardness of the ionizing background due to the growing dominance of AGN (e.g., Songaila 1998; cf. Boksenberg, Sargent, & Rauch 1998), then the correspondence of high HeII transmissivity with the observed galaxy and CIV overdensities would be only a coincidence, and much of our evidence for a connection between galaxies and HeII would be removed. It is pointless to speculate much further when we have data along only a single line of sight.

4.3.6 Summary

This completes our brief overview of the data. Their major qualitative characteristics may be summarized as follows. On scales of ~ 1 to $\sim 5h^{-1}$ comoving Mpc we see a strong statistical association of Lyman-break galaxies with neutral hydrogen and metals in the intergalactic medium. On scales smaller than $\sim 1h^{-1}$ Mpc we may see an anti-correlation between galaxies and neutral hydrogen. The following two

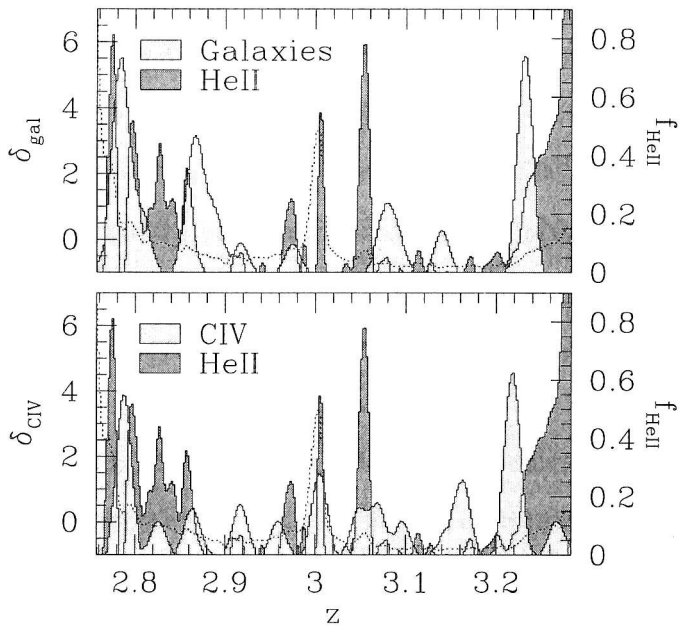

Figure 4.11 The correlation between galaxies, CIV systems, and the HeII transmissivity of the IGM. The curves in the foreground show the overdensity of galaxies and CIV systems as a function of redshift; they were produced by smoothing the list of redshifts with a Gaussian of width $\sigma_z = 0.008$. The shaded curve in the background shows the HeII Lyman-α absorption seen in the spectrum of Q0302-0019 (Heap et al. 2000) in units of 10^{-16} erg s^{-1} cm^{-2} Å^{-1} (refer to right axis). The dotted line is the error spectrum. The HeII content of the IGM is detectably reduced from its mean value in regions where the spectrum significantly exceeds its uncertainty. These regions often coincide with galaxy and CIV overdensities.

sections will consider these results in more detail.

4.4 Small scales—the galaxy proximity effect

The cross-correlation between galaxies and intergalactic material may be the most interesting at small separations. It is surely the most difficult to measure. Recall the large and relatively uncertain offsets that were required to estimate galaxies' systemic redshifts from the redshifts of the absorption and emission lines in their optical spectra (§ 4.2.2). One need not contemplate figure 4.7 for long to realize that

even minor changes to our estimated systemic redshifts could drastically alter the inferred Lyman-α transmissivity of the intergalactic medium close to Lyman-break galaxies. A few judiciously applied redshift adjustments of $\delta z \sim 0.003$ could easily erase the inflection from figure 4.8, for example, and $\delta z = 0.003$ is hardly a large adjustment. It is small compared to the range of redshifts seen in most Lyman-break galaxy spectra. It barely exceeds our optimistic estimates of the 1σ redshift uncertainty from § 4.2.2. The points with $r \lesssim 2h^{-1}$ Mpc on figure 4.8 should be viewed with some suspicion.

One way to assess how much redshift errors might have compromised our estimate of the mean intergalactic transmissivity at different distances from Lyman-break galaxies is to change each of our redshifts by an amount similar to its uncertainty, then recalculate the implied mean transmissivity. Figure 4.12 shows the result. Circles mark the average estimated transmissivity at each distance after adding a Gaussian deviate with $\sigma_z = 0.002$ to each of our redshifts; their vertical error bars show the 1σ range observed when we repeated the exercise many times. $\sigma_z = 0.002$ is roughly the redshift uncertainty that follows from the analysis of § 4.2.2, and so these points suggest that the true redshifts of our galaxies could lie anywhere within our confidence intervals without much affecting our conclusion that the Lyman-α opacity of the intergalactic medium decreases near galaxies. But our conclusion could be altered if the redshifts were actually somewhat less accurate than we believe. This is illustrated by the square points in figure 4.12, which show the mean transmissivity derived when each of our galaxy redshifts was perturbed by a Gaussian deviate with $\sigma_z = 0.004$. If we made the most pessimistic assumptions about the accuracy of our redshifts, we would be able to whittle down the significance of the proximity effect to about 1 sigma. The true significance of our detection likely lies somewhere between this estimate of 1 sigma and the estimate of ~ 3 sigma that figure 4.8 might inspire. This is not much of a foundation to build on. It may be useful to consider what

physical processes could lead to a lack of neutral hydrogen within $\sim 0.5h^{-1}$ comoving Mpc of galaxies and look for other signatures of their existence.

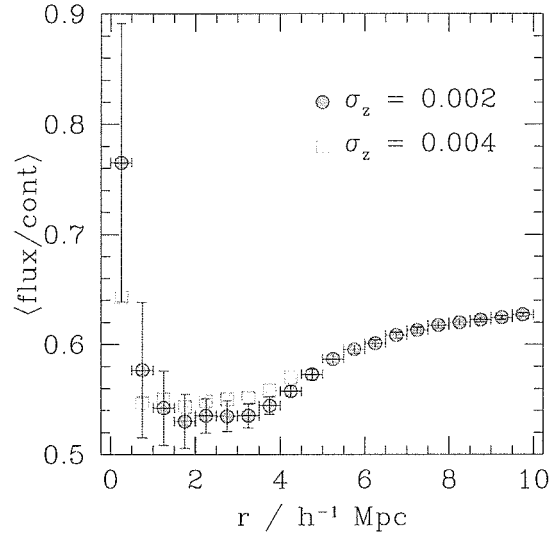

Figure 4.12 The top panel of figure 4.8 recalculated after modifying each galaxy's redshift by an amount similar to its uncertainty. Numerous fake data sets were generated by adding to each galaxy's redshift a Gaussian deviate with the standard deviation σ_z shown. Points show the average value of the transmissivity among the fake data sets; error bars show the 1σ spread. The error bars for $\sigma_z = 0.004$, suppressed for clarity, are similar to those for $\sigma_z = 0.002$. If σ_z were equal to the uncertainty in each galaxy's redshift, then each of the fake data sets would be roughly as compatible with the data as the actual data set, and any differences between the mean transmissivities in the fake and real sets would suggest that the mean transmissivity measured in the real set may have been compromised by an unusual combination of redshift measurement errors.

4.4.1 Physical origin

Ionizing radiation

Reduced Lyman-α absorption is observed in the intergalactic medium surrounding high-redshift QSOs, a fact that presumably reflects a decrease in the hydrogen neutral fraction in regions where a quasar's radiation overwhelms the ambient ionizing field (see, e.g., Weymann, Carswell, & Smith 1981; Murdoch et al. 1986; Bajtlik, Duncan,

& Ostriker 1988; Scott et al. 2000). Could a similar physical cause account for the lack of HI absorption in the vicinity of Lyman-break galaxies? A rough argument suggests that this is unlikely to be the case. Consider the mean transmissivity within $0.5h^{-1}$ comoving Mpc of an LBG, $\langle \text{flux/cont} \rangle \gtrsim 0.8$, which is substantially higher than the mean transmissivity $\langle \text{flux/cont} \rangle \sim 0.5$ we might expect in the absence of a proximity effect (cf. figure 4.8). In the SPH simulation described in White, Hernquist, & Springel (2001), an increase in the ionizing background by a factor of ~ 8 is required to increase the mean transmissivity of a random section of the Lyman-α forest from 0.5 to 0.8, and so we might guess that the ionizing flux within $0.5h^{-1}$ Mpc of a Lyman-break galaxy would have to be ~ 8 times higher than its universal mean if ionizing radiation from the galaxies were responsible for the observed proximity effect. The Lyman-break galaxies in our sample could not easily produce an ionizing flux so large, as the following crude calculation shows. If our sample can be approximated as a uniform population of galaxies with ionizing luminosity L (energy time^{-1} frequency^{-1}) and comoving number density ρ that produces a fraction $f_{\rm bg}$ of the total ionizing background $J_\nu^{\rm tot}$ (energy time^{-1} frequency^{-1} area^{-1} steradian^{-1}) at $z \sim 3$, then the contribution to the ionizing background from a single galaxy at radius r is

$$J_\nu^1 = L/(4\pi r)^2 \tag{4.12}$$

while the net contribution to the ionizing background from the population as a whole is roughly

$$J_\nu^{\rm LBG} \sim L\rho(d/c)(c/4\pi) \equiv f_{\rm bg} J_\nu^{\rm tot} \tag{4.13}$$

where d is the average distance traveled by an ionizing photon before it is absorbed. The ionizing flux will therefore be more than n times higher than its universal average $J_\nu^{\rm tot}$ within a radius

$$r_n \sim [4\pi\rho(n-1)d/f_{\rm bg}]^{-1/2} \tag{4.14}$$

of a Lyman-break galaxy. Assuming an $\Omega_M = 0.3$, $\Omega_\Lambda = 0.7$ cosmology, and substituting $\rho \sim 4 \times 10^{-3} h^3 \mathrm{Mpc}^{-3}$ for the comoving number density of Lyman-break galaxies and $d \sim 117 h^{-1}$Mpc (i.e., $\Delta z \sim 0.18$) for the comoving effective absorption distance (Madau, Haardt, & Rees 1999), we find

$$r_n \sim \sqrt{f_{\mathrm{bg}}/(n-1)} \times 0.4 h^{-1} \text{comoving Mpc.} \tag{4.15}$$

In the extreme case where all of the hydrogen-ionizing background is produced by Lyman-break galaxies with $\mathcal{R} < 27$ (see, e.g., Steidel, Pettini, & Adelberger 2001), only $\sim 50\%$ of it will be produced by Lyman-break galaxies with $\mathcal{R} < 25.5$, provided that the ratio $f_\lambda(1500\text{Å})/f_\lambda(900\text{Å})$ is independent of luminosity and that the rest-frame 1500Å luminosity distribution of Lyman-break galaxies is a Schechter function with knee $\mathcal{R}_* = 24.5$ and faint-end slope $\alpha = -1.6$ (Adelberger & Steidel 2000), and so we can take 0.5 as a rough upper limit on f_{bg}. This implies an upper limit of $r_{\mathrm{max}} \lesssim 0.1 h^{-1}$ comoving Mpc for the radius within which ionizing radiation from Lyman-break galaxies could raise the ionizing flux to ~ 8 times its universal value and increase the mean transmissivity from 0.5 to 0.8. The argument is crude in a number of ways, but the observed radius with $\langle \mathrm{flux/cont} \rangle \sim 0.8$ is ~ 5 times larger than r_{max} and r_{max} does not depend strongly on any of its parameters f, n, d, or ρ. The change in mean transmissivity near Lyman-break galaxies appears unlikely to be produced solely by the Lyman-continuum radiation they emit.

Galactic superwinds

Could winds driven by the combined force of numerous supernova explosions within Lyman-break galaxies be responsible instead? Strong winds with velocities exceeding the escape velocity have been observed around a large fraction of starburst galaxies in the local universe (e.g., Heckman et al. 2000). Similar outflows are seen in Lyman-break galaxies as well (cf. § 4.2.2; Pettini et al. 2001; Pettini et al. 2002). Though

the typical velocity of a Lyman-break galaxy's interstellar lines relative to its nebular lines is only $\sim 170\mathrm{km\,s^{-1}}$, the velocity exceeds $300\mathrm{km\,s^{-1}}$ for roughly one third of the galaxies in the sample of § 4.2.2. Moreover the interstellar material within an individual Lyman-break galaxy does not all flow outward at a single rate. Instead a reasonable fraction of the absorbing interstellar material has been accelerated to velocities significantly higher the mean interstellar velocity. Pettini et al. (2002) found absorbing interstellar gas with blueshifts of up to ~ 750 km s^{-1} in MS1512-cB58, for example, a galaxy with a mean interstellar blueshift of ~ 250 km s^{-1}. The large velocity widths of most Lyman-break galaxies ($\sigma_v \sim 180$–320 km s^{-1}; Steidel et al. 1996) show that this situation must be common. The typical Lyman-break galaxy apparently contains absorbing material flowing outwards with a range of velocities $0 \lesssim v \lesssim 600$ km s^{-1}.

In local galaxies, where similar outflows are observed, a distribution of velocities from 0 to v_{max} is generally interpreted as evidence that winds from supernovae are stripping material from interstellar clouds and accelerating it to the velocity v_{max} (e.g.. Heckman et al. 2000). If Lyman-break galaxies' absorption spectra were interpreted in the same way, one would conclude that most of the absorbing material will eventually be accelerated to a velocity of ~ 600 km s^{-1}. Appendices 4.E, 4.F, and 4.G consider the implications of 600 km s^{-1} outflows from Lyman-break galaxies. Appendix 4.E argues that ~ 600 km s^{-1} winds would be able to escape potential wells as deep as those that presumably surround Lyman-break galaxies, and shows that the release of supernova energy implied by the galaxies' star-formation rates and stellar masses would be sufficient to set massive ~ 600 km s^{-1} winds in motion. Appendix 4.F considers the likely effects of the escaping winds on the intergalactic medium, showing first that regions through which the shock from the wind has passed will likely produce little Lyman-α absorption while the galaxy is forming stars, and second that the ultimate effect of the shocks should be an increase in the HI content

of the intergalactic medium. Appendix 4.G considers simple models for the winds' propagation into the intergalactic medium. We argue that $r \sim 0.5h^{-1}$ comoving Mpc, the observed radius of the galaxy proximity effect, is comparable to the radius these winds are expected to reach during the typical $\sim$ 300Myr star-formation time-scale of Lyman-break galaxies. A further rough calculation suggests that a galaxy's wind shell will continue to coast for $\sim$ 1 Gyr after star formation has ceased, and that the enclosed rarefied cavity will last another $\sim$ Gyr before being crushed by gravitational instability. We argue that the wind from a galaxy at $z \sim 3$ will typically disturb the surrounding intergalactic medium for a total time of 2–3 Gyr, or roughly ten times the estimated star-formation time-scale of the galaxies. While the total volume affected by the winds from Lyman-break galaxies observed at any particular time would only be $\sim$ 2%, the total volume filling factor of wind-influenced regions could therefore be $\sim$ 20%, and might approach unity in the regions with the largest galaxy overdensities.

The upshot is that these winds could plausibly escape their galaxies' potentials and drive the intergalactic material from a cavity of radius $r \sim 0.5$ comoving Mpc surrounding each galaxy. Superwinds might therefore be responsible for the apparent lack of neutral hydrogen near Lyman-break galaxies. In the remainder of this section we will look for other evidence that this might be the case.

4.4.2 Metals

If Lyman-break galaxies drive winds into their surroundings, one might expect to see an increase in the number density of metal-line absorption systems near them. The discussion above and in the appendices suggests that any material ejected by a Lyman-break galaxy would be likely to lie within $\sim$ 0.5 comoving Mpc of the galaxy and to have a redshift difference $\lesssim 600$ km s^{-1}. These numbers are uncertain. Aside from our crude spherical model and its poorly constrained parameters (e.g., fraction of supernova energy that might be imparted to the winds), there are the

complications that winds from different galaxies will have advanced to different radii, that winds slow as they advance, and that much of a wind's velocity may be directed perpendicular to the sightline. Nevertheless the numbers above tell us roughly where we should search for metals that might have been ejected from Lyman-break galaxies.

Catalogs of the CIV absorption systems in each QSO's spectrum were constructed by scanning by eye for double absorption lines with the correct spacing and relative strengths for the redshifted CIVλ1549 doublet. Rough column densities for each system were estimated with equation 4.E.1 after fitting $e^{-\tau_\lambda}$, with τ_λ a Gaussian, to both components of the doublet. CIV systems with similar redshifts were treated as independent systems if their velocity differences exceeded twice the quadrature sum of their velocity full widths. In the case of Q1422+2309, our CIV catalog agrees well with the more carefully constructed catalog of Ellison et al. (2000), though it differs somewhat in the arbitrary grouping of neighboring CIV systems into single absorption complexes.

Ten galaxies in our primary sample lie within $\Delta\theta = 35''$ ($\sim 0.75h^{-1}$ comoving Mpc for $\Omega_M = 0.3$, $\Omega_\Lambda = 0.7$) of the QSO sightline. In nine of the ten cases there is detectable CIV absorption in the QSO spectrum within 600 km s^{-1} of the galaxy's redshift. The lone exception lies near the sightline to SSA22D13, a faint QSO whose moderate resolution spectrum reveals only the strongest CIV systems. In three cases, shown in figure 4.13, the CIV absorption is exceptionally strong and absorption due to many species is evident. The galaxies shown in the figure, SSA22-MD36, Q2233-MD34, and SSA22-C35, lie $17''$, $31''$, and $33''$, respectively, from their background QSO's sightline; of all the galaxies in our sample, their angular separations to the sightline are the 3rd, 6th, and 8th closest. The metal line system close to Q2233-MD34 has the largest CIV column density of any in our QSO spectra; the system close to SSA22-MD36 has the third largest. Does this correspondence of metal line systems with galaxies near the sightline imply some physical connection between the

two, or could it be a coincidence? Should we be surprised that 2 of the 3 strongest CIV systems in our sample lie within $\Delta z = 600\mathrm{km\,s^{-1}}$ and $\Delta\theta = 35''$ of a Lyman-break galaxy?

To address this question, we need some estimate of the observed overdensity of Lyman-break galaxies near CIV systems relative to what would be expected if they were distributed independently in space. We can estimate the number of Lyman-break galaxies that would lie so close to the 3 strongest CIV systems if galaxies and metal systems were independently distributed by generating a large ensemble of fake data sets where each galaxy within $\Delta\theta = 35''$ of the sightline is assigned a redshift drawn at random from our selection function. See appendix 4.C. Among these fake data sets, the mean number of galaxies that lie within $\Delta z = 600\mathrm{km\,s^{-1}}$ of one of the three strongest CIV systems is 0.049. Since the observed number is 2, the implied overdensity of Lyman-break galaxies is $\bar{\xi}_{cg} \sim 40$. Only 1 time in 1000 will sampling from a Poisson distribution with a true mean of 0.049 yield a value of ≥ 2, so we can conclude with confidence that strong CIV systems and Lyman-break galaxies are not distributed independently.

But this does not show that the observed metals were driven out of the galaxy by a superwind. The number density of Lyman-break galaxies in cells centered on other Lyman-break galaxies is much higher than the number density in randomly placed cells, for example, yet few believe that one galaxy ejected the next. Is it possible that galaxies and CIV-systems tend to fall near each other for the same reason that galaxies fall near each other, because they all trace the same large-scale structure? A simple way to address this issue is to use the observation of Quashnock & Vanden Berk (1998) that the correlation function of CIV systems at $z \sim 3$ is similar to the correlation function of Lyman-break galaxies, a fact compatible with the idea that CIV systems and Lyman-break galaxies are similar objects. Suppose CIV systems and Lyman-break galaxies were in fact the same objects, but the CIV

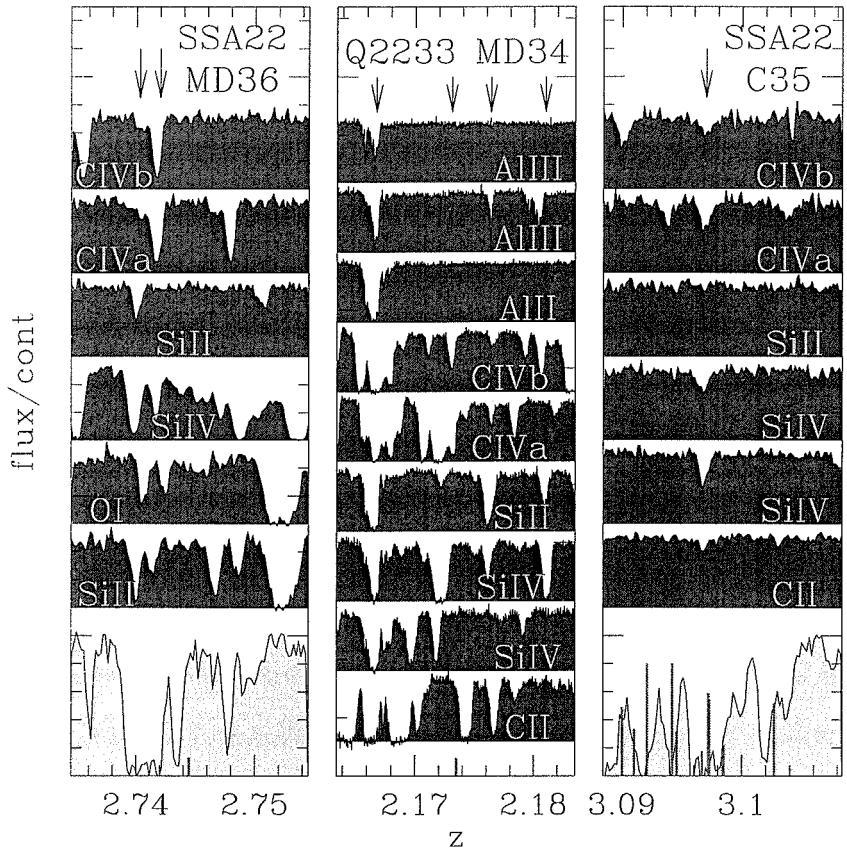

Figure 4.13 The Lyman-α and metal absorption along three QSO sightlines than pass within (from left to right) 17″, 31″, and 33″ (100, 210, 170 proper h^{-1} kpc) of known $z \sim 3$ Lyman-break galaxies. Sections of the QSO spectrum corresponding to different species were extracted and aligned. The bottom spectrum segment shows the HI absorption; upper segments show the associated metal line absorption as indicated. Bluer lines are on the bottom. Redshifts with detected metal lines are marked by arrows. Absorption in the extracted spectral segments can be produced by other metal lines at other redshifts, and (in some cases) intergalactic Lyman-α at higher redshift, and the observed absorption can believably be associated with metals at the galaxy's redshift only when it is observed in more than one line. Galaxy locations are marked with vertical bars, as in figure 4.4; the galaxy closest to the sightline lies in the middle of the extracted spectrum. The velocity offsets between the absorption in the QSO spectrum and the galaxy itself ($\sim 100 - 600$ km s^{-1}) are comparable to the measured outflow velocities of the galaxies (e.g., Pettini et al. 2001).

associated with each galaxy extended only to radii small compared to the smallest galaxy-QSO impact parameter in our sample, so that the detected CIV absorption

could never have been produced by a galaxy we observed. In this case we would expect the overdensity of galaxies within $\Delta\theta = 35''$ and $\Delta z = 600\mathrm{km\,s^{-1}}$ of a CIV system to be roughly equal to the mean overdensity of Lyman-break galaxies within the same distance of another Lyman-break galaxy. Among the 697 Lyman-break galaxies with the most certain redshifts in 13 fields of our survey, 31 unique pairs have a separation $\Delta\theta < 35''$ and $\Delta z < 600\mathrm{km\,s^{-1}}$ while 3.92 would have been expected if the galaxies were distributed uniformly. The implied galaxy-galaxy overdensity $\bar{\xi}_{gg} = 6.9$ is significantly smaller than the measured galaxy-CIV overdensity $\bar{\xi}_{gc} = 40$. This suggests the spatial coincidence of Lyman-break galaxies and CIV systems may be too strong to be explained by arguing that both trace the same large scale structure, that both tend to reside in the same clusters and shun the same voids. A more direct connection between the observed CIV systems and galaxies appears to be required.

This sort of argument can be formalized with a statistical inequality derived in appendix 4.B. If f is a discrete (i.e., Poisson) realization of the continuous function f', g is a discrete realization of the continuous function g', and $\bar{\xi}_{fg}$ denotes the mean value within some volume of the cross-correlation function ξ_{fg} between f and g, then $\bar{\xi}_{fg}$ can exceed $(\bar{\xi}_{ff}\bar{\xi}_{gg})^{1/2}$ only if the locations of particles in g are influenced by where particles happen to lie in f or vice versa. This would be the case if (for example) g' were equal to f' and the particles in g were a random subset of those in f, or if each particle in f were surrounded by a cloud of particles in g. The statement holds provided the correlation functions are volume averaged with one of a class of 3D weighting functions that includes the Gaussian. If we could show that the Gaussian-weighted cross-correlation function of galaxies and CIV systems $\bar{\xi}_{gc}$ exceeded the root-product of the Gaussian-weighted autocorrelation functions $(\bar{\xi}_{gg}\bar{\xi}_{cc})^{1/2}$, we would have evidence that the number density of galaxies in a random volume directly affected (or was directly affected by) the number density of CIV systems in the same volume.

The mean overdensity of Lyman-break galaxies in Gaussian ellipsoids with $\sigma_z =$

$350\mathrm{km\,s^{-1}}$ and $\sigma_\theta = 20''$ that are centered on the strongest three CIV systems in our sample is $\bar{\xi}_{gc} = 21$. The mean overdensity of Lyman-break galaxies in similar ellipsoids centered on other Lyman-break galaxies is $\bar{\xi}_{gg} = 7$. The mean overdensity of CIV systems in similar ellipsoids centered on other CIV systems will be comparable, $\bar{\xi}_{cc} \sim 7$, if Quashnock & Vanden Berk's (1998) estimate of the CIV correlation function remains accurate on small spatial scales. $\bar{\xi}_{gc}$ evidently exceeds $(\bar{\xi}_{gg}\bar{\xi}_{cc})^{1/2}$ by a large amount. This may be an aberration. The sample is small. But if the result holds in a much larger sample of galaxies and CIV systems, we would have solid evidence for a physical link between galaxies and the strong CIV absorption observed $\sim 0.5h^{-1}$ comoving Mpc away.

In any case, the connection between Lyman-break galaxies and CIV systems clearly weakens as the column density of the CIV systems is reduced. If we take the 20 strongest CIV systems, for example, rather than the 3 strongest, the mean overdensity of Lyman-break galaxies in similar Gaussian ellipsoids surrounding the CIV systems is $\bar{\xi}_{gc} = 9.0$. This still exceeds $\bar{\xi}_{gg} = 7 \sim \bar{\xi}_{cc}$, but probably not by a significant amount. The mean overdensity in Gaussian ellipsoids surrounding every CIV system in our sample is a paltry $\bar{\xi}_{gc} = 2.8$, showing that there is little evidence that the weakest CIV systems are directly associated with the observed galaxies. The dependence of the cross-correlation strength $\bar{\xi}_{gc}$ on column-density is shown in figure 4.14. Also shown is $\bar{\xi}_{gg}$ and its uncertainty. Cylindrical cells with $\Delta\theta < 35''$ and $\Delta z < 600\mathrm{km\,s^{-1}}$ were used when calculating the mean overdensities $\bar{\xi}$, rather than the ellipsoidal Gaussians discussed above. This simplified the calculation of the uncertainties in $\bar{\xi}$, which we optimistically took to be Poisson, but it means that $\bar{\xi}_{gc}$ does not formally need to satisfy inequality 4.B.7. But similar conclusions about the column densities where 4.B.7 is and is not satisfied would follow had we averaged in Gaussian ellipsoids instead.

It is interesting to address the association of galaxies and metals in a slightly

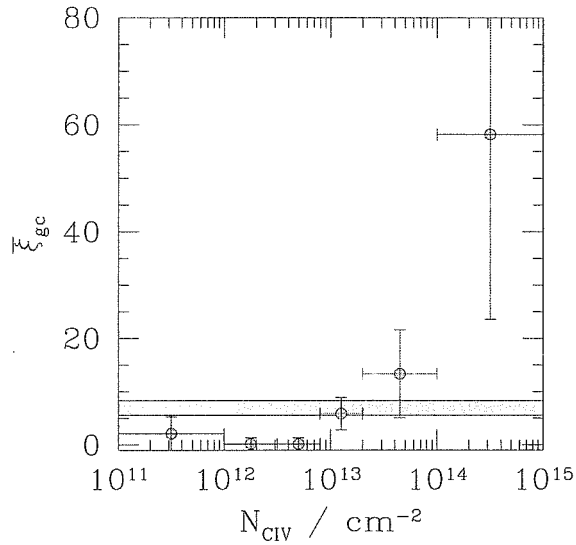

Figure 4.14 The observed overdensity of CIV systems within $\Delta z = 600$ km s^{-1} and $\Delta\theta = 35''$ of a Lyman-break galaxy as a function of CIV column density. The spatial association of Lyman-break galaxies and CIV systems increases strongly with column density. The shaded horizontal region shows the overdensity of Lyman-break galaxies within a similar distance of another Lyman-break galaxy. As explained in § 4.4.2, the presence of CIV points above this region suggests strong CIV systems and Lyman-break galaxies may be identical objects.

different way. What fraction of detectable CIV absorption is produced by gas within $\Delta\theta < 35''$, $\Delta z < 600\mathrm{km\,s^{-1}}$ of a Lyman-break galaxy? Because only a small fraction of the Lyman-break galaxies[7] in any field at $z \sim 3$ are included in our spectroscopic sample, we would not expect most CIV systems to lie near a galaxy in the sample even if every CIV system had a Lyman-break galaxy nearby. Limited observing time allowed us to obtain spectra for fewer than half of the photometrically detected Lyman-break galaxies in each field, for example, and Monte-Carlo simulations (Steidel et al. 1999) suggest that only $\sim 50\%$ of all Lyman-break galaxies are included in our photometric sample even at $z = 3.0$ where our selection is most efficient. We know our sample is seriously incomplete; but we can attempt to correct for this and

[7]i.e., the galaxies with optical magnitude $\mathcal{R} \lesssim 25.5$ and dust reddening $0 < E(B-V) \lesssim 0.5$ that have a non-zero probability of satisfying our photometric selection criteria; see Steidel et al. (1999).

estimate what fraction of CIV systems would have been found to lie within $\Delta\theta < 35''$, $\Delta z < 600\mathrm{km\,s^{-1}}$ of a Lyman-break galaxy if we had been able to measure the redshifts of every Lyman-break galaxy our fields. The result is shown in figure 4.15. Circles mark the fraction f_{LBG} of detected CIV systems with different column densities that lie within $\Delta\theta < 35''$, $\Delta z < 600\mathrm{km\,s^{-1}}$ of a galaxy in our spectroscopic sample. Stars mark the expected fraction if every CIV system lay within this distance of one (and only one) Lyman-break galaxy. Crosses mark the expected fraction if CIV systems and Lyman-break galaxies were distributed independently. At column densities $N_{\mathrm{CIV}} \gtrsim 10^{13.5}\mathrm{cm^{-2}}$ the observed number of Lyman-break galaxies close to CIV systems significantly exceeds the number expected if only one Lyman-break galaxy lay within $\Delta\theta < 35''$, $\Delta z < 600\mathrm{km\,s^{-1}}$ of each CIV system. This apparently shows that the strongest CIV absorption is produced in gas with several Lyman-break galaxies nearby, an interesting observation for which we have no ready explanation. Confidence limits on the fraction of CIV systems that have at least one Lyman-break galaxy within $\Delta\theta < 35''$ and $\Delta z < 600\mathrm{km\,s^{-1}}$ can be crudely derived by estimating the mean number of Lyman-break galaxies within this distance of a CIV system, $\bar{N}_{\mathrm{LBG}}$, then using Poisson statistics to work out how frequently sampling from a distribution with this mean would yield one or more galaxies $(1 - e^{-\bar{N}_{\mathrm{LBG}}})$. Averaging over the range of $\bar{N}_{\mathrm{LBG}}$ compatible with the data leads to the rough confidence intervals shown in figure 4.15. The data evidently suggest that the majority of CIV absorption with $N_{\mathrm{CIV}} \gtrsim 10^{13}\mathrm{cm^{-2}}$ is produced by gas that lies no farther than $\Delta\theta < 35''$ and $\Delta z < 600\mathrm{km\,s^{-1}}$ from a Lyman-break galaxy, i.e., by gas that could plausibly have been ejected from the galaxies in an outflow.

How might weaker metal-line absorption systems with $N_{\mathrm{CIV}} \lesssim 10^{13}\mathrm{cm^{-2}}$ be associated with Lyman-break galaxies? This question can be straightforwardly addressed with results presented in § 4.6 below. The numerous weak CIV absorbers dominate the cross-correlation function of galaxies and CIV systems, which (as we will show)

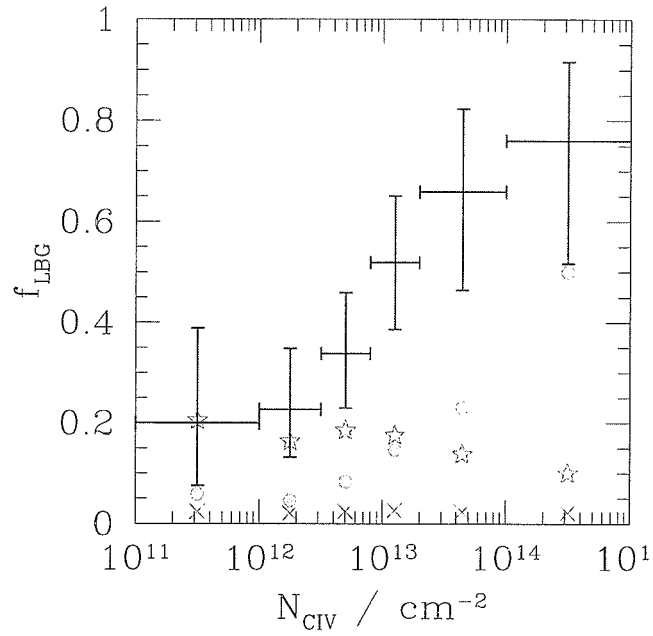

Figure 4.15 The fraction $f_{\rm LBG}$ of detected CIV systems that lie within $\Delta z = 600$ km s^{-1} and $\Delta\theta = 35''$ of a Lyman-break galaxy as a function of CIV column density. Circles mark the fraction that lie within this distance of a galaxy in our spectroscopic sample. Stars mark the expected fraction if each CIV system had one galaxy within this distance. Crosses mark the expected fraction if CIV systems and Lyman-break galaxies were independently distributed. The low value of $f_{\rm LBG}$ of the stars reflects the severe incompleteness of our spectroscopic sample; simulations suggest that only $\sim$ one fifth of Lyman-break galaxies with redshifts similar to those of the CIV systems would satisfy our photometric selection criteria and be included in our final spectroscopic catalogs. Error bars mark the estimated fraction of CIV systems that lie within $\Delta z = 600$ km s^{-1} and $\Delta\theta = 35''$ of a Lyman-break galaxy once our selection effects are corrected.

is roughly a power-law of the form $\xi_{\rm gc} = (r/r_{\rm gc})^{-\gamma_{\rm gc}}$ with $r_{\rm gc} \simeq 3.2h^{-1}$ comoving Mpc and $\gamma_{\rm gc} = 1.6$. The mean number of Lyman-break galaxies within a distance r of a randomly chosen CIV system is therefore

$$N_{\rm LBG} \simeq \frac{4}{3}\pi r^3 n_{\rm LBG}\left(1 + \frac{3r^{-\gamma}}{(3-\gamma)r_{\rm gc}^{-\gamma}}\right), \tag{4.16}$$

where $n_{\rm LBG} \simeq 4 \times 10^{-3}h^3$ Mpc^{-3} is the comoving number density of Lyman-break galaxies. This shows that the numerous weak CIV systems will typically have ~ 1 Lyman-break galaxy within a comoving distance of $\sim 2.4h^{-1}$ Mpc. If they were

randomly distributed, the nearest Lyman-break galaxy would lie $\sim 3.9h^{-1}$ Mpc away. Weak CIV systems also tend to lie close to Lyman-break galaxies, though not as close as their higher column-density counterparts.

We conclude that metals in the intergalactic medium are closely connected with the star-forming galaxies we observe. Most CIV systems lie within $\sim 2.4h^{-1}$ Mpc of a Lyman-break galaxy; higher column density systems tend to lie closer still; and the highest column density systems are so strongly correlated with Lyman-break galaxies that we may be forced to conclude that they are the same objects, a result that is remarkable because the absorbing gas is typically $\sim 0.5h^{-1}$ comoving Mpc from the galaxies' stars. One might enlarge upon this. We will not. It is the subject of another paper (Steidel et al. 2002, in preparation; but see § 4.6 below). For now we will mention only that the large HI column densities of the metal line systems provide one argument against an outflow origin for them. The column densities significantly exceed our naive expectations from § 4.F; shells of fast-moving winds might be too hot to contain so much neutral hydrogen. But because the properties of wind shells are difficult to predict, this argument is not damning. A plausibly high metallicity in the outflow, for example, might lead to significant cooling and an enhancement in the shell's neutral fraction (see § 4.F).

4.4.3 Dust

Figure 4.16 shows a curious characteristic of our data. The observed surface density of Lyman-break galaxy candidates (i.e., objects whose colors satisfy equation 4.1) is significantly lower within $\sim 30''$ of the background QSOs than elsewhere in our images. The QSOs tend to lie $\sim 200h^{-1}$ comoving Mpc behind the typical galaxy in our sample, so it is hard to imagine they could influence the observed number density of Lyman-break galaxies near the sightline. Perhaps the result is merely a statistical fluctuation. Roughly six of the 110 data points with error bars on the figures of this

paper should be 2σ fluctuations. This may be one. Another obvious possibility is that the photons from the QSO are affected by passing within $\sim 30''$ of a Lyman-break galaxy. For $\Omega_M = 0.3$, $\Omega_\Lambda = 0.7$, $30''$ corresponds to $0.65h^{-1}$ comoving Mpc at $z = 3$, roughly the observed radius of the galaxy proximity effect. Heckman et al. (2000) have shown that superwinds from local galaxies sometimes contain dust, and Shapley et al. (2001) claim that the rest-frame optical colors of Lyman-break galaxies suggest a similar ejection of dust at $z \sim 3$. Could metal-enriched material flowing out of Lyman-break galaxies be dusty enough to partially obscure background QSOs? This would mean that a sample biased towards the brightest QSOs, such as ours, would tend to contain QSOs whose sightlines do not pass within $\sim 30''$ of many Lyman-break galaxies. The required level of dust obscuration is not large, as the following simple calculation shows. We observed an average of 1.0 Lyman-break galaxy within $30''$ of each QSO sightline, and would have expected 1.9 if Lyman-break galaxy positions were uncorrelated with the QSO position. The difference is consistent with the idea that QSOs will tend to be included in our sample if their sightlines pass within $30''$ of 0, 1, or 2 Lyman-break galaxies and excluded otherwise. How faint would a QSO have to become to be excluded from our sample? We chose to observe each QSO field in our sample largely because the QSO was the brightest one that (a) fell in the right redshift range, (b) lay in a region of the sky with acceptably low 100μm emission from Galactic cirrus, and (c) could be observed for most of the night during our allocated telescope time. If a QSO's apparent luminosity were reduced enough to make it the second brightest object satisfying these criteria rather than the first, it would likely not be in our sample. Assuming that the bright end of the QSO luminosity distribution has the shape $n(l) \propto l^{-\alpha}$ with $\alpha = 3.7$ (e.g., Pei 1995), the second brightest object satisfying our criteria would typically have been $2^{-1/(\alpha-1)} \sim 0.8$ times as bright as the first. Figure 4.16 could be explained if the presence of 3 Lyman-break galaxies within $30''$ of a QSO sightline were sufficient to dim the QSO by $\sim 20\%$. The implied

extinction per galaxy is not large, $20/3 \sim 7\%$, only about one hundredth of the dust extinction that Lyman-break galaxies' own stars are thought to suffer (e.g., Adelberger & Steidel 2000), but the net effect of similar extinction from galaxies at all redshifts might be significant (e.g., Ostriker & Heisler 1984; Fall & Pei 1993). If low level dust obscuration on $\sim 0.6h^{-1}$ Mpc scales is responsible for the observed anti-correlation of galaxy and QSO positions, we would expect the effect to be most pronounced for the brightest QSOs, which have the steepest luminosity function, and to be completely absent in samples selected without regard to the QSO luminosity. Both predictions will be easy to test. It is interesting (if not particularly significant) that the only QSO in our sample without a reduced density of Lyman-break galaxies near the sightline, SSA22D13, lies in the one field we chose to observe without any knowledge of the QSO it contained.

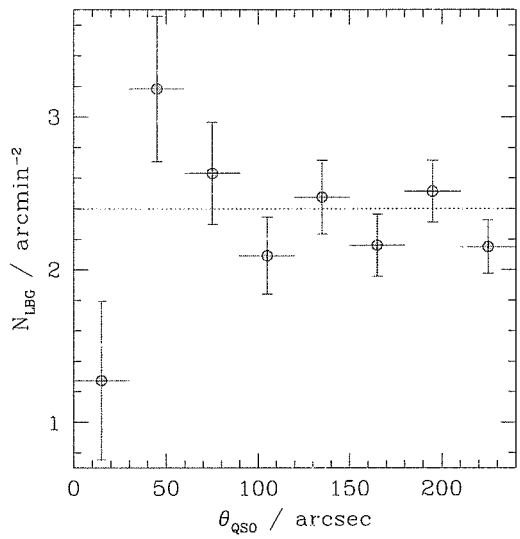

Figure 4.16 The mean number density of Lyman-break galaxies in circular annuli surrounding each background QSO. There is marginally significant evidence of a anti-correlation of foreground galaxy and background QSO positions.

Low-level dust obscuration extending $\sim 0.6h^{-1}$ comoving Mpc from each Lyman-break galaxy might also have a measurable effect upon the galaxies' angular correlation function, since the more distant member of each Lyman-break galaxy pair could be partially obscured by the nearer member's dust. If the typical obscuration within $\sim 0.6h^{-1}$ comoving Mpc is $\sim 7\%$, as estimated above, then the effective magnitude limit of our survey would be reduced from $\mathcal{R} = 25.50$ to 25.43 within $\sim 30''$ of foreground Lyman-break galaxies, and the observed number density of background Lyman-break galaxies would consequently be reduced by $\sim 9\%$ for a Schechter luminosity distribution with $\mathcal{R}_* = 24.5$, $\alpha = -1.6$. Assuming the true angular correlation function of Lyman-break galaxies is $\omega(\theta) \propto \theta^{-\beta}$ with $\beta \sim 0.5$ and $\omega(30'') = 0.1$ (Giavalisco & Dickinson 2001), the mean surface density of background Lyman-break galaxies within $30''$ of a foreground Lyman-break galaxy would be lowered from $\left[1+2\omega(30'')\right]\bar{\Sigma}/(2-\beta) \simeq 1.13\bar{\Sigma}$ to $\sim 1.03\bar{\Sigma}$ where $\bar{\Sigma}$ is the mean surface density of Lyman-break galaxies. Dust obscuration of $\sim 7\%$ from Lyman-break galaxies' winds would therefore be sufficient to make the galaxies' angular correlation function approach zero on angular scales just below $30''$. The data (Porciani & Giavalisco 2001) appear consistent with this possibility.

4.5 Large scales—the galaxy/forest correlation coefficient

In the previous section we examined the intergalactic medium within $\sim 1h^{-1}$ comoving Mpc of Lyman-break galaxies and found evidence that the galaxies were influencing the intergalactic gas in their vicinity. In this section we will turn our attention to the correlation between galaxy and HI density on $\sim 10h^{-1}$ Mpc comoving scales that figure 4.5 makes apparent. Our thesis is that this correlation is remarkably strong,

strong enough to have interesting implications.

One can appreciate the surprising strength of this correlation by considering the geometrical situation that the figure represents. One the x axis is $\bar{f}_{0.02}$, the mean Lyman-α transmissivity of the intergalactic medium along a line segment of length $\Delta z = 0.02$ ($\sim 13.4h^{-1}$ comoving Mpc for $\Omega_M = 0.3$, $\Omega_\Lambda = 0.7$). On the y axis is $\langle \delta_{\rm gal} | \bar{f}_{0.02} \rangle$, the average galaxy density in a surrounding rectangular parallelepiped of depth $\Delta z = 0.02$ and of length and width $\Delta\theta \sim 7'$–$14'$ (~ 9–$18h^{-1}$ comoving Mpc; the actual lengths and widths of each cell differ from field to field and are given in table 4.1). The large correlation coefficient between $\bar{f}_{0.02}$ and $\delta_{\rm gal}$ shows that one can predict the number density of galaxies in a cell of comoving volume $\sim 13^3 h^{-3}$ Mpc^3 with reasonable accuracy by measuring the Lyman-α transmissivity along a single skewer through the center of the cell.

It is generally believed that variations in the density of galaxies and of HI are closely connected with variations in the underlying density of matter, but measuring the baryon density along a $\sim 13h^{-1}$ Mpc skewer would not allow one to predict the matter density in the surrounding cell with similar accuracy. As shown in appendix 4.A.2, if the spatial distribution of baryons is proportional to the spatial distribution of matter smoothed by a Gaussian with standard deviation $R_f \equiv \sqrt{2}/k_F \sim 0.04h^{-1}$ comoving Mpc comparable to the Jeans length (Gnedin & Hui 1998; McDonald *et al.* 2000; Zaldarriaga, Hui, & Tegmark 2001), then the correlation coefficient of baryon density along the skewer with the matter density in the cell can be written

$$r_{\rm mass} = \frac{\int d^3k P(\mathbf{k}) W_c(\mathbf{k}) W_l^*(\mathbf{k}) e^{-(k/k_F)^2}}{\left(\int d^3k_1 P(\mathbf{k}_1) |W_c|^2(\mathbf{k}_1) \int d^3k_2 P(\mathbf{k}_2) |W_l|^2(\mathbf{k}_2) e^{-2(k/k_F)^2} \right)^{1/2}} \tag{4.17}$$

where $W_c(\mathbf{k})$ is the Fourier transform of the cell, $W_l(\mathbf{k})$ is the Fourier transform of the skewer, $P(\mathbf{k}) \simeq (1 + k_z^2/|\mathbf{k}|^2) P(k)$ is the power-spectrum of matter fluctuations in redshift space, and $P(k)$ is the power-spectrum of matter fluctuations in real space.

The relationship between $P(\mathbf{k})$ and $P(k)$ takes into account peculiar velocity distortions from the linear growth of perturbations; see, e.g., Kaiser 1987. For the $\sigma_8 = 0.9$, $\Gamma = 0.21$ CDM power-spectrum $P(k)$ measured in the $\Omega_M = 0.3$, $\Omega_\Lambda = 0.7$, $h = 0.7$, $L_{\rm box} = 141h^{-1}$ comoving Mpc GIF N-body simulation at $z = 3$ (Kauffmann et al. 1999), and for cubical cells with side-length equal to the skewer length $l = 13.4h^{-1}$ comoving Mpc, equation 4.17 is roughly equal to $r_{\rm mass} \simeq 0.35$, significantly smaller than the observed correlation coefficient ($|r_{gf}| = 0.63 \pm 0.07$, § 4.3) between transmissivity on the skewer and galaxy density in the surrounding cell. The difference between the correlation coefficient of equation 4.17 and our observed correlation coefficient justifies our statement that the observed correlation coefficient is surprisingly large.

How might the large observed correlation coefficient arise, given the (presumed) weakness of the correlation in the underlying distribution of matter? One idea is that galaxy bias might be responsible, since we have observed the density of galaxies in the surrounding cell, not the density of matter. Could some complicated relationship between galaxy and matter fluctuations lead to an increase in the strength of the cell-skewer correlation coefficient? A little thought shows that it cannot. Suppose for now that the mean transmissivity along the skewer $\bar{f}_{0.02}$ is a linear function of the mean baryon density along the skewer $\delta^m_{0.02}$. Which among the infinite arbitrary relationships $\delta^g_{\rm cell} = u(\delta^m_{\rm cell})$ between galaxy density $\delta^g_{\rm cell}$ and matter density $\delta^m_{\rm cell}$ in the cell would produce the strongest correlation between $\delta^g_{\rm cell}$ and $\bar{f}_{0.02}$ (or, equivalently, between $\delta^g_{\rm cell}$ and $\delta^m_{0.02}$)? As shown in appendix 4.A.3, the correlation coefficient between $u(y)$ and x is maximized if $u(y)$ is proportional to $E(x|y)$, the expectation value of x given y. This shows that the function $u(\delta^m_{\rm cell})$ most strongly correlated with $\delta^m_{0.02}$ is $E(\delta^m_{0.02}|\delta^m_{\rm cell})$, but $E(\delta^m_{0.02}|\delta^m_{\rm cell})$ is equal to $\delta^m_{\rm cell}$—the mean density along a large ensemble of skewers through a cell must equal the mean density of the cell itself—and so the correlation coefficient between the skewer matter density and the

cell galaxy density will be maximized if galaxy bias is linear, $\delta^g_{\rm cell} \propto \delta^m_{\rm cell} + \text{constant}$. Nonlinearities in the biasing relationship can make the correlation between skewer matter density and cell galaxy density weaker than the correlation between skewer matter density and cell matter density, but they cannot make it stronger.

In fact the mean transmissivity along the skewer $\bar{f}_{0.02}$ is not a linear function of the mean baryon density along the skewer, as we have temporarily assumed, but a similar result still holds. This can be shown in a number of ways. One way exploits the fact that in numerical simulations the expectation value of $\bar{f}_{0.02}$ is a roughly linear function of $\delta^m_{\rm cell}$, $E(\bar{f}_{0.02}|\delta^m_{\rm cell}) \propto \delta^m_{\rm cell} + \text{constant}$ (e.g., McDonald, Miralda-Escudé, & Cen 2002). The arguments of the previous paragraph then show again that the correlation coefficient between $\delta^g_{\rm cell} = u(\delta^m_{\rm cell})$ and $\bar{f}_{0.02}$ will be maximized if the biasing function u is linear.

A more general way takes into account the possibility that in principle neither the galaxy biasing function $\delta^g_{\rm cell} = u(\delta^m_{\rm cell})$ nor the forest biasing function $\bar{f}_{0.02} = v(\delta^m_{0.02})$ need be linear. Because the initial cosmological distribution of matter was (presumably) a Gaussian random field, at sufficiently early times the joint distribution of baryon density along the skewer $\delta^{m,0}_{0.02}$ and matter density in the cell $\delta^{m,0}_{\rm cell}$ would have been a bivariate Gaussian with a correlation coefficient that can be straightforwardly calculated by inserting the linear power-spectrum for $P(k)$ in equation 4.17. Nonlinear growth of matter fluctuations at later times will distort the shape of the joint distribution away from a bivariate Gaussian, but the skewer and cell densities will be largely determined by their initial linear densities (e.g., Weinberg 1992; Pando, Feng, & Fang 2001; cf. Kayo, Taruya, & Suto 2001). If the Lyman-α transmissivity of the intergalactic medium were controlled by the local density of matter, and if a cell's galaxy density were controlled by its matter density, we would therefore expect the mean transmissivity along the skewer to be largely controlled by the initial linear matter density along the skewer, $\bar{f}_{0.02} \simeq \phi(\delta^{m,0}_{0.02})$, and the galaxy density in the cell to

be largely controlled by the linear matter density in the cell, $\delta^g_{\rm cell} \simeq \psi(\delta^{m,0}_{\rm cell})$. As shown in appendix 4.A.3, the correlation coefficient $|r_{\psi\phi}|$ between two arbitrary functions $\phi(x)$, $\psi(y)$ of the bivariate Gaussian variables x, y will be maximized if ϕ and ψ are both linear functions, in which case $|r_{\psi\phi}|$ is equal to $|r_{xy}|$, the correlation coefficient of x and y. This suggests that no possible relationships between matter density and galaxy density or between matter density and HI density would allow the observed correlation coefficient $|r_{gf}|$ of $\delta^g_{\rm cell}$ with $\bar{f}_{0.02}$ to exceed the correlation coefficient $|r_{\rm lin}|$ of $\delta^{m,0}_{\rm cell}$ with $\delta^{m,0}_{0.02}$. In practice one might not even expect $|r_{gf}|$ to approach $|r_{\rm lin}|$ very closely: the actual relationships $\delta^g_{\rm cell} = \psi(\delta^{m,0}_{\rm cell})$ and $\bar{f}_{0.02} \simeq \phi(\delta^{m,0}_{0.02})$ will not be the linear relationships that maximize the correlation coefficient, and will in any case be somewhat stochastic, reducing the correlation coefficient by adding terms that contribute to the denominator but not the numerator of equation 4.A.1.

The remarkable fact is that the observed correlation coefficient between galaxy density and intergalactic Lyman-α transmissivity is very close to the maximum value estimated above. This is shown in figure 4.17, which compares the observed correlation coefficients between galaxy density $\delta^g_{\rm cell}$ in $10h^{-1}$ comoving Mpc cubes and the mean transmissivity $\bar{f}_R$ along Gaussian skewers of varying comoving standard deviation R for $\Omega_M = 0.3$, $\Omega_\Lambda = 0.7$ to the upper limits derived from the linear cold dark matter power-spectrum (equations G2 and G3 of Bardeen et al. 1986 with $q = k/\Gamma h$, $\Gamma = 0.21$, and a $P(k) \propto k$ long-wavelength limit). Points with error bars show the observed correlation coefficients r_{gf}, calculated with equation 4.9, and their 1σ uncertainties, estimated from the the observed fluctuations from one field to the next. The dashed line shows the theoretical upper limits on the correlation coefficients, $r_{\rm lin}$, derived from equation 4.17 and the linear CDM power-spectrum. Also shown, for reference, is the correlation strength between the density of matter in the cube and the density of baryons along the skewer, estimated from the (non-linear) $z = 3$

power-spectrum of the ΛCDM GIF simulation of Kauffmann et al. (1999). The spectra of only Q0256, Q0933, Q1422, SSA22D13, and Q2233 were used in calculating the observed correlation coefficients. Faint Q1422b was excluded because it lies very close to Q1422 and its noisy spectrum provides few independent constraints on the large scale distribution of HI; Q0302 was excluded because the QSO lies at the edge rather than the center of the region that was spectroscopically observed. Data at redshifts $z < 2.6$, $z > 3.4$, and $z > z_{\rm QSO} - 0.05$ were also removed from the analysis, as were parts of the QSO spectra contaminated by Lyman-β absorption from gas at higher redshifts or by damped Lyman-α absorption. Adjacent cells had their centers displaced by one fifth of a side-length, leading to oversampling by a factor of 5 and (consequently) a small decrease in the shot noise.

The plot shows that if one were given complete freedom to set the relationships between a skewer's matter density and its intergalactic transmissivity, and between a cell's matter density and its galaxy density, then it would be just possible to reproduce the strong correlation between galaxy density and Lyman-α transmissivity that we have observed.

But the required relationships would be somewhat implausible. First, galaxy bias would have to be nearly linear and hardly stochastic. In this limit the correlation coefficient r_{gf} between galaxy density in the cell and mean transmissivity along the skewer would roughly satisfy $r_{gf} \simeq r_{mf} r_{mg}$ (cf. equation 4.19 below), where r_{mf} is the correlation coefficient between matter fluctuations in the cell and mean skewer transmissivity, and r_{mg} is the correlation coefficient between galaxy density and matter density in the cell. The upper limit $|r_{mf}| \lesssim r_{\rm lin}$ therefore implies a 3σ lower limit on the correlation coefficient between galaxy and mass fluctuations of $(|r_{gf}| - 3\sigma_{r_{gf}})/r_{\rm lin} \sim 0.9$. This seems suspiciously high. Star formation in Lyman-break galaxies appears to be episodic (Papovich et al. 2001; Shapley et al. 2001) and dusty (e.g., Adelberger & Steidel 2000), and the number density of galaxies that are

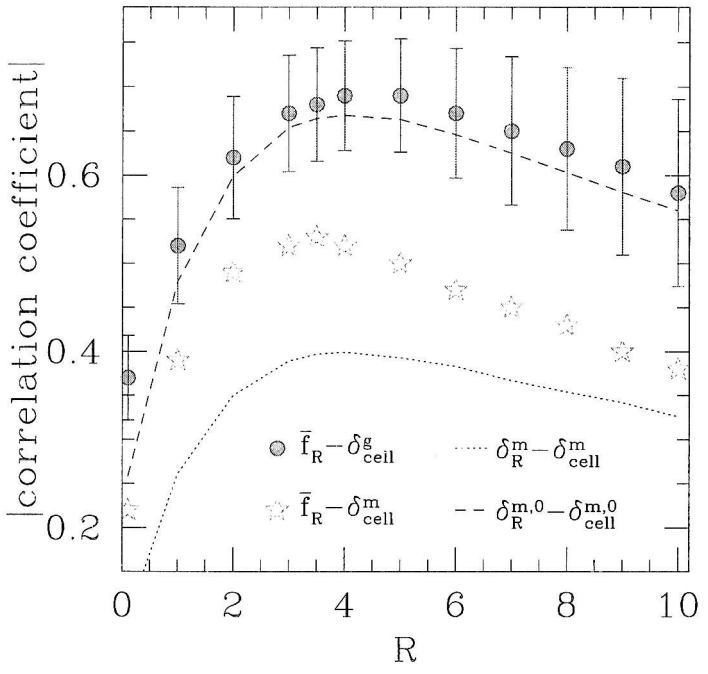

Figure 4.17 The correlation strength between fluctuations along a Gaussian skewer and within an enclosing cubical cell of side-length $10h^{-1}$ comoving Mpc. The abscissa shows the length of the skewer (1σ). Circles with error bars show the observed correlation coefficient $|r_{gf}|$ ($\pm 1\sigma$) between galaxy density in the cell and mean transmissivity of the skewer. Stars show the correlation coefficient between a cell's matter density and a skewer's mean transmissivity in the numerical simulations of McDonald et al. (2002). The dashed (dotted) line shows the correlation coefficient between mean baryonic density along the skewer and mean matter density in the cell for the linear (non-linear) density field.

bright enough to detect will vary according to the vagaries of dust obscuration and star-formation history. We would be surprised if the number density of detectable Lyman-break galaxies in a $\sim 10h^{-1}$ Mpc cell were as thoroughly controlled by the cell's mass as the correlation coefficient $r_{gm} = 0.9$ implies. Second, the relationship between transmissivity and local matter density would have to differ significantly from what has been found in recent numerical simulations. This is illustrated by the stars in figure 4.17, which show the correlation coefficient between $\bar{f}_R$ and $\delta^m_{\rm cell}$ in the

simulations of McDonald et al. 2002 (their figure 1). The correlation between $\bar{f}_R$ and $\delta^m_{\rm cell}$ in the simulations is not as tight as the observed correlation between $\bar{f}_R$ and $\delta^g_{\rm cell}$, and the arguments above suggest that we cannot appeal to galaxy bias to explain the difference. Though our observations do not rule out the idea that the Lyman-α transmissivity of the intergalactic medium is controlled solely by the local density of matter, and that the number of galaxies in a cell is solely controlled by the matter density of the cell, they show it to be physically implausible.

The qualitative conclusion is that the Lyman-α forest knows more about the number density of nearby galaxies than it could learn from the local density of matter alone. This conclusion can be made quantitative by considering the mutual correlations of galaxy density $\delta^g_{\rm cell}$, matter density $\delta^m_{\rm cell}$, and intergalactic transmissivity $\bar{f}_R$ in a more general way. Any possible relationships between these variables can be expressed in the form

$$\delta^g_{\rm cell} = b\delta^m_{\rm cell} + \epsilon(\delta^m_{\rm cell}, \bar{f}_R) \qquad \bar{f}_R = c\delta^m_{\rm cell} + \zeta(\delta^m_{\rm cell}, \delta^g_{\rm cell}) \tag{4.18}$$

where b and c are arbitrary constants and $\epsilon(\delta^m_{\rm cell}, \bar{f}_R)$ and $\zeta(\delta^m_{\rm cell}, \delta^g_{\rm cell})$ are random variables uncorrelated with $\delta^m_{\rm cell}$ whose distributions $P(\epsilon|\delta^m_{\rm cell}\bar{f}_R)$, $P(\zeta|\delta^m_{\rm cell}\delta^g_{\rm cell})$ take into account any stochasticity or nonlinearity in the $\delta^m_{\rm cell}$–$\delta^g_{\rm cell}$ or $\delta^m_{\rm cell}$–$\bar{f}_R$ relationships. 0th-order terms may also be incorporated into ϵ and ζ, but correlation coefficients are unaffected by additive constants and so we may assume $\langle\epsilon\rangle = \langle\zeta\rangle = 0$ without loss of generality. Let r_{gf} denote the correlation coefficient between the cell's galaxy density $\delta^g_{\rm cell}$ and the skewer's mean transmissivity $\bar{f}_R$, let r_{mf} denote the correlation coefficient between cell matter density $\delta^m_{\rm cell}$ and $\bar{f}_R$, let r_{mg} denote the correlation coefficient between $\delta^g_{\rm cell}$ and $\delta^m_{\rm cell}$, and let $r_{\epsilon\zeta}$ denote the correlation coefficient between ϵ and ζ. Repeated substitution into equation 4.A.1 of different pairs of variables from equation 4.18 shows that r_{gf}, which we have observed, must satisfy

$$r_{gf} = r_{mf}r_{mg} + r_{\epsilon\zeta}(1 - r^2_{mg})^{1/2}(1 - r^2_{mf})^{1/2}. \tag{4.19}$$

The correlation coefficient r_{mg} is unknown but cannot be greater than one and is almost certainly greater than zero. The fact that r_{gf} is more negative than r_{mf} (as estimated by McDonald et al. 2002; see our figure 4.18) therefore shows that $r_{\epsilon\zeta} < 0$. Since ϵ and ζ represent deviations of the actual values of $\delta^g_{\rm cell}$ and $\bar{f}_R$ around the linear relationships $\delta^g_{\rm cell} = b\delta^m_{\rm cell} + \text{constant}$ and $\bar{f}_R = c\delta^m_{\rm cell} + \text{constant}$, this shows that cells with galaxy density higher than the linearly expected value $b\delta^m_{\rm cell}$ will tend to have Lyman-α forest transmissivity lower than the linearly expected value $\bar{f}_R = c\delta^g_{\rm cell}$. That may partly reflect the fact that non-linearities in the $\delta^g_{\rm cell}$–$\delta^m_{\rm cell}$ relationship will tend to occur in the same cells as nonlinearities in the $\bar{f}_R$–$\delta^m_{\rm cell}$ relationship, but numerical simulations suggest that the $\bar{f}_R$–$\delta^m_{\rm cell}$ relationship ought to be nearly linear (McDonald et al. 2002). A more likely explanation may be that the HI content of the intergalactic medium is affected not only by the local density of matter but also by the presence or absence of nearby galaxies: the negative correlation of ϵ with ζ implies that if one were to take all the cells in the universe with a given value of $\delta^m_{\rm cell}$ and measure the mean Lyman-α transmissivity along random skewers through them, one would find that skewers with unexpectedly low transmissivities $\bar{f}_R < c\delta^m_{\rm cell}$ tended to lie within cells with unexpectedly high galaxy density $\delta^g_{\rm cell} > b\delta^m_{\rm cell}$, a result consistent with the idea that galaxies increase the HI content of the intergalactic medium in their vicinity (cf. §§ 4.3, 4.4, and 4.F).

The value of the correlation coefficient $r_{\epsilon\zeta}$ can be translated straightforwardly into the fraction of the variations about the mean relationship $\bar{f}_R = c\delta^m_{\rm cell}$ that can be explained by the variations in the actual galaxy density about the relationship $\delta^g_{\rm cell} = b\delta^m_{\rm cell}$. Figure 4.18 shows the implied value of $r_{\epsilon\zeta}$ as a function of the unknown correlation coefficient r_{mg} between galaxy and mass fluctuations (cf. equation 4.19). The fraction of the variance in the $\delta^m_{\rm cell}$–$\bar{f}_R$ relationship due to the presence or absence of nearby galaxies, $r^2_{\epsilon\zeta}$, is shown on the right axis. The plot assumes $R = 4h^{-1}$ comoving Mpc, so that $|r_{mf}| = 0.52$ and $|r_{gf}| = 0.69 \pm 0.06$. The shaded region is

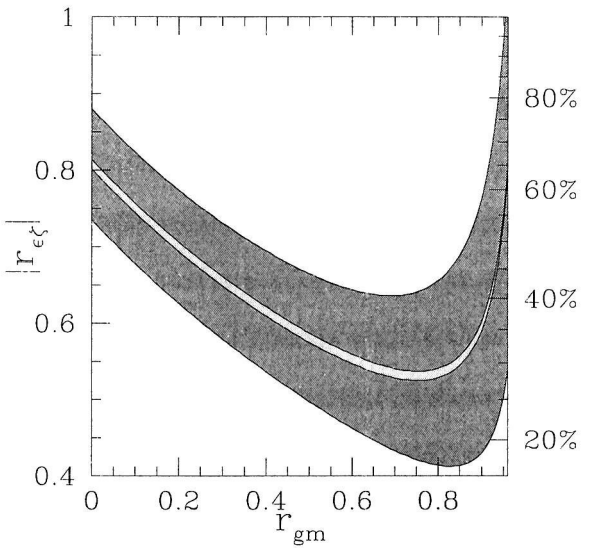

Figure 4.18 The implied correlation coefficient $r_{\epsilon\zeta}$ as a function of the unknown correlation coefficient r_{gm}. The left axis shows $r_{\epsilon\zeta}$, the right axis $100 \times r^2_{\epsilon\zeta}$. ϵ corresponds to deviations in the true galaxy density $\delta^g_{\rm cell}$ in a cell about the best linear relationship $\delta^g_{\rm cell} = b\delta^m_{\rm cell} + \text{constant}$; ζ corresponds to deviations in the true mean skewer transmissivity $\bar{f}_{0.02}$ about the best linear relationship $\bar{f}_{0.02} = c\delta^m_{\rm cell} + \text{constant}$. The non-zero correlation of ϵ with ζ shows that cells whose galaxy densities deviate significantly from the linear expectation will tend to have skewer transmissivities that deviate significantly from the linear expectation. Knowledge of how the actual galaxy density deviates from the linear expectation would therefore allow one to predict the skewer transmissivity with increased accuracy. The right axis shows how much of the variance about the best linear $f_{0.02}$–$\delta^m_{\rm cell}$ relationship could be removed by linearly scaling the galaxy deviation—if it were known.

appropriate to our 1σ confidence interval $0.63 > |r_{gf}| > 0.75$. We conclude that a significant fraction ($\sim$ 20–50%) of the deviations about the mean $\bar{f}_R$–$\delta^m_{\rm cell}$ relationship may be due to the influence of galaxies on the intergalactic medium.

We will end this section with a brief summary. Fluctuations in galaxy density and intergalactic Lyman-α transmissivity are strongly correlated on scales of $\sim 10h^{-1}$ comoving Mpc. This strong correlation is not easy to understand if the density of HI in the intergalactic medium is solely controlled by the local density of dark matter. It appears instead that galaxies have a non-negligible influence on the intergalactic medium, a result that is not obviously consistent with recent numerical simulations

of the intergalactic medium (cf. § 4.8). We are not saying, however, that there is no mean relationship between local matter density and HI density. Any possible matter and HI distributions will have *some* relationship between matter density and HI density, a relationship that could be estimated (for example) by binning together the HI densities associated with various ranges of matter densities. Our conclusion can instead be expressed as two statements. First, the strong association of Lyman-α forest and galaxy density fluctuations shows that there must be significant scatter around the mean $\rho_{\rm HI}$–$\rho_{\rm baryon}$ relationship. If there were not, our observed correlation coefficients could not exceed the $\delta^m_{\rm cell}$–$\bar{f}_R$ correlation coefficients calculated by McDonald et al. (2002; see our figure 4.17). Second, the required spatial variations in the HI density associated with a given baryon density must be strongly correlated with spatial variations in the galaxy density. Otherwise fluctuations in the galaxy density on $10h^{-1}$Mpc scales could not be more strongly correlated than matter fluctuations on $10h^{-1}$Mpc scales with the HI content of the IGM.

4.6 Correlation functions

The previous sections were primarily concerned with spatial averages over the auto- and cross-correlation functions of galaxies, CIV systems, and Lyman-α forest flux decrements. These averages highlighted the aspects of the spatial association of galaxies, metals, and gas that we found most interesting. But readers may wonder how our conclusions would alter if we averaged the correlation functions over different volumes, or may wish to know how galaxies and intergalactic material are associated on spatial scales other than those we considered. This section presents the correlation functions with no spatial averaging imposed.

4.6.1 Two dimensional

Figures 4.19 and 4.20 show the two dimensional correlation functions of galaxies with galaxies, of galaxies with detected CIV systems, and of galaxies with Lyman-α forest flux decrements. The data used to generate the two figures is identical; figure 4.20 is less heavily smoothed to help bring out the behavior of the correlation functions on small spatial scales. The abscissae correspond to angular separations r_θ on the plane of the sky; the ordinates correspond to redshift separations r_z. Separations were converted to comoving distances by assuming a $\Omega_M = 0.3$, $\Omega_\Lambda = 0.7$ cosmology. The value of the correlation function ξ_{gc} between galaxies and CIV systems at separation r_θ, r_z was estimated with the statistic

$$\hat{\xi}_{gc} = (D_g D_c - D_g R_c - R_g D_c + R_g R_c)/R_g R_c \tag{4.20}$$

(e.g., Landy & Szalay 1993) where $D_g D_c$ is the observed number of galaxy–CIV-system pairs with separation r_θ, r_z, $D_g R_c$ is the number of pairs with the same separation between our galaxy catalog and a random catalog of CIV systems, and $R_g R_c$ is the number of pairs with the same separation between a random galaxy catalog and random CIV catalog. The correlation functions ξ_{gf} of galaxies with Lyman-α flux decrements and ξ_{gg} of galaxies with galaxies were estimated similarly. The random galaxy catalogs were generated by assigning each galaxy in the true catalog 1000 redshifts drawn at random from our selection function; the angular positions of galaxies in the random and real catalogs were the same. The random CIV catalogs were generated by assigning each CIV system in the true catalog 1000 redshifts drawn from a uniform distribution between the minimum and maximum redshifts where our QSO spectra allowed us to detect CIV systems; the observed number density of detected CIV systems among our QSO spectra at each redshift is closely approximated by a constant once the different redshift selection ranges are taken into account. The random flux decrement spectra were linear functions with the form of equation 4.10,

but scaled to match the observed mean transmissivity in each of our QSO spectra. The galaxy-galaxy correlation function was calculated using only data in the redshift range $2.6 < z < 3.4$, to minimize the effect on our result of the poorly determined wings of the selection function. The calculation of the galaxy-flux cross-correlation function excluded data with $z < 2.6$, with $z > 3.4$, with $z > z_{\rm QSO} - 0.05$, and with $z < (1 + z_{\rm QSO}) \times 1026/1216 - 1$. The final criterion excludes portions of the Lyman-α forest that are contaminated by Lyman-β absorption from material at higher redshifts. Also excluded were data at the DLA-contaminated redshifts $2.91 < z < 2.98$ in SSA22 and $3.214 < z < 3.264$ in Q0933+2841. The galaxy-CIV cross-correlation function calculation excluded data with $z < 2.6$, with $z > 3.4$, $z > z_{\rm QSO} - 0.05$, and with $z < (1 + z_{\rm QSO}) \times 1216/1549 - 0.99$. The final criterion excludes CIV lines that lie close to the QSO redshift or in the Lyman-α forest. To help guide the eye, the resulting raw two-dimensional correlation functions were finally smoothed by two-dimensional Gaussians with $\sigma_\theta = \sigma_z = 0.5h^{-1}$ (figure 4.19) or $\sigma_\theta = \sigma_z = 0.2h^{-1}$ (figure 4.20) Mpc comoving.

Aside from some elongation in the redshift direction at small separations, which is at least partly due to errors in galaxy redshifts, these two-dimensional correlation functions are similarly isotropic. This can be seen in figure 4.21. The figure shows the average value of each correlation function in three-dimensional ellipses of comoving volume $4\pi(4h^{-1}{\rm Mpc})^3/3$ as a function of axial ratio r_z/r_θ. The averages hit an extremum at $r_z/r_\theta = 1.0 \pm 0.2$ for each correlation function, demonstrating their isotropy on $\sim 4h^{-1}$ Mpc scales. If one were convinced that these correlation functions should be isotropic despite possible peculiar velocity distortions and despite the significant errors in our galaxy redshifts, figure 4.21 would show that the Alcock-Paczynski (1979) test at $z \sim 3$ favors a Λ cosmology; if we had assumed $\Omega_M = 1.0$, $\Omega_\Lambda = 0$ or $\Omega_M = 0.3$, $\Omega_\Lambda = 0$ instead of $\Omega_M = 0.3$, $\Omega_\Lambda = 0.7$, we would have found that the

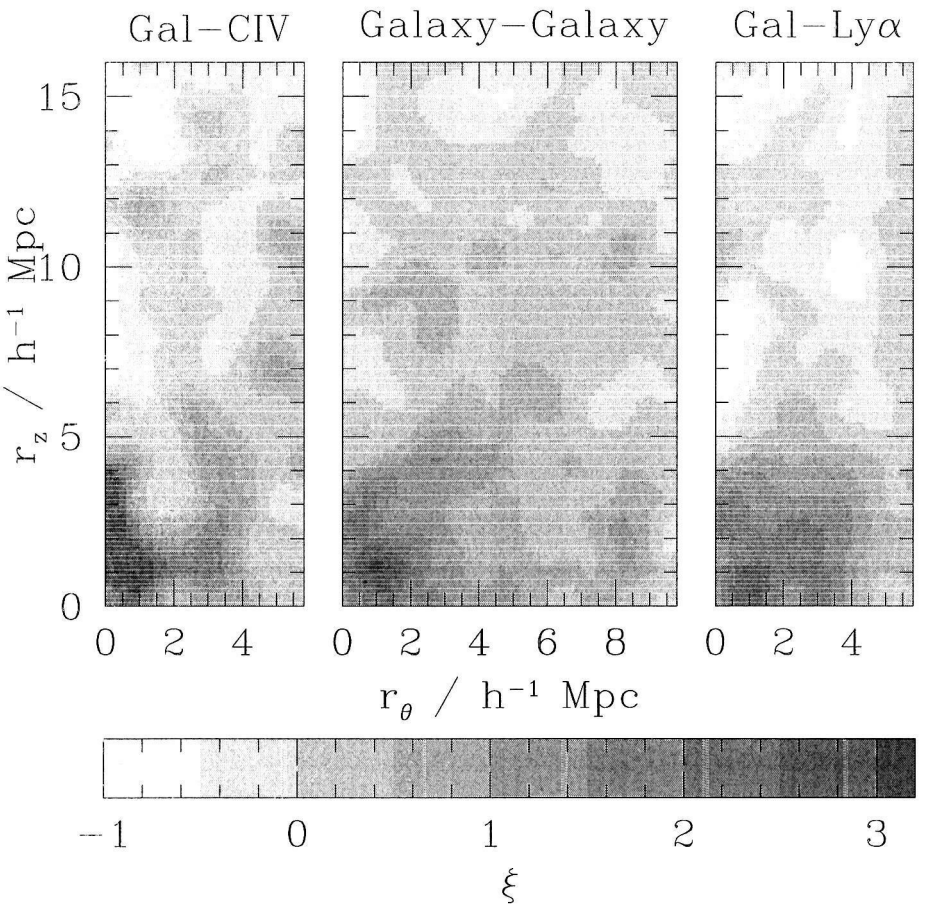

Figure 4.19 The two dimensional auto- and cross-correlation functions of galaxies with galaxies, with CIV systems, and with intergalactic Lyman-α transmissivity. The galaxy–transmissivity correlation function is multiplied by -10. Each correlation function was smoothed by a two-dimensional Gaussian with $\sigma = 0.5h^{-1}$ comoving Mpc.

averages hit their extrema at $r_z/r_\theta \sim 0.8$ not $r_z/r_\theta \sim 1.0$. In any case, one unsurprising implication of the similar angular dependence of the correlation functions is that the bulk of intergalactic absorbing material is nearly at rest with respect to nearby galaxies; the peculiar velocities of intergalactic material relative to galaxies is not sufficient to make the galaxy–intergalactic material cross-correlation functions have a significantly different shape from the galaxy–galaxy correlation function. There is no

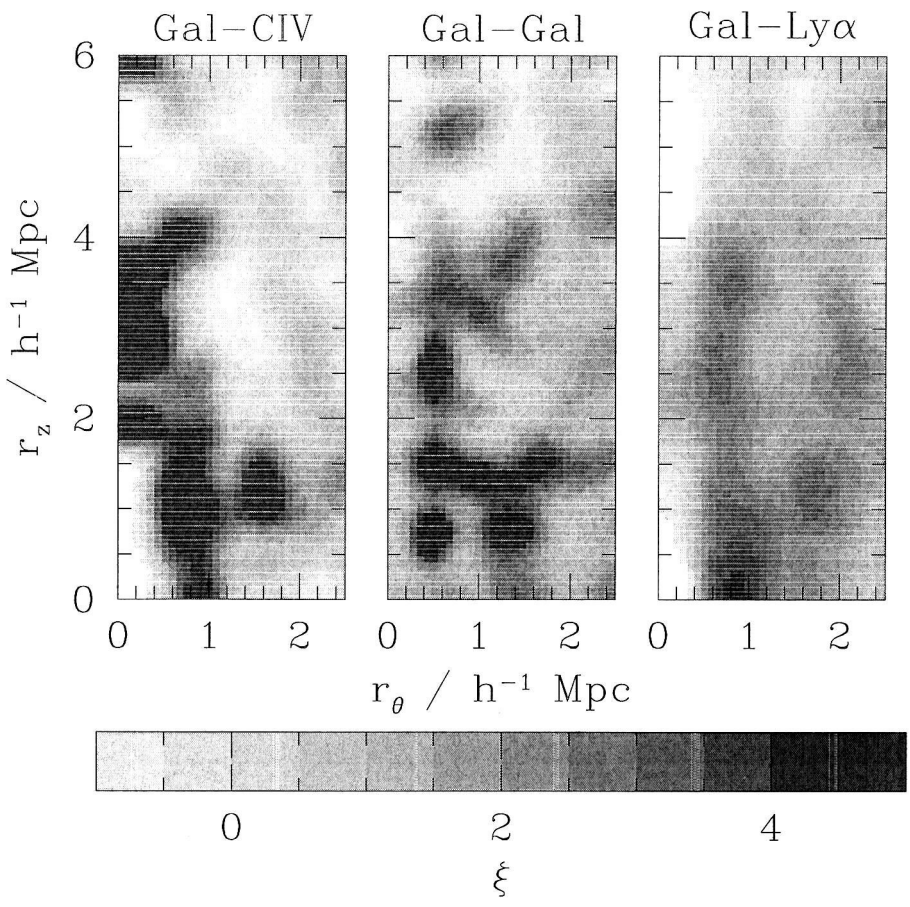

Figure 4.20 The correlation functions of figure 4.19 less heavily smoothed ($\sigma = 0.2h^{-1}$ comoving Mpc).

contradiction with the galactic superwind hypothesis because a wind's evolution is dominated by its stalling phase and because only a small fraction of the intergalactic volume would be affected by active winds at any time (§ 4.G).

The scale dependence of correlation functions is often easiest to apprehend when they are presented as one-dimensional rather than two-dimensional functions. It would be trivial to average the correlation functions of figure 4.19 in circular annuli,

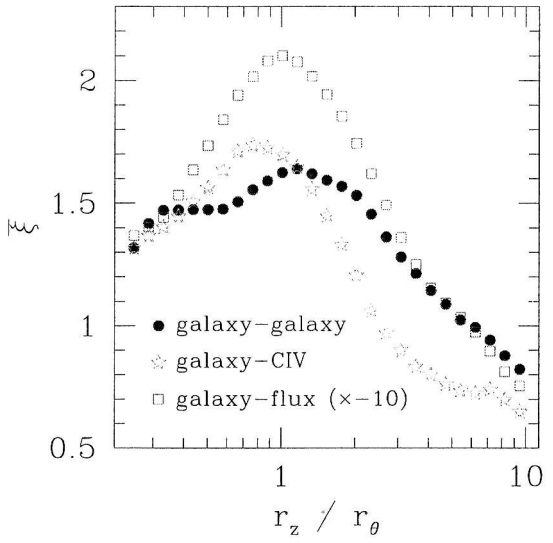

Figure 4.21 Average value $\bar{\xi}$ of the auto- and cross-correlation functions of figures 4.19 and 4.20 within ellipses of volume $4\pi(4h^{-1})^3/3$ comoving Mpc^3 as a function of the axial ratio r_z/r_θ. $\bar{\xi}$ reaches an extremum close to $r_z/r_\theta = 1$ for each correlation function, showing that they are nearly isotropic on these scales.

but because of peculiar velocities and redshift measurement errors, a more robust estimate of the one-dimensional correlation functions will come from another approach.

4.6.2 One dimensional

Appendix 4.D describes the approach adopted by Adelberger (2000) to estimate the one-dimensional auto-correlation function of Lyman-break galaxies at $z \sim 3$. Following Davis & Peebles (1983), we first estimated the projected correlation function, which is a marginalization in the redshift direction of the two dimensional correlation function (e.g., of figures 4.19 and 4.20). We then estimated the shape of the one-dimensional correlation function from a power-law fit to the projected correlation function. See appendix 4.D. An identical approach can be used to estimate the cross-correlation function of galaxies with CIV systems. Figures 4.22 and 4.23 show the

auto-correlation function of the ~ 700 galaxies with the most secure redshifts in the Lyman-break sample of Steidel et al. (2002; in preparation) and the cross-correlation function of galaxies and CIV systems in the sample of this paper. In both cases the data appear to be reasonably well fit by a power-law of the form $\xi(r) = (r/r0)^{-\gamma}$, justifying the method we have adopted. The best-fit values and 1σ uncertainties of γ and r_0 are shown in the figures.

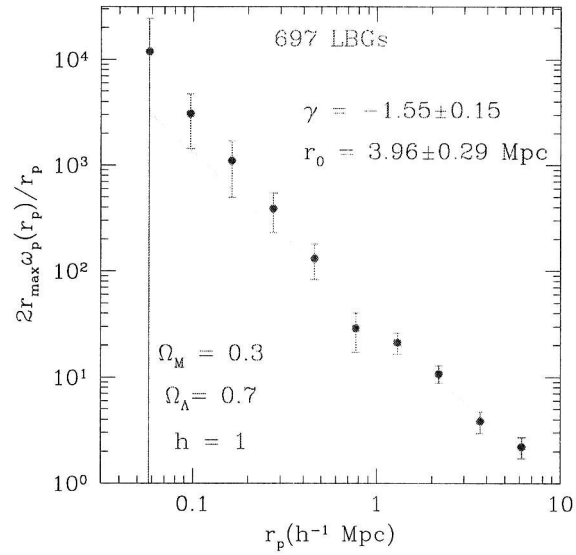

Figure 4.22 The projected correlation function of Lyman-break galaxies. The parameters of the best power-law fit to the three-dimensional correlation function $\xi(r) = (r/r_0)^{\gamma}$ are shown.

The galaxy-CIV cross-correlation function resembles the galaxy-galaxy correlation function to a large extent. The slopes are identical; the correlation lengths differ by only $\sim 20\%$. This suggests that galaxies and CIV systems may be similar objects, a point that has been made by Sargent et al. (1988), Quashnock & Vanden Berk (1998) and by us (§ 4.4.2 above) on slightly different grounds.

Unfortunately we were unable to estimate the cross-correlation function between galaxies and Lyman-α transmissivity with a similar approach. The lack of HI near

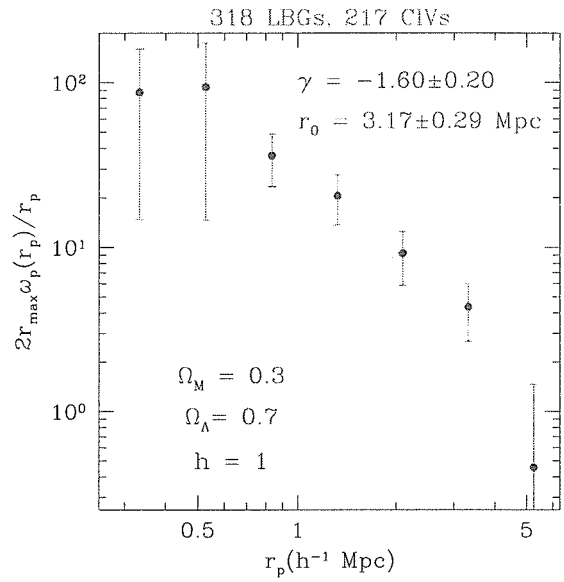

Figure 4.23 The projected cross-correlation function of CIV systems and Lyman-break galaxies.

Lyman-break galaxies is evident even after marginalizing the two-dimensional cross-correlation function over 6–$15h^{-1}$ comoving Mpc, and as a result the projected cross-correlation function is poorly fit by a single power-law. A single power-law may fit the data reasonably well at $1 \lesssim r_p \lesssim 5h^{-1}$ comoving Mpc, but the comparatively weak correlation of galaxies with Lyman-α transmissivity does not provide much constraint on the slope given so small a range of radii. Slopes $\gamma \leq 1.0$ appear consistent with the data, and for these slopes our approach breaks down completely. We shall defer a proper estimate of the galaxy-transmissivity correlation function.

The uncertainty in the shape of the galaxy-flux correlation function does not stop us from making one final observation: the ratio of CIV to HI in the intergalactic medium almost certainly increases as one approaches a Lyman-break galaxy. The mean Lyman-α transmissivity of the intergalactic medium does not change much with distance from a Lyman-break galaxy, only by $\lesssim 30\%$ (cf. figure 4.8), so it may be a reasonable first approximation to assume that the density of intergalactic HI is roughly independent of distance to a Lyman-break galaxy. But the number

density of CIV systems depends very strongly on distance to a Lyman-break galaxy; according to the power-law fit described above, the density of CIV systems is ~ 6.4 times higher at $r = 1h^{-1}$ comoving Mpc than at $r = 10h^{-1}$ Mpc. The significantly different strengths of the galaxy-CIV and galaxy-flux correlation functions make it seem almost inevitable that the ratio of intergalactic CIV to HI density increases dramatically close to Lyman-break galaxies. As shown in appendix 4.H, the radiation that the galaxies emit would not lead to an enhancement in the CIV density near them, and plausible changes in the intergalactic density and temperature near the galaxies would be unlikely to change $n_{\rm CIV}/n_{\rm HI}$ by a factor of ~ 6. The simplest explanation for the (apparently) strong change of $n_{\rm CIV}/n_{\rm HI}$ with radius may be that the intergalactic metallicity is higher near the galaxies. See Steidel et al. (2002; in preparation) for a less superficial analysis.

4.7 Summary

The goal of this paper was to compare the spatial distributions of galaxies, metals, and neutral hydrogen at high redshift. We conducted a redshift survey of $z \sim 3$ Lyman-break galaxies in 6 primary fields containing QSOs at $3.1 \lesssim z \lesssim 3.6$ whose spectra revealed the locations of HI and metals along sightlines through the galaxy distributions. We quantified the relationship between galaxies and intergalactic material by calculating two-point correlation functions or closely related statistics. Various averages over the correlation functions were presented in §§ 4.3, 4.4, and 4.5; the one-dimensional and two-dimensional correlation functions of galaxies with galaxies, with CIV systems, and with Lyman-α forest transmissivity were presented in § 4.6. The most lasting contribution of this paper may be its methodolgy, which will be applied to a larger sample in the future. Applying these statistical methods to the present sample leads to the following major conclusions:

1. The HI content of the intergalactic medium is closely correlated with the positions of nearby galaxies. The material within $r \sim 0.5h^{-1}$ comoving Mpc of Lyman-break galaxies absorbs Lyman-α photons less heavily than the material at random points in the intergalactic medium (§§ 4.3.3, 4.4, and 4.6); the material at slightly larger radii $1 \lesssim r \lesssim 5h^{-1}$ Mpc absorbs Lyman-α photons more heavily (§§ 4.3.1, 4.5, and 4.6) than average.

2. The gas within the largest galaxy overdensities at $z \sim 3$, presumably the young intracluster medium, is rich in HI and CIV (§§ 4.3.1, 4.3.2, 4.4, 4.5, and 4.6).

3. The cross-correlation function of galaxies with CIV systems is similar to the auto-correlation function of galaxies with galaxies, showing that CIV systems and Lyman-break galaxies are found in similar parts of the universe and suggesting that they may be similar objects (§ 4.6).

4. The ratio of the number density of CIV systems to HI density (§ 4.6) and to HII density (§ 4.3.2) almost certainly increases within a few comoving Mpc of Lyman-break galaxies. Most detectable CIV systems ($N_{\rm CIV} \gtrsim 10^{11.5}$ cm^{-2}) lie within $2.4h^{-1}$ comoving Mpc of a Lyman-break galaxy (§ 4.4). Stronger CIV systems tend to lie even closer. The strongest CIV systems ($N_{\rm CIV} \gtrsim 10^{13.5}$cm^{-2}) appear to be so strongly correlated with nearby ($r \lesssim 0.5h^{-1}$ comoving Mpc) Lyman-break galaxies that they should be considered the same object despite the large distance between the galaxy and CIV-absorbing gas (§ 4.4).

5. Damped Lyman-α systems appear to reside in different environments than Lyman-break galaxies (§ 4.3.4). Though the sample is small and the statistics are poor, the available data suggest that they should not be considered similar objects.

6. The strong correlation between the HI density in the Lyman-α forest and the galaxy density within $\sim 5h^{-1}$ comoving Mpc is not easily compatible with the standard assumption that the HI content of the intergalactic medium is solely controlled by the local density of dark matter (§ 4.5).

Taken together, these observations (aside from 5) suggest to us that the $\sim$ 600 km s^{-1} outflows common to Lyman-break galaxies (§ 4.2; Pettini et al. 2001, 2002) are able to escape the galaxies' potentials and propagate $\sim 0.5h^{-1}$ comoving Mpc into the surrounding intergalactic medium. Simplistic calculations presented in appendices 4.E, 4.F, and 4.G show that this scenario might be capable of producing the observed relationship between galaxies and the intergalactic medium: the supernovae that explode during the assembly of a typical Lyman-break galaxy's $10^{10}M_{\odot}$ of stars would emit enough energy to accelerate much of its gas to $\sim$ 600 km s^{-1}, a velocity that likely exceeds its escape velocity, and this outflowing gas would plausibly drive at least $0.5h^{-1}$ comoving Mpc into the surrounding intergalactic medium before being brought to rest. Winds from galaxies may have driven a significant fraction of the intergalactic medium away from the equilibrium relationship between dark matter density and temperature that would otherwise hold. The implications of this conclusion, and its weaknesses, are discussed in § 4.8.

4.8 Concluding remarks

The existence of galactic winds at high redshift is hardly unexpected. Galactic winds are commonly observed around starbursts in the local universe, and, as reviewed in the introduction, it has long been recognized that similar winds at high redshift would help explain a wide range of otherwise puzzling observations and help reconcile hierarchical models of structure formation with the data. It would have been easy to guess that our data would reveal some trace of winds from Lyman-break galaxies.

The surprise is the observed strength of the winds. Because gravitational potential energy is proportional to M^2 while the amount of material that can be converted into stars (and hence the energy that supernovae can release) is proportional to M, it has been widely assumed that galaxies with small masses would have the strongest

winds. But Lyman-break galaxies appear to be the most massive galaxies that have formed by $z \sim 3$. They are certainly the brightest in the rest-frame UV, and large masses are implied by their spatial clustering (e.g., Adelberger et al. 1998) and are (apparently) required by their stellar masses of $\sim 10^{10} M_{\odot}$ (e.g., Pettini et al. 2001; Shapley et al. 2001) since only the most massive collapsed objects at $z \sim 3$ contain so many baryons in a standard ΛCDM model. Nevertheless the large radius of their proximity effect shows that their wind velocities easily exceed their escape velocities, and the strong association of metal line systems with Lyman-break galaxies suggests that a large fraction of the metals in the $z \sim 3$ intergalactic medium may have been produced by them. The only explanation that we can offer for the unexpected strength of the winds is that the star-formation efficiency in Lyman-break galaxies appears to be exceptionally high. If the average mass of a Lyman-break galaxy is $\sim 10^{11} M_{\odot}$ (§ 4.E), then the average measured stellar mass of $\sim 10^{10} M_{\odot}$ implies that the typical Lyman-break galaxy has converted more than about half of its baryons into stars. For comparison, only $\sim 5\%$ of baryons appear to have formed into stars by $z = 0$ (Balogh et al. 2001). The typical collapsed objects in the universe cannot have had star-formation efficiencies nearly as high as those of Lyman-break galaxies. One may be tempted to doubt the derived stellar masses, but the large implied release of supernova energy is consistent with and perhaps even required by the observed size of regions with low HI opacity surrounding Lyman-break galaxies (§ 4.G). Perhaps our data show that the IGM is affected most strongly by galaxies with the highest star-formation efficiencies and not necessarily those with the smallest gravitational binding energies—though one should recall that our estimated star-formation efficiencies depend strongly on the assumed shape of the initial mass function, on the assumed cosmological model, and on the assumed shape of the matter power-spectrum.

In any case, if winds from supernovae are trivially able to escape the deep potential wells of Lyman-break galaxies, they will presumably be able to escape the potential wells of other high-redshift galaxies as well. The physical state of the intergalactic medium may have been significantly affected by galaxy feedback. This could have far-reaching implications. Some of the heavier elements that compose the earth may have been fused in a galaxy as distant as Andromeda. Further star formation might be suppressed in the $r \sim 0.5h^{-1}$ comoving Mpc rarefied cavities surrounding currently star-forming galaxies, and might be enhanced in the dense shells at slightly larger radii (e.g., Ostriker & Cowie 1981; Natarajan, Sigurdsson, & Silk 1998). This would complicate theoretical interpretations of the spatial clustering of star-forming galaxies at high redshift (e.g., Adelberger et al. 1998). Estimates of the matter power-spectrum derived from the Lyman-α forest (e.g., Croft et al. 1998) would be contaminated by the power-spectrum of galaxies. The peculiar velocities of outflowing material might obscure the redshift-space anisotropies of the Lyman-α forest that could otherwise be used to measure the geometry of the universe through a variant of the Alcock-Paczynski (1979) effect (e.g., Hui et al. 1999; but see § 4.6). Because winds would increase the opacity of the Lyman-α forest for a given ionizing background and baryon density (§ 4.F), estimates of the baryon density from the mean observed transmissivity (e.g., Rauch et al. 1997; Weinberg et al. 1997) might be systematically too high. The physics of galaxy formation might be significantly affected as well. If the winds are strong enough to blow out a large fraction of a galaxy's baryonic mass, as argued in appendix 4.E, then the total amount of star formation a galaxy can sustain might depend critically upon the small-scale physics that determines how long cool interstellar clouds can survive and produce stars before they are destroyed by the hot surrounding winds. At present neither numerical nor semi-analytical models of galaxy formation are able to treat the complex physical processes in a way that inspires absolute confidence.

Standard assumptions about the universe at high redshift may need to be profoundly revised if superwinds from galaxies affected the intergalactic medium as strongly as we suggest. Before entertaining this possibility, one ought to review our arguments with a skeptical eye. Here are their major weaknesses as we see them. The evidence for a lack of neutral hydrogen within $\sim 0.5h^{-1}$ comoving Mpc of Lyman-break galaxies has a significance of only a few sigma at best. It may be easier to believe that this is a statistical fluctuation than that the standard picture of the high-redshift universe is wrong. Even if the observed galaxy proximity effect is real, the typical radius $r_{\rm GPE}$ with lowered HI opacity around a galaxy is uncertain; our sample contains only 10 galaxies with $0.75h^{-1}$ comoving Mpc of a QSO sightline and only 3 within $0.40h^{-1}$Mpc. A typical radius of $r_{\rm GPE} \sim 0.2h^{-1}$ Mpc would make the data marginally consistent with an ionizing radiation origin for the proximity effect, and this would take away much of the force of our argument. It would become plain how weakly the outflow argument is shored by the association of metals with nearby galaxies. We would be left with the excess of HI on larger spatial scales, but the evidence for this is not unimpeachable. We presented no justification for our correlation coefficient estimator (equation 4.9), no analysis of its possible biases, no estimate of its variance. Our conclusions about the incompatibility of our data with the fluctuating Gunn-Peterson approximation (i.e., the idea that intergalactic transmissivity is solely controlled by the local baryon density) were based on the fact that the mean value of the correlation coefficients calculated with this estimator were several observed standard deviations away from the theoretically expected correlation coefficients. Familiarity with Gaussian statistics may lull us into thinking that the sample mean is unlikely to stray farther from the true mean than a few times the observed standard deviation, but this is not necessarily true. When statistics are non-Gaussian, as they are here, both the observed mean and observed variance can differ significantly from their true values. When estimators involve the ratios of moments, as does ours, biases

can be especially significant (e.g., Hui & Gaztañaga 1999). We derive some comfort from the fact that when we scramble the assignment of galaxy redshift catalogs to QSO fields, and remeasure the mean and standard deviation of the mean for the correlation coefficient, we find $r_{gf} = -0.03 \pm 0.08$. The sample mean lies within one sample rms of 0, as it should. One might reasonably hope that possible problems with the estimator equation 4.9 have not seriously compromised our statistical analysis. But it is worth remembering that the derived estimate of the correlation coefficient r and its uncertainty were based upon observations of r in only 5 independent fields. Our theoretical estimate of r is subject to significant uncertainties as well. These are due to the unknown shape of the matter power-spectrum on ~ 0.1–$10h^{-1}$ comoving Mpc spatial scales. The power-spectrum we have assumed is physically motivated, is consistent with the best empirical constraints on larger spatial scales, and is commonly adopted in theoretical treatments of the high-redshift universe, but it may yet be wrong. Numerous authors (see, e.g., Spergel & Steinhardt 2000) have argued on other grounds that the power-spectrum on small scales ($\lesssim 1h^{-1}$ comoving Mpc) may differ significantly from what we have assumed, and the direction of the difference would help to explain our result. It is conceivable that our data are telling us something about the matter power-spectrum, not about galaxy winds.

These uncertainties are not easy to dismiss. Our qualified confidence in the existence of large-scale winds from Lyman-break galaxies is founded on the winds' ability to explain three seemingly disparate observations—the galaxies' velocity shift between interstellar and nebular lines, the lack of neutral hydrogen within $\sim 0.5h^{-1}$Mpc, the excess of neutral hydrogen on larger scales—but taken individually none of the observations clearly requires $\sim$ megaparsec-sized superwinds. Readers determined to believe in the standard paradigm of the Lyman-α forest will find nothing in this paper to shatter their conviction.

Nevertheless we should emphasize that our results and the standard paradigm are

not wholly incompatible. It is easy to imagine a scenario in which the fluctuating Gunn-Peterson approximation holds in regions with the lowest density—in the low column-density Lyman-α forest, which is in fact the only regime where its validity has been claimed—and breaks down in small high-density regions surrounding galaxies. This scenario provides one way of reconciling our observations with the successes of the fluctuating Gunn-Peterson approximation: volume weighted statistics such as the distribution function or power-spectrum of Lyman-α forest transmissivities might agree with predictions from the FGPA, while statistics that are strongly affected by the locations of saturated pixels, such as our estimates the mean transmissivity $\bar{f}$ close to galaxies (§ 4.5), might not. Because the volume filling factor of the hot bubbles surrounding Lyman-break galaxies is apparently quite small, $n_{\rm LBG} V_{\rm bubble} \sim 2\%$ for $n_{\rm LBG} = 4 \times 10^{-3} h^3 {\rm Mpc}^{-3}$ and $r_{\rm bubble} = 1 h^{-1}$ Mpc, one might imagine further that the observed winds will require only a negligible adjustment to our understanding of the intergalactic medium. But this can be a misleading argument: the intergalactic medium will presumably have been disturbed not only by $z \sim 3$ Lyman-break galaxies with magnitude $\mathcal{R} \lesssim 25.5$ but also by fainter galaxies at the same redshift and (more seriously) by all previous generations of galaxies. A superwind's effect on intergalactic medium is likely to be enduring. Although temperatures will begin to equilibrate on the adiabatic cooling time-scale of $\sim$ 1Gyr (at $z \sim 3$), density perturbations will persist; if it takes a time Δt for high-Mach shock to sweep gas into a thin shell, it will take many times Δt for the shell to dissipate from thermal motions. In the case of Lyman-break galaxies, for example, $\sim$ 10Gyr will pass before intergalactic gas moving at a sound speed of $\sim$ 20 km s^{-1} fills the evacuated cavity of radius $r \sim 1$ comoving Mpc. In fact the wind cavities will likely be destroyed by further gravitational collapse, not thermal motions (§ 4.G), but the time for destruction is still long. As a result, the total fraction of the intergalactic volume at $z \sim 3$ that has been disturbed by winds is difficult to estimate and may be quite large ($\sim$ 20%; § 4.G). To

the extent that galaxies preferentially form where the large-scale dark-matter density is high (e.g., Kaiser 1984), Lyman-break galaxies will tend to form surrounded by the relict superbubbles of previous generations of galaxies. If a significant fraction of the intergalactic medium had been lastingly disturbed by the passage of winds, we might therefore expect to see the signs of it especially clearly in the properties of intergalactic gas close to Lyman-break galaxies. It is interesting in this context to return our attention to figure 4.17 and the accompanying discussion. The correlation coefficient between the local Lyman-α transmissivity of the IGM and the galaxy density on 10 Mpc scales is (for a standard ΛCDM model) about twice as large as the correlation coefficient between the local transmissivity and the matter density on 10 Mpc scales. If we were asked to predict the Lyman-α transmissivity at a given point in intergalactic space on the basis of a single number, and had to choose whether that number would be the galaxy or the matter density in a surrounding 10Mpc cube, we would choose the galaxy density every time. Our analysis suggests that that would allow a more accurate prediction. This could be construed as an argument that the HI content of the intergalactic medium is affected at least as strongly by the presence or absence of nearby galaxies as by the density of dark matter. Some characteristics of the Lyman-α forest can be explained if competition between cooling from the cosmic expansion and heating from photoionization has set up a simple relationship between neutral hydrogen density and dark matter density. Other characteristics require superwinds from galaxies to have destroyed this simple relationship in places. The relative importance of superwinds remains unclear, but we hope to have shown that they should not be ignored.

4.A Statistical background: the correlation coefficient

4.A.1 Definition

The correlation coefficient

$$r \equiv \frac{\langle (x-\mu_x)(y-\mu_y)\rangle}{\langle (x-\mu_x)^2\rangle^{1/2}\langle (y-\mu_y)^2\rangle^{1/2}} \tag{4.A.1}$$

provides a convenient quantification of the strength of association between two random variables x and y with means μ_x and μ_y. r ranges from -1 to 1; if $r = 0$, knowing that $x > \mu_x$ tells us nothing at all about how much larger or smaller than μ_y the corresponding value of y will be, but as $|r| \to 1$ observations of x are able to predict y with increasing accuracy. If x and y are drawn from a bivariate Gaussian distribution, for example, and if we observe that x is $n \times \sigma_x$ larger than its mean value μ_x, then we can deduce with 68.3% confidence that the accompanying value of y will lie within $\pm\sigma_y\sqrt{1-r^2}$ of $\mu_y + rn\sigma_y$.

4.A.2 Theoretical estimates

In the text we were interested in deriving the theoretically expected correlation coefficient between galaxy and Lyman-α forest fluctuations. This requires us to calculate expectation values of the form $\langle f(\mathbf{r})g(\mathbf{r})\rangle$ where $f(\mathbf{r})$ and $g(\mathbf{r})$ might represent the forest and galaxy overdensity at spatial position $\mathbf{r}$. The calculation is often easiest in Fourier space. If $f(\mathbf{r})$ and $g(\mathbf{r})$ are two arbitrary functions of position, then the average value of their product in a volume V satisfies

$$\langle f(\mathbf{r})g(\mathbf{r})\rangle \equiv \frac{1}{V}\int dV fg = \left(\frac{1}{2\pi}\right)^3 \int d^3k f_k(\mathbf{k})g_k(-\mathbf{k}) \tag{4.A.2}$$

where f_k and g_k are the Fourier transforms of f and g in the convention of Peebles (1980). The second equality is Parseval's theorem.

In practice we will often be interested in the correlation coefficient between two random fields that have been binned. For example, to compare to Figure 4.17 we might want to calculate the correlation coefficient between the mass observed along a $\sim$ 10Mpc skewer and the mass in the surrounding $10 \times 10 \times 10$ Mpc^3 cube. Let $f'(\mathbf{r})$ represent the mean overdensity in a 10Mpc cube centered on $\mathbf{r}$ and let $f(\mathbf{r})$ represent the unsmoothed overdensity at each position $\mathbf{r}$. With a little thought we can see that $f'(\mathbf{r})$ is equal to $f(\mathbf{r})$ convolved by a cube, and so, by the convolution theorem, $f'_k(\mathbf{k}) = f_k(\mathbf{k})W_f(\mathbf{k})$ where $W_f(\mathbf{k})$ is the Fourier transform of the cube. If the underlying functions $f(\mathbf{r})$ and $g(\mathbf{r})$ have been smoothed by arbitrary functions with Fourier transforms $W_f(\mathbf{k})$ and $W_g(\mathbf{k})$, the average value of their product in a volume V will therefore be

$$\langle f'(\mathbf{r})g'(\mathbf{r})\rangle \equiv \frac{1}{V}\int dV f'g' = \left(\frac{1}{2\pi}\right)^3 \int d^3k f_k(\mathbf{k})W_f(\mathbf{k})g_k(-\mathbf{k})W_g(-\mathbf{k}) \qquad (4.A.3)$$

(cf. 4.A.2).

These equations are all we need to work out the expected correlation strength between galaxy and Lyman-α forest fluctuations under the assumption that both reflect fluctuations in the underlying distribution of matter. An example can help illustrate. Suppose that the baryon density at each spatial position $\mathbf{r}$ at high redshift is proportional to the mass density smoothed by a spherical Gaussian with sigma R_f comparable to the Jeans length (e.g., Gnedin & Hui 1998), and suppose further that the galaxy bias is linear, so that galaxy and mass overdensities are precisely proportional to each other when averaged over a suitably large spatial scale. How strong a correlation would we expect to see between the baryonic overdensity at a given position and the galaxy overdensity in a larger surrounding Gaussian sphere with sigma equal to R_g? Let f_k and g_k denote the Fourier transforms of the Gaussian-smoothed baryon and galaxy overdensities respectively. We have by assumption $f_k = \delta_k W_f$ and $g_k \propto \delta_k W_g$, where δ_k is the Fourier transform of mass overdensities, $W_f \propto$

$\exp[-(kR_f)^2/2]$ is the "Jeans" smoothing kernel, and $W_g \propto \exp[-(kR_g)^2/2]$. Using equation 4.A.2 to calculate the necessary variances and covariances in equation 4.A.1, and recalling that $\mu_f = \mu_g = 0$ by definition, we see that the expected correlation coefficient between baryon and galaxy fluctuations in this scenario would be

$$r_{bg} \equiv \frac{\langle fg \rangle}{\langle f^2 \rangle^{1/2} \langle g^2 \rangle^{1/2}} = \frac{\int d^3k P(\mathbf{k}) W_f(\mathbf{k}) W_g^*(\mathbf{k})}{\left(\int d^3k_1 P(\mathbf{k}_1) |W_f(\mathbf{k}_1)|^2 \int d^3k_2 P(\mathbf{k}_2) |W_g(\mathbf{k}_2)|^2 \right)^{1/2}} \quad (4.A.4)$$

where $P(\mathbf{k}) \equiv \langle |\delta(\mathbf{k})|^2 \rangle$ is the power-spectrum of mass fluctuations. If $P(\mathbf{k})$ is an isotropic power law, $P(\mathbf{k}) \propto |\mathbf{k}|^n$, this reduces analytically to

$$r_{bg} = [2R_f R_g/(R_f^2 + R_g^2)]^{(n+3)/2} \simeq (2R_f/R_g)^{(n+3)/2}. \quad (4.A.5)$$

The approximate equality holds provided $R_g \gg R_f$.

This equation illustrates two arguments made above. First, for a given value of R_g, the strength of the correlation will depend on two factors, the Jeans length R_f and the shape of the power spectrum. Even if galaxy and Lyman-α forest fluctuations are both perfect tracers of mass fluctuations, we would not expect a measurement of the forest opacity in a single pixel to be able to predict the number of neighboring galaxies with perfect accuracy because the forest measurement would tell us only about the mass within a radius R_f, not within the larger radius R_g. One way to increase the correlation between forest and galaxy fluctuations is to make the Jeans length larger, so that it approaches R_g. Another is to change the slope of the power spectrum towards $n \sim -3$ so that nothing significant happens in the mass distribution on scales between R_f and R_g. Figure 4.24 illustrates this qualitatively.

Second, we can see that in general we should expect a very weak correlation between the local baryon density and the number of galaxies in a surrounding $\sim$ 10Mpc region if standard assumptions about the Jeans length and power-spectrum shape at $z \sim 3$ are correct. Substituting into equation 4.A.5 the values $R_f \sim 0.04h^{-1}$ Mpc (e.g., Gnedin & Hui 1998; McDonald *et al.* 2000; Zaldarriaga, Hui, & Tegmark

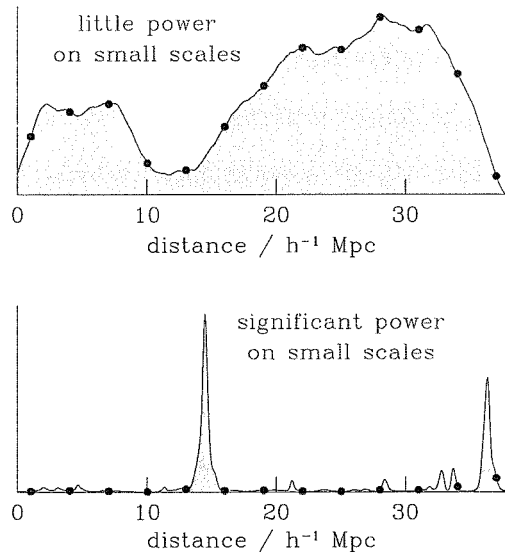

Figure 4.24 Subsampling accuracy and power-spectrum shape. The shape of a function can be estimated from measurements at a small number of points, but the reliability of our estimate will depend on how much power the function has on wavelengths smaller than the interpoint spacing Δ. When the function has no power at frequencies greater than the Nyquist frequency $1/2\Delta$, subsampling determines its exact value at all points. The top panel shows an example of a function that is close to this limit. The function is shaded; points mark positions where we are imagining that its value has been observed. As the power above the Nyquist frequency increases, reconstructions of a function are subject to increasing uncertainty. This uncertainty can be quantified through equation 4.A.4 or obvious variants. The CDM power-spectrum has a significant amount of power on small scales, as one can see from the density along a random line of sight through the SPH simulation described in White et al. (2001; bottom panel), and as a result subsampling can provide only loose constraints on the matter density at places that have not been observed. This figure presents a lower-dimension analog of the actual situation described in the text.

2001) for the Jeans length, $n \sim -1.5$ for the power-spectrum slope, and $R_g \sim 5h^{-1}$ comoving Mpc (roughly appropriate for our survey) for the size of the galaxy cells, we estimate a tiny correlation coefficient of $r \sim 0.04$ between the local baryon density and the galaxy overdensity in surrounding $R \sim 5h^{-1}$ Mpc region, even if galaxy fluctuations traced matter fluctuations perfectly. The reason can be easily grasped by referring to Figure 4.24. A significant fraction of the mass in a CDM density field resides within small objects that coarse subsampling may not detect.

Calculating correlation coefficients from the matter power-spectrum tells us how reliably we can predict the mass that is contained in one region (e.g., a 10Mpc cube) from a measurement of the mass contained in another region (e.g., a region the size of Jeans' length at the center of the cube). But masses are not what we can measure. Instead we have measured the galaxy density in the 10Mpc cube and the Lyman-α forest transmissivity along the sightline. The galaxy density may be a complicated function of the mass in the cube, and the forest transmissivity may be a complicated function of the mass along the sightline. What limits can we place on the correlation coefficient between our observables given the underlying correlations in the mass distribution? This is the primary subject of the next section. The text describes how the inequalities below can be applied to the problem at hand.

4.A.3 Maximizing the correlation coefficient

Manipulating one random variable

Suppose that x and y are two random variables drawn from an arbitrary distribution $P(xy)$, and that we are interested in predicting x as reliably as possible from a measured value of y. What function $f(y)$ with non-zero variance has the largest possible correlation coefficient with x? Assume without loss of generality that $\langle x \rangle = \langle f(y) \rangle = 0$. Maximizing $|r|$ with respect to f is equivalent to maximizing

$$\frac{\langle x f(y) \rangle^2}{\langle f^2(y) \rangle} \equiv \frac{\left(\int dy\, f(y) m(y) P(y) \right)^2}{\int dy f^2(y) P(y)} \tag{4.A.6}$$

where $P(y)$ is the marginal distribution of y and $m(y) \equiv \int dx P(x|y) x$ is the expectation value of x given y. By the Cauchy-Schwarz inequality, the right-hand side of equation 4.A.6 attains its maximum value of $\int dy P(y) m^2(y)$ for $f(y) = Cm(y)$, where C is a non-zero constant. This shows that no function of y is more strongly correlated with x than is $m(y)$, the expectation value of x given y.

Manipulating both random variables

Suppose x and y are drawn from a bivariate Normal distribution with correlation coefficient r_g and with $\mu_x = \mu_y = 0$. What is the maximum possible correlation coefficient between any two arbitrary functions $\phi(x)$ and $\psi(y)$? The covariance of $\phi(x)$ and $\psi(y)$ is given by

$$\langle \phi(x)\psi(y) \rangle - \langle \phi(x) \rangle \langle \psi(y) \rangle = \sum_{p=1}^{\infty} a_p b_p r_g^p \tag{4.A.7}$$

where a_p and b_p are the pth order coefficients of Hermite polynomial expansions of $\phi(x)$ and $\psi(y)$ respectively (e.g., Houdré & Pérez-Abreu 1995 §3). Therefore, the correlation coefficient of $\phi(x)$ and $\psi(y)$ satisfies

$$r^2 = r_g^2 \frac{\left(\sum_{i=1}^{\infty} a_i b_i r_g^{i-1}\right)^2}{\left(\sum_{j=1}^{\infty} a_j^2\right)\left(\sum_{k=1}^{\infty} b_k^2\right)}. \tag{4.A.8}$$

According to the Cauchy-Schwarz inequality, $(\sum a_i b_i)^2/(\sum a_j^2)(\sum b_k^2) \leq 1$ for all a_i, b_i, so it must be true *a fortiori* that $(\sum a_i b_i r_g^{i-1})^2/(\sum a_j^2)(\sum b_k^2) \leq 1$ since $r_g \leq 1$. This shows that

$$r^2 \leq r_g^2. \tag{4.A.9}$$

No functions $\phi(x)$, $\psi(y)$ of the bivariate Normal random variables x and y can be more strongly correlated than the variables x and y themselves. Equality is achieved in equation 4.A.9 if $r_g = 1$ and $a_i = b_i$ for all i, or if $a_i = b_i = 0$ for $i > 1$ which implies that ϕ and ψ depend linearly on x and y. In other cases the presence of terms with the form r_g^n in the numerator of 4.A.8 makes equality very difficult to approach. This is especially true since any stochasticity in ϕ and ψ will add terms that contribute to the denominator but not the numerator of 4.A.8.

The optimal line-of-sight window function

Let us return to the idealized case of § 4.A.2 where we have measured the density along a line and wish to estimate the density in a surrounding cube. What linear

combination of the line-of-sight densities will give us the most reliable estimate of the mean density in the cube? One might simply average the density along the sightline segment that lies within the cube, but it is easy to see that this is not optimal: the density at the center of the cube ought to be more strongly correlated with the cube's mean density than the density at one edge of the cube, for example, while the large scale correlations in the density field mean that even parts of the sightline lying outside the cube will have densities that are correlated with the cube's to some extent. An optimal approach would use a smoothly varying weighted average of the line-of-sight density, not a simple boxcar. But what weighting function is optimal? Let $\delta_c(x, y, z)$ be the mean density in a cube centered at (x, y, z), let $\delta_l(x, y, z)$ be weighted-mean value of the sightline density at the same position, let $W_c(k_x, k_y, k_z)$ be the Fourier transform of the cube, and let $W_l(k_z)$ be the Fourier transform of the line-of-sight weighting function. We want to find the weighting function $W_l(k_z)$ that leads to the highest possible correlation-coefficient between δ_l and δ_c. This function will clearly be symmetric about the origin, so $W_l(k_z)$ is real. Since $\langle \delta_c^2 \rangle$ is independent of W_l, maximizing the correlation coefficient is equivalent to finding the function W_l that maximizes $\langle \delta_l \delta_c \rangle^2 / \langle \delta_l^2 \rangle$. Because

$$\langle \delta_l^2 \rangle = \int dk_z \, |W_l(k_z)|^2 \alpha(k_z) \tag{4.A.10}$$

with

$$\alpha(k_z) \equiv \int dk_x dk_y \, P(k_x, k_y, k_z), \tag{4.A.11}$$

and

$$\langle \delta_l \delta_c \rangle = \int dk_z \, W_l(k_z) \beta(k_z) \tag{4.A.12}$$

with

$$\beta(k_z) \equiv \int dk_x dk_y \, P(k_x, k_y, k_z) W_c(k_x, k_y, k_z), \tag{4.A.13}$$

the quantity $\langle \delta_l \delta_c \rangle^2 / \langle \delta_l^2 \rangle$ can be written

$$\frac{\langle \delta_l \delta_c \rangle^2}{\langle \delta_l^2 \rangle} = \frac{\left(\int dk_z \, f(k_z) g(k_z) \right)^2}{\int dk_z \, f^2(k_z)} \tag{4.A.14}$$

where $f \equiv W_l \sqrt{\alpha}$ and $g \equiv \beta / \sqrt{\alpha}$. g is fixed by our choice of power-spectrum. According to the Cauchy-Schwarz inequality, the function f that maximizes 4.A.14 must be proportional to g. This requirement $f \propto g$ tells us that the Fourier-transform of the optimal weighting function will satisfy

$$W_{\mathrm{opt},l}(k_z) \propto \beta(k_z) / \alpha(k_z). \tag{4.A.15}$$

$\alpha(k_z)$ and $\beta(k_z)$ can be calculated for any power-spectrum through simple numerical or analytical integrations. Taking the Fourier transform of their ratio will produce the optimal real-space weighting function of sightline densities. Figure 4.25 shows an example of an optimal weighting function. Call this function $W_l^r(z)$. For a power-spectrum similar to that of the $z = 3$ output of the $\Omega_\Lambda = 0.7$, $\Omega_M = 0.3$ CDM GIF N-body simulation (Kauffmann et al. 1999), no linear combination of densities along a sightline is more strongly correlated with the mean density in a surrounding $13h^{-1}$ comoving Mpc cube than the linear combination $\bar{\rho}_l(z) \equiv \int dz' \, W_l^r(z') \rho(z - z')$ with $W_l^r(z)$ shown in figure 4.25.

But the gain from this sort of weighting can be surprisingly small. The correlation coefficient between the density in a 13Mpc cube and the optimally weighted sightline density is 0.28, for example, compared to a correlation coefficient of 0.26 for boxcar weighting. This justifies our adoption of boxcar weighting in the text. Having committed ourselves to putting our galaxies in cubical cells, we do not lose much by using a simple boxcar (or Gaussian) to bin the sightline density.

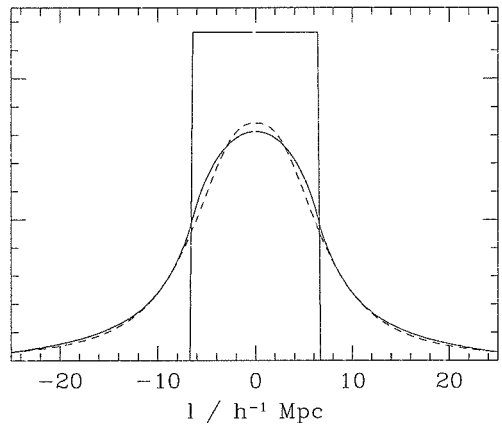

Figure 4.25 The boxcar window function used to average line-of-sight densities compared to the optimal window function (solid lines). The dashed line shows the uninspired fitting formula $W_{\rm opt}(z) \simeq \left(1 + |1.83z/l_z|^{2.6}\right)^{-1}$ where l_z is the width of the boxcar.

4.B General limits on the association of two random fields

§ 4.A was primarily concerned with the idealized case where two observed random fields (e.g., the spatial distributions of galaxies and of intergalactic HI) are both closely related to a single underlying random field (e.g., the spatial distribution of matter) that we cannot observe. The limits that we placed on the possible association of the two observed random fields followed from their assumed association with the same underlying random field. But some limits can be placed on the possible association of two random fields even if they are not related to each other in this simple way.

Let $f(\mathbf{r})$, $g(\mathbf{r})$, $f_k(\mathbf{k})$, and $g_k(\mathbf{k})$ be two arbitrary random fields and their Fourier transforms. The Cauchy-Schwarz inequality in the form

$$|\langle a^* b \rangle|^2 \leq \langle a^* a \rangle \langle b^* b \rangle \tag{4.B.1}$$

leads to the following two inequalities:

$$\xi_{fg}^2(\mathbf{r}) \leq \xi_{ff}(0)\xi_{gg}(0), \tag{4.B.2}$$

where ξ_{ff} is the auto-correlation function of f and ξ_{fg} is the cross-correlation function of f with g, and

$$|P_{fg}(\mathbf{k})|^2 \leq P_{ff}(\mathbf{k})P_{gg}(\mathbf{k}), \tag{4.B.3}$$

where P_{ff} is the power-spectrum of f and P_{fg} is the cross-spectrum of f and g. Equations 4.B.2 and 4.B.3 result from inserting $a = f(\mathbf{r}')$, $b = g(\mathbf{r}-\mathbf{r}')$ and $a = f_k(\mathbf{k})$, $b = g_k(\mathbf{k})$ into equation 4.B.1.

Equation 4.B.2 does not appear to be particularly useful, because the RHS is independent of r and depends on the value of the correlation function at zero lag, which is often difficult to estimate. Fortunately the possible association of f and g in real space can be limited by a large number of other inequalities. Consider, for example, the mean value of the correlation function ξ_{fg} weighted by an arbitrary function $W(\mathbf{r})$,

$$\bar{\xi}_{fg} \equiv \int d^3r\, \xi_{fg}(\mathbf{r})W(\mathbf{r}) \Big/ \int d^3r W(\mathbf{r}). \tag{4.B.4}$$

If W were equal to a constant for $|\mathbf{r}| < r_{\rm sph}$ and to zero elsewhere, $\bar{\xi}_{fg}$ would be the mean value of the correlation function ξ_{fg} within a sphere of radius $r_{\rm sph}$. Written in Fourier space, equation 4.B.4 becomes

$$\bar{\xi} \propto \int d^3k\, P_{fg}(\mathbf{k})W_k(\mathbf{k}) \tag{4.B.5}$$

or

$$\bar{\xi}^2 \propto \left| \int d^3k\, \langle f_k(\mathbf{k})g_k^*(\mathbf{k})\rangle W_k(\mathbf{k}) \right|^2 \tag{4.B.6}$$

where $P_{fg}(\mathbf{k})$ is the cross-spectrum of f and g and $W_k(\mathbf{k})$ is the Fourier transform of $W(\mathbf{r})$. If $W_k(\mathbf{k})$ is real and positive, $W_k(\mathbf{k})^{1/2}$ can be absorbed into each of f_k and g_k in equation 4.B.6, leading through equation 4.B.1 to the inequality

$$\bar{\xi}_{fg}^2 \leq \bar{\xi}_{ff}\bar{\xi}_{gg} \tag{4.B.7}$$

which holds only if the correlation functions are averaged in a suitably chosen way. Because the Fourier transform of a spherical Gaussian centered on the origin is real and positive, correlation functions averaged within a spherical Gaussian must obey inequality 4.B.7.

The derivation of 4.B.7 relies on the assumption that the correlation function $\xi(\mathbf{r})$ and power-spectrum $P(\mathbf{k})$ are Fourier transforms of each other. When a random field is composed of discrete objects (i.e., when it can be thought of as a collection of Dirac delta functions rather than a smoothly varying function), however, it is customary to modify the definition of the correlation function to exclude the correlation of an object with itself. In this case the power-spectrum is equal to the Fourier transform of the correlation function plus an additive constant (see, e.g., Peebles 1980 §41), and equation 4.B.7 accordingly becomes

$$\bar{\xi}_{gf}^2 \leq (\bar{\xi}_{ff} + 1/\bar{n}_f)(\bar{\xi}_{gg} + 1/\bar{n}_g), \tag{4.B.8}$$

where n_f is the global number density of delta functions in f and $\bar{n}_f \equiv n_f \int d^3r\, W(\mathbf{r})/W(0)$, rather than 4.B.7.

It is worth giving a moment's thought to the difference between equations 4.B.7 and 4.B.8. Suppose f and g are two continuous but intrinsically uncorrelated functions, two functions with $\xi_{ff}(r) = \xi_{gg}(r) = 0$ for all $r > 0$ so that $\bar{\xi}_{gg}(r) = \bar{\xi}_{ff}(r) = 0$. f and g might represent white noise. Could $\bar{\xi}_{fg}$ be anything other than zero? One might imagine that the noise peaks of f could be made to align with those of g in a way that led to a positive cross-correlation $\bar{\xi}_{fg}$, but in fact this is not true; even in the best case where the noise peaks and troughs of f and g line up perfectly, i.e., $g \simeq f$, we would have $\bar{\xi}_{fg} \simeq \bar{\xi}_{ff}$ and $\bar{\xi}_{ff}$ is zero by hypothesis. In this case equation 4.B.7 holds.

Now suppose that f is a collection of randomly distributed delta functions, so that $\xi_{ff} = 0$, and suppose that g is identical to f. Here too $\bar{\xi}_{ff} = \bar{\xi}_{gg} = 0$. But if we

estimated $\bar{\xi}_{fg}$ by counting the number of objects in g within Gaussian spheres of radius r_G centered on each object in f, we would find that $\bar{\xi}_{fg}$ could be arbitrarily large: even as $r_G \to 0$, every Gaussian sphere would still contain one member of g, and the implied overdensity of g objects in the spheres, $1 + \bar{\xi}_{fg} = n_{\rm obs}/n_{\rm exp} = W(\mathbf{0})/n_g \int d^3r W(\mathbf{r})$, would approach infinity. This is an example of a case where 4.B.8 applies.

Suppose finally that f and g are two different collections of randomly distributed delta functions. One might imagine that f was created by associating an independently and identically distributed random number with each volume element dV, then placing a particle in every volume element whose random number exceeded some threshold, and that g was subsequently created in the same way with a different set of random numbers. Once again $\xi_{ff} = \xi_{gg} = 0$ by construction. But this time f and g would not align in any special way; the mean number of g particles in Gaussian spheres centered on f particles would be the same as the mean number of g particles in randomly placed Gaussian spheres, making $\xi_{fg} = 0$. Once again the correlation functions satisfy 4.B.7.

These heuristic examples were designed to illustrate the fact the one can search for a possible direct connection between two sets of objects (e.g., galaxies and CIV systems) by seeing if their cross-correlation function violates 4.B.7. All possible sets f and g of particles must obey 4.B.8, but most will obey 4.B.7 as well. The cross-correlation function of f and g will violate 4.B.7 only if the shot noise in f is correlated with the shot noise in g. It may be helpful to think in terms of the Poisson process model of Peebles (1980; §33). Suppose the collection of particles f is generated by placing objects at random positions x with a probability given by the continuous function $f'(x)$, and suppose that g is generated similarly from $g'(x)$. If the continuous functions f' and g' are both determined before creating f and g, the cross-correlation function of f and g will satisfy 4.B.7. Their cross-correlation function will violate 4.B.7 only if we would choose a different function g' for different random

realizations f of the same function f'. This would be the case if (for example) we set g' equal to f convolved by a Gaussian, so that objects in g could only fall close to the locations of objects in f.

In picturesque terms, one might say that although pedestrians, eyeglasses, and fire hydrants all tend to be found in similar places on the earth's surface, the cross-correlation function of pedestrians and eyeglasses obeys 4.B.8 while (except in very unfortunate circumstances) the cross-correlation function of pedestrians and fire hydrants obeys 4.B.7. Not all pedestrians wear eyeglasses, and not all eyeglasses are on pedestrians, but the locations of at least some eyeglasses are determined by where pedestrians happen to be standing. The locations of fire hydrants are not.

4.C Estimating an overdensity

Suppose we would like to estimate the universal average overdensity of Lyman-break galaxies in cells centered on CIV systems from a measurement of $\{N_i\}$, the number of Lyman-break galaxies in cells centered on each of the $\mathcal{N}_c$ CIV systems in our sample. What estimator should we use? If an average of μ galaxies were expected to lie in each CIV system's cell in the absence of a correlation between galaxies and CIV systems, a natural choice for the estimator would be

$$\bar{\xi}_{cg} = \frac{1}{\mathcal{N}_c} \sum_{i=1}^{\mathcal{N}_c} N_i/\mu - 1, \tag{4.C.1}$$

the mean of the observed galaxy overdensity $N_i/\mu - 1$ around each of the i CIV systems. But in practice we would not expect to observe μ Lyman-break galaxies around each CIV system if galaxies and CIV systems were independently distributed; because the selection function of our galaxy survey peaks around $z \simeq 3.0$, we would expect to see more Lyman-break galaxies close to a CIV system at $z = 3.0$ than to a CIV system at (say) $z = 2.2$ or $z = 3.5$. The expected number of galaxy neighbors

is not a constant but instead depends on each CIV system's redshift, and we must estimate the global mean overdensity not from $\{N_i\}$ and μ but from $\{N_i\}$ and $\{\mu_i\}$ where μ_i is the expected overdensity around the ith CIV system given the system's redshift and the shape of our selection function. What estimator should we use now?

Let $\bar{\xi}_{cg}$ be the average value of the galaxy-CIV cross-correlation function in the cell (i.e., the global mean overdensity of galaxies in cells centered on CIV systems), and let $n_i \equiv \mu_i(1+\bar{\xi}_{cg})$ be the expected number of galaxies in a cell centered on z_i given that there is a CIV system at z_i. Approximating the probability of observing N_i galaxies when n_i were expected with the Poisson distribution, $P(N_i|n_i) = e^{-n_i} n_i^{N_i}/N_i!$, and assuming that different cells are independent, one finds that the probability of observing the set of actual $\{N_i\}$ and expected $\{n_i\}$ galaxy numbers in cells surrounding CIV systems is equal to the product of the individual probabilities:

$$P(\{N_i\}|\{n_i\}) = \exp\left[-(1+\bar{\xi}_{cg})\sum_i \mu_i\right]\left(1+\bar{\xi}_{cg}\right)^{\sum_i N_i} \prod_i \mu_i^{N_i}/N_i!. \qquad (4.C.2)$$

The $\bar{\xi}_{cg}$ dependence of equation 4.C.2 is identical to the $\bar{\xi}_{cg}$ dependence of a single Poisson distribution of the form $P(x|\bar{x}) = e^{-\bar{x}}\bar{x}^x/x!$ with $x \equiv \sum_i N_i$ and $\bar{x} \equiv (1+\bar{\xi}_{cg})\sum_i \mu_i$. Since the likelihood $P(x|\bar{x})$ is maximized for $x = \bar{x}$, we can see immediately that we should adopt

$$\bar{\xi}_{cg} = \frac{\sum_i N_i}{\sum_i \mu_i} - 1 \qquad (4.C.3)$$

as the maximum likelihood estimator of $\bar{\xi}_{cg}$. In practice the assumptions leading to equation 4.C.3 are somewhat incorrect—different cells are not completely independent, for example—and so the estimator is not optimal; but it provides an attractively simple and reasonably good way to correct for the complexities of our selection bias.

In the notation of equation 4.20, estimator 4.C.3 would be written $D_c D_g/D_c R_g - 1$. The point of this section is not to advocate this particular estimator—in our more careful calculations the superior estimator of equation 4.20 (Landy & Szalay 1993) was adopted instead—but to justify our practice of estimating $\bar{\xi}$ by summing the

number of observed and expected pairs in our full sample and then dividing, rather than (e.g.) by averaging together the values of $N_i/\mu_i - 1$ observed around individual CIV systems or in individual fields.

4.D Spatial clustering of Lyman-break galaxies

Because of peculiar velocities and redshift uncertainties, our estimate of any Lyman-break galaxy's position along the line-of-sight is imprecise. This imprecision complicates our attempts to measure the correlation function of galaxies at small separations. With a redshift uncertainty of $\sigma_z \sim 0.0025$ (~ 1.8 Mpc) we cannot estimate the strength of the correlation function at separations $r < 1$ Mpc (say) by counting the number of galaxies that lie within 1 Mpc of each other and comparing to the expected number if galaxies were uniformly distributed; the number of galaxies within 1 Mpc of each other is something we do not know.

One way around this problem (e.g., Davis & Peebles 1983) is to count not the number of galaxies whose estimated redshifts place them within a distance r of each other, but instead the number of galaxies with angular separation $r_\theta \pm dr_\theta$ and redshift separation $|\Delta z| < r_z$. If r_z is significantly larger than each galaxy's positional uncertainty Δl, the resulting function of r_θ, $n(r_\theta, < r_z)$, will be unaffected by the size of our redshift errors. $n(r_\theta, < r_z)$ can then be inverted to produce an estimate of the correlation function $\xi(r)$ that is not corrupted by redshift uncertainties.

Different schemes can be used to estimate $\xi(r)$ from $n(r_\theta, < r_z)$ (see, e.g., Davis & Peebles 1983). Here is our approach. It is designed for the low signal-to-noise regime where one can only hope to estimate the gross features of the correlation function. The expected number of galaxy neighbors with angular separation r_θ and radial separation within $\pm r_z$ is

$$\langle n(r_\theta, < r_z) \rangle = \bar{n}\left(1 + \frac{1}{r_z}\int_0^{r_z} dl\, \xi(\sqrt{l^2 + r_\theta^2})\right) \qquad (4.D.1)$$

where $\bar{n}$ is the number of galaxies we would expect to observe along a similar line randomly placed. If the correlation function is a power law, $\xi(r) \equiv (r/r_0)^{-\gamma}$, dull algebra shows that the expected excess number of pairs is

$$\omega_p(r_\theta, < r_z) \equiv \frac{\langle n \rangle}{\bar{n}} - 1 = \frac{r_o^\gamma r_\theta^{1-\gamma}}{2r_z} B\Big(1/2, (\gamma-1)/2\Big) I_x\Big(1/2, (\gamma-1)/2\Big) \qquad (4.D.2)$$

where B and I_x are the beta function and incomplete beta function in the convention of Press et al. (1992, §6.4) and $x \equiv r_z^2(r_z^2 + r_\theta^2)^{-1}$. We estimate the correlation function parameters r_0, γ by fitting equation 4.D.2 to observed number of galaxies with similar redshifts that lie at angular separation r_θ.

In principle any value of r_z can be used, provided $r_z \gg \sigma_z$, but in practice some choices of r_z are better than others. If r_z is too small we will miss some correlated pairs. The incomplete beta function in equation 4.D.2 will correct for this only imperfectly. If r_z is too large our sample will include a needlessly large number of uncorrelated pairs, and statistical fluctuations in the number of uncorrelated pairs may obscure the number of correlated pairs. Our choice of r_z was designed to fall between these two extremes. We took r_z to be the greater of $1000\mathrm{kms}^{-1}(1+z)/H(z)$ and $7r_\theta$. $1000\mathrm{kms}^{-1}$ is several times larger than our redshift uncertainty, and so the first lower limit helps ensure that redshift errors will not make us fail to recognize correlated pairs. The second limit ensures that we will integrate far enough down the correlation function to include at least 80% of correlated pairs for $\gamma \gtrsim 1.6$. The derived correlation function does not change significantly if the $1000\mathrm{kms}^{-1}$ is changed by a factor of 2 in either direction or if we adopt (say) $15r_\theta$ rather than $7r_\theta$ as the lower limit on r_z.

Figure 4.22 shows the observed excess galaxy counts as a function of angular separation r_θ. Overlaid are the expected excess galaxy counts at each separation for the best power-law fit to $\xi(r)$. The data are reasonably consistent with a power-law correlation function. ω_p was estimated with the Landy-Szalay (1993) estimator

$(DD-2DR+RR)/RR$; this nomenclature and method of generating random catalogs are described in the main body of the text below equation 4.20. The only change is that here DD (e.g.) is the observed number of galaxy pairs with angular separation r_θ and redshift separation $|\Delta z| < r_z$, rather than the number of pairs with separation r_θ, r_z. As described above, near equation 4.20, the angular locations of objects in the random and real catalogs were the same. This eliminated any artificial clustering signal due to angular variations in the fraction of Lyman-break galaxies with measured redshifts, an inevitable result of our sparse multislit spectroscopy, but also eliminated any contribution from the true angular clustering of Lyman-break galaxies to our estimate of $\xi(r)$. As the angular correlation $\omega(\theta)$ of Lyman-break galaxies is almost undetectably weak (Giavalisco & Dickinson 2001), however, the resulting bias in $\xi(r)$ should be small.

The estimates $r_0 = 3.96 \pm 0.29h^{-1}$ comoving Mpc, $\gamma = -1.55 \pm 0.15$ follow from fitting equation 4.D.2 to the data by minimizing χ^2 with Powell's direction set method (Press et al. 1992; §10.5). The uncertainties were calculated by generating a large number of fake realizations of ω_p by adding to our estimated ω_p at each r_θ a Gaussian deviate with standard deviation equal to the observed uncertainty, then fitting these fake realizations of ω_p to equation 4.D.2 with Powell's method. 68.3% of the fake realizations had best fit parameter values in the range listed above.

We should emphasize that figure 4.22 provides little support for or against Porciani & Giavalisco's (2002) claim that the correlation function of Lyman-break galaxies becomes negative at very small separations. Any small-scale anticorrelation would be washed out in the redshift direction by our redshift uncertainties and by the integration of equation 4.D.1; any anti-correlation in the angular positions of galaxies would be missed in our analysis because of the way we generated our random catalogs.

In any case, the correlation function estimated here agrees well with the clustering strength estimated from a counts-in-cells analysis. Using the statistic $\mathcal{S}$ of Adelberger

et al. (1998) on our current full sample of Lyman-break galaxies, we estimate the relative variance of galaxy number density in cubical cells of side-length $11.6h^{-1}$ Mpc ($\Omega_M = 0.3$, $\Omega_\Lambda = 0.7$) to be $\sigma^2_{\rm gal} = 0.8 \pm 0.2$, which corresponds roughly to a correlation length of $r_0 = 4.65 \pm 0.75h^{-1}$ comoving Mpc for $\gamma = -1.55$ (see Adelberger et al. 1998).

4.E Can winds escape Lyman-break galaxies?

We described in § 4.2.2 the evidence that the gas responsible for the absorption lines in a spectrum of a Lyman-break galaxy is usually being driven out of the galaxy. The speed of the outflow is uncertain but probably approaches or exceeds $\sim 600 {\rm km\,s^{-1}}$. Is it likely that the outflowing material will escape the galaxy's potential altogether? The answer depends on the depth of the galaxy's potential, on the energy of the outflow, and on how far out of the galaxy's potential the outflow has already climbed.

4.E.1 Radius of the observed absorbing gas

Little is known about the typical distance $r_{\rm ISM}$ between the stars in Lyman-break galaxies and the colder, outflowing material that produces the interstellar absorption lines. Because strong interstellar absorption is observed in virtually all Lyman-break galaxies (Shapley et al. 2002, in preparation), the absorbing material cannot generally be closer to the observed stellar centroid than the typical galaxy's half-light radius. This sets a lower limit of $r_{\rm ISM} \gtrsim 1.6h^{-1}$ proper kpc for $\Omega_M = 0.3$, $\Omega_\Lambda = 0.7$ (Giavalisco et al. 1996).

A robust empirical upper limit follows from the lack of absorption in the spectra of the background QSOs at redshifts near those of Lyman-break galaxies near the sightline. A total of 22 Lyman-break galaxies in our sample lie within a projected separation $1h^{-1}$ comoving Mpc (for $\Omega_M = 0.3$, $\Omega_\Lambda = 0.7$) of the QSO sightline.

Of these galaxies, with impact parameters ranging from 0.30 to $0.99h^{-1}$ comoving Mpc, most can be plausibly associated with detectable metal absorption lines in the QSO spectrum (see figure 4.13), but none produces metal line absorption in the QSO spectrum that is nearly as strong as the absorption observed in its own spectrum. This shows that the interstellar absorption observed in Lyman-break galaxies is generally produced by material within $r_{\rm ISM} \sim 0.3h^{-1}$ comoving Mpc of the observed stars.

More stringent upper limits on $r_{\rm ISM}$ follow from consideration of the HI column density of the absorbing material. The optical depth at line center produced by a column density N_x of ion x for an electronic transition with wavelength λ_{xij} and oscillator strength f_{xij} is

$$\tau_\lambda^{\rm peak} = N_x \frac{\pi e^2}{m_e c} f_{xij} \frac{\lambda_{xij}}{\sigma_v \sqrt{2\pi}} \qquad (4.E.1)$$

where σ_v is the ion's 1D velocity dispersion, assumed to be a Gaussian, and e and m_e are the charge and mass of an electron. It is difficult to use this equation to estimate the HI column density from Ly-α, because Ly-α is heavily saturated and often contaminated by nebular emission. More promising is OIλ1302, which is not contaminated by nebular emission, is far less saturated due to its low oscillator strength ($f = 0.0486$) and low abundance, and yet has a strength closely related to the HI column density because of the charge-exchange reaction (e.g., Osterbrock 1989, §2.8). OIλ1302 is usually detected in our low signal-to-noise, 10Å resolution spectra with an equivalent width that implies $\sigma_v \sim 200$ km s^{-1}. This shows that the opacity at line center usually exceeds $\sim$ unity, and places a lower limit on the OI column of $\sim 3 \times 10^{15}{\rm cm}^{-2}$. The associated HI column is $\sim 5 \times 10^{19}{\rm cm}^{-2}$ for an assumed metallicity of $Z_{\rm LBG} \sim 0.1 Z_\odot$ (Pettini et al. 2001). Though the metallicity of Lyman-break galaxies could conceivably be as high as $0.5 Z_\odot$ (Pettini et al. 2001), this is nevertheless likely to be a lower limit on the column density: we cannot tell from our spectra if $\tau_{\rm OI}$ significantly exceeds unity at line center, and the observed equivalent width of

OI absorption could in principle be produced by a number of highly saturated systems with small velocity dispersions rather than a single moderately saturated system with a large velocity dispersion. In MS1512-cB58, the one Lyman-break with a high signal-to-noise echellette spectrum, for example, the interstellar lines are black at line center ($\tau_{\rm OI} \gg 1$) and the HI column density is $7 \times 10^{20}{\rm cm}^{-2}$ (Pettini et al. 2002). In any case, a large lower limit $\sim 5 \times 10^{19}{\rm cm}^{-2}$ on the HI column densities of typical Lyman-break galaxies would not necessarily conflict with the high escape fraction of hydrogen-ionizing photons reported by Steidel, Pettini, & Adelberger (2001): our low resolution data are unable to reveal if saturated interstellar absorption lines in Lyman-break galaxies are always black at line center, and it is possible that only some fraction of the $\sim (1.6{\rm kpc})^2$ faces of Lyman-break galaxies are obscured by large hydrogen columns along any sightline.

Relatively few absorption systems with $N_{\rm HI} > 5 \times 10^{19}{\rm cm}^{-2}$ are observed in the spectra of background QSOs, and this sets an upper limit on the allowed cross-sectional area of the interstellar material in Lyman-break galaxies. According to Storrie-Lombardi & Wolfe (2000), the number density per unit redshift of systems with column density $N_{\rm HI} > 2 \times 10^{20}$ cm^{-2} at redshift $z \sim 3$ is ~ 0.25, and the distribution of column densities for $10^{12} < N_{\rm HI} < 10^{22}$ cm^{-2} can be crudely fit by a function of the form $P(N_{\rm HI}) \propto N_{\rm HI}^{-1.46}$. The implied number density per unit redshift of systems with $N_{\rm HI} > 5 \times 10^{19}$ is roughly 0.5 at $z \sim 3$. The comoving distance per unit redshift at $z = 3$ is $\sim 670h^{-1}$ Mpc for an $\Omega_M = 0.3$, $\Omega_\Lambda = 0.7$ cosmology, and so Lyman-break galaxies' measured comoving density of $4 \times 10^{-3}h^3$ Mpc^{-3} (e.g., Adelberger et al. 2002, in preparation) translates to a comoving surface density per unit redshift of $\sim 2.7h^2$ Mpc^{-2}. Lyman-break galaxies would produce more systems with $N_{\rm HI} > 5 \times 10^{19}$ than are observed in the spectra of background QSOs if the cross-section of their absorbing material exceeded $0.5/2.7 \simeq 0.19h^{-2}$ comoving Mpc^2. We conclude that $r_{\rm ISM} < 0.24h^{-1}$ comoving Mpc. If cB58's HI column of $7 \times 10^{20}{\rm cm}^{-2}$

were typical, rather than the lower limit $\sim 5 \times 10^{19}\mathrm{cm}^{-2}$ estimated above, the same arguments would lead to an implied upper limit of $r_{\mathrm{ISM}} < 0.13h^{-1}$ comoving Mpc.

The most restrictive but least robust upper limit on r_{ISM} comes from our desire that any implied mass outflow rates not be unreasonably large. The rest-frame ultraviolet and optical colors of Lyman-break galaxies suggest that they have been forming stars (and presumably suffering outflows) for $\sim$ 300Myr (Shapley et al. 2001; cf. Papovich, Dickinson, & Ferguson 2001). A typical total mass of $\sim 10^{11}h^{-1}M_{\odot}$ for Lyman-break galaxies (see § 4.E.2) corresponds to a baryon mass of $\sim 2\times10^{10}h_{70}^{-3}M_{\odot}$, which would be exhausted in fewer than 300 Myr if the outflow rate exceeded $\sim 70h_{70}^{-3}M_{\odot}\mathrm{yr}^{-1}$. Our observables—the column density and velocity of interstellar material—do not uniquely determine the outflow rate, but it will likely be of order $\dot{M} \sim 4\pi r_{\mathrm{ISM}} v_{\mathrm{ISM}} N_{\mathrm{HI}} m_p$. For $v_{\mathrm{ISM}} = 600$ km s^{-1} and $N_{\mathrm{HI}} \sim 5 \times 10^{19}\mathrm{cm}^{-2}$, our limit $\dot{M} \lesssim 70h_{70}^{-3}M_{\odot}\mathrm{yr}^{-1}$ implies an upper limit of $r_{\mathrm{ISM}} \lesssim 20h_{70}^{-3}$ proper kpc.

None of the upper limits are particularly constraining, but they appear to be all we have. For the remainder of this section we shall adopt $r_{\mathrm{ISM}} = 3h^{-1}$ proper kpc as the best estimate of the typical distance between a Lyman-break galaxy's stars and its observed interstellar material. This arbitrary choice has significant implications, as we discuss below. We can offer little justification except to note that $r_{\mathrm{ISM}} = 3h^{-1}$ kpc is close to the lower limit of $r_{1/2} = 1.6h^{-1}$ kpc, which makes our choice both conservative, since it will tend to minimize the outflows' estimated impact on the intergalactic medium by forcing them to climb out of a large fraction of the galaxies' potential wells, and physically plausible, since cold material entrained in a hot wind will become heated and cease to produce low-excitation lines relatively quickly, before it can travel far from its origin (e.g., Klein, McKee, & Colella 1994 §9.2).

4.E.2 The escape velocity

We can estimate the typical escape speed at $r \sim 3$kpc by assuming that the dark matter density in Lyman-break galaxies follows a Navarro, Frenk, & White (1997) profile,

$$\rho_{\rm DM}(r) \propto \frac{1}{(1+cr/r_{\rm vir})^2 cr/r_{\rm vir}}, \tag{4.E.2}$$

with implied escape velocity

$$v_{\rm esc}^2(r) = \frac{2GM_{\rm vir}}{r}\frac{\ln(1+cr/r_{\rm vir})}{\ln(1+c)-c/(1+c)}. \tag{4.E.3}$$

Here $M_{\rm vir}$ is the galaxy's total mass within the virial radius $r_{\rm vir}$ and $c(M)$ parametrizes the central concentration of the mass distribution. A value of $c \sim 7$ is appropriate for objects at $z \sim 3$ with the comoving number density of Lyman-break galaxies in a standard $\Omega_M = 0.3$, $\Omega_\Lambda = 0.7$ CDM model (e.g., Navarro et al. 1997). The virial masses of Lyman-break galaxies are not known. A lower limit of $M_{\rm vir} \sim 10^{10}h^{-1}M_\odot$ follows from their observed stellar velocity dispersions within the innermost ~ 2 kpc (e.g., Pettini et al. 2001), but this tells us little about how much mass might reside at larger radii. If the universe evolves similarly to an $\Omega_M = 0.3$, $\Omega_\Lambda = 0.7$, $h = 0.7$, $\Gamma = 0.2$, $\sigma_8 = 0.9$ CDM model, we can set an upper limit on Lyman-break galaxies' masses of $M_{\rm vir} \sim 5 \times 10^{11}h^{-1}M_\odot$; objects more massive than this do not exist in sufficient numbers at $z \sim 3$ to be associated with them (e.g., Adelberger et al. 1998). As our best guess we shall take $M_{\rm vir} = 10^{11}h^{-1}M_\odot$, which is roughly the mass implied by the spatial clustering of Lyman-break galaxies (e.g., Giavalisco & Dickinson 2001) for the ΛCDM cosmology above. The corresponding virial radius (i.e., radius within which the mean density is ~ 200 times the universal mean) is $r_{\rm vir} \sim 40$ proper kpc, and the escape velocity implied by equation 4.E.3 is $\sim$ 360km s^{-1}. The precise value of the escape velocity is uncertain, but the allowed range of escape velocities ($150 \lesssim v_{\rm esc}(3h^{-1}{\rm kpc}) \lesssim 650$ km s^{-1} for $10^{10} \lesssim M_{\rm vir} \lesssim 5 \times 10^{11}M_\odot$, after accounting for the M dependence of c) is almost entirely lower than the observed wind speeds

of 600 km s^{-1}. This suggests that the outflowing gas can plausibly escape the galaxy potential well.

But the limitations of the calculation should be remembered. First, our physical interpretation of the observed absorption-line blueshifts is not unique. The absorbing material may be accelerated from 0 to $\sim$ 600 km s^{-1} by an entraining hotter flow, as observations of local starbursts have led us to assume, but other phase-space configurations are equally compatible with the data. Second, the observed gas is unlikely to move ballistically. The hot gas that presumably fills Lyman-break galaxies' halos can decelerate it or accelerate it further after it becomes heated and can no longer be observed. On balance the evidence may suggest that winds from Lyman-break galaxies have traveled far from their origin, but the simple calculation presented here does not prove on its own that this is the case.

4.E.3 Energetics

We have seen that if supernova feedback accelerates some of a Lyman-break galaxy's interstellar material to $v_i \sim 600$ km s^{-1}, the material may plausibly escape the galaxy's potential. But do supernova release enough energy to set such a wind in motion? The energy required to accelerate *every* baryon in a Lyman-break galaxy to a velocity v_i is

$$\begin{aligned} E &= \frac{\Omega_b M_{\rm LBG} v_i^2}{2\Omega_M} \\ &= 4.8 \times 10^{58} \left(\frac{7.5\Omega_b}{\Omega_M}\right)\left(\frac{M_{\rm LBG}}{10^{11} M_\odot}\right)\left(\frac{v_i}{600 {\rm km\ s^{-1}}}\right)^2 \quad {\rm erg} \end{aligned} \qquad (4.E.4)$$

which is the energy released by $\sim 5 \times 10^7$ supernovae. More than 5×10^7 supernovae are required to impart this energy to the wind, however, because not all of the energy released by supernovae will be converted into the kinetic energy of an outflow. Some fraction will be radiated away. Although we argue below that radiative cooling will

generally not be important as the winds propagate into the intergalactic medium, the same is not true within Lyman-break galaxies themselves. Pettini et al. (2001) find, for example, that a mass of roughly $10^{10}h^{-1}M_{\odot}$ is enclosed within the $6.5h^{-1}$ kpc comoving half-light radius of a typical Lyman-break galaxy, which implies a mean comoving density within $r_{1/2}$ of $\sim 8 \times 10^{15}h^2 M_{\odot}\mathrm{Mpc}^{-3}$, roughly 10^5 times larger than the global mean density $\bar{\rho} \simeq 8.4 \times 10^{10}(\Omega_M/0.3)h^2 M_{\odot}\mathrm{Mpc}^{-3}$. At this density the cooling times are very short, as figure 4.27 shows. The actual situation is complicated by the fact that the interstellar media of Lyman-break galaxies are presumably multiphase, with dense regions that radiate away the energy imparted by supernova and rarefied regions that do not. The fraction of supernova energy that goes into the kinetic energy of the outflowing gas is highly uncertain, but the required kinetic energy is only half the energy emitted by the $\sim 10^8$ supernovae that would explode during the assembly of Lyman-break galaxies' estimated stellar masses of $\sim 10^{10}h^{-1}M_{\odot}$ (e.g., Papovich, Dickinson, & Ferguson 2001; Shapley et al. 2001). A Lyman-break galaxy could send a fraction $f_{\mathrm{ej}} \sim 0.2$ of its baryons into the surrounding intergalactic medium even if $\sim 90\%$ of the energy emitted by supernovae were radiated away. 90% is roughly the radiated fraction found in numerical simulations of single supernova explosions in a uniform medium (e.g., Thornton et al. 1998), and it is likely that the radiated fraction would be significantly lower in a starburst galaxy where previous generations of supernova have stripped out a large fraction of the interstellar medium and heated much of the rest. The energy required by these winds would not be hard to supply. This is especially true since we have neglected another energy source that could be comparably large, the active nuclei that most Lyman-break galaxies may host for brief periods during their evolution.

4.F Winds and the Lyman-α forest

Suppose superwinds from Lyman-break galaxies were able to drive far into the intergalactic medium. What mark might they leave on the Lyman-α forest absorption spectrum of a background QSO? The complicated hydrodynamics of winds are difficult to model even with the most sophisticated numerical calculations, and we can hardly hope to provide a definitive answer in this section. Our goal instead will be to provide a rough answer with order-of-magnitude arguments. We shall assume a spherically symmetric outflow throughout. This assumption may be poor; but the usual arguments against spherical outflows are weakened in the case of Lyman-break galaxies because (a) the presumed large number of supernovae explosions in Lyman-break galaxies would produce enough energy to blow out a large fraction of the galaxies' baryons, and (b) the disk-like geometry that is thought to produce bi-polar outflows may be rarer at $z \sim 3$, when the halo merging time is short. In any case, the rough numbers derived in this section will at best be only broadly indicative of the physical situation.

The velocity of a wind as it leaves its galaxy's potential $v_0 \sim (v^2(3\mathrm{kpc}) - v_{\mathrm{esc}}^2(3\mathrm{kpc}))^{1/2}$ will be $v_0 \sim 500$ km s^{-1} for the estimates $v(3\mathrm{kpc}) = 600$ km s^{-1} and $v_{\mathrm{esc}}(3\mathrm{kpc}) = 360$ km s^{-1} discussed above. The surrounding intergalactic material has a sound speed of $c_s \sim \sqrt{3kT/m_p} \sim 20$ km s^{-1} (e.g., Schaye et al. 1999; Ricotti, Gnedin, & Shull 2000; Bryan & Machacek 2000), and so a shock will result when it is struck by the galaxy's wind. Idealized treatments of spherically symmetric shocks (e.g., Weaver et al. 1977; Ostriker & McKee 1988) show that an advancing shock will sweep up the material it encounters, leaving behind it a largely empty cavity surrounded by a thin dense shell. The situation resembles an expanding bubble. Will the shell produce detectable Lyman-α absorption?

At first it may not. In the strong shock limit $v_{\mathrm{sh}} \gg c_s$, the Rankine-Hugoniot

jump conditions for an ionized gas with an adiabatic index $\gamma = 5/3$ imply that material just behind the shock will have a temperature of $T = 3\mu v_{\rm sh}^2/16k_B \simeq 3.4\times10^6(v_{\rm sh}/500{\rm km\,s^{-1}})^2$ K and a density $\rho_{\rm gas}$ of 4 times the global mean $(1+z)^3\Omega_b\rho_{\rm cr}$. Here $\mu \sim 16m_p/27$ is the mean mass per particle in the (ionized) gas, and Ω_b is the baryon density expressed in units of the critical comoving density $\rho_{\rm cr} = 1.88h^2\times10^{-29}$ gm cm^{-3}. The hydrogen neutral fraction in the shocked gas should be close to its equilibrium value, since recombination and photoionization can both significantly alter the neutral hydrogen density on short time-scales: $|n_{\rm HI}/\dot{n}_{\rm HI}|$ is roughly equal to $t_{\rm rec} \equiv \eta/n_e\alpha \sim 10^5$yr when the change in $n_{\rm HI}$ is solely due to recombination and is equal to $t_{\rm photo} \equiv 1/\Gamma_{\gamma H} \sim 10^4$yr for when the change in $n_{\rm HI}$ is solely due to photoionization. The numerical value for $t_{\rm rec}$ assumes a neutral fraction $\eta \sim 10^{-5}$, a temperature of 10^6K, and an electron number density n_e equal to 20 times the cosmic mean hydrogen density at $z \sim 3$, and uses Cen's (1992) fitting formula for the recombination coefficient α; the numerical value for $t_{\rm photo}$ assumes an ionization rate $\Gamma_{\gamma H}$ appropriate for the ionizing background of equation 4.F.1 below. Except for very early in the shock's evolution, the total mass of the shocked material and its characteristic temperature or density will not change significantly on time scales so short. Figure 4.26 shows contours of constant hydrogen neutral fraction in photoionization equilibrium as a function of overdensity and temperature for a gas that is 76% H and 24% He by mass. The abundances of different species were calculated as described in Katz, Weinberg, & Hernquist (1996, §3) for an assumed ionizing background radiation intensity of

$$J_\nu = 1.2(h\nu/13.6{\rm eV})^{-1.8}\times10^{-21} \qquad {\rm erg\,s^{-1}\,cm^{-2}\,Hz^{-1}\,sr^{-1}} \tag{4.F.1}$$

(e.g., Steidel, Pettini, & Adelberger 2001).

If all the material within a proper radius r_p has been swept into a thin spherical

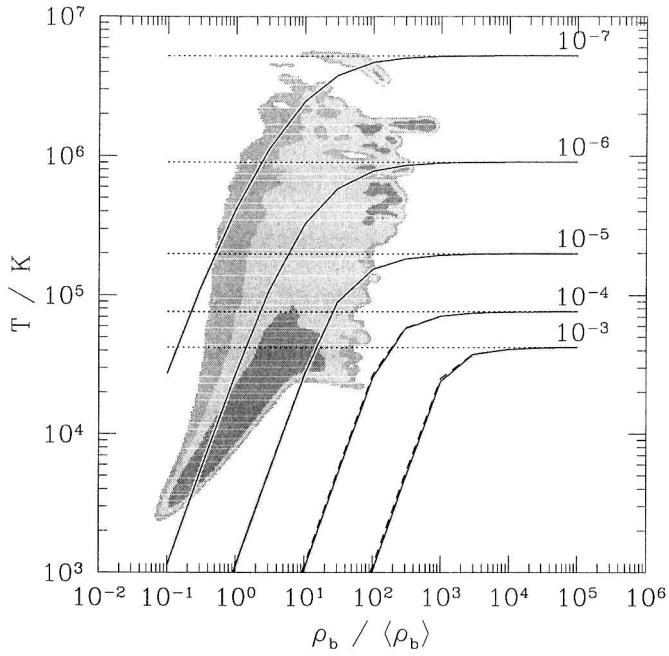

Figure 4.26 Neutral fraction at $z \sim 3$ in photoionization equilibrium. Lines show contours of constant neutral fraction in the temperature-density plane for a gas that is 76% H and 24% He by mass. Densities are expresses in terms of the universal mean proper baryon density $\langle\rho_b\rangle \equiv \Omega_b(1+z)^3\rho_{\rm cr}$ where $\rho_{\rm cr}$ is the (comoving) critical density of the universe. Solid lines assume the ionizing background of equation 4.F.1; dotted lines assume a negligible ionizing background. The shaded regions show the temperature and density of 68%, 90%, and 95% of the baryonic mass at $z = 3$ in the SPH simulation described in White et al. 2001.

shell, the HI column density along a line from the outside to the center of the shell is

$$\begin{aligned} N_{\rm HI} &= \eta r_p \Omega_b \rho_{\rm cr}(1+\bar{\delta})(1+z)^3/4m_H \\ &\simeq 1.25\eta \times 10^{19} \left(\frac{r_p}{125{\rm kpc}}\right)\left(\frac{\Omega_b h^2}{0.02}\right)\left(\frac{1+\bar{\delta}}{9}\right)\left(\frac{1+z}{4}\right)^3 \quad {\rm cm}^{-2} \quad (4.{\rm F}.2) \end{aligned}$$

where η is the hydrogen neutral fraction and $\bar{\delta}$ was the mean overdensity of material in the sphere before it was swept into the shell. Equation 4.F.2 assumes a hydrogen mass fraction of 3/4. The value $\bar{\delta} \sim 8$ follows from assuming that the galaxy–mass cross-correlation function is a power-law, $\xi_{\rm gm} \simeq (r_c/r_{gm})^{-\gamma}$, which implies that the mean overdensity in a large sphere of comoving radius $r_c \equiv (1+z)r_p = 0.5h^{-1}$ Mpc

surrounding a Lyman-break galaxy is

$$\bar{\delta} \sim \frac{3r^{-\gamma}}{(3-\gamma)r_{gm}^{-\gamma}}, \tag{4.F.3}$$

and from adopting $\gamma = 1.55$ and $r_{gm} = 300h^{-1}$ proper kpc. The adopted slope is similar to the slopes of the galaxy–galaxy or matter–matter correlation functions; the adopted cross-correlation length is not much lower than the maximum $r_{gm} \sim r_0 b^{-1/\gamma} \sim 500h^{-1}$kpc that Lyman-break galaxies' correlation length r_0 and bias b can allow (see, e.g., appendix 4.B). Equations 4.F.2 and 4.F.3 both assume that the mass of swept up material dominates the mass of the galaxy's ejecta, and so they do not hold at arbitrarily early times (see below). Since $\eta \sim 10^{-6}$–10^{-7} at the shell temperature of a few times 10^6K appropriate to a shock moving at ~ 500 km s^{-1}, equation 4.F.2 shows that a young and fast-moving wind shell from a galaxy will produce little Lyman-α absorption. The total absorption will be no stronger than the absorption due to the weakest lines in the forest, and the high temperature will spread the absorption over a wide range of velocities and make it hard to detect. This illustrates one weakness in attempts to use the similarities of the Lyman-α forest along adjacent QSO sightlines to place limits on the fraction of the ISM that has been disturbed by winds (e.g., Rauch et al. 2001): young winds will tend to erase absorption in the intergalactic medium and make the Lyman-α forests in the spectra of QSO pairs resemble each other more, not less. This is especially true since most of the volume affected by the wind will be occupied by the hot rarefied gas of the bubble's interior. The cooler and denser shell may produce some Lyman-α absorption, but the hot interior certainly will not.

As the shell propagates into the intergalactic medium, it will be slowed by the material it encounters and the post-shock temperature will begin to drop. Eventually the shell will stall. If this happens at a radius of $\sim 0.5h^{-1}$ comoving Mpc, the final density of the shell will be roughly 4 times the ambient density at this radius, or ~ 15

times the mean baryon density (using the approximate galaxy-matter correlation function above), and the temperature will be of order 10^5K. The shell's equilibrium neutral fraction will be $\eta \sim 10^{-5}$, corresponding to a somewhat stronger absorption line with $N_{\rm HI} \sim 1 \times 10^{14}$ cm^{-2}. The estimated column density is uncertain because it is not obvious what the density of the shell will be; the weakening of the shock will lower the post-shock density, but material in the interior will tend to pile up at the shock front and increase the density (e.g., Ostriker & McKee 1988, §9).

These calculations neglect another potentially important complication: the shell may cool significantly from its high post-shock temperature. Figure 4.27 shows the cooling time $E_{\rm gas}/\dot{E}_{\rm gas}$ in photoionization equilibrium as a function of overdensity and temperature for a gas at $z = 3$ that is 76% H and 24% He by mass. The abundances of different species and the resulting heating and cooling rates were calculated as described in Katz, Weinberg, & Hernquist (1996, §3). Curves of constant cooling time are shown for the ionizing background of equation 4.F.1; for an ionizing background similar to 4.F.1 except with a large decrement at 4Ryd, which is more appropriate if galaxies are the source of the background or if HeII has not yet been reionized at $z \sim 3$; and for no ionizing background at all, which is appropriate for regions with the highest optical depths. The plot suggests that hydrogen and helium cooling is unlikely to be important for most of the evolution of a shell at $z \sim 3$. Cooling times are long for the temperatures $T \gtrsim 10^6$K appropriate to the early phases of the shell's evolution, and they remain longer than Lyman-break galaxies' star-forming lifetimes of $\sim 3 \times 10^8$yr (Shapley et al. 2001) even as the shell begins to stall with $\rho_b/\langle\rho_b\rangle \lesssim 20$ and $T \lesssim 10^5$K.

The metals in the wind might be able to increase the importance of cooling, however. The outflow's metallicity is not necessarily low. We can place an upper limit on the metallicity as follows. Each supernova ejects approximately one solar mass of metals (e.g., Woosley & Weaver 1995). Roughly 10^8 supernovae will explode

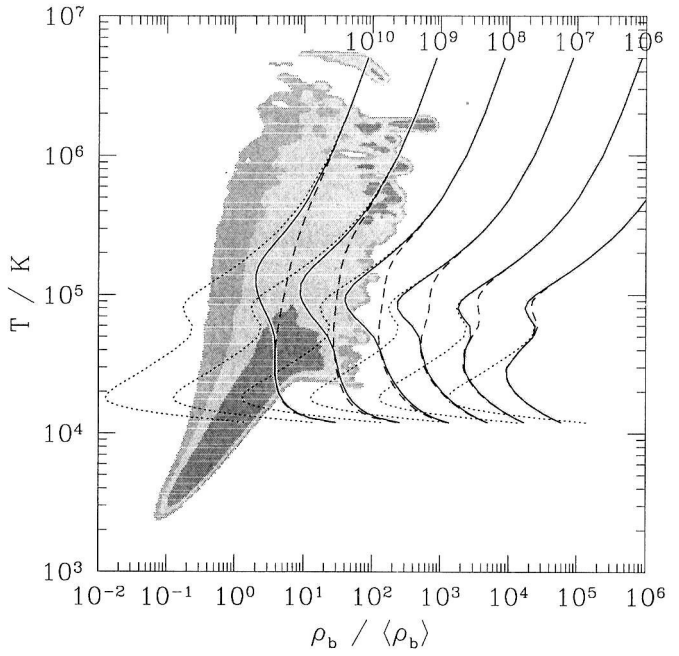

Figure 4.27 Cooling time $|\dot{E}/E|$ at $z = 3$ for a gas in photoionization equilibrium that is 76% H and 24% He by mass. Dashed lines are appropriate for the ionizing background of equation 4.F.1; solid lines for the same background except with a large decrement at 4Ryd; and dotted lines for a negligible ionizing background. Labels show the cooling times in years. Shaded regions show the characteristic density and temperature of most baryons at this redshift in the SPH simulation described in White et al. 2001. See figure 4.26.

during the formation of the typical Lyman-break galaxy's stellar mass of $\sim 10^{10} M_\odot$ (see, e.g., Shapley et al. 2001). Because the sun is approximately 2% metals by mass, the $\sim 10^8 M_\odot$ of metals ejected by the supernovae will be sufficient to pollute $\sim 5 \times 10^9 M_\odot$ of pristine baryons to solar metallicity. At a comoving radius of $0.5h^{-1}$ Mpc, the swept-up mass of the shell will be $\sim 2.5 \times 10^{10} M_\odot$ for $\bar{\delta} = 8$ and $\Omega_b h^2 = 0.02$, and so the shell could have a metallicity of $\sim 0.2 Z_\odot$ if it contained all the metals ejected by its galaxy's supernovae. Cooling rates can be significantly altered at a metallicity this high, especially for $T \gtrsim 10^5$K. The uncertainty in shells' metallicity is one of many things that makes it difficult to predict their absorption spectra with much confidence.

One thing appears reasonably likely, however: the ultimate effect of large-scale winds from galaxies should be an increase in the HI content of the intergalactic medium. In the photoionization-dominated regime where the neutral fraction is proportional to the recombination rate, $\eta \propto \rho T^{-0.7}[1 + (T/10^6\mathrm{K})^{0.7}]^{-1}$ (Cen 1992, equation 27a), the equilibrium HI content of a volume element of gas with $T \ll 10^6$K will increase when it is swept up by a shock and compressed by a factor of 4 provided that its temperature is raised by less than a factor of 7.25. If the typical temperature of the IGM is $\sim$ 20000K, this occurs when the post-shock temperature is lower than $\sim$ 150000K, or when the shock speed is $\lesssim 100$ km s^{-1}. A more careful calculation takes into account the dependence of the post-shock density and temperature on Mach number M (see, e.g., Shu 1992, equations 15.35 and 15.37). In the regime where the neutral fraction is proportional to the recombination rate, this calculation shows that the density of neutral hydrogen in the shell will be higher than the density in an unshocked medium with $T = 20000$K provided $M \lesssim 8.9$, and that the neutral fraction in the shell will be higher than the neutral fraction in the unshocked medium provided $M \lesssim 3.4$. There are two implications. First, shells will contain a higher density of neutral hydrogen than unshocked regions when the shock velocity has lowered to $8.9c_s \sim 180$ km s^{-1}. This is roughly the velocity where one might expect shells to stand out in absorption. Second, by the time the shock has slowed to $3.4c_s \sim 70$ km s^{-1}, the shocked volume will contain more neutral hydrogen than it contained before it was shocked. These quantitative statements depend upon our poor assumption that the wind shells are spherically symmetric and do not cool. But the qualitative result is more general. Winds driven by galaxies will stall eventually. When this happens, the shells' temperatures will be similar to the temperature of the surrounding medium, but their density, recombination rate, and neutral fraction will remain significantly enhanced. This is especially true because cooling will be accelerated by the metals winds contain.

4.G Wind evolution

We argued above that a typical outflow at $z \sim 3$ could plausibly escape its galaxy's potential. This section will consider what happens to the outflow as it propagates into the intergalactic medium.

4.G.1 Initial

We begin by discussing how the wind propagates into the intergalactic medium while the galaxy is still forming stars. Fits to the spectral energy distributions of Lyman-break galaxies (e.g., Shapley et al. 2001) suggest that they typically form stars for $\sim$ 300Myr. The behavior of the wind will depend on the mass of the ejecta $M_{\rm ej}$ relative to the mass of swept up intergalactic material $M_{\rm swept}$. At early times, when $M_{\rm ej} \gg M_{\rm swept}$, the wind will tear ballistically through the IGM without being significantly slowed. But usually $M_{\rm swept}$ grows more rapidly than $M_{\rm ej}$ as the wind advances. When $M_{\rm swept} \sim M_{\rm ej}$ the wind will have noticeably slowed, and the pace of its advance will begin to be set by the need to accelerate the intergalactic gas it pushes against. How soon will the ejected and swept-up masses be roughly equal? If a Lyman-break galaxy ejects in a wind with initial velocity v_0 a fraction $f_{\rm ej}$ of its baryons at a constant rate during its lifetime $t_{\rm sf}$, the ratio of ejected to swept-up mass at time t will be

$$\frac{M_{\rm ej}}{M_{\rm swept}} = \frac{200 f_{\rm ej} r_{\rm vir}^3 t/t_{\rm sf}}{r_{\rm wind}(t)^3} \tag{4.G.1}$$

where $r_{\rm wind}$ is the distance the wind has advanced, $r_{\rm vir}$ is the galaxy's virial radius, and 200 is the mean overdensity within a virialized object. The equation holds provided the wind advances into intergalactic material at the global mean density. $r_{\rm wind}$ will be roughly equal to $v_0 t$ at early times when $M_{\rm ej}/M_{\rm swept} \lesssim 1$. Substituting $r_{\rm wind} = v_0 t$ into equation 4.G.1 leads to the conclusion that the ejected and swept-up masses will be roughly equal when $t = 250(f_{\rm ej}/0.2)^{1/2}$ Myr. This is nearly equal to the

typical Lyman-break galaxy lifetime of 300Myr. If the IGM surrounding Lyman-break galaxies has close to the global mean density, it is reasonable to assume that the winds move almost ballistically as long as the galaxies are forming stars. The typical wind cavity radius in this case would be roughly equal to the ballistic radius $r_{\rm ball} \equiv v_0 t_{\rm sf} \sim 150$ proper kpc.

It may be more realistic to assume that Lyman-break galaxies tend to be found in dense regions of the universe. If the typical intergalactic overdensity within a radius r of Lyman-break galaxies follows equation 4.F.3, then the ratio of ejected to swept-up mass at time t is

$$\frac{M_{\rm ej}}{M_{\rm swept}} = \frac{200(3-\gamma) f_{\rm ej} t r_{\rm vir}^3 r_{gm}^{-\gamma}}{3 t_{\rm sf} r_{\rm wind}(t)^{3-\gamma}} \qquad (4.G.2)$$

where $r_{gm} \sim 300$kpc is the galaxy–mass correlation length in proper units (§4.F). Under the approximation $r_{\rm wind} \simeq v_0 t$ we find that the ejected and swept-up masses will be roughly equal when $t = 110(f_{\rm ej}/0.2)^{1/(2-\gamma)}$ Myr. This is small enough compared to $t_{\rm sf}$ that the the wind cavity radius may not be roughly equal to the ballistic radius $r_{\rm ball} \equiv v_0 t$ for much of the wind's evolution. A more accurate estimate of $r_{\rm wind}(t)$ will come from solving the equation

$$\dot{r}(t) = v_0 \sqrt{\frac{M_{\rm ej}(t)}{M_{\rm swept}(t) + M_{\rm ej}(t)}}. \qquad (4.G.3)$$

which is inspired by the observation that radiative losses are small and so kinetic energy should be conserved. In the limit $M_{\rm swept} \gg M_{\rm ej}$, the analytic solution to equation 4.G.3,

$$r(t) = \left(200(5-\gamma)^2(3-\gamma) f_{\rm ej} t / 27 t_{\rm sf}\right)^{1/(5-\gamma)} r_{\rm ball}^{2/(5-\gamma)} r_{\rm vir}^{3/(5-\gamma)} r_{gm}^{-\gamma/(5-\gamma)}, \qquad (4.G.4)$$

agrees to better than 6% with the more accurate result of Ostriker & McKee (1988). This limit is unlikely to be reached in practice, however, because the swept-up and ejected masses grow at very similar rates when the density decreases with radius. A numerical solution of 4.G.3 for $\gamma = -1.55$, $r_{\rm vir} = 40$ proper kpc, $r_{gm} = 300$ proper

kpc, $v_0 = 500$ km s^{-1} and an initial radius $r_0 \sim r_{\rm vir}$ shows that in this scenario we should expect a Lyman-break galaxy's wind to advance to $r \sim 150$, 110 proper kpc and slow to ~ 330, 220 km s^{-1} for $f_{\rm ej} = 1.0$, 0.2 during the ~ 300Myr when the galaxy is forming stars.

The observed radius of (apparently) lowered Lyman-α opacity, $\sim 0.5h^{-1}$ comoving Mpc, is comparable to the 300Myr wind radius for any of the scenarios considered here. We conclude that superwinds could plausibly be responsible.

4.G.2 Final

What will happen to a wind once its galaxy stops forming stars? This question has interesting implications for the volume filling factor of perturbed intergalactic material at $z \sim 3$. The calculations above show that the swept-up mass $M_{\rm swept}$ will probably be greater than the ejected mass $M_{\rm ej}$ by the time star-formation ceases at $t_{\rm sf} \sim 300$ Myr. The evolving bubble will likely be in or close to the regime where most of the material lies in a thin dense shell surrounding a hot cavity. In the thin shell approximation (e.g., Weaver et al. 1977; Ostriker & Cowie 1988; Tegmark, Silk, & Evrard 1993), the equations governing the evolution of the bubble after the end of star formation can be expressed as

$$\begin{aligned} \dot{E} &= 0 \\ \dot{E} &= \dot{r}^2 \dot{M}_{\rm swept}/2 - p\dot{V} \\ E &= 3pV/2 \end{aligned} \tag{4.G.5}$$

if radiative losses are small and the thermalized energy of the shock is conducted into the hot interior of the bubble, or

$$\begin{aligned} d(M_{\rm swept} dr/dt)/dt &= 4\pi r^2 p \\ \dot{E} &= -4\pi r^2 p \dot{r} \end{aligned}$$

$$E = 3pV/2 \tag{4.G.6}$$

if radiative cooling of the shell dissipates most of its thermalized energy. E and p are the energy and pressure of the hot interior of the bubble; r is the bubble's radius.

If we set $t = 0$ when the central source turns off, the solution to the set of equations 4.G.5 that matches the boundary conditions is $p(t) \propto (t+a)^{-3\alpha}$ and $r(t) \propto (t+a)^{\alpha}$ with $\alpha = 2/(5-\gamma)$ and $a = \alpha r(0)/\dot{r}(0)$. The solution to 4.G.6 is $p(t) \propto (t+b)^{-5\beta}$, $r(t) \propto (t+b)^{\beta}$, with $\beta = 2/(7-\gamma)$ and $b = \beta r(0)/\dot{r}(0)$.

According to these formal solutions the wind will propagate indefinitely. But in practice it will be brought to rest by one of four effects that our simple treatment has neglected. The wind will stall if (a) the interior pressure in the cavity p becomes comparable to the pressure of the undisturbed intergalactic medium, or (b) the wind slows to the sound speed of the intergalactic medium and dissipates in acoustic waves, or (c) the wind travels far enough to encounter and be subsumed into the receding Hubble flow, or (d) the wind depletes its kinetic energy fighting against the gravitational attraction of the interior matter.

Which of these effects will stall the wind first? When star formation stops, the pressure in the cavity $p = 2E/3V \sim E_i/3V$. The second relationship assumes that roughly half of the total energy E_i ejected from the galaxy will end up in the hot interior cavity (e.g., Weaver et al. 1977). The ratio of the pressure inside and outside the bubble can therefore be approximated as

$$\begin{aligned} \frac{p_{\rm int}}{p_{\rm igm}} &\sim \frac{\mu E_i}{4\pi r_{\rm end}^3 \rho_{\rm igm} k T_{\rm igm}}, \\ &\sim 2300 \left(\frac{E_i}{10^{59}{\rm erg}}\right)\left(\frac{20000}{T_{\rm igm}}\right)\left(\frac{0.02h^{-2}\rho_{\rm cr}}{\rho_{\rm igm}}\right)\left(\frac{120{\rm kpc}}{r_{\rm end}}\right)^3 \end{aligned} \tag{4.G.7}$$

where $\rho_{\rm cr}$ is the proper critical density at $z = 3$, $r_{\rm end} = 120$ is the proper radius of the wind cavity when star formation ceases, and $\mu \sim 16 m_p/27$ is the mean mass per particle in the ionized gas. When the bubble expands after the end of star formation,

its pressure will steadily decrease, as $p_{\rm int} \propto r^{-3}$ if thermalized energy is conserved or $p_{\rm int} \propto r^{-5}$ if it is radiated away. The interior pressure in the bubble will equal the intergalactic pressure when the bubble's radius has grown by a factor of 13 in the former case, 5 in the latter. This sets an upper limit of approximately 2.5–6 comoving Mpc on the stalling radius of the wind. The rapid decline of pressure as the shell expands makes these estimates somewhat insensitive to the numerical values adopted in equation 4.G.7.

We saw above the speed of the shock when star formation stops, $v_{\rm end} \sim v_i(1 + M_{\rm swept}/M_{\rm ej})^{-1/2}$, will likely be $\sim$ 300 km s^{-1}. After the central source turns off, the shock speed declines as $\dot{r} \propto r^{(\gamma-3)/2}$ for adiabatic shocks and as $\dot{r} \propto r^{(\gamma-5)/2}$ for radiative shocks. The shock will dissipate into sound waves when its speed decreases by a factor of $\sim$ 15 and becomes equal to the $\sim$ 20 km s^{-1} sound speed in the intergalactic medium. This will happen when the shell radius has grown by a factor of 40 and 5, respectively. These limits on the stalling radius are not more restrictive than the limits derived above.

If a wind travels far from a Lyman-break galaxy, the material it encounters will be flowing away from the galaxy with the general cosmic expansion. Eventually the encountered material will be moving away from the galaxy almost as rapidly as the wind itself. At this point the wind is effectively dead. The hot interior will cool adiabatically without the input of heat from shock collisions at the frontiers. The shell, robbed of its central engine, will drift in the cosmic flow. How soon will this happen? We need some estimate of how the matter surrounding Lyman-break galaxies is moving relative to the galaxies. A rough estimate of the velocity profile of material around a Lyman-break galaxy can be derived if we assume that each galaxy resides in a spherically symmetric overdensity. The proper radius r_p of a spherically symmetric

region with mean overdensity $\bar{\delta}$ evolves according to

$$\frac{\dot{r}_p}{r_p} = H - \frac{1}{3(1+\bar{\delta})}\frac{d\bar{\delta}}{dt} \tag{4.G.8}$$

where $H(t)$ is the Hubble parameter. This follows from the fact that concentric shells of matter do not cross until just before final collapse. In the spherical Zeldovich approximation, where the linear overdensity density $\bar{\delta}_L$ is related to the true overdensity through $1 + \bar{\delta} = (1 - \bar{\delta}_L/3)^{-3}$, equation 4.G.8 reduces to

$$\frac{\dot{r}_p}{r_p} = H\Big[1 + f - f\,(1 + \bar{\delta}(r_p))^{1/3}\Big] \equiv Hg(r_p) \tag{4.G.9}$$

where $f \equiv d\ln D/d\ln a \simeq 1$, $D(t)$ is the linear growth factor and $a(t)$ is scale factor of the universe. The approximate equality for f holds provided $\Omega_M \simeq 1$, which is true at $z \sim 3$. Equation 4.G.9 provides a simple but rough estimate of the proper velocity of the material that surrounds a perturbation with mean density $\bar{\delta}$. If $\bar{\delta} = 0$, there is no overdensity and neighboring material simply moves with the unperturbed Hubble flow; if $\bar{\delta} = 7$, we are at the edge of a perturbation that is just turning around and nearby material will be at rest with respect to the perturbation's center; if $\bar{\delta} > 7$ the surrounding material will be approaching on the center of the perturbation. The actual overdensity at turn-around for a spherical perturbation is $\bar{\delta} \sim 4.5$, showing that equation 4.G.9 is acceptably accurate only for rough calculations.

The velocity of the surrounding material must be compared to the velocity of the wind itself. If the growth of the wind cavity obeys $r(t) \propto (t + a)^{\alpha}$ (see above), then $\dot{r}/r = \alpha/(t + a)$. A few lines of algebra show that the proper velocity of the perturbed Hubble flow $\dot{r}_p$ will equal the proper velocity of the wind at a radius that satisfies $r_{\rm stall}g^{\alpha}(r_{\rm stall}) = r(0)(\dot{r}(0)/Hr(0))^{\alpha}$ where $r(0)$ and $\dot{r}(0)$ are the wind's radius and velocity at $t = 0$. Adopting $r(0) = 130$ proper kpc and $\dot{r}(0) = 270$ km s^{-1} for the sake of illustration (see above), calculating $\bar{\delta}$ from the values $r_{gm} = 300$ proper kpc, $\gamma = 1.55$, and taking $H = 450h$ km s^{-1} Mpc^{-1}, which is roughly appropriate

for an $\Omega_M = 0.3$, $\Omega_\Lambda = 0.7$ cosmology at $z = 3$, we find $r_{\rm stall} \sim 400$ proper kpc for $\alpha = 2/(5-\gamma)$ and $r_{\rm stall} \sim 300$ proper kpc for $\alpha = 2/(7-\gamma)$. The rapid decline of the wind velocity with radius implies first that these stalling radii are relatively insensitive to the adopted values of the parameters, and second that the wind velocity will be much bigger than the recession velocity of the surrounding material (as our treatment assumes) until just before the end.

How far out of the galaxy's potential will the wind be able to push the intergalactic medium before its kinetic energy is exhausted? Suppose the distribution of matter around a Lyman-break galaxy is roughly spherically symmetric. The work required to bring a shell of baryonic mass $\delta M = 4\pi r^2 \rho_b(r) dr$ from radius r_1 to r_2 is $\delta W = \delta M \int_{r_1}^{r_2} dr' \, GM(<r')/r'^2$ where $M(<r)$ is the total (dark plus baryon) mass within radius r. Provided $\Omega_b \ll \Omega_M$, the work required to lift all baryons within the radius r_2 to the radius r_2 is

$$W \simeq \int_0^{r_2} dr_1 \, 4\pi r_1^2 \rho_b(r_1) \int_{r_1}^{r_2} dr' \, \frac{GM(<r')}{r'^2}, \tag{4.G.10}$$

which reduces to

$$\begin{aligned} W &\simeq \frac{16\pi^2 G \bar\rho_b \bar\rho_M r_{gm}^{2\gamma}}{(3-\gamma)(2-\gamma)} \left[\frac{r_2^{5-2\gamma}}{3-\gamma} - \frac{r_2^{5-2\gamma}}{5-2\gamma} \right] \\ &\simeq 1.2 \times 10^{59} \left(\frac{r_{gm}}{300{\rm kpc}} \right)^{2\gamma} \left(\frac{r_2}{300{\rm kpc}} \right)^{5-2\gamma} \quad {\rm erg} \end{aligned} \tag{4.G.11}$$

if the original density of baryons and matter around the galaxy had a power-law radial dependence, $\rho_b(r) = \bar\rho_b (r/r_{gm})^{-\gamma}$ and $\rho_M(r) = \bar\rho_M (r/r_{gm})^{-\gamma}$, with $\bar\rho_b$ and $\bar\rho_M$ the universal proper densities of baryons and matter. The numerical values in equation 4.G.11 assume $\Omega_b h^2 = 0.02$, $\Omega_M = 0.3$, $\Omega_\Lambda = 0.7$, $h = 0.7$, $\gamma = -1.55$, and $z = 3$. Since 10^{59} erg is roughly the energy emitted by a typical Lyman-break galaxy's $\sim 10^8$ supernovae (§ 4.E.3), the equation shows that the wind's kinetic energy will be exhausted at a proper radius $r_{\rm stall} \sim 300 f_k^{1/(5-2\gamma)}{\rm kpc} \sim 300 f_k^{1/2}{\rm kpc}$ where f_k is the fraction of the supernova energy that goes into the kinetic energy of the wind. This

is the most restrictive limit on the wind radius that we have seen. Gravity will likely cause the winds to stall, and this will happen when they reach a comoving radius of ~ 1 Mpc.

It is easy to calculate the time it would take the wind to reach this radius in the absence of gravity. A wind whose radius evolves as $r(t) \propto (t+b)^{\nu}$ will reach a radius x times larger than its initial ($t = 0$) radius at a time $(x^{1/\nu} - 1)b$. We saw above that $b = \nu r(0)/\dot{r}(0)$, and that $r(0)/\dot{r}(0)$, the shell's ratio of radius to velocity when star formation terminates, is roughly 400Myr. The time required for the wind to advance from $r(0) = 120$kpc to $r(t) = 300$kpc ($x \sim 2.5$) in the absence of gravity is therefore ~ 900 Myr for adiabatic shocks ($\nu = 2/(5-\gamma)$) and ~ 1.6Gyr for radiative shocks ($\nu = 2/(7-\gamma)$). The winds set in motion by Lyman-break galaxies will coast for roughly this time before gravity brings them to rest at a comoving radius of ~ 1Mpc.

What will become of a stalled wind? Denser parts of the shell may become gravitationally unstable, collapse, begin to form stars (e.g., Natarajan, Sigurdsson, & Silk 1998). The material in less dense parts of the shell may begin to stream back into the emptied cavity, though any progress would be slow: at a sound speed of $c_s \sim 20$ km s^{-1} it would take $\sim 10^{10}$ years for it to reach the center of the cavity. In practice the material of the shell will be brought towards the center more quickly by the continued action of gravitational instability. This will also crush the empty cavity itself. The time it will take for gravitational collapse to decrease the cavity's volume by a factor of two can be estimated as follows. If the dark matter overdensity within the cavity when the shell stalls is $\bar{\delta}_i \sim 2$, the density will be $\bar{\delta}_f \sim 5$ by the time gravitational collapse has shrunk the cavity and the dark matter it contains to half of the initial volume. According to Mo & White's (1996) fit to the relationship between linear and non-linear densities (δ_L, δ_{NL}) in the spherical collapse model,

$$\delta_L = -1.35(1+\delta_{NL})^{-2/3} + 0.78785(1+\delta_{NL})^{-0.58661} - 1.12431(1+\delta_{NL})^{-1/2} + 1.68647, \quad (4.G.12)$$

the linear densities corresponding to $\bar{\delta}_i = 2$ and $\bar{\delta}_f = 5$ are $\bar{\delta}_L = 0.80$, 1.09. For an $\Omega_M \simeq 1$ universe (e.g., the universe at $z \sim 3$), linear overdensities grow by a factor $1.09/0.80 \sim 1.36$ when the scale factor of the universe increases by a factor of 1.36, and so a baryon-free cavity that stalled at $z = 3$ would not be crushed to half of its initial volume until $z \simeq 1.93$, some 1.3 Gyr later. The total lifetime of a shell, including its initial expansion while the galaxy shone, its subsequent coasting to a stalling radius of $\sim$ 1 comoving Mpc, and its final collapse, would therefore be $\sim$ 2–3 Gyr, or roughly 10 times the typical Lyman-break galaxy's estimated lifetime. If each shell has a time-averaged radius of $\sim$ 1 comoving Mpc, and the total number density of shells is $\sim$ 10 times the observed comoving number density of Lyman-break galaxies $n_{\rm LBG} \sim 4 \times 10^{-3} h^3$ Mpc^{-3}, then the mean volume filling fraction of shells would be $\sim$ 20% and might approach unity within the largest galaxy overdensities. Although any metals in the wind may have temporarily escaped the galaxy's potential, a simple calculation suggests that many of them will be re-incorporated into the galaxy eventually: the total mass enclosed within the final shell radius of $\sim 1 h^{-1}$ comoving Mpc, $\sim 10^{12} M_\odot$, is significantly smaller than the expected mass of most Lyman-break galaxies' descendents at $z \sim 0$ (e.g., Governato et al. 1998).

4.H CIV in the Lyman-α forest

A full discussion of the relationship between metals in the Lyman-α forest and galaxies will be presented elsewhere (Steidel et al. 2002, in preparation). The aim of this section is to justify a few general statements about the relationship between CIV systems and Lyman-break galaxies that we have observed. The distribution among different ionization states for a small amount of carbon in ionization equilibrium with a gas that is 76% H and 24% He by mass can be straightforwardly calculated by recognizing that in equilibrium the rate of ionization from the ith to the $i+1 \equiv j$th

ionization state will equal the rate of recombination from the jth to the ith ionization state. This leads to a set of six coupled equations of the form

$$\Gamma_{e,i\to j} n_e n_i + \Gamma_{\gamma,i\to j} n_i + \Gamma_{\mathrm{HII},i\to j} n_i n_{\mathrm{HII}} = (\alpha^R_{j\to i} + \alpha^D_{j\to i}) n_j n_e + \alpha_{\mathrm{HII},j\to i} n_{\mathrm{HII}} n_j + \alpha_{\mathrm{HeI},j\to i} n_{\mathrm{HeI}} n_j \quad (4.\mathrm{H}.1)$$

for the relative density of carbon n_i, n_j in the ith and jth ionization states. The terms Γ and α are reaction rates, for collisional ionization ($\Gamma_{e,i\to j}$; Voronov 1997), photoionization ($\Gamma_{\gamma,i\to j}$; derived from the cross-sections of Verner et al. 1996), HII charge-transfer ionization ($\Gamma_{\mathrm{HII},i\to j}$; Kingdon & Ferland 1996), radiative recombination ($\alpha^R_{j\to i}$; Verner & Ferland 1996; Shull & van Steenberg 1982), dielectric recombination ($\alpha^D_{j\to i}$; Shull & van Steenberg 1982; Nussbaumer & Storey 1983), and HI and HeI charge-transfer recombination ($\alpha_{\mathrm{HI},j\to i}$, $\alpha_{\mathrm{HeI},j\to i}$; Kingdon & Ferland 1996). The equilibrium density of electrons, n_e, and of hydrogen and helium in different ionization states, $n_{\mathrm{H}x}$, $n_{\mathrm{He}x}$, can be roughly estimated under the assumption that the gas is composed solely of hydrogen and helium (see, e.g., Katz, Weinberg, & Hernquist 1996 §3). The six equations above therefore contain seven unknowns, the n_i. The system of equations is closed by a seventh relationship $\sum_i n_i = n_{\mathrm{C}}$ stating that the sum of the densities of carbon in each ionization state must equal the total density of carbon. Solving these equations for the equilibrium density CIV leads to the results shown in figures 4.28, 4.29, and 4.30.

Figure 4.28 shows the fraction of carbon f_{CIV} that is in the fourth ionization state as a function of baryon temperature T and density ρ_b. The shape of the f_{CIV} contours is easy to understand. As $\rho_b \to \infty$, the ionization balance of carbon is dominated by collisions and the background radiation becomes unimportant. In this regime f_{CIV} peaks at $T \sim 10^5$K; at lower temperatures the weak collisions can only rarely create CIV, while at higher temperatures the strong collisions destroy CIV. In the opposite limit $\rho_b \to 0$, the background radiation field will ionize carbon many times before a

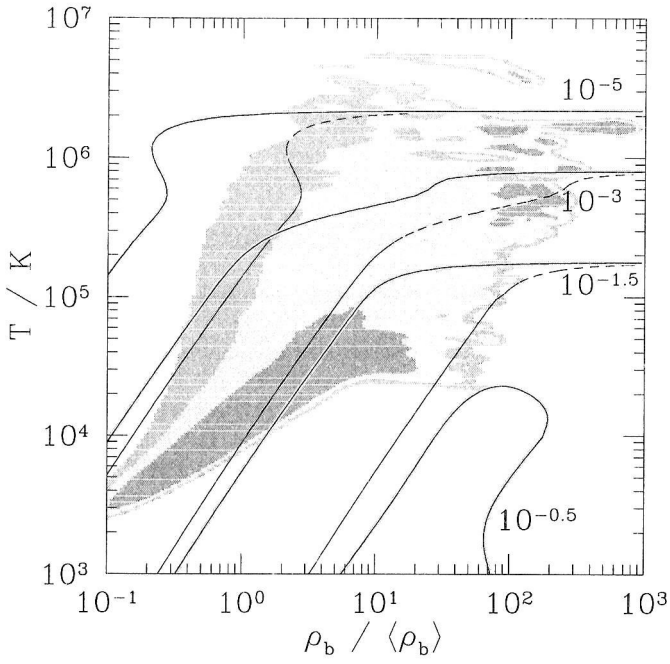

Figure 4.28 The fraction of carbon that is triply ionized (CIV) for a gas of nearly primordial composition in ionization equilibrium with a uniform radiation field. Thin dashed lines are appropriate for the background radiation of equation 4.F.1; thick solid lines for the same background except with a factor of 10 reduction at $h\nu > 4$Ryd. The shaded region shows the expected density and temperature of intergalactic material at $z \sim 3$; see the caption of figure 4.26.

collision leads to recombination. In this regime the equilibrium state of carbon is set by the need for photoionizations to happen as rarely as recombinations, and that will be the case only if carbon is so highly ionized that its cross-section for further photoionization becomes tiny. Only as the density increases and recombinations become more common can ionization equilibrium tolerate a photoionization cross-section as large as CIV's. This explains the increase of $f_{\rm CIV}$ with ρ_b in the low density regime. Also shown on the figure are the characteristic densities and temperatures of particles in the $z \sim 3$ SPH simulation described by White et al. (2001). The intergalactic medium at $z \sim 3$ evidently lies closer to the second (low density) regime than the first. The gas near galaxies will presumably be denser than the global average, and as

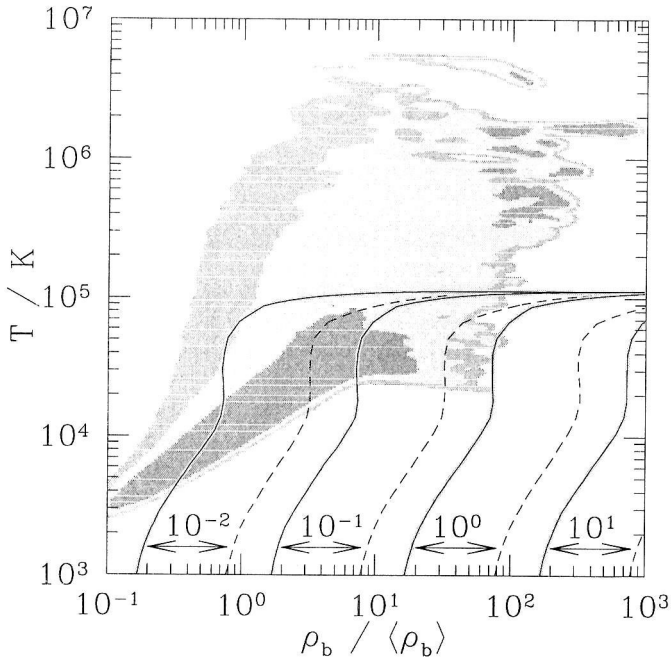

Figure 4.29 Similar to figure 4.28, except now the contours show the intensity of the background radiation field that will maximize the fraction of carbon that is triply ionized. Labels on the contours refer to the intensity of the background radiation at $h\nu = 1\text{Ryd}$ in units of 10^{-21} erg s^{-1} cm^{-2} Hz^{-1} sr^{-1}.

a result its CIV fraction $f_{\rm CIV}$ will be elevated compared to the global mean. This may account for some of the association between galaxies and CIV systems that we have observed (cf. figure 4.6): even if [C/H] were constant in the intergalactic medium, the density of carbon would be higher than average in the dense environments where galaxies reside, and the density of CIV would be particularly enhanced due to changes with density in carbon's ionization state.

Figure 4.29 shows the intensity of background radiation $J_{21}^{\rm max}$ required to maximize $f_{\rm CIV}$ at each density and temperature. The shape of the contours on this plot are closely related to the shape of the contours on figure 4.28. In the high density limit, intense background radiation will increase $f_{\rm CIV}$ when temperatures are low and CIV is rarely created by collisions, but will aid collisional ionization in the destruction of

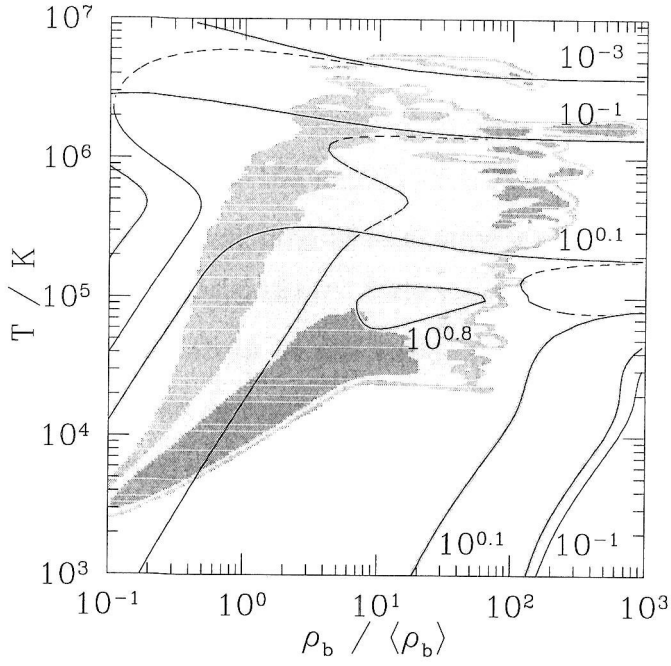

Figure 4.30 Similar to figure 4.28, but these contours show the ratio $n_{\rm CIV}/n_{\rm HI}$ for a gas with solar carbon abundance. The upper limit $n_{\rm CIV}/n_{\rm HI} \lesssim 6$ for solar carbon abundance shows that gas at the mean intergalactic metallicity [C/H] ~ -2.5 should not have a ratio $n_{\rm CIV}/n_{\rm HI}$ greater than ~ 0.02. The measured ratio in gas near to Lyman-break galaxies can exceed this maximum by a large amount, showing that the gas is enriched well beyond the intergalactic mean.

CIV at temperatures $T \gtrsim 10^5$K. In the low density limit, the equilibrium requirement that photoionizations happen as seldom as recombinations will force carbon into ever high ionization states as the radiation intensity is increased. The comparatively low ionization state of CIV will be significantly populated only if the radiation intensity is low. This explains the decrease in $J_{21}^{\rm max}$ towards lower density in the figure. Comparison of the contours in figure 4.29 to the expected temperature and density of the intergalactic medium shows that the density of CIV would (in most cases) increase if the intensity of the ionizing background were lowered from its likely value $J_\nu \sim 0.1\text{–}1\times10^{-21}$ erg s^{-1} cm^{-2} Hz^{-1} sr^{-1}. This demonstrates that the strong CIV

absorption observed within $\sim 0.5h^{-1}$ comoving Mpc of some Lyman-break galaxies (cf. figure 4.14) cannot be attributed to the ionizing radiation they may emit. The effect goes in the opposite direction; any increase in radiation intensity close to Lyman-break galaxies would likely reduce the density of CIV.

Figure 4.30 shows the ratio $\eta \equiv n_{\rm CIV}/n_{\rm HI}$ in ionization equilibrium for a (76% H, 24% He) gas with solar carbon abundance. This ratio depends sensitively on the possible presence of a break at 4Ryd in the background radiation field, since reducing the radiation at $h\nu > 4$Ryd makes it harder for CIV to be ionized to CV but does not much affect the density of HI. Nevertheless the plot suggests that most intergalactic gas would likely have $0.1 \lesssim \eta \lesssim 3$, though the ratio could be driven as high as ~ 6 if the temperature and density were carefully chosen and if the intensity of the background radiation decreased sharply at $h\nu > 4$Ryd. If the actual abundance of carbon in the gas were [C/H] ~ -2.5, or $\sim$ one 300th solar, characteristic of the intergalactic medium at $z \sim 3$ (e.g., Davé et al. 1998), one would expect η typically to be $\sim 10^{-3}$–10^{-2} and never to exceed $\eta_{-2.5}^{\rm max} \sim 2 \times 10^{-2}$. The fact that the observed ratio $n_{\rm CIV}/n_{\rm HI}$ in gas close to Lyman-break galaxies sometimes exceeds $\eta_{-2.5}^{\rm max}$ by an order of magnitude (cf. the final entry in table 4.2) shows that the metallicity of this gas must be significantly higher than the mean [C/H] ~ -2.5, an observation consistent with the idea that we are observing galaxies enriching their surroundings with metals.

Adelberger, K. L. & Steidel, C. C. 2000, *Astrophys. J.*, **544**, 218.

Adelberger, K. L., Steidel, C. C., Giavalisco, M., Dickinson, M., Pettini, M., & Kellogg, M. 1998, *Astrophys. J.*, **505**, 18.

Adelberger, K. L. 2000, in Clustering at High Redshifts, eds. A. Mazure, O. Le Fèvre, & V. Le Brun, *Astron. Soc. Pac. Conf. Ser.*, **200**, 13.

Alcock, C. & Paczynski, B. 1979, *Nature*, **281**, 358.

Balogh, M. L., Pearce, F. R., Bower, R. G., & Kay, S. T. 2001, *Mon. Not. Roy. Astron. Soc.*, **326**, 1228.

Bajtlik, S., Duncan, R. C., & Ostriker, J. P. 1988, *Astrophys. J.*, **327**, 570.

Bardeen, J.M., Bond, J.R., Kaiser, N., & Szalay, A.S. 1986, *Astrophys. J.*, **304**, 15.

Bryan, G.L. & Machacek, M.E. 2000, *Astrophys. J.*, **534**, 57.

Cen, R. 1992, *Astrophys. J. Suppl.*, **78**, 341.

Cen, R., Miralda-Escudé, J., Ostriker, J. P., & Rauch, M. 1994, *Astrophys. J. Lett.*, **437**, 9.

Cole, S., Aragón-Salamanca, A., Frenk, C. S., Navarro, J. F., & Zepf, S. E. 1994, *Mon. Not. Roy. Astron. Soc.*, **271**, 781.

Cowie, L. L., Songaila, A., Kim, T.-S., & Hu, E. M. 1995, *Astron. J.*, **109**, 1522.

Croft, R. A. C., Weinberg, D. H., Hernquist, L., & Katz, N. 1998, *Astrophys. J.*, **495**, 44.

Davé, R., Hellsten, U., Hernquist, L., Katz, N., & Weinberg, D.H. 1998, *Astrophys. J.*, **509**, 661.

Davis, M. & Peebles, P. J. E. 1983, *Astrophys. J.*, **267**, 465.

Dekker, H., D'Odorico, S., Kaufer, A., Delabre, B., & Kotzlowski, H. 2000, *SPIE*, **4008**, 534.

Ellison, S. L., Songaila, A., Schaye, J., & Pettini, M. 2000, *Astron. J.*, **120**, 1175.

Fall, S. M. & Pei, Y. C. 1993, *Astrophys. J.*, **402**, 479.

Gawiser, E., Wolfe, A.M., Prochaska, J.X., Lanzetta, K.M., Yahata, N., & Quirrenbach, A. 2001, *Astrophys. J.*, **562**, 628.

Giavalisco, M., Steidel, C. C., & Macchetto, F. D. 1996, *Astrophys. J.*, **470**, 189.

Giavalisco, M. & Dickinson, M. 2001, *Astrophys. J.*, **550**, 177.

Gnedin, N. Y. & Hui, L., 1998, *Mon. Not. Roy. Astron. Soc.*, **296**, 44.

Governato, F., Baugh, C. M., Frenk, C. S., Cole, S., Lacey, C. G., Quinn, T., & Stadel, J. 1998, *Nature*, **392**, 359.

Heap, S. R., Williger, G. M., Smette, A., Hubeny, I., Sahu, M. S., Jenkins, E. B., Tripp, T. M., & Winkler, J. N. 2000, *Astrophys. J.*, **534**, 69.

Heckman, T. M., Lehnert, M. D., Strickland, D. K. & Armus, L. 2000, *Astrophys. J. Suppl.*, **129**, 493.

Hernquist, L., Katz, N., Weinberg, D., & Miralda-Escudé, J. 1996, *Astrophys. J. Lett.*, **457**, 51.

Hogan, C.J., Anderson, S.F., & Rugers, M.H. 1997, *Astron. J.*, **113**, 1495.

Houdré, C. & Pérez-Abreu, V. 1995, *Annals of Probab.*, **23**, 400.

Hui, L. & Gnedin, N. Y. 1997, *Mon. Not. Roy. Astron. Soc.*, **292**, 27.

Hui, L. & Gaztañaga, E. 1999, *Astrophys. J.*, **519**, 622.

Hui, L., Stebbins, A., & Burles, S. 1999, *Astrophys. J. Lett.*, **511**, 5.

Kaiser, N. 1984, *Astrophys. J. Lett.*, **284**, 9.

Kaiser, N. 1987, *Mon. Not. Roy. Astron. Soc.*, **227**, 1.

Kaiser, N. 1991, *Astrophys. J.*, **383**, 104.

Katz, N., Weinberg, D.H., & Hernquist, L. 1996, *Astrophys. J. Suppl.*, **105**, 19.

Kauffmann, G., Colberg, J. M., Diaferio, A., & White, S. D. M. 1999, *Mon. Not. Roy. Astron. Soc.*, **303**, 188.

Kayo, I., Taruya, A., & Suto, Y. 2001, *Astrophys. J.*, **561**, 22.

Kells, W., Dressler, A., Sivaramakrishnan, A., Carr, D., Koch, E., Epps, H., Hilyard, D., & Pardeilhan, G. 1998, *Proc. Astron. Soc. Pac.*, **110**, 1489.

Kingdon, J.B. & Ferland, G.J. 1996, *Astrophys. J. Suppl.*, **106**, 205.

Klein, R.I., McKee, C.F., & Colella, P. 1994, *Astrophys. J.*, **420**, 213.

Landy & Szalay 1993, *Astrophys. J.*, **412**, 64.

Madau, P., Haardt, F., & Rees, M. J. 1999, *Astrophys. J.*, **514**, 648.

Mathews, W. G. & Baker, J. C. 1971, *Astrophys. J.*, **170**, 241.

McDonald, P., Miralda-Escudé, J., Rauch, M., Sargent, W. L. W., Barlow, T. A., Cen, R., Ostriker, J. P. 2000, *Astrophys. J.*, **543**, 1.

McDonald, P., Miralda-Escudé, J., & Cen, R. 2002, *Astrophys. J.*, submitted.

McLean, I.S. et al. 1998, *SPIE*, **3354**, 566.

Miralda-Escudé, J., Haehnelt, M., & Rees, M. J. 2000, *Astrophys. J.*, **530**, 1.

Murdoch, H.S., Hunstead, R.W., Pettini, M., & Blades, J.C. 1986, *Astrophys. J.*, **309**, 19.

Mushotzky, R. F. & Loewenstein, M. 1997, *Astrophys. J. Lett.*, **481**, 63.

Natarajan, P., Sigurdsson, S., & Silk, J. 1998, *Mon. Not. Roy. Astron. Soc.*, **298**, 577.

Navarro, J., Frenk, C., & White, S. D. M. 1997, *Astrophys. J.*, **490**, 493.

Nussbaumer, H. & Storey, P.J. 1983, *Astron. Astrophys.*, **126**, 75.

Oke, J. B. et al. 1995, *Proc. Astron. Soc. Pac.*, **107**, 3750.

Osterbrock, D. E. 1989, in *Astrophysics of Gaseous Nebulae and Active Galactic Nuclei* (Mill Valley: University Science Books.)

Ostriker, J. P. & Cowie, L. L., 1981, *Astrophys. J. Lett.*, **243**, 127.

Ostriker, J. P. & Heisler, J. 1984, *Astrophys. J.*, **278**, 1.

Ostriker, J. P. & McKee, C. F. 1988, *Rev. Mod. Phys.*, **60**, 1.

Pando, J., Feng, L.-L., & Fang, L.-Z. 2001, *Astrophys. J.*, **554**, 841.

Papovich, C., Dickinson, M., & Ferguson, H.C. 2001, *Astrophys. J.*, **559**, 620.

Peebles, P.J.E. 1980, in *The Large-Scale Structure of the Universe* (Princeton: Princeton University Press.)

Pei, Y. C. 1995, *Astrophys. J.*, **438**, 623.

Pen, U.-L. 1999, *Astrophys. J. Lett.*, **510**, 1.

Pettini, M., Shapley, A. E., Steidel, C. C., Cuby, J.-G., Dickinson, M., Moorwood, A. F. M., Adelberger, K. L., & Giavalisco, M. 2001, *Astrophys. J.*, **554**, 981.

Pettini, M., Rix, S.A., Steidel, C.C., Adelberger, K.L., Hunt, M.P., & Shapley, A.E. 2002, *Astrophys. J.*, in press.

Ponman, T.J., Cannon, D.B., & Navarro, J.F. 1999, *Nature*, **397**, 135.

Porciani, M. & Giavalisco, M. 2002, *Astrophys. J.*, in press.

Press, W. H., Flannery, B. P., Teukolsky, S. A., & Vetterling, W. T. 1992, in *Numerical Recipes in C* (Cambridge: Cambridge University Press.)

Quashnock, J.M. & Vanden Berk, D.E. 1998, *Astrophys. J.*, **500**, 28.

Rauch, M., Miralda-Escudé, J., Sargent, W. L. W., Barlow, T. A., Weinberg, D. H., Hernquist, L., Katz, N., Cen, R., & Ostriker, J. P. 1997, *Astrophys. J.*, **489**, 7.

Rauch, M., Sargent, W.L.W., Barlow, T.A., & Carswell, R.F. 2001, *Astrophys. J.*, **562**, 76.

Ricotti, M., Gnedin, N.Y., & Shull, J.M. 2000, *Astrophys. J.*, **534**, 41.

Sargent, W.L.W., Steidel, C.C., & Boksenberg, A. 1988, *Astrophys. J. Suppl.*, **68**, 539.

Schaye, J., Theuns, T., Leonard, A., & Efstathiou, G. 1999, *Mon. Not. Roy. Astron. Soc.*, **310**, 57.

Scott, J., Bechtold, J., Dobrzycki, A. & Kulkarni, V., 2000, *Astrophys. J. Suppl.*, **130**, 67.

Shapley, A.E., Steidel, C.C., Adelberger, K.L., Dickinson, M., Giavalisco, M., & Pettini, M. 2001, *Astrophys. J.*, **562**, 95.

Sheinis, A.I., Miller, J.S., Bolte, M., & Sutin, B.M. 2000, *SPIE*, **4008**, 522.

Shu, F. H. 1992, in *The Physics of Astrophysics, Vol. II: Gas Dynamics* (Mill Valley: University Science Books.)

Shull, J.M. & van Steenberg, M. 1982, *Astrophys. J. Suppl.*, **48**, 95.

Songaila, A. 1998, *Astron. J.*, **115**, 2184.

Spergel, D.N. & Steinhardt, P.J. 2000, *Phys. Rev. Lett.*, **84**, 3760.

Steidel, C. C., Giavalisco, M., Pettini, M., Dickinson, M., & Adelberger, K. L. 1996, *Astrophys. J. Lett.*, **462**, 17.

Steidel, C. C., Pettini, M., & Adelberger, K. L., 2001, *Astrophys. J.*, **546**, 665.

Steidel, C. C., Adelberger, K. L., Giavalisco, M., Dickinson, M., & Pettini, M. 1999, *Astrophys. J.*, **519**, 1.

Steidel, C. C., Adelberger, K. L., Dickinson, M., Giavalisco, M., Pettini, M., & Kellogg, M. 1998, *Astrophys. J.*, **492**, 428.

Storrie-Lombardi, L.J. & Wolfe, A.M. 2000, *Astrophys. J.*, **543**, 552.

Tegmark, M., Silk, J., & Evrard, A. 1993, *Astrophys. J.*, **417**, 54.

Tenorio-Tagle, G., Silich, S. A., Kunth, D., Terlevich, E., & Terlevich, R. 1999, *Mon. Not. Roy. Astron. Soc.*, **309**, 332.

Theuns, T., Mo, H.-J., & Schaye, J. 2001, *Mon. Not. Roy. Astron. Soc.*, **321**, 450.

Thornton, K., Gaudlitz, M., Janka, H.-Th., & Steinmetz, M. 1998, *Astrophys. J.*, **500**, 95.

Verner, D.A., Ferland, G.J., Korista, K.T., & Yakovlev, D.G. 1996, *Astrophys. J.*, **465**, 487.

Verner, D.A. & Ferland, G.J. 1996, *Astrophys. J. Suppl.*, **103**, 467.

Vogt, S.S. et al. 1994, *SPIE*, **2198**, 362.

Voronov, G.S. 1997, *Atom. Dat. Nucl. Dat. Tab.*, **65**, 1.

Weaver, R., McCray, R., Castor, J., Shapiro, P. & Moore, R. 1977, *Astrophys. J.*, **218**, 377.

Weinberg, D. H. 1992, *Mon. Not. Roy. Astron. Soc.*, **254**, 315.

Weinberg, D. H., Miralda-Escudé, J., Hernquist, L., & Katz, N. 1997, *Astrophys. J.*, **490**, 564.

Weinberg, D.H., Katz, N., & Hernquist, L. 1998, *Astron. Soc. Pac. Conf. Ser.*, **148**, 21.

Weymann, R. J., Carswell, R. F., & Smith, M. G. 1981, *Ann. Rev. Astron. Astrophys.*, **19**, 41.

White, M., Hernquist, L., & Springel, V. 2001, *Astrophys. J. Lett.*, **550**, 129.

White, S.D.M. & Rees, M.J. 1978, *Mon. Not. Roy. Astron. Soc.*, **183**, 341.

Woosley, S. E. & Weaver, T. A. 1995, *Astrophys. J. Suppl.*, **101**, 181.

de Young, D. S. 1978, *Astrophys. J.*, **223**, 47.

Zaldarriaga, M., Hui, L., & Tegmark, M. 2001, *Astrophys. J.*, **557**, 519.

Zhang, Y., Anninos, P., & Norman, M. L. 1995, *Astrophys. J. Lett.*, **453**, 57.